



**University of
Leicester**

**Modelling the prompt and afterglow
emission of gamma-ray bursts**

Owen Madoc Littlejohns

Supervisors:

Richard Willingale

Paul O'Brien

Thesis to be submitted for the degree of

Doctor of Philosophy

at the University of Leicester

X-ray & Observational Astronomy Group

Department of Physics and Astronomy

University of Leicester

March 18, 2013

Modelling the prompt and afterglow emission of gamma-ray bursts

Owen Madoc Littlejohns

ABSTRACT

This thesis studies the broadband behaviour of GRBs by fitting a detailed spectral/temporal model to both the prompt and afterglow hard and soft X-ray emission observed by the *Swift* satellite. The prompt emission is decomposed into pulses which are fitted individually while the afterglow is modelled using a smoothly varying broad pulse which evolves into a power-law decay at late times.

Using this model a comprehensive study of GRB 080310 is presented and followed by similar analyses of GRB 061121, GRB 080810 and GRB 081008. The optical behaviour is found to be inconsistent with the high-energy model: a spectral break between the X-ray and optical band is necessary and for many prompt pulses the self-absorption mechanism is required. The latter three bursts have optical afterglows that are shown to be inconsistent with those fitted to the X-ray regime, peaking earlier in the lower energy bands and requiring a low-energy spectral break. The prompt optical emission seen from GRB 061121 has pulse-like features which match reasonably well with contemporaneous high-energy features, but have longer durations.

The same model was used to study the expected evolution of GRB properties when moved to higher redshifts. Using a sample of bright *Swift* GRBs, the changes in measured duration with redshift were found to be driven by a combination of time dilation, gradual loss of pulse tails and sudden loss of pulses as the flux falls below instrumental sensitivity. A realistic sample of synthetic bursts is produced which, when simulated at high redshift, are found to be significantly longer in duration than the observed high redshift GRBs. Also demonstrated is that several bright bursts seen by *Swift* could be detected if they occurred at a redshift > 10 encouraging the use of GRBs as probes of the early Universe.

Acknowledgments

There are a large number of people without whom I could not have finished (and in some cases started) this PhD. To all of you, thank you!

I would like to first thank Dick Willingale, my supervisor, for guiding me through the last three years. While it is often claimed there is no such thing as a stupid question, I have doubtlessly asked a few and Dick has never failed to provide an answer. Admittedly some of the locations of our meetings have been unusual and over the course of the last three years I've had to strategically plan when I wear my purple jumper. Paul O'Brien (another man with a similarly purple jumper) and Nial Tanvir have both also been hugely influential in the writing of this thesis.

I have been very lucky to have an office of helpful postdocs and colourful characters. Phil and Klaas have never tired in dealing with some of the more trivial problems I might have. I promise you have inspired more than the filing system currently employed on my desk. There has also been a succession of interesting postgraduate officemates who I must thank for making my time productive and entertaining (although rarely both at the same time). There are countless other people in the department who have helped along the way. I don't think I have ever communicated with anyone at 3am as much as Kim Page, who always helped me out of a pickle when *Swift* was being tricky.

Of course there are the other postgraduate students who have been in the XROA and TA over the last three years. Whilst it has seemed strange for good friends to be constantly moving on to pastures new, their replacements have helped keep life interesting! Without the procrastinating emails back and forth, lunchtime running, departmental tea, table tennis, Herman and the pub quiz (and numerous non-quiz related pub outings), life would have been far less exciting.

Contrary to popular belief, we physicists also have lives outside the department, and I am lucky to have some incredible friends. There are too many of you to mention all by name, but it would be criminal not to mention my long-suffering house mate, Penzy. For evenings, both in and out, gym sessions, trips to London, *HIMYM* and being there when I needed you, thank you all.

As ever I want to thank my family. Without their constant love and support I wouldn't be here.

Declaration

I hereby declare that no part of this thesis has been previously submitted to this or any other University as part of the requirement for a higher degree. The work described herein was conducted by the undersigned except for contributions from colleagues as acknowledged in the text.

Owen Littlejohns
March 18, 2013

Publications

The work in Chapter 2 has been published in the following paper:

O. M. Littlejohns et al.

The origin of the early-time optical emission of Swift GRB 080310,
MNRAS, 421, 2692–2712 (2012).

© Owen Littlejohns 2013
This thesis is copyright material and no quotation from it may be published without proper
acknowledgment.

Contents

1	Introduction	1
1.1	Discovery and distance	1
1.2	<i>Swift</i>	4
1.3	GRB taxonomy	6
1.3.1	The long and short of it	8
1.3.2	A fuller picture	11
1.4	The fireball model	11
1.5	Multi-wavelength observations of GRBs	16
1.6	Modelling the prompt emission with pulses	19
1.6.1	The physical model	20
1.6.2	The pulse profile	23
1.6.3	The pulse spectrum	24
1.7	The afterglow spectrum	26
1.7.1	Emission from the minimal photon, ν_m	26
1.7.2	The cooling break, ν_c	27
1.7.3	Synchrotron self-absorption, ν_a	29
1.7.4	Combining the spectral breaks	30
1.8	This thesis	32
2	GRB 080310	34
2.1	Chapter overview	34
2.2	Observations of GRB 080310	35
2.2.1	BAT	37
2.2.2	XRT	37
2.2.3	UVOT	38
2.2.4	Faulkes Telescope North	40
2.2.5	Robotic Optical Transient Search Experiment (ROTSE)	40
2.2.6	REM	40
2.2.7	VLT	41

2.2.8	WHT	42
2.2.9	PAIRITEL	42
2.2.10	KAIT	42
2.2.11	Gemini	43
2.2.12	Observations from literature	44
2.3	Modelling high–energy GRB light curves	44
2.3.1	Initial modelling of the high–energy emission	45
2.4	Extrapolating to the optical and NIR	47
2.5	Modifications to the model	50
2.5.1	An additional spectral break	50
2.5.2	The afterglow	51
2.6	Afterglow dominated fit	53
2.6.1	Light curves	53
2.7	Early–time prompt dominated fit	60
2.7.1	Light curves	60
2.7.2	Spectral energy distributions	65
2.8	Discussion	66
2.8.1	Physical implications of ν_a	72
2.9	Conclusions	74
3	Broadband modelling of further GRBs	77
3.1	Chapter overview	77
3.2	Introduction	78
3.3	GRB 061121	78
3.3.1	Observations	78
3.3.2	High–energy model	83
3.3.3	Extending to low energies	85
3.4	GRB 080810	92
3.4.1	Observations	92
3.4.2	High–energy model	96
3.4.3	Extending to low energies	97
3.5	GRB 081008	103
3.5.1	Observations	103
3.5.2	High–energy model	107
3.5.3	Extending to low energies	109

3.6	Conclusions	116
4	Simulations of bright <i>Swift</i>–BAT GRBs	120
4.1	Chapter overview	120
4.2	The <i>Swift</i> T_{90} distribution	121
4.3	Previous work	122
4.4	Observations	123
4.5	Modelling	125
4.5.1	High redshift simulations made directly from BAT data	125
4.5.2	Simulations using the prompt pulse model	129
4.5.3	Rate Triggering algorithm	131
4.5.4	Measuring T_{90}	132
4.6	Discussion	135
4.6.1	Selecting a bright subsample of bursts	135
4.6.2	Choosing a simulation method	137
4.6.3	Evolution of morphological features	139
4.6.4	Evolution of T_{90}^*	140
4.6.5	Evolution of hardness ratio	146
4.6.6	Evolution in the hardness–duration plane	149
4.6.7	An alternative measure of duration	152
4.6.8	Dependences of z_{max}^* on pulse characteristics	154
4.7	Conclusions	156
5	Simulations of GRBs at high redshifts	161
5.1	Chapter overview	161
5.2	Introduction	162
5.3	Observations	163
5.3.1	High redshift GRBs	164
5.4	Modelling	169
5.4.1	Creating a sample of synthetic bursts	169
5.4.2	A critical evaluation of synthetic pulse parameters	176
5.5	Discussion	179
5.5.1	Pulse simulations of real bursts	179
5.5.2	The synthetic population of bursts	186
5.5.3	Comparisons to previous work	192

5.5.4	An improved instrument	195
5.6	Conclusions	199
6	Conclusions and future work	203
6.1	Conclusions	203
6.1.1	GRB 080310	203
6.1.2	GRB 061121, GRB 080810 and GRB 081008	204
6.1.3	Simulations of bright GRBs	205
6.1.4	Simulations at high redshifts	206
6.2	Future work	207
	References	209

List of Tables

2.1	Properties of the prompt pulses identified in the BAT and XRT light curves of GRB 080310	46
2.2	Pulse p_a values and afterglow parameters for both the prompt- and afterglow-dominated early-time optical emission models of GRB 080310	67
2.3	Initial bulk Lorentz factors for the prompt- and afterglow-dominated early-time optical emission of GRB 080310 in both an ISM and wind-like environment	72
2.4	Magnetic field strengths, number densities and isotropic energies for individual pulses in GRB 080310	74
3.1	Parameters of the prompt pulses identified in the BAT and XRT light curves of GRB 061121	83
3.2	Parameters of the high-energy fitted afterglow for GRB 061121	83
3.3	Parameters of the optical fitted afterglow models for GRB 061121	88
3.4	Physical properties of the prompt pulses for GRB 061121	91
3.5	Parameters of the prompt pulses identified in the BAT and XRT light curves of GRB 080810	96
3.6	Parameters of the high-energy fitted afterglow for GRB 080810	98
3.7	Parameters of the optically fitted afterglow for GRB 080810	99
3.8	Physical properties of the prompt pulses for GRB 080810	101
3.9	Physical properties of the optically fitted afterglow for GRB 080810	102
3.10	Parameters of the prompt pulses identified in the BAT and XRT light curves of GRB 081008	108
3.11	Parameters of the high-energy fitted afterglow for GRB 081008	108
3.12	Physical properties of the prompt pulses for GRB 081008	111
3.13	Parameters of the optically fitted afterglow for GRB 081008	112
3.14	Parameters of the Yuan et al. (2010) optical fitted afterglow for GRB 081008 .	114
4.1	Bright subset of GRBs identified for morphological study	136

List of Figures

1.1	The <i>Vela</i> light curves of GRB 700722	2
1.2	Sky distribution of bursts in the BATSE 4Br catalogue	3
1.3	T_{90} distribution of the BATSE 4Br catalogue	7
1.4	Hardness–duration plot of the BATSE 4Br catalogue	8
1.5	Comparison of BATSE and BAT T_{90} distributions	11
1.6	A collection of high–energy light curves taken from the first BATSE catalogue.	15
1.7	Canonical afterglow X–ray light curve	16
1.8	<i>Swift</i> /XRT flux light curve for GRB 061121	17
1.9	<i>Swift</i> /XRT flux light curve for GRB 061007	18
1.10	BAT and RAPTOR–S light curves for GRB 041219A	18
1.11	XRT and PROMPT light curves for GRB 060607A	19
1.12	Illustration of EATSs taken from Genet & Granot (2009)	21
1.13	Schematic of Willingale et al. (2010) pulse profile	24
1.14	Possible broadband spectra of GRB afterglows taken from Granot & Sari (2002)	31
2.1	<i>Swift</i> /UVOT v –band image for GRB 080310	35
2.2	<i>Swift</i> /XRT image of GRB 080310	36
2.3	<i>Swift</i> prompt light curves for GRB 080310	38
2.4	<i>Swift</i> and ground based light curves for GRB 080310	39
2.5	PAIRITEL and KAIT light curves for GRB 080310	43
2.6	Willingale et al. (2010) model fit to <i>Swift</i> BAT and XRT data for GRB 080310	48
2.7	Initial optical and IR modelling of GRB 080310, extrapolating the pulse Band functions	49
2.8	Pulse spectrum including additional spectral break	51
2.9	Light curves for GRB 080310, fitted in optical, IR, XRT and BAT bands, with early–time optical and IR dominated by afterglow emission	54
2.10	GRB 080310 SEDs with afterglow–dominated early–time emission	58
2.11	Light curves for GRB 080310, fitted in optical, IR, XRT and BAT bands, with early–time optical and IR dominated by prompt emission	62
2.12	GRB 080310 SEDs with prompt–dominated early–time emission	64

2.13	Modelled H band light curve showing only the prompt component for the afterglow–dominated fit to GRB 080310	68
3.1	<i>Swift</i> /BAT light curve of GRB 061121	79
3.2	<i>Swift</i> /XRT light curve for GRB 061121	80
3.3	Optical data for GRB 061121	81
3.4	Willingale et al. (2010) model fit to <i>Swift</i> BAT and XRT data for GRB 061121	85
3.5	Optical fit for GRB 061121 extrapolated from the high–energy model	86
3.6	Fit achieved to optical afterglow of GRB 061121	87
3.7	Fit for optical light curves of GRB 061121	90
3.8	<i>Swift</i> /BAT light curve of GRB 080810	93
3.9	<i>Swift</i> /XRT light curve for GRB 080810	94
3.10	Optical data for GRB 080810	95
3.11	Willingale et al. (2010) model fit to <i>Swift</i> BAT and XRT data for GRB 080810	97
3.12	Optical fit for GRB 080810 extrapolated from the high–energy model	99
3.13	Fitted optical afterglow light curves of GRB 080810 (ISM density profile) . .	100
3.14	Fitted optical afterglow light curves of GRB 080810 (wind–like medium) . .	101
3.15	<i>Swift</i> /BAT light curve of GRB 081008	105
3.16	<i>Swift</i> /XRT light curve for GRB 081008	106
3.17	Optical data for GRB 081008	106
3.18	Willingale et al. (2010) model fit to <i>Swift</i> BAT and XRT data for GRB 081008	109
3.19	Optical fit for GRB 081008 extrapolated from the high–energy model	110
3.20	Best achieved to optical light curves of GRB 081008 in an ISM density profile	112
3.21	Best achieved to optical light curves of GRB 081008 in a wind–like medium .	113
3.22	Yuan et al. (2010) fit to optical light curves of GRB 081008 assuming an ISM density profile.	114
3.23	Yuan et al. (2010) fit to optical light curves of GRB 081008	115
4.1	Observed distribution of T_{90} as a function of redshift	122
4.2	<i>Swift</i> –BAT light curves of GRB 050525A	124
4.3	The BAT effective area per detector as a function of energy	128
4.4	Comparison of T_{90}^* with T_{90}	134
4.5	Comparison of T_{90}^* with T_{90} as a function of the average significance of the light curve	135
4.6	$T_{90}^*(z)$ for GRB 110422A using both simulation methods	137

4.7	Maximum redshifts at which the bright subset are detected for both simulations methods	138
4.8	Simulated light curves of GRB 100814A	140
4.9	$T_{90}^*(z_{sim})$ for the bright subset of bursts	142
4.10	Simulated light curves of GRB 100906A	144
4.11	Hardness ratio evolution with z_{sim} for the bright subset of bursts	148
4.12	Evolution of the hardness–duration plot as a function of z_{sim} for the bright subset of bursts	150
4.13	$T_c^*(z_{sim})$ for the bright subset of bursts	153
4.14	$z_{max}^*(L_{pk})$ for the most luminous pulse in each of the bright subset of GRBs .	155
4.15	$z_{max}^*(b_1)$ for the most luminous pulse in each of the bright subset of GRBs . .	156
4.16	$z_{max}^*(z_{obs})$ for the most luminous pulse in each of the bright subset of GRBs .	157
5.1	Simulated duration as a function of redshift from Kocevski (2012)	163
5.2	15 – 350 keV BAT light curve of GRB 080913	165
5.3	15 – 350 keV BAT light curve of GRB 090423	165
5.4	15 – 350 keV BAT light curve of GRB 090429B	166
5.5	15 – 350 keV BAT light curve of GRB 100905A	166
5.6	0.3 – 10 keV XRT light curve of GRB 080913	167
5.7	0.3 – 10 keV XRT light curve of GRB 090423	168
5.8	0.3 – 10 keV XRT light curve of GRB 090429B	168
5.9	0.3 – 10 keV XRT light curve of GRB 100905A	169
5.10	Fitted model of duration as a function of the T_{90} value as measured by BAT .	171
5.11	Actual and synthetic distributions of N_p	172
5.12	Distribution of $\frac{T_f}{T_f}$ for all bursts corrected to a common redshift of $z = 2$. . .	172
5.13	Observed and synthetic values of S_{pk} as a function of T_f	173
5.14	Observed and synthetic values of spectral index, b_1 , as a function of T_f	174
5.15	Observed and synthetic values of T_r as a function of T_f	174
5.16	Comparison between observed and synthetic T_f distributions	176
5.17	Scatter in b_1 real and synthetic distributions	177
5.18	Scatter in T_r real and synthetic distributions	178
5.19	Simulations of the 15 – 350 keV band for GRB 060814	180
5.20	N_p vs z_{obs} for observed population of bursts	181
5.21	Detected fraction of real burst population as a function of z_{sim}	182
5.22	The evolution of geometric mean T_{90}^* as a function of z_{sim} for real bursts . . .	185

5.23	The evolution of the average hardness ratio $S(50 - 100keV)/S(25 - 50keV)$ as a function of z_{sim} for real bursts	186
5.24	Distributions of T_{90}^* corrected to $z_{sim} = 2$	187
5.25	Detection frequency of synthetic burst population as a function of simulated redshift	188
5.26	The evolution of synthetic geometric mean T_{90} with redshift for the synthetic sample of GRBs	189
5.27	The evolution of the average hardness ratio $S(50 - 100keV)/S(25 - 50keV)$ as a function of z_{sim} for synthetic bursts	192
5.28	Measured duration of synthetic light curves containing a single pulse varying L_{pk}	193
5.29	Measured duration of simulated light curves containing a single pulse varying b_1	195
5.30	Detected fraction of the synthetic sample of GRBs using an improved instrument	196
5.31	The evolution of synthetic geometric mean T_{90} with redshift for the synthetic sample of GRBs as detected by an improved instrument	197
5.32	The evolution of the average hardness ratio $S(50 - 100keV)/S(25 - 50keV)$ as a function of z_{sim} for synthetic bursts using an improved instrument	199

1

Introduction

1.1 Discovery and distance

Gamma-ray bursts (GRBs) were first discovered by the *Vela* satellites, which were launched to monitor the near Earth environment for the unsanctioned detonation of nuclear weaponry (Klebesadel et al., 1973). The *Vela* satellites operated in pairs to provide full sky coverage and it was in checking the data for events that could simultaneously trigger the scintillators on both of the *Vela IV* satellites that the signal for GRB 670707 was first found. Whilst the detection of the first GRBs is often termed serendipitous, it is worth noting the painstaking nature of trawling through the paper listings to find coincidental events observed by both satellites (Klebesadel, 2010). What the data revealed was a brief pulse of high-frequency electromagnetic radiation, lasting approximately 10 seconds. There was, however, no detected signal from the neutron or charged particle detectors, also flown on the *Vela* satellites. The first published light curve for a GRB is shown in Figure 1.1 and is taken from Klebesadel et al. (1973).

Following their discovery, GRBs proved to be a source of controversy within the scientific community. It was clear that the progenitors of these high-energy events were extraterrestrial,

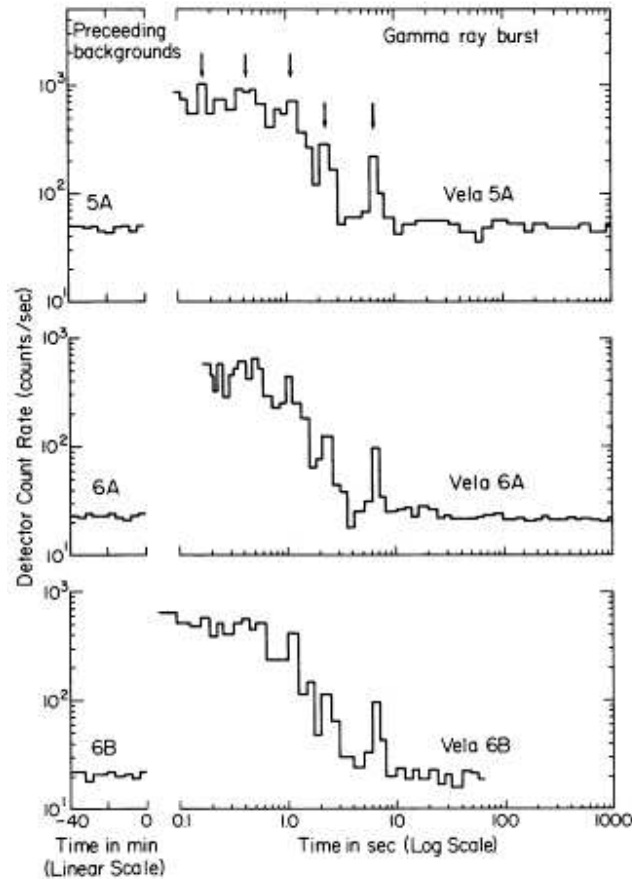


Figure 1.1: Figure taken from Klebesadel et al. (1973) showing the count rate as a function of time for GRB 700722. The panels show the light curve from each of the three *Vela* satellites which observed the event. The flat period of the light curve prior to the main emission shows the background level, whilst common structure between the three light curves are indicated by arrows. Additionally, the *Vela* 5A count rates have been reduced by $100 \text{ counts}\cdot\text{s}^{-1}$ for scaling purposes.

but at the Texas Symposium, which was just one year after Klebesadel et al. (1973) published the first scientific paper on GRBs, there were already 140 different proposed theories to explain the origins of the detected electromagnetic radiation (Ruderman, 1975).

With limited directional information available from instruments such as the scintillators on board the *Vela* satellites, localisation, and therefore the determination of distance to a given burst was impossible. This led to the formation of two opposing hypotheses: that gamma-ray bursts were of a Galactic origin (Fishman et al. 1978; Schmidt 1978) or that they were at cosmological distances (Paczynski, 1986).

Whilst Paczynski (1986) clearly advocated that at least some of the then observed bursts occurred at cosmological distances, due to the potential isotropy of the early observed GRB

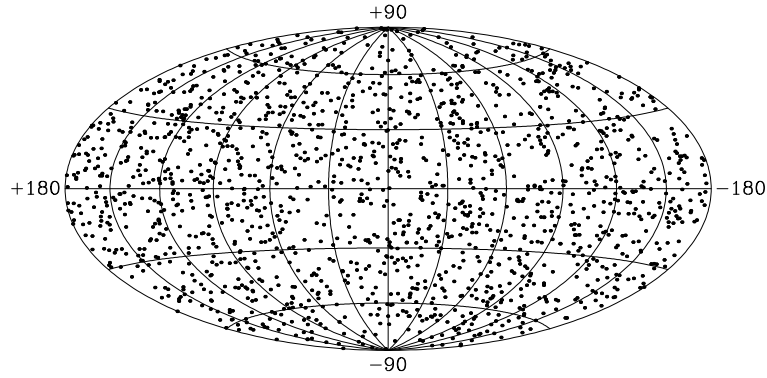


Figure 1.2: Sky distribution of bursts in the BATSE 4Br catalogue taken from Paciesas et al. (1999). All 1,637 bursts in the BATSE 4Br catalogue are displayed on an Aitoff–Hammer projection in Galactic coordinates.

population, the implied energetics of such events (then thought to be $\sim 10^{51}$ ergs.s⁻¹) were unprecedented. With many finding it hard to reconcile the vast required energies with what was already known about the Universe, the Galactic theory of origin seemed, at this point, to be more plausible. Hartmann et al. (1990) explained such events as being consistent with a population of Galactic neutron stars observed at distances out to no greater than 2 kpc.

Shortly after this, on the 5th of April 1991, the *Compton Gamma-Ray Observatory (CGRO)* was launched. As part of its suite of instruments, *CGRO* had a series of sodium iodide scintillators which were arranged to provide full (unocculted) sky coverage. These were collectively known as the Burst and Transient Source Experiment (BATSE; Fishman et al. 1985) and compiled the largest catalogue of GRBs to date (1,637; Paciesas et al. 1999). Importantly, it was soon apparent that the distribution of burst location on the sky was isotropic (Meegan et al., 1992) as shown in Figure 1.2. This placed strong constraints on the progenitor population for GRBs to be either extragalactic or potentially from the extended Galactic halo.

It wasn't until 1997, however, that the matter was settled. It was in this year that the Italian-Dutch satellite, *Beppo-SAX* (Boella et al., 1997), was launched. With the capability of slewing its X-ray telescope to point at a GRB location within hours, it was possible to obtain positions with much higher precision. These locations were now useful to other satellites or ground-based facilities, enabling the search for emission at lower energies in the electromagnetic spectrum. Finally, in May of 1997, such abilities led to the determination of the first redshift to a GRB afterglow. By showing the GRB 970508 had a redshift of $z \sim 0.835$,

Metzger et al. (1997) at last proved that GRBs occurred at cosmological distances.

1.2 *Swift*

To gain insight into the nature of the central engine of a GRB multi-wavelength observations are required. With sufficient coverage, both spectrally and temporally, a fuller picture of the spectral energy distribution (SED) from the early time emission, and how it evolves, can be obtained. This is not possible without accurate, rapid locations, which at present can only be provided by the *Swift* satellite (Gehrels et al., 2004).

Swift was launched on the 20th of November 2004, and between becoming fully operational and the 14th of February 2013 has detected 740 GRBs (see the Goddard Space Flight Center GRB archive at: http://heasarc.nasa.gov/docs/swift/archive/grb_table). The majority of these bursts triggered the Burst Alert Telescope (BAT) (Barthelmy et al., 2005), which operates in the 15 to 350 keV energy range. BAT has a field of view of approximately 2 steradians and detects GRBs using a coded mask aperture. Because of the high energies of γ -ray photons, it is not possible to image them in a traditional sense, as they would be absorbed by the focusing optics. By using a coded mask, which consists of 32,768 CdZnTe tiles randomly distributed to create a pattern with a 50% filling factor, the BAT optics produce an image that is very well characterised. This means that any change to this shadow not corresponding to a known or constant source can be attributed to a transient object.

BAT has two different triggering criteria, which can be met at any time during regular satellite operations. The first of these criteria is termed a ‘rate trigger’ and looks for sudden increases in the event rate above a 6.4σ threshold at any point across the detector. The alternative method of detection is an ‘image trigger’, which is the result of producing a sky image every 64 seconds and searching this image for new sources.

Providing there are no observational constraints (such as proximity to the Sun, Earth or Moon) the satellite will slew to a new source position located by BAT allowing the narrow field instruments to also view the source. These initial positions typically have an error circle of 1–4 arcminutes, and so the X-ray Telescope (XRT; Burrows et al. 2005) and the Ultraviolet and

Optical Telescope (UVOT; Roming et al. 2005) are required to provide more accurate locations for ground based follow-up. Such re-pointing is rapid, with the XRT and UVOT observations beginning typically in the second minute after the BAT trigger.

BAT is sensitive to photons in the 15 keV to 350 keV range, with measured events typically being split into four bands. These are the 15 keV to 25 keV, 25 keV to 50 keV, 50 keV to 100 keV and 100 keV to 350 keV bands. The BAT response is such that the effective area above 150 keV is small which, when combined with typical spectrum of a GRB, means that the contribution above this energy is small. While received events can be binned at a number of different temporal resolutions, typically the four channel light curves are seen with 64 millisecond time bins.

In the X-ray regime, unlike at lower energy wavebands, photons at normal incidence to standard mirrors are absorbed. Fortunately, if the angle of incidence becomes large, commonly known as grazing incidence, X-ray photons are reflected from the mirror surface rather than absorbed by the material from which it is constructed. For this reason the XRT focuses X-rays on to its CCD detector using a Wolter-I telescope. Such optics consist of nested, concentric shells of mirrors (in this case 12 shells).

The XRT provides coverage in the 0.3 keV to 10 keV range, which in the study of GRBs is often split into two bands: a 0.3 keV to 1.5 keV band and a 1.5 keV to 10 keV band. This demarcation in the XRT coverage is designed to minimise the error in hardness ratio between the two by obtaining an approximately equal number of counts in each. The division at 1.5 keV is also where the effective area curve peaks. Data is taken in three different modes: windowed timing (WT), photon counting (PC) and image (IM) mode. In image mode 0.1 second or 2.5 second exposures are taken and the CCD is read out in a similar manner to an optical detector. Such exposures suffer highly from pile-up, and so offer no spectral information, but are good for centroiding. In addition to these, the XRT was also designed to operate in photodiode (PD) mode. PD data was designed to offer time resolution of 0.14 ms by integrating all detector pixels to one point. Sadly, a micrometeorite impact early in the mission prevented the implementation of PD observations.

Following the detection of a standard GRB, WT data are taken initially, when the burst

is at its brightest, until the count rate drops below 2 counts.s^{-1} . In this mode, the data taken are summed over pixel columns to produce a one dimensional image. By reducing the spatial information, the detector can be read quicker, which ensures that the pixels illuminated by the GRB are less likely to saturate. Once the count rate has dropped sufficiently PC mode data are taken, which provide two dimensional spatial information, allowing for the production of an image across the detector plane. Should significant re-brightening be observed in the transient source, and the count rate exceed 10 counts.s^{-1} whilst in PC mode, WT data will once more be taken.

The UVOT is a 30 cm Ritchey-Chrétien telescope (Wynne, 1968), which focuses light on to a micro-channel plate that amplifies the signal before it reaches the detector. The micro-channel plate takes input signal, and causes a cascade of electrons that intensifies the observed signal, increasing the gain of the detector, and allowing the detection of smaller signals.

The UVOT operates in a 170 nm to 600 nm wavelength range, with 11 filters (including a broad white-light-filter) and both an optical and UV-grism. Once slewed on target an initial image known as a finding chart is taken using the *white* filter. This is to determine if an optical afterglow is detected before then beginning observations with the narrower filters. It is with the UVOT that the most accurate *Swift* positions can be determined, however it is often the case that an associated optical transient is not found. In these instances a UVOT-enhanced XRT position is used. Goad et al. (2007) describe the method by which this is accomplished; by firstly taking the promptly determined positions from the XRT (which have accuracies of order 3.5 arcseconds) and using the UVOT as a star tracker to astrometrically correct them.

The work in this thesis makes extensive use of data directly from all three instruments of *Swift*, particularly BAT. The early-time optical data presented in Chapters 2 and 3 were only able to be taken thanks to the fast response of both the satellite to the trigger and the rapid distribution of the localised position to ground-based facilities.

1.3 GRB taxonomy

With different instruments both on board satellites and on Earth, GRBs can be observed in a variety of regimes. This has given observers the tools required to subdivide the total population in an effort to further understand the detected characteristics of GRBs and ultimately their progenitors and emission mechanisms.

Perhaps the first, and most enduring, proposed paradigm used to split the total sample was one of duration. Using data from BATSE Kouveliotou et al. (1993) defined a parameter, T_{90} , which could be used to measure the duration of the high-energy prompt emission of a burst. To find T_{90} the counts of a burst are cumulated, and the times at which the cumulative distribution reaches both 5% and 95% of the total are found. The interval between the two, in which 90% of the burst fluence is detected, is taken to be T_{90} (see Figure 1.3). It was noticed that when making this divide, those bursts which belonged to the short category of bursts ($T_{90} < 2$ seconds) were spectrally harder meaning the photons detected had, on average, higher energies. Conversely, the long GRBs ($T_{90} > 2$ seconds) were found to have photons which were slightly less energetic and therefore had softer spectra as shown in Figure 1.4. Whilst T_{90} is not without its caveats, such as being measured in the observed frame (and therefore affected by cosmological time dilation) it has become one of the key parameters used in describing the high-energy emission as detected by a number of instruments. The long-short dichotomy has also proved successful, with the two classes of bursts now being believed to arise from different progenitors.

1.3.1 The long and short of it

The same long-short paradigm has also been observed in subsequent instruments, such as BAT and also the Gamma-ray Burst Monitor (GBM; Meegan et al. 2009) on board the *Fermi* satellite. Due to the differing spectral responses of these instruments, the observed populations are slightly different. For example, there is a noticeably lower rate of short GRBs amongst those detected by *Swift* compared to those seen by BATSE (see Figure 1.5). Further differences are discussed in §1.3.2.

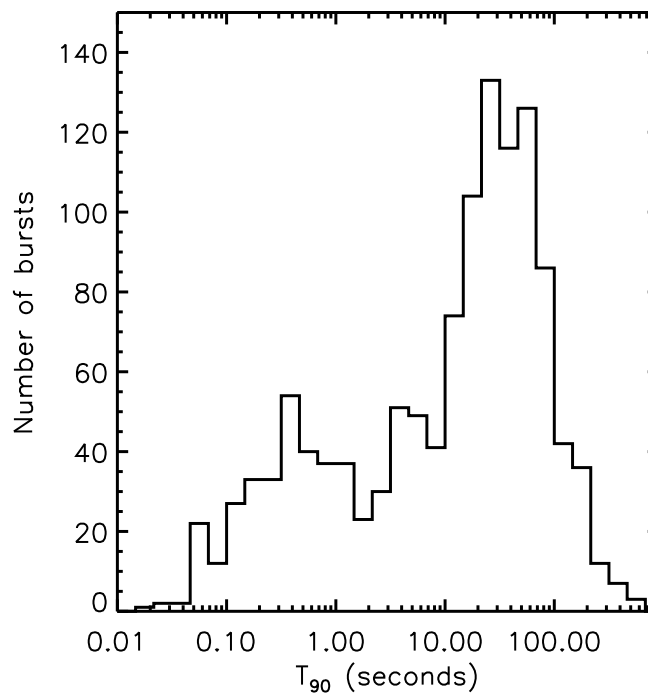


Figure 1.3: T_{90} distribution of the BATSE 4Br catalogue. The data to produce this figure were taken from Paciesas et al. (1999) and the 1,234 bursts with duration measures are included in this figure.

Long GRBs have long been identified as originating from blue, star forming galaxies (Christensen et al., 2004; Le Floc’h et al., 2003; Fruchter et al., 1999) of low stellar mass (Castro Cerón et al., 2010; Savaglio et al., 2009; Castro Cerón et al., 2006). In galaxies which can be resolved to a high level of accuracy, it has been possible to show that long GRBs are found specifically in their brightest regions (Svensson et al., 2010; Fruchter et al., 2006; Bloom et al., 2002), which is indicative of an association with star formation occurring within these regions. It wasn’t until 1998, however, that a much clearer identification of the burst progenitors could be made. GRB 980425 was discovered to be coincidental with supernova 1998bw (Galama et al., 1998). Since GRB 980425 there have been a handful of bursts with both supernova bumps in their optical light curves and spectroscopic evidence confirming their association with an observed supernova. These include GRB 030329 being linked with SN 2003dh (Stanek et al., 2003), GRB 031203 with SN 2003lw (Malesani et al., 2004), GRB 060218 with SN 2006aj (Campana et al., 2006), GRB 100316D with SN 2010bh (Starling et al., 2011) and more recently GRB 120422A being connected to SN 2012bz (Melandri et al., 2012; Wiersema

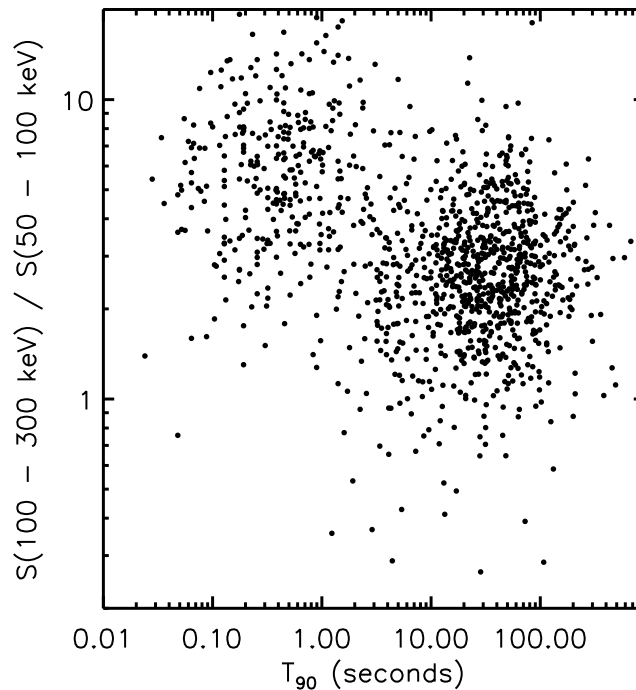


Figure 1.4: Hardness ratio $\left(\frac{S(100 - 300 \text{ keV})}{S(50 - 100 \text{ keV})}\right)$ as a function of T_{90} for the 1,185 GRBs in the BATSE 4Br catalogue with both duration and spectral hardness measures. $S(50 - 100 \text{ keV})$ and $S(100 - 300 \text{ keV})$ are measured fluences in units of ergs.cm^{-2} in the respective standard BATSE bands.

et al., 2012). Aside from these bursts, there are other optical light curves which exhibit potential supernova bumps in them, however the evidence is more tentative in these cases.

The SNe all associated with GRBs are of type Ib and Ic, meaning that they are due to the collapse of the iron cores of massive stars forming either a neutron star or a black hole (Woosley & Janka, 2005). This agrees with the locations in which long bursts are found, as such stars evolve rapidly along the Main Sequence allowing their explosions to occur whilst star formation is still ongoing. It also agrees with earlier predictions made by both Colgate (1968) and later supported by Paczynski (1986) prior to the subsequent observational evidence.

Whilst the prompt emission is often considered the best diagnostic of the central engine powering a burst, it is the afterglow that is used to identify (where possible) a host galaxy for a GRB, and therefore a redshift to the source (for example, see Xiao & Schaefer 2011). Such information is vital in attempting to distinguish what the progenitor population of such events may be. Nakar (2007) discusses some of the observational difficulties in detecting the

afterglows of the short burst population. First, an approximate localisation must be determined for an X-ray instrument to follow up from small number of photons. Typically, BAT can provide positions from the prompt emission with uncertainties of a few arcminutes. This X-ray instrument, such as the XRT, must then be pointed rapidly at this region to allow for a more accurate position to be ascertained from the X-ray afterglow. This is usually sufficient to allow optical and ground-based observations, although even with this more accurate position there can often be multiple host galaxy candidates (for example, see Levan et al. 2007).

Coverage from the XRT commonly begins at between a minute and 100 seconds after the initial trigger time. As the X-ray afterglow tends to fade quicker for short GRBs, once observations begin the X-ray afterglows of short GRBs are typically fainter than those of the long burst sample. As such a fast decay is also often seen in the optical regime, deep ground-based follow-up to a higher degree than the typical GRB is required.

From the data that have been obtained, several key facts have been established concerning the short GRB population. The first of these is that short bursts occur in a variety of host galaxies of both early and late types (Berger, 2011, 2009; Levan et al., 2007). On average, though, the host galaxies of short GRBs tend to be larger than those in which the long burst population occur (Wainwright et al., 2007). Aside from having a distinctly different host galaxy population, short GRBs also occur in different regions within these galaxies, having been shown to be more diffusely distributed throughout their hosts (Fong et al., 2010). Leibler & Berger (2010) studied the locations within host galaxies of short bursts, and found that short GRBs can be shown to belong to older stellar populations, tracing star formation, but with a delay time between this star formation and the occurrence of a burst.

A final piece of interesting evidence is that there are a number of short GRBs for which no host has been identified, or the proposed host lies at a significant offset from the position of the burst (Fong et al., 2010).

Combining what is known for short GRBs has led to the currently favoured theory for their progenitors. Namely, that short bursts are the result of the merger of either two neutron stars or a neutron star with a black hole (Fox et al., 2005; Berger et al., 2005). In such an event the majority of the mass becomes the final black hole remnant, with a fraction (0.1 – 0.2

M_{\odot}) of matter being expelled to form an accretion disk. Such progenitors would be expected to roughly trace star formation, with a delay time as the compact objects would need time to form from Main Sequence stars before then spiralling inwards in their binary system. In the supernova required to produce the compact objects it is possible that a kick in velocity ($\sim 300 \text{ km.s}^{-1}$) is imparted to the binary system (Bloom et al., 1999). This would lead to the binary leaving the original site of birth, and can account for the offset seen between some bursts and their potential hosts.

Such a theory of burst progenitor is not new, with literature dating back to the 1980s (Eichler et al., 1989; Paczynski, 1986). However, the causes of short GRBs remain more uncertain than their longer counterparts with, as yet, no ‘smoking–gun’ observations taken.

1.3.2 A fuller picture

Complications with the long–short divide arise from instrumental effects. A recent study by Bromberg et al. (2012) has compared the GRB populations as observed by BATSE, BAT and *Fermi* GBM. Due to the differences in sensitivity and spectral response, the sample of detected bursts varies between each instrument. In cases of detection by multiple instruments, the T_{90} duration measured by each varies by a small amount. As such, the T_{90} distributions are different, as shown in Figure 1.5. The division between long and short GRBs is therefore also different depending on the instrument used, with the minima in the two distributions being 2.4 ± 0.4 and 1.2 ± 0.2 for BATSE and BAT respectively. As a result of this, Bromberg et al. (2012) propose that the location of the long–short demarcation is nearer 0.8 seconds for the *Swift* BAT population of bursts.

1.4 The fireball model

Whilst long and short GRBs both have different progenitors that form the central engine of the burst, it is commonly held that both produce the same central engine, which then leads to similar emission processes in both populations (Piran, 1999).

From either the collapse of a massive star, or the merger of two compact objects, a black

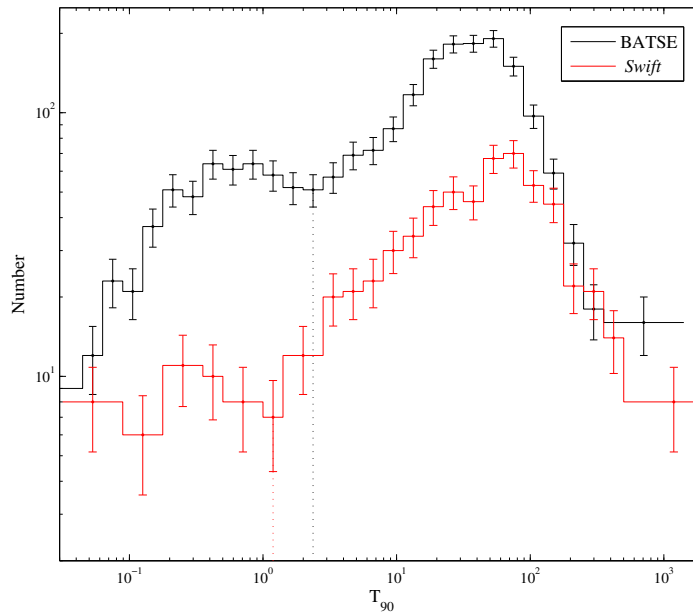


Figure 1.5: Figure taken from Bromberg et al. (2012) showing the $\log T_{90}$ distributions ($dN/d\log T_{90}$). Bins with less than five events are merged with their neighbours to reduce statistical errors.

hole is formed. In the case of the merger scenario there is the potential for a short-lived intermediate stage, where an unstable millisecond pulsar exists briefly before collapsing to a stellar mass black hole (Ruderman et al., 2000; Spruit, 1999; Thompson, 1994). An unstable millisecond pulsar (or ‘magnetar’) is a neutron star which is both rapidly rotating and has an incredibly high magnetic field.

Assuming the observed prompt and afterglow emission originate from a central engine consisting of a stellar mass black hole, there is also a surrounding torus of debris (Mészáros, 2006). It is the accretion of this debris on to the black hole which powers the GRB. Such a torus is the result of the conservation of angular momentum from the progenitor. In the case of a collapsar, even a moderate rotation about its axis naturally imparts large quantities of angular momentum to the debris. The general form for angular momentum, L , is shown in Equation 1.1, where m denotes mass, r radius and v the tangential velocity at which the material is orbiting the central engine.

$$L = mv \times r. \quad (1.1)$$

Equation 1.1 has two important effects; the first is that a reduction in radius results in an increased tangential velocity per unit mass. This implies a rapidly rotating central engine. The second effect is that the debris from either the outer layers of a collapsed star or a binary merger should form a disk-like structure. It is this rapid rotation that prevents the dense torus from simply falling straight on to the black hole.

The collapse or merger event effectively liberates a large quantity of gravitational energy in both a short timescale and a small volume, which is supplemented over a slightly longer timescale by accretion from the debris disk on to the central engine. This is released as neutrinos, anti-neutrinos and gravitational waves. Above and below the accretion disk, where the density of material is lower, the neutrinos easily annihilate forming highly energetic photons. These photons are sufficiently energetic and contained within a small enough region of space that the production of electron and positron pairs can occur. A plasma of electrons, positrons, photons and some baryons is therefore formed, which has a high optical depth. This optical depth prevents observers from seeing these first photons, as they are trapped within this high temperature ($kT \geq 1$ MeV) fireball.

The fireball is emitted along the rotation axis of the black hole central engine (Popham et al., 1999), and as the photon luminosity exceeds the Eddington luminosity, thereby meaning radiation pressure is dominant over self-gravity, the fireball expands (see Equation 1.2). In Equation 1.2, G is the gravitational constant, M is the mass of the fireball, m_p is the mass of a proton, c is the speed of light and σ_T is the Thompson scattering cross section. As most of these are constants, it can be seen that the Eddington luminosity, L_{Edd} varies only due to the mass of the fireball. The velocity associated with its expansion is dependant on the baryon loading of the fireball (Paczynski, 1990).

$$L_{Edd} = \frac{4\pi GMm_p c}{\sigma_T}. \quad (1.2)$$

As the fireball expands the energy stored as photons within it is converted to kinetic energy of the electrons, positrons and baryons. This continues until a maximum velocity is achieved, which is a significant fraction of the speed of light. Such velocities are best described in terms of the Lorentz factor, Γ , which is given in Equation 1.3 (where v is the outflow velocity and c

is the speed of light):

$$\Gamma = \frac{1}{\sqrt{1 - \left(\frac{v}{c}\right)^2}}. \quad (1.3)$$

Eventually, enough of the radiation is converted to kinetic energy to allow the fireball to no longer be opaque to its own photons. This point is often termed the ‘photosphere’ and is the first point at which observers can see the emission from the GRB. After accelerating to ultra-relativistic speeds ($\Gamma \geq 100$, or $v = 0.99995c$) the viewing angle of such radiation is restricted by the relativistic Doppler effect, which states that the opening angle, θ_{beam} , (the angle from the axis of emission within which an observer must be to see the radiation) is as follows:

$$\theta_{beam} \propto \frac{1}{\Gamma}. \quad (1.4)$$

As the Lorentz factor associated with the outflow is incredibly high, the beaming angle is therefore low. This Lorentz factor, however is not constant for the duration of the jet. If this were the case, there would be no prompt emission. Instead, the jet is more like a series of episodic shells, each with different values of Γ . Whilst the exact mechanism is not known, it is thought that the later shells have slightly higher Lorentz factors, allowing them to advance on their earlier counterparts. When the two meet, a collision-less shock is formed (Rees & Meszaros, 1994), where kinetic energy is converted to radiation and is released in the form of a Fast Rise Exponential Decay (FRED) pulse in the prompt emission (Fishman & Meegan, 1995). Such events can occur multiple times, as each burst has an unknown number of these shells, leading to many (sometimes approaching 20) FRED pulses seen in the high-energy light curves of bursts. Examples of the varied nature of the prompt emission are shown in Figure 1.6, in which light curves are taken from the first BATSE catalogue.

Eventually, the jetted outflow strikes the surrounding medium, which causes it to rapidly decelerate. This has several effects, the first of these is the conversion of further kinetic energy into radiation, which is seen as the afterglow (Piran, 2004). This is light which is visible in lower parts of the electromagnetic spectrum, rather than the previous high-energy prompt emission. The afterglow is sometimes observed from radio wavelengths (Frail et al., 2003)

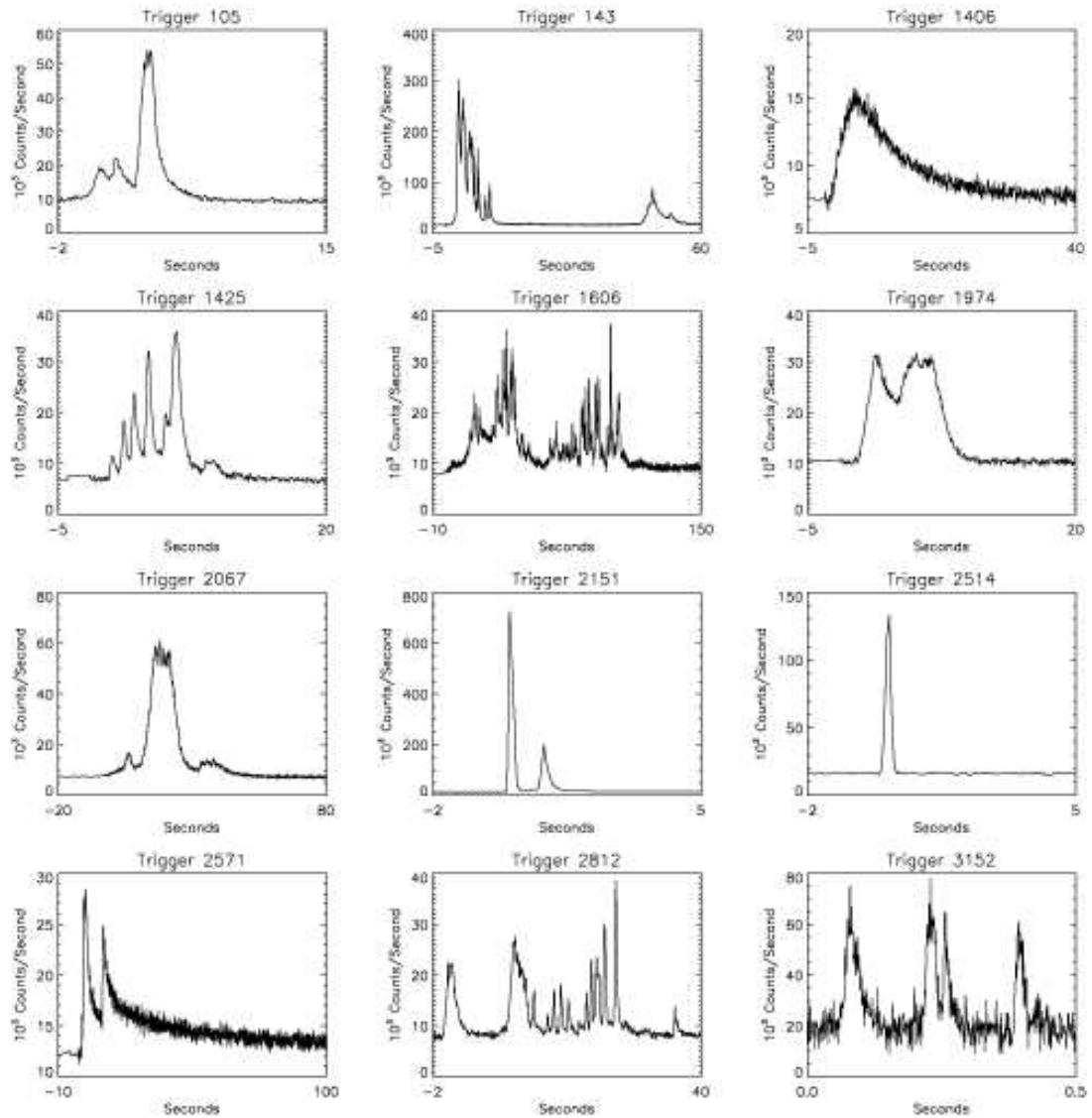


Figure 1.6: A collection of high-energy light curves taken from the first BATSE catalogue. Demonstrated is the variety in several characteristics of the prompt emission, including of the number of pulsed episodes, the duration of each burst and also the strength of the observed signal.

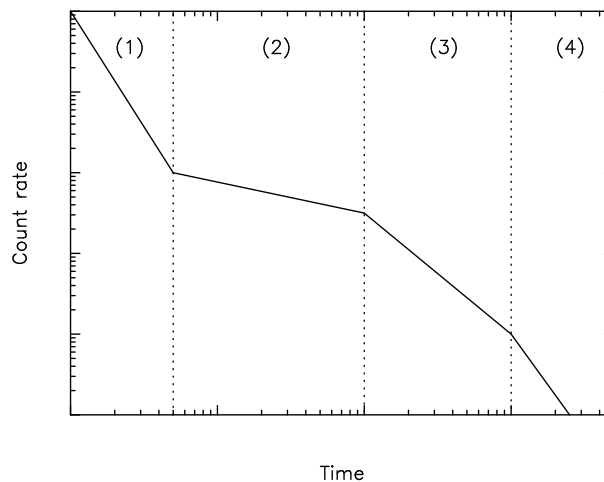


Figure 1.7: Canonical afterglow X-ray light curve showing the four main stages of the X-ray afterglow: (1) the steep decay phase, (2) the plateau phase, (3) normal decay phase and (4) post jet break phase.

right through to the X-rays detected by the XRT on board *Swift* (Evans et al., 2009).

Figure 1.7 shows the proposed canonical morphology of the X-ray afterglow (see for example Evans et al. 2009). The first of the observed phases is the steep decay phase, which is now attributed to the high latitude emission of prompt pulses thanks to both its temporal and spectral characteristics (O’Brien et al., 2006). Following this is the plateau phase, during which energy is continually injected into the forward shock to maintain the observed flux (Zhang et al., 2006). The next stage is often referred to as the ‘normal’ decay phase, in which the light curve follows a power-law decay with $\alpha \sim 1-1.5$. At this point, the beaming angle is such that the observer cannot perceive the edge of the jet. However, as the outflow is slowed, according to Equation 1.4 the beaming angle increases, until a point when it is larger than the jet opening angle. There is then a break in the light curve, as the flux now reduces more rapidly (Panaitescu et al., 2006). Jet breaks are not commonly observed in light curves, largely due to the low level of flux at the times when they might occur.

The increase in beaming angle has led to the proposal of events termed ‘orphan afterglows’, for which an observer is outside the beaming angle for the prompt emission, but within it for the afterglow. This would lead to the observation of a burst without the associated prompt emission. To date, no orphan afterglow has been detected.

The afterglow is long-lived in comparison to the prompt phase, often being detectable for weeks after the initial prompt emission. Indeed, as the spectrum associated with the afterglow

is thought to be synchrotron it can be months or years before the afterglow peaks at radio wavelengths, as the spectrum must soften significantly for the radiation to do so.

1.5 Multi-wavelength observations of GRBs

The existing data for GRBs seen at multiple wavelengths present a confusing picture. X-ray observations within the first few hours after the BAT trigger using the XRT often show a rapid decay phase (RDP), which is considered to be the smooth decay of the prompt component before the onset of afterglow emission (O'Brien et al., 2006) and is one of the proposed phases of canonical light curve models (Nousek et al., 2006). Whilst the RDP is nearly ubiquitous in GRBs with necessary XRT coverage, the additional morphology seen in their X-ray light curves varies highly between bursts (Evans et al., 2009). Some GRBs show strong flaring, such as GRB 061121 (Page et al., 2007), where the observed flux has significant peaks at times after the beginning of the XRT observations as shown in Figure 1.8. Conversely, there are those GRBs which have very simple decays. GRB 061007 is an example of such and is shown in Figure 1.9. Its X-ray light curve can be described by a single power-law (Schady et al., 2007). Past work has shown that the flares observed in X-ray light curves are both spectral and temporal analogues of the pulses observed in higher energy instruments such as BAT (Margutti et al., 2010).

As there are such differences between individual bursts in one wavelength it is therefore unsurprising, perhaps, that there appears no consistent relation between what is observed at these higher energies and other wavelengths, such as optical light. There are examples of bursts where the available optical data traces the X-ray and γ -ray observations, such as GRB 041219A (Vestrand et al., 2005). The available optical data are overlaid on the BAT γ -ray light curve in Figure 1.10.

Other GRBs do not show simultaneous features in their optical and X-ray or γ ray light curves. GRB 060607A (Nysewander et al., 2009) is an example of this, as shown in Figure 1.11. The X-ray data show clear flaring during the first ten minutes of observations, followed by a plateau and then a sharp decay. The optical light curve from the Panchromatic Robotic

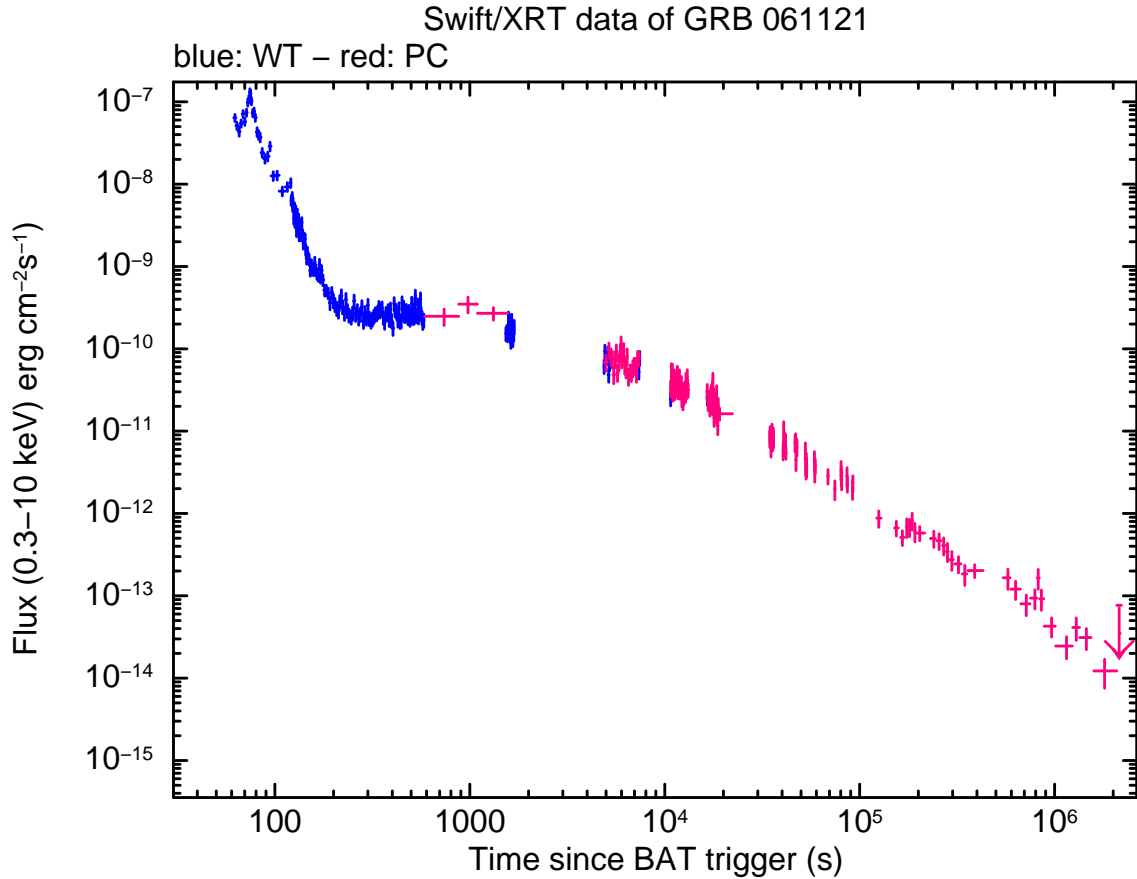


Figure 1.8: Swift/XRT flux light curve for GRB 061121. Blue data points show the WT data, and the magenta data are PC mode. This is the total XRT band, spanning 0.3 keV to 10.0 keV.

Optical Monitoring and Polarimetry Telescope (PROMPT; Reichart et al. 2005) shows a rise, as might be expected from an afterglow component, that peaks at approximately three minutes. However, there are variations seen at 42 and 64 minutes, which do not coincide with the X-ray light curve. Despite of the lack of X-ray coverage at some of the times of interest, the data does appear to have reached a plateau in the X-rays at this time.

To reconcile the observations taken at these different energies, data with good simultaneous coverage are required for a large sample of GRBs. This is only viable for bright bursts with long durations to their prompt phases. With such durations it is possible to trigger ground based facilities to begin their observations whilst the prompt emission is still being observed in the γ -rays. A final prerequisite for such data is that the GRB location must be favourably positioned in the sky to allow these facilities to access the positions determined by *Swift*.

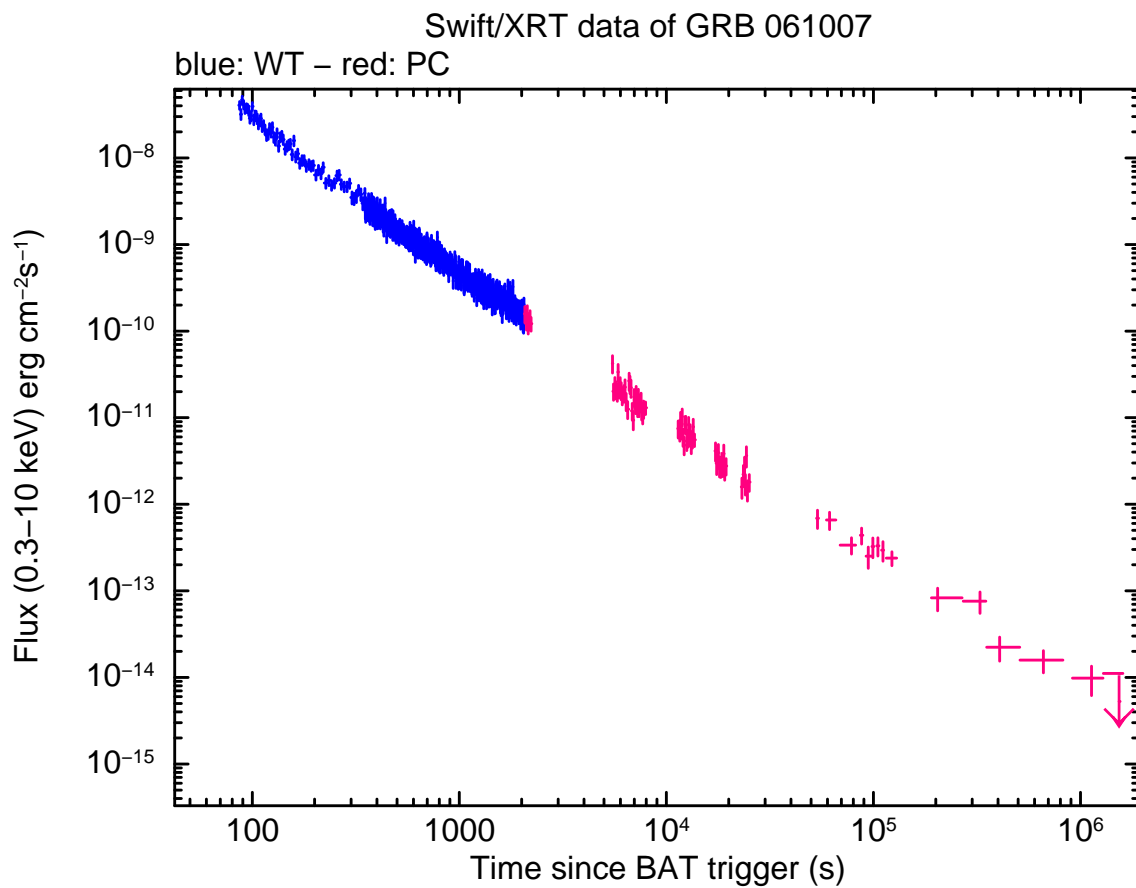


Figure 1.9: Swift/XRT flux light curve for GRB 061007. Blue data points show the WT data, and the magenta data are PC mode. This is the total XRT band, spanning 0.3 keV to 10.0 keV.

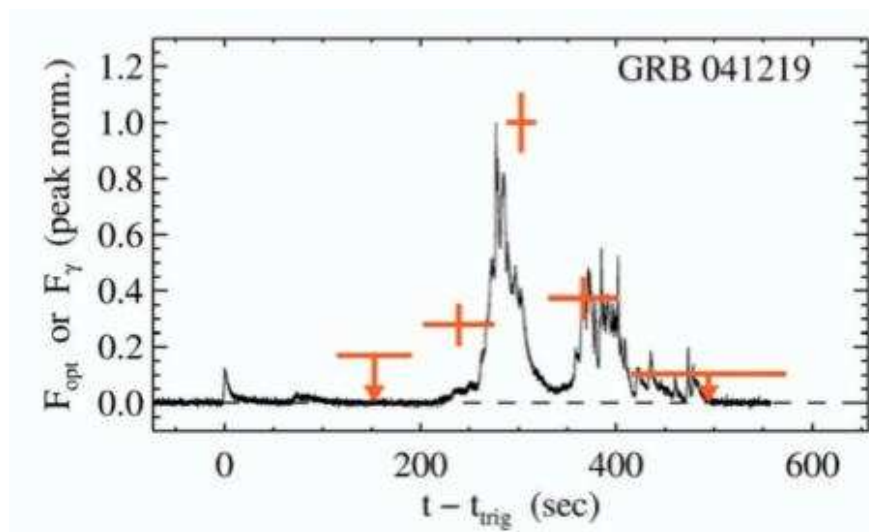


Figure 1.10: Figure taken from Vestrand et al. (2005), showing the BAT light curve (black curve) and the corresponding RAPTOR-S optical observations (oranges points).

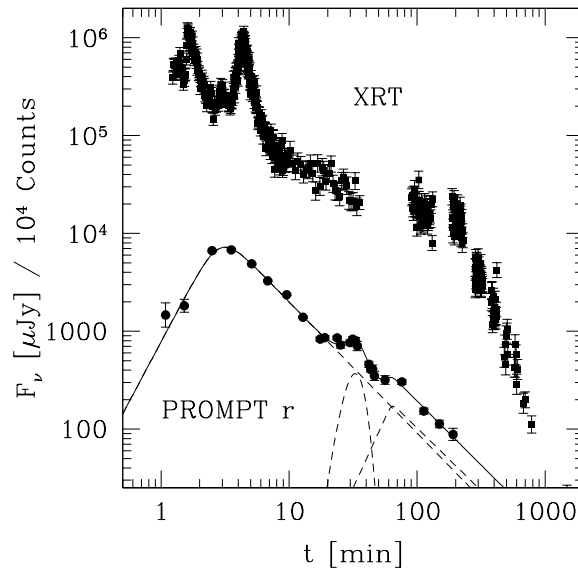


Figure 1.11: Figure taken from Nysewander et al. (2009) showing both the PROMPT r -band and XRT light curves for GRB 060607A. Optical fluctuations can be seen during a gap in the XRT coverage, however, the X-ray light curve suggests a plateau at this time. Also the rate of decay appears to be different in the two bands.

1.6 Modelling the prompt emission with pulses

The work presented in this thesis is underpinned by a single model for the prompt emission as observed at high energies. In this model the prompt emission is decomposed into a series of pulses, using the methodology presented in Willingale et al. (2010). Initially, Willingale et al. (2010) were attempting to see whether emission from high latitudes could account for the rapid decay phase (RDP) seen in XRT light curves. To fully perform this work the authors required a profile for each of the pulses observed in the prompt light curves, a pulse spectrum and a recipe for the time evolution of this spectrum.

1.6.1 The physical model

The profile of each pulse was based on a slightly modified version of that presented in Genet & Granot (2009), in which each pulse was attributed to an ultrarelativistic ($\Gamma \gg 1$) thin shell ejected from a central engine. In this instance ‘thin’ means that each shell has a thickness $\Delta R \ll R/\Gamma^2$. Each such shell is modelled to be expanding spherically and is seen to emit between radii R_0 and $R_f = R_0 + \Delta R$. Additionally, the emission is thought to be isotropic and

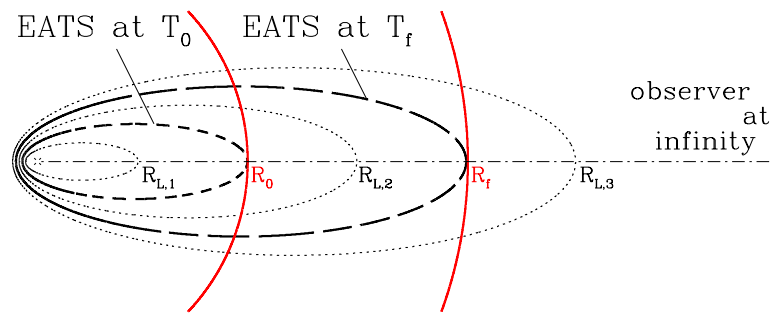


Figure 1.12: Illustration of EATSs taken from Genet & Granot (2009). Shown are EATS for coasting shells with a constant Lorentz factor. Emission occurs within the shell, between R_0 and R_f .

uniform across each shell, meaning the comoving spectral luminosity, L'_{ν} , is only dependent on the radius of the shell.

For each shell, the Lorentz factor of the expansion was assumed to remain constant with time (and therefore radius) during the prompt emission phase:

$$\Gamma^2 = \Gamma_0 \left(\frac{R}{R_0} \right)^{-m}, \quad (1.5)$$

where Γ is the bulk Lorentz factor at a radius from the central engine R . Γ_0 corresponds to the Lorentz factor at R_0 . m is the coasting index, and as it has been assumed to remain constant with time (and therefore radius), meaning $m = 0$. The Lorentz factor is determined by the velocity of the outflow (v), as shown in Equation 1.3.

For such coasting shells, with isotropic and uniform emission, radiation which occurs further from the line of sight takes longer to reach an observer. This is simply a consequence of the longer distance over which the photons must travel. The locus of points which describe the regions that emit at different times but arrive at the observer simultaneously is known as the Equal Arrival Time Surface (EATS; Sari 1998; Granot et al. 1999a). The shape of this surface, in three dimensions is an ellipsoid due to relativistic effects as first described in Rees (1966). The central engine ejecting the shells is located at the focus of the ellipsoid furthest from the observer. A representation of this is shown, in a two dimensional plane, in Figure 1.12.

At R_0 , only radiation that is emitted directly along the line of sight can be observed, and

so the measured flux is small. After a short time, when the shell is at a radius greater than R_0 , emission from larger angles can also be observed. This is because the radiation emitted at R_0 , but further from the line of sight, has had sufficient time to reach the observer. This leads to a corresponding increase in measured flux, until the shell reaches R_f when it switches off. After this, the tip of the EATS leaves the region from which emission can occur, and the flux begins to drop as only emission from higher latitudes remains to be received.

As discussed below, an important spectral parameter is the peak of the νF_ν spectrum, which is denoted below by ν'_p . In the following sections all primed quantities are in the co-moving frame of the shell being considered. The evolution of ν'_p is described by Equation 1.6, where ν'_0 is the value of ν'_p at radius R_0 .

$$\nu'_p = \nu'_0 \left(\frac{R}{R_0} \right)^d. \quad (1.6)$$

To derive the value of d , it is assumed that the emission process is synchrotron emission and in the fast cooling regime. These are assumptions that are made under the standard internal shock model. If it is assumed that the emission is synchrotron, and then the peak energy in the νF_ν spectrum corresponds to ν'_m which is given below in Equation 1.7, where B' is the comoving magnetic field and γ_m is the electron energy at the peak of the spectrum.

$$\nu'_m \propto B' \gamma_m^2. \quad (1.7)$$

As the Lorentz factor of the shell is constant, the energy of the electron is therefore also constant. This means that,

$$\nu'_p = \nu'_m \propto B'. \quad (1.8)$$

The comoving magnetic field is normal to the radius, and is expected to be approximately $B' \sim \frac{B}{\Gamma}$. As $B \propto R^{-1}$, this can be compared to Equation 1.6 to show that $d = -1$.

Further to this, if the number of particles crossing the shock and the average energy of the particles remain constant, as is expected for a uniform shell, then this implies a constant rate at which internal energy is generated:

$$\frac{dE'_{int}}{dt'} \propto R^0. \quad (1.9)$$

As the shell is in the fast cooling regime, then the comoving luminosity must also be constant with radius.

$$L' \sim L'_{\nu'} \propto R^0, \quad (1.10)$$

where,

$$L' = L'_0 \left(\frac{R}{R_0} \right)^a S \left(\frac{\nu'}{\nu'_p} \right). \quad (1.11)$$

In Equation 1.11 L'_0 is the luminosity at ν' at a radius R_0 . $S(x)$ is the spectral function, and is discussed at length below. It can be seen that as $L' \propto R^0$, combining Equations 1.6 and 1.11 that $a + d = 0$. As $d = -1$, the corresponding value of $a = 1$. This is consistent with expectations from synchrotron emission.

Having established the physical mechanism with which to fit the observed emission, the pulse profile and spectrum must now be considered. This pulse profile must be both consistent with the physical processes outlined and also account for the effects of relativistic beaming. Both the profile and the spectral model are discussed in more depth below.

1.6.2 The pulse profile

The general form of the pulse profile is shown in Equation 1.12, which gives the total number of counts, N , received per unit energy, per unit area, per unit time, at a given time:

$$\frac{dN}{dEdAdT} (E, T \geq T_{ej} + T_0) = P(T - T_{ej}, T_f, T_{rise}) B \left(\frac{E}{E_f}, \frac{T - T_{ej}}{T_f} \right), \quad (1.12)$$

where,

$$P(T - T_{ej}, T_f, T_{rise}) = \left[\left(\min \left(\frac{T - T_{ej}}{T_f}, 1 \right)^{a+2} - \left(\frac{T_f - T_{rise}}{T_f} \right)^{a+2} \right) \times \left(1 - \left(\frac{T_f - T_{rise}}{T_f} \right)^{a+2} \right)^{-1} \right] \left(\frac{T - T_{ej}}{T_f} \right)^{-1}. \quad (1.13)$$

Equation 1.13 gives the temporal form of the pulse derived from the those regions in which the shell emits. The profile is composed of two contributions. The first of these is the term in the square brackets, which controls the rise of the pulse. As T begins at T_0 , with the difference between this and T_{ej} being significantly larger than the difference between T_f and T_{rise} , the term in the square brackets remains positive. This is due to the increase in the total area of emission which can be received by the observer.

At the point $T = T_f + T_{ej}$, the term within the square brackets becomes exactly equal to 1, as does the remaining part of the pulse profile. At this moment, the pulse profile reaches the maximum, as shown in Figure 1.13, and is termed T_{pk} . After this, the value of $\frac{T - T_{ej}}{T_f} > 1$, so the first term in the square brackets takes the value of 1^{a+2} . This means that the square bracket remains equal to 1 whenever $T \geq T_{pk}$, and so the behaviour is dependent only on the final term of Equation 1.13. In this regime, the shape of the pulse is proportional to T^{-1} , and so with increasing time the profile decreases in strength. This accounts for the tip of the EATS passing beyond R_f , and the resulting reduction in the region from which emission can be received by the observed. This term also is dependent on the radius of the emitting region from the central engine, as this affects the geometry of the high-latitude emission. The pulse profile is depicted in Figure 1.13.

1.6.3 The pulse spectrum

In Willingale et al. (2010) the assumed spectrum $S(\nu')$ was taken to be a Band function (Band et al., 1993), which is a phenomenological spectral model first developed to fit time averaged GRB spectra as seen by the spectroscopic detectors (SDs) on board BATSE (Fishman et al., 1985). Subsequent instruments, such as those on *Swift* or the *Fermi* satellite (Meegan et al., 2009) have largely corroborated that the shape of this model well describes the majority of

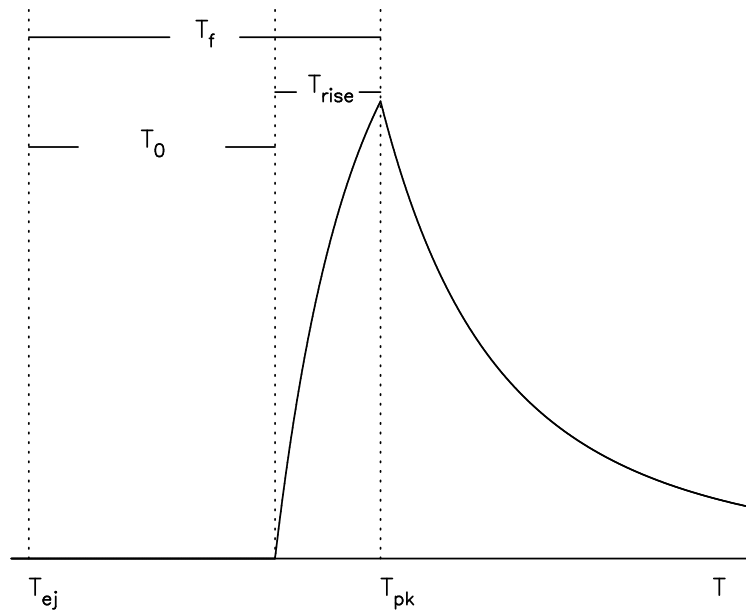


Figure 1.13: Schematic of pulse profile taken from Willingale et al. (2010), as described by Equation 1.13, showing the characteristic times T_{ej} , T_{pk} , T_0 and T_f .

GRBs (Sakamoto et al. 2008d, Bissaldi et al. 2011) indicating that the model is not due to instrumental effects of BATSE. In the case of the *Fermi* satellite, however, there is some suggestion of an additional component in the spectra of some bright bursts, but this has not been yet confirmed by the instruments of any other satellite (Ackermann et al., 2010).

The shape of the Band function is that of a smoothly broken power-law. At high energies, above a break energy of E_{pk} the spectrum is well represented by a power-law of index β , as shown in the second line of Equation 1.14. Below this energy, the equation becomes marginally more complicated, consisting of a power-law of shallower index, α , and an exponential cutoff, related to the break energy. This is illustrated in the top line of Equation 1.14.

$$B \propto \begin{cases} E^\alpha \exp \frac{E}{E_{pk}}, & E < E_{pk}, \\ E^\beta, & E \geq E_{pk}. \end{cases} \quad (1.14)$$

The break energy (E_{pk}) is often also called the peak energy. The Band function models the number of counts at a certain photon energy rather than the total energy received by those photons. This information can be folded into the spectrum by multiplying the counts by their photon energy, which alters the shape of the spectrum as the dependence on energy is now

one power higher. As α typically lies in the range $-1 < \alpha < 0$ and generally β takes a more negative value such that $\beta < -1$, the energy spectrum rises in the low energy regime, before dropping after the break energy. Due to this the spectrum, when no longer in units of counts, peaks at the break energy.

As can be seen from Equation 1.14, there are four free parameters to the Band function: α , β , E_{pk} and a normalization factor. In some work such as Sakamoto et al. (2008d) a cutoff power-law is used in preference to the Band function because, despite being an equally valid fit to the data, the Band function has a larger number of free parameters. This larger number of free parameters would require a notable improvement in fit statistic to justify its use over the simpler cutoff power-law model.

Genet & Granot (2009) altered the Band function as shown in Equation 1.15, to include temporal evolution.

$$B(z) = B \begin{cases} z^{b_1-1} e^{-z}, & z \leq b_1 - b_2, \\ z^{b_2-1} (b_1 - b_2)^{b_1-b_2} e^{-(b_1-b_2)}, & z > b_1 - b_2, \end{cases} \quad (1.15)$$

where

$$z = \left(\frac{E}{E_f} \right) \left(\frac{T - T_{ej}}{T_f} \right)^d. \quad (1.16)$$

The times in Equation 1.16 are all in the observed frame, where T_{ej} is the time of shell ejection from the central engine and T_f is the time at which the last photon arrives from the shell along the line of sight. B is the normalization to the Band function, with b_1 and b_2 being the low- and high-energy photon indices of the Band function, respectively. The spectral shape of each pulse evolves in time as determined by the temporal index d . As previously discussed in §1.6.1, $d = -1$, which is consistent with the emission process being synchrotron radiation, which is an assumption of the standard internal shock model. It was this value that was used in Willingale et al. (2010) and Genet & Granot (2009), and is adopted throughout this thesis.

1.7 The afterglow spectrum

As with the prompt emission the underlying physical mechanism of the afterglow is thought to be synchrotron radiation (Sari et al., 1998) which occurs when relativistic particles are accelerated by a magnetic field (Rybicki & Lightman, 1979).

The associated photon spectrum is a series of power-laws that meet at characteristic break frequencies. The frequency of an emitted photon, ν , can be related to the Lorentz factor of the electron from which it is radiated, γ_e , using Equation 1.17 which is taken from Sari et al. (1998) and is in the frame of an observer near the fluid.

$$\nu(\gamma_e) = \Gamma \gamma_e^2 \frac{q_e B}{2\pi m_e c}. \quad (1.17)$$

In Equation 1.17, Γ refers to the Lorentz factor of the emitting material, B is the magnetic field strength the electrons experience and m_e and q_e are the mass and charge of an electron, respectively.

The spectral breaks seen in the photon spectrum are detailed below, with explanations of their physical origins. Following that the spectra arising from different scenarios, in which the spectral breaks differ in their ordering, are discussed.

1.7.1 Emission from the minimal photon, ν_m

The observed radiation is emitted from the population of relativistic electrons which have a power-law distribution of energies (Fermi, 1949).

$$N(\gamma_e) \sim \gamma_e^{-p}, \quad \gamma_e > \gamma_{e,min}, \quad (1.18)$$

where p is the power-law index of the electron distribution. This distribution does not extend to a Lorentz factor of zero but instead has a minimum cut off at γ_m . By considering the energy of the typical electron and the energy and particle densities (as given in Blandford & McKee 1976), γ_m can be found to be:

$$\gamma_m = \Gamma \frac{m_p}{m_e} \left(\frac{p-2}{p-1} \right) \epsilon_e. \quad (1.19)$$

The factor ϵ_e details the fraction of the shock energy which is transferred to the electron population. Typically it is assumed that $\epsilon_e \sim 0.1$ (Wu et al., 2004).

By combining Equations 1.19 and 1.17 an expression for the frequency of the photon associated with the minimal electron of the population can be found.

$$\nu_m \equiv \nu(\gamma_m) = \frac{\epsilon_e^2 q_e \Gamma^3 B m_p^2}{2\pi m_e^3 c} \left(\frac{p-2}{p-1} \right)^2. \quad (1.20)$$

This shows ν_m to be dependent on several physical characteristics of the relativistic flow. These are the Lorentz factor of the emitting material, the fraction of shock energy deposited in the electron population, the surrounding magnetic field strength and the power-law index of the electron population distribution.

If the photons were all of a single energy, corresponding to γ_m , then below ν_m a power-law segment which is dependent on $\nu^{\frac{1}{3}}$ would be expected. Above ν_m there would be an exponential cut-off in the spectrum. For a population of electrons with a variety of energies the resulting spectrum is more complicated. However, as can be seen in the top panel of Figure 1.14, such a regime of $F \propto \nu^{\frac{1}{3}}$ can occur.

1.7.2 The cooling break, ν_c

The electrons in the distribution cool via the radiation they produce. For an electron losing a significant fraction of its energy to radiation Equation 1.21 must hold (Sari et al., 1998):

$$P(\gamma_c) t = \gamma_c \Gamma m_e c^2, \quad (1.21)$$

where $P(\gamma_c)$ is the emitted power of an electron and γ_c is the critical value of Lorentz factor above which an electron can cool sufficiently quickly. Sari et al. (1998) also give a suitable definition of for P , as shown in Equation 1.22 where σ_T is the Thompson cross-section:

$$P(\gamma_e) = \frac{4}{3}\sigma_T c \Gamma^2 \gamma_e^2 \frac{B^2}{8\pi}. \quad (1.22)$$

Combining Equations 1.21 and 1.22 means that the critical value of Lorentz factor can be expressed as shown:

$$\gamma_c = \frac{6\pi m_e c}{\sigma_T \Gamma B^2 t}. \quad (1.23)$$

In a similar method to the definition of ν_m a photon frequency can be associated with γ_c as $\nu_c \equiv \nu(\gamma_c)$:

$$\nu_c = \frac{18\pi m_e c q_e}{\sigma_T^2 \Gamma B^3 t^2} \quad (1.24)$$

The relative values of γ_m and γ_c , and therefore ν_m and ν_c , have an important physical effect on the nature of the cooling which takes place (Sari et al., 1998). If $\gamma_c < \gamma_m$ all of the electrons in the population can cool, this is called ‘fast cooling’. However, if $\gamma_c > \gamma_m$ then there are electrons with Lorentz factors below the critical value. Due to the shape of the electron distribution, most of the population have Lorentz factors $\gamma_e \sim \gamma_m$, meaning most cannot lose energy via radiation rapidly. This is therefore termed ‘slow cooling’.

As can be seen in Figure 1.14, the power-law segment between ν_m and ν_c changes depending on which is higher. In the fast cooling regime, an example of which is panel 5, the electron energy is proportional to γ_e . From Equation 1.17, $\nu_e \propto \gamma_e^2$, resulting in a spectrum that varies as $\nu^{-\frac{1}{2}}$.

In the slow cooling regime, such as panel 1 of Figure 1.14, the shape of the electron distribution is also important. The range $\nu_m < \nu < \nu_c$ contains the majority of the electron population, as due to the shape of the distribution, most of the electrons begin with Lorentz factors of order $\sim \gamma_m$. Accordingly, the shape of the spectrum depends on $\nu^{\frac{(1-p)}{2}}$.

Also shown on Figure 1.14 is the time evolution for each of the spectral breaks. With ν_m evolving more rapidly than ν_c it is expected that the early afterglow is in the fast cooling regime, and evolves to the slow cooling regime at later times.

1.7.3 Synchrotron self-absorption, ν_a

A further process that affects the shape of the broadband spectrum is synchrotron self-absorption (Granot et al., 1999b). The electrons responsible for the emission of the photons are also capable of absorbing them. This occurs at low frequencies, leading to a deficit of flux in this regime.

The self-absorption frequency ν_a is defined as being where the optical depth due to synchrotron self-absorption, τ , is unity. This optical depth describes how easily flux can escape from a region. In regions where $\tau > 1$ it becomes difficult for radiation to escape, and so they are termed ‘optically thick’.

In the co-moving frame, the synchrotron self-absorption frequency can be found if the Rayleigh–Jeans part of the black body spectrum is equated to the synchrotron flux at that frequency:

$$2kT' \frac{\nu_a'^2}{c^2} = f'_\nu(\nu_a'), \quad (1.25)$$

where k is the Boltzmann constant and T' is the electron temperature in the frame of the electrons. This temperature can be expressed in the comoving frame as:

$$T' = \begin{cases} \frac{\gamma_a m_e c^2}{k}, & \gamma_m < \gamma_a, \\ \frac{\gamma_m m_e c^2}{k}, & \gamma_a < \gamma_m. \end{cases} \quad (1.26)$$

As it has already been shown that for synchrotron emission $\nu_e \propto \gamma_e^2$, this shows that the emission below ν_a is proportional to either ν^2 or $\nu^{\frac{5}{2}}$ depending on whether $\gamma_m < \gamma_a$. At ν_a the thermal and synchrotron fluxes are equal in magnitude, and so can be equated. Taking the expressions derived for both, Shen & Zhang (2009) expressed a relation for ν_a that depended on key physical characteristics of the emitting region:

$$\nu_a = \begin{cases} \left(\frac{C_1}{2}\right)^{\frac{3}{5}} \left(\frac{q_e B c^3}{2\pi m_e}\right)^{\frac{3}{10}} \Gamma^{-\frac{3}{10}} (1+z)^{-\frac{9}{10}} \nu_p^{-\frac{3}{5}\beta_1} \nu_m^{\frac{3\beta_1}{5}-\frac{1}{2}} f_{\nu_p}^{\frac{3}{5}} \left(\frac{D_L}{R}\right)^{\frac{6}{5}}, & \nu_a < \nu_m, \\ \left(\frac{C_2}{2}\right)^{\frac{1}{\frac{5}{2}-\beta_1}} \left(\frac{q_e B c^3}{2\pi m_e}\right)^{\frac{1}{5-2\beta_1}} \Gamma^{\frac{-1}{5-2\beta_1}} (1+z)^{\frac{-3}{5-2\beta_1}} \nu_p^{\frac{-\beta_1}{\frac{5}{2}-\beta_1}} f_{\nu_p}^{\frac{1}{\frac{5}{2}-\beta_1}} \left(\frac{D_L}{R}\right)^{\frac{2}{\frac{5}{2}-\beta_1}}, & \nu_m < \nu_a. \end{cases} \quad (1.27)$$

In Equation 1.27, β_1 is the spectral index below the peak frequency, ν_p , and the terms C_1 and C_2 are numerical factors that depend solely on β_1 (Shen & Zhang, 2009). Also, D_L is the luminosity distance to the source and R is the distance of the emission from the centre of the explosion.

As can be seen from Equation 1.27 the important physical parameters that determine the nature of the ν_a are the peak of the νF_ν spectrum, the low-energy spectral index, the Lorentz factor of the emitting material, distance from the initial explosion and the applied magnetic field strength. Also important is the redshift of the explosion, due to cosmological effects.

1.7.4 Combining the spectral breaks

With up to three possible spectral breaks, which evolve differently with time, there are several different potential shapes to afterglow spectra. These are illustrated in Figure 1.14 which is taken from Granot & Sari (2002). In Figure 1.14 ν_{sa} is equivalent to ν_a as used elsewhere in this thesis.

The top panel describes the canonical slow cooling case also considered in Sari et al. (1998). In addition to this ordering of the ν_m and the cooling break, self-absorption is also included. $\nu_a < \nu_m$, meaning therefore self-absorption is occurring below the minimum energy emitted from the initial electron population and the power-law segment below ν_a is proportional to ν^2 . Such a spectrum might be expected during the later phases of the afterglow.

The second panel is again a slow cooling spectrum, however it is modified by the self-absorption break occurring at a higher frequency than ν_m . Because there are now electrons in the population contributing to the spectrum below ν_a , the power-law has a different index, this time varying as $\nu^{\frac{5}{2}}$. This behaviour continues until ν_m , below which the standard power-law of ν^2 is evident.

The third panel shows a spectrum that could be either fast or slow cooling. In this instance ν_a is larger than both ν_m and ν_c , and as such the order of the latter two frequencies are unimportant. Instead there is a broadband spectrum composed of three segments. The first is above ν_a , the slope of which is dependent upon the electron population. Next, for $\nu_m < \nu < \nu_a$ a power-law related to $\nu^{\frac{5}{2}}$ as discussed by Rybicki & Lightman (1979) is expected. Below ν_m a

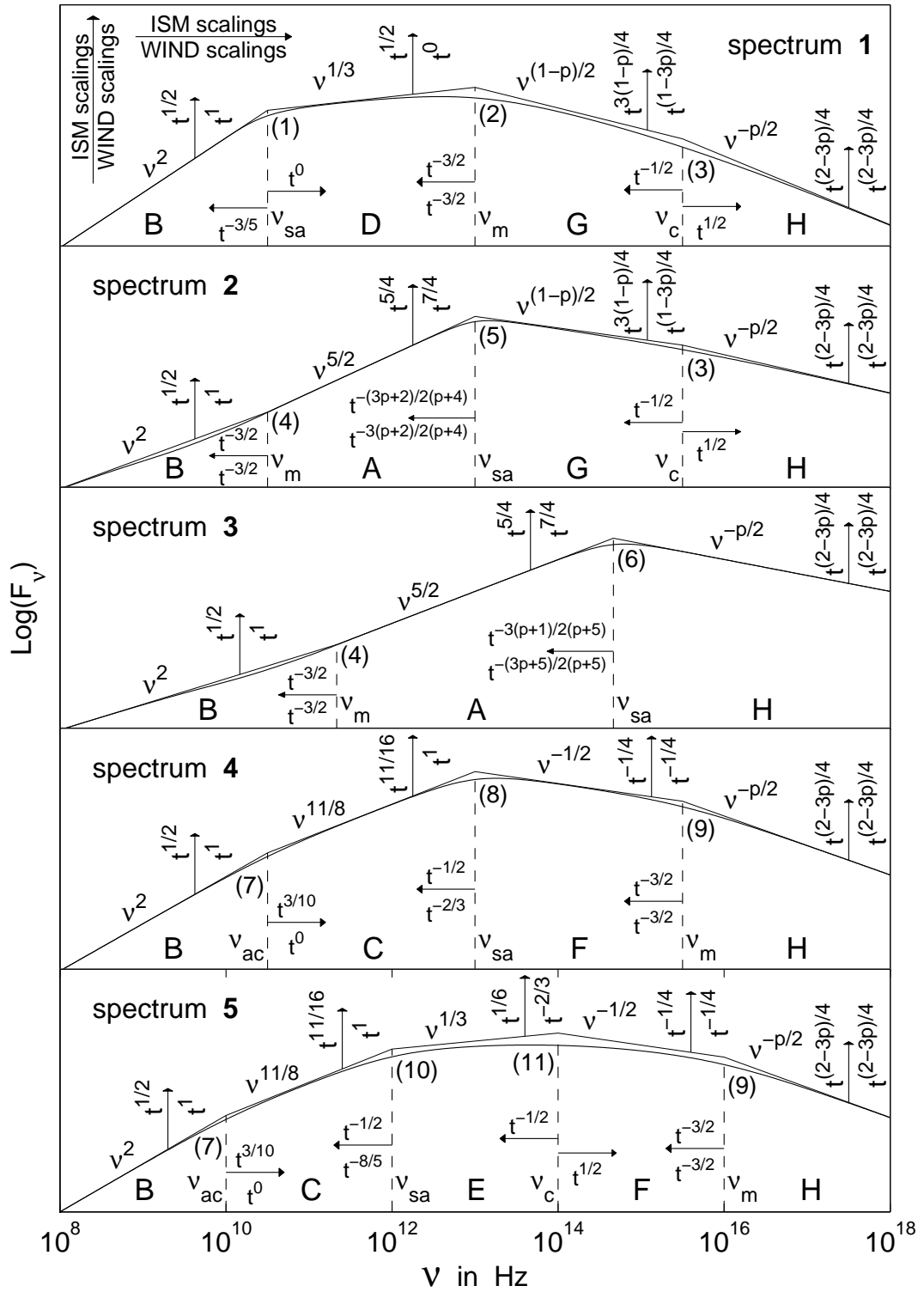


Figure 1.14: Figure taken from Granot & Sari (2002) showing the different possible broadband synchrotron spectra of GRB afterglows. The top two panels show slow cooling scenarios ($\nu_m < \nu_c$), the bottom two panels show fast cooling scenarios, whilst the middle panel could be used for either as $\nu_{sa} > \nu_m, \nu_c$. The time evolution of each spectral break is also shown, for both an ISM and wind-like environment.

power-law of ν^2 is theoretically expected.

The fourth panel shows a fast cooling spectrum, although in this instance the cooling break is not present. This is because, as with the third panel, $\nu_a > \nu_c$ and so self-absorption dominates the part of the spectrum in which ν_c would appear. An additional frequency ν_{ac} is also shown. This arises because a fast cooling plasma is expected to be inhomogeneous, with electrons nearer the shock front not having cooled, unlike those further downstream. Granot et al. (2000) discuss this scenario, and propose that the optical depths of the cooled and uncooled electrons vary. ν_{ac} and ν_a correspond to where the optical depth is unity for uncooled and all electrons, respectively. The additional interim power-law segment is expected to follow $\nu^{\frac{11}{8}}$.

The final panel is fast cooling once more, but in this instance the break frequencies are ordered: $\nu_a < \nu_c < \nu_m$. As $\nu_a < \nu_c$, the cooling break can be seen once more, with a $\nu^{\frac{1}{3}}$ power-law being present for $\nu_c < \nu_m$. As this is a fast cooling case, the additional break discussed by Granot et al. (2000) is also included at ν_{ac} , again due to the optical depth from the noncooled electrons reaching unity at a different frequency to the cooled electrons further downstream from the shock front.

1.8 This thesis

This thesis focuses on modelling the prompt and afterglow emission. In Chapters 2 and 3 the Genet & Granot (2009) model is applied in an attempt to reconcile observations in both the X-ray and γ -ray regimes with optical and near infrared (NIR) data.

Chapter 2 analyses GRB 080310 in an attempt to ascertain the origins of the early-time low-energy emission which is observed. In chapter 3 three bursts are considered in more detail, with more emphasis being placed on the afterglow morphology for each.

Chapter 4 presents analysis of a sample of bright bursts whose prompt light curves are evolved to see how they would have appeared if they occurred at higher redshifts. The evolution in easily measured parameters such as duration or hardness ratio are discussed in detail. An alternative duration measure is also presented in an attempt to find a better indicator of the

active period of a burst.

To extend the statistics of the work in Chapter 4, a larger synthetic sample is created in Chapter 5. With an increased sample size, comparisons are made to the few observed high redshift GRBs that have been detected by *Swift* BAT. The composition of T_{90} is also discussed and comparisons of the results from this methodology are made to existing simulations of a similar nature.

The final chapter of this thesis summarises all of the conclusions from each of the science Chapters. Chapter 6 also discusses the manner in which it is hoped work from this thesis can be expanded in the future.

2

The origin of the early time optical and infrared emission of GRB 080310

2.1 Chapter overview

In an effort to understand the radiation mechanism responsible for the prompt emission in GRBs, broadband multi—wavelength observations of GRB 080310 are presented. Using these, a simultaneous model of the available γ -ray, X-ray, optical and NIR data is applied using a series of pulses to model the prompt emission before an afterglow component is also included.

This Chapter begins by presenting the observations of GRB 080310, both from the *Swift* satellite and ground based observatories. The high energy data obtained from instruments on board *Swift* are then fitted using the methodology adopted in Willingale et al. (2010) and the results directly extrapolated to the optical and NIR regimes. Seeing that this leads to a vast over-prediction in the optical and NIR flux, the next sections detail the alterations made to the prompt pulse and afterglow models to obtain a better representation of the data.

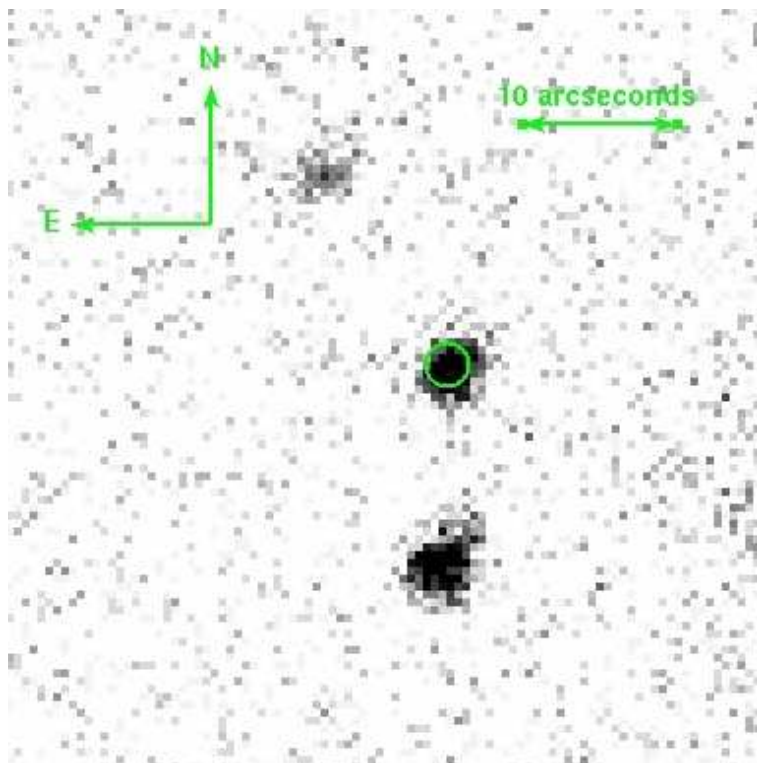


Figure 2.1: UVOT ν -band image from T_0 (+79) seconds to T_0 (+1539) seconds. The enhanced *Swift* XRT position is shown, with an error circle of radius $1''.4$, corresponding to the 90% confidence limit, containing the optical afterglow candidate at an average ν -band magnitude of 17.49.

Two alternative scenarios are proposed; one where the optical and NIR data at early times are the result of afterglow emission and the other where they are due to prompt emission. The relative merits of each are discussed.

2.2 Observations of GRB 080310

On March the 10th 2008 the *Swift* BAT triggered and located GRB 080310 (trigger number 305288) on board at 08:37:58 UT (Cummings et al., 2008). *Swift* slewed immediately which enabled the narrow field instruments to begin observing the burst 89 seconds after the trigger. The burst was detected by the XRT and UVOT (*white* filter), with the latter providing the best *Swift* position of RA(J2000) = $14^{\text{h}}40^{\text{m}}13^{\text{s}}.80$, Dec(J2000) = $-00^{\circ}10'29''.6$ with a 1σ error radius of 0.6 arcseconds. Figure 2.1 shows a UVOT ν -band image from the early-time data and Figure 2.2 shows the XRT image obtained by summing all observations.

The *Swift* light curves obtained in multiple bands from each of the three on-board instru-

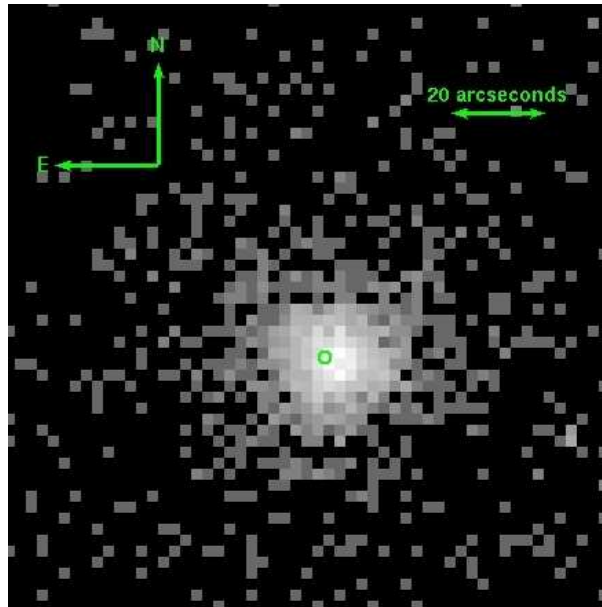


Figure 2.2: XRT image over all nine XRT observational segments, giving a total exposure time of 106.9 ks. The circular region is the *Swift* enhanced XRT position, and with an error radius of 1.4'' arcseconds (90% confidence).

ments are presented in Figure 2.3 and most of the available data sets from an extensive number of other facilities are shown in Figure 2.4. Data from the Peters Automated Infrared Imaging Telescope (PAIRITEL; Perley et al. 2008) and Katzman Automatic Imaging Telescope (KAIT) instruments are shown separately in Figure 2.5.

In addition to *Swift* observations, and those instruments already mentioned, GRB 080310 was also observed on the ground with numerous optical and NIR facilities, including the Rapid Eye Mount (REM; Covino et al. 2008), Very Large Telescope (VLT; Covino et al. 2008) and the Faulkes Telescope North (FTN). These observations are shown alongside the XRT light curve in Figure 2.4.

The Kast dual spectrometer at the Lick Observatory, California, obtained the first redshift measurement for this bursts of $z = 2.4266$ (Prochaska et al., 2008) using strong absorption features from silicon, carbon and aluminium. This was later corroborated by the VLT–Ultraviolet and Visual Echelle Spectrograph (UVES) instrument (Vreeswijk et al., 2008) and the Keck Deep Imaging Multi–Object Spectrograph (DEIMOS; Prochaska et al. 2008).

The following subsections describe the observations in more detail. The *Swift* data analysis was performed using release 2.8 of the *Swift* software tools. Parameter uncertainties are

estimated at the 90% confidence level. It is also important to note that the optical data sets have been reduced using different methods, and the effects of cross-calibration errors were fully investigated, ensuring that the later analysis remained insensitive to them.

2.2.1 BAT

The BAT data were processed using the standard `BATGRBPRODUCT` script. The top four panels of Figure 2.3 show the BAT light curves displayed in the four standard energy band of 15–25, 25–50, 50–100 and 100–150 keV, plotted with respect to the BAT trigger time (T_0). The binning is such that each bin satisfies a minimum signal-to-noise ratio of 5 and a minimum time bin size of 1 second.

The γ -ray light curve shows many peaks with the first at T_0 (–60) seconds. The brightest peak extends from T_0 (–12) to T_0 (+7) seconds. This is followed by a period of no detectable γ -ray emission before a weaker, broad series of peaks is seen from T_0 (+180) to T_0 (+360) seconds (Tueller et al., 2008). The latter peak is consistent with the first strong flare seen in the XRT (see below). The BAT emission is strongest in the lower energy bands, below ~ 100 keV. The T_{90} is estimated to be 365 ± 20 seconds (where the error includes systematics).

The total spectrum from T_0 (–71.76) to T_0 (+318.75) seconds is well fit by a power-law of photon index 2.32 ± 0.16 , with a total fluence of $2.3 \pm 0.2 \times 10^{-6}$ ergs.cm $^{-2}$ over the 15–150 keV band. The fluence ratio $S(25 - 50 \text{ keV}) / S(50 - 100 \text{ keV})$ is 1.27 ± 0.17 which puts GRB 080310 on the border of the X-ray rich gamma-ray bursts (XRRs) and X-ray flashes (XRFs) according to the definition of Sakamoto et al. (2008a).

2.2.2 XRT

The *Swift*-XRT began observing GRB 080310 89 seconds after the trigger, with windowed timing data ranging from T_0 (+95) to T_0 (+799) seconds and photon counting data thereafter (Beardmore et al., 2008). As can be seen in Figure 2.3 the soft XRT light curve initially fades until T_0 (+130) seconds, before the burst re-brightens. This flaring activity continues until T_0 (+420) seconds before the count rate drops again briefly. A further flaring event is seen between T_0 (+500) and T_0 (+620) seconds, which is approximately half as bright

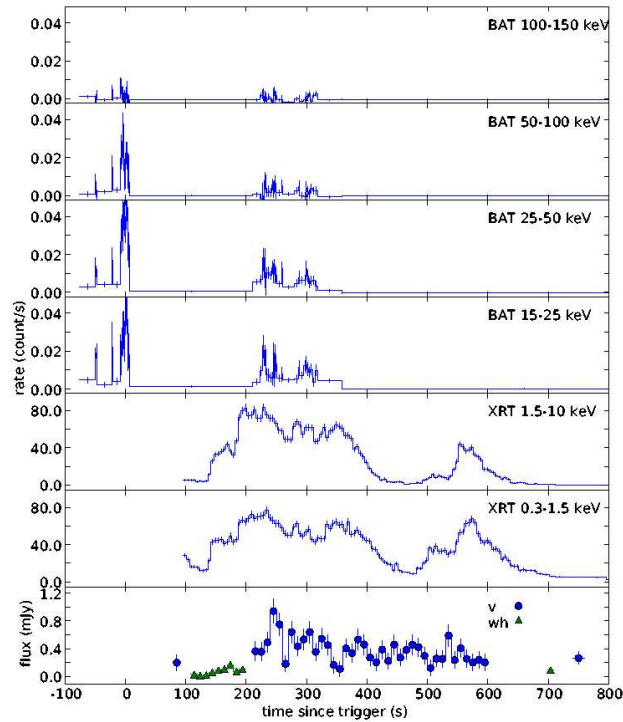


Figure 2.3: *Swift* prompt light curves from GRB 080310. From top to bottom, BAT 100–150 keV, BAT 50–100 keV, BAT 25–50 keV, BAT 15–25 keV, XRT 1.5–10.0 keV, XRT 0.3–1.5 keV and UVOT v and *white* bands.

as the first. There is significant spectral evolution during these flaring events, where the $S(1.5 - 10 \text{ keV}) / S(0.3 - 1.5 \text{ keV})$ ratio shows a hardening in the spectrum at $T_0 (+135)$ to $T_0 (+200)$ seconds and $T_0 (+500)$ to $T_0 (+565)$ seconds before, in both instances, there is a softening as the flaring behaviour declines.

2.2.3 UVOT

UVOT observations began with a 100 second finding chart exposure taken at $T_0 (+99)$ seconds (Hoversten & Cummings, 2008). This finding chart exposure was the sum of 10 individual 10 second frames, with GRB 080310 being detected in all but the first. At the time of GRB 080310 UVOT observations during the first orbit were taken in the event mode, which allows for higher temporal resolution, while during subsequent orbits observations were taken in imaging mode. UVOT photometry was done using the publicly available FTOOLS data reduction suite, and

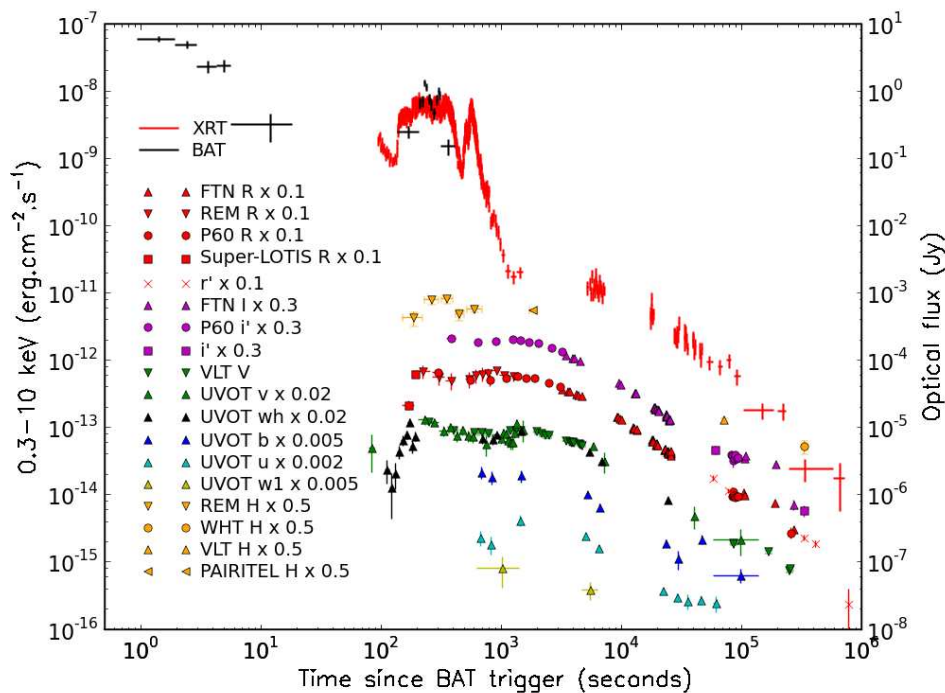


Figure 2.4: Gamma-ray to NIR light curves for GRB 080310, showing the energy bands used to observe the GRB and the instruments used to take the measurements. Data have been scaled from their actual values for viewing purposes.

is in the UVOT photometric system described in Poole et al. (2008). During the first 1,000 seconds the light curve is complex as shown in Figure 2.3, after which the burst can be seen to fade in all the observed optical bands (Figure 2.4).

There are available data for the UVOT *white*, *v*, *b*, *u* and *uvw1*. As this burst has a measured redshift of $z = 2.43$, it is important to consider absorption from the intervening medium through which the emission must travel. Correction factors were calculated for Lyman absorption using the *GRBz* code described in Curran et al. (2008). *GRBz* uses the model presented by Madau (1995) to calculate the absorption from neutral hydrogen in the intergalactic medium. Having found the correction factor for all the optical and near infrared bands presented in this work, it was found that only the data in the *b*, *u* and *uvw1* bands required this correction. Whilst the correction to both the *u* and *b* bands was not large, it was found that the *uvw1* data required a significant correction, within which there was a large uncertainty. Given that there were only two data points from UVOT in this band, these were removed from any further analysis.

2.2.4 Faulkes Telescope North

Observations with the Faulkes Telescope North (FTN) started at 09:31:07.3 UT, on the 10th of March 2008, 3.188 ks after the trigger. Data were reduced in a standard fashion using IRAF (Tody, 1986). Calibration was performed using Sloan Digital Sky Survey (SDSS) data for the region (Adelman-McCarthy et al., 2007). For the *I* and *R* filters, the SDSS photometry was converted to the Johnson–Cousins system¹. Photometry was then performed using an aperture matched to the average seeing of the (combined) frames. For the conversion from magnitude to flux, the data were first corrected for Galactic extinction using the *Cosmic Background Explorer* (COBE) Diffuse Infrared Background Experiment (DIRBE) extinction maps from Schlegel et al. (1998), and then converted using flux zero–points from Fukugita et al. (1995) for optical and Tokunaga & Vacca (2005) for IR. AB magnitudes were converted following Oke & Gunn (1983).

2.2.5 Robotic Optical Transient Search Experiment (ROTSE)

ROTSE–IIIb, located at McDonald Observatory, Texas, responded to GRB 080310 and began imaging 5.7 seconds after the Gamma–ray Coordinates Network (GCN) notice time (Yuan et al., 2008). Observations were carried out under fluctuating weather conditions. The optical transient (OT) was detected between 25 minutes and 3.5 hours after the trigger. To improve detection signal–to–noise ratio, sets of four to 11 images were co–added and exposures badly affected by weather were excluded. The OT is slightly blended with two nearby stars in the ROTSE images. Scaled point spread functions (PSFs) of these two nearby stars were therefore subtracted and then PSF–matching photometry on the OT using a custom RPHOT package (Quimby et al., 2006) was applied. The analysis was further complicated by large seeing variation, particularly towards the end of the observation. The structure seen in the light curve during this time is likely not significant. The ROTSE–III unfiltered magnitudes are calibrated to SDSS *r* using standard stars in the pre–burst SDSS observations (Cool et al., 2008).

¹See Lupton (2005) at <http://www.sdss.org/dr6/algorithms/sdssUBVRITransform.html>

2.2.6 REM

Early-time optical and NIR data were collected using the 60-cm robotic telescope Rapid Eye Mount (REM: Zerbi et al. 2001; Covino et al. 2004) located at the European Southern Observatory (ESO) La Silla observatory (Chile). The telescope simultaneously feeds, by means of a dichroic, the two focal instruments: REMIR (Conconi et al., 2004) a NIR camera, operating in the range 1.0 to 2.3 μm (z' , J , H and K) and ROSS (REM Optical Slitless Spectrograph; Tosti et al. 2004) an optical imager with spectroscopic (slitless) and photometric capabilities (V , R , I). Both cameras have a field of view of $10 \times 10 \text{ arcmin}^2$.

REM reacted automatically after receiving the *Swift* alert for GRB 080310, and began observing about 150 seconds after the GRB trigger time (Covino et al., 2008).

Optical and NIR data were reduced following standard procedures. In particular, each single NIR observation with REMIR was performed with a dithering sequence of five images shifted by a few arcseconds. These images were automatically elaborated using the proprietary routine AQUA (Testa et al., 2004). The script aligns the images and co-adds all the frames to obtain one average image for each sequence. Astrometry was performed using United States Naval Observatory (USNO)–B1² (Monet et al., 2003) and Two Micron All Sky Survey (2MASS)³ (Skrutskie et al., 2006) catalogue reference stars.

Photometry was derived by a combination of the SExtractor package (Bertin & Arnouts, 1996) and the photometric tools provided by the GAIA⁴ package. The photometric calibration for the NIR was accomplished by applying average magnitude shifts computed using 2MASS isolated and non-saturated stars. The optical data were calibrated using instrumental zero-points and checked with observations of standard stars in the field provided by Henden (2008).

2.2.7 VLT

VLT Focal Reducer and Spectrograph (FORIS1; Appenzeller et al. 1998) V and R observations for GRB 080310 were automatically activated with the RRM mode⁵ which allows the telescope

²<http://tdc-www.harvard.edu/catalogs/ub1.html>

³<http://pegasus.phast.umass.edu/>

⁴<http://star-www.dur.ac.uk/pdraper/gaia/gaia.html>

⁵<http://www.eso.org/sci/observing/phase2/SMSpecial/RRMObservation.html>

to react promptly to any alert. The field was acquired and the observations began less than seven minutes after the GRB trigger. Later VLT observations were obtained with the Infrared Spectrometer and Array Camera (ISAAC) at about one day after the burst with the *J*, *H* and *K* filters. In addition linear polarimetry observations were carried out with FORS1 with the *V* filter at approximately one, two and three days after the trigger.

Optical and NIR data were reduced following standard procedures with the tools of the ESO–ECLIPSE package (Devillard, 1997). Polarimetric data were reduced again following standard procedures as discussed in Covino et al. (1999, 2002, 2003). Photometry was performed by means of the tools provided by the GAIA package and with PSF photometry with the ESO–MIDAS⁶ DAOPHOT context (Stetson, 1987).

The photometric calibration for the NIR was accomplished by applying average magnitude shifts computed using the Two Micron All Sky Survey (2MASS; Skrutskie et al. 2006) isolated and non–saturated stars. The optical data were calibrated using instrumental zero–points and checked with observations of standard stars in the field provided by Henden (2008). Linear polarimetry position angle was corrected by means of observations of polarimetric standard stars in the NGC 2024 region.

2.2.8 WHT

Late imaging was obtained with the 4.2m William Herschel Telescope (WHT), at Roque de los Muchachos Observatory (La Palma, Spain) using the Long–slit Intermediate Resolution Infrared Spectrograph (LIRIS) in its imaging mode. Observations consisted of 36×25 second exposures in *H* band, obtained on the 14th March 2008 from 04:36:28 to 04:53:41 UT. The data were reduced following standard procedures in IRAF. For the photometric calibration, stars from the 2MASS catalogue were used as reference.

2.2.9 PAIRITEL

PAIRITEL (Bloom et al., 2006) responded to GRB 080310 and began taking data at 09:04:58 (UT) in the *J*, *H*, and *K* filters simultaneously (Perley et al., 2008). The afterglow (Chornock

⁶<http://www.eso.org/sci/software/esomidas/>

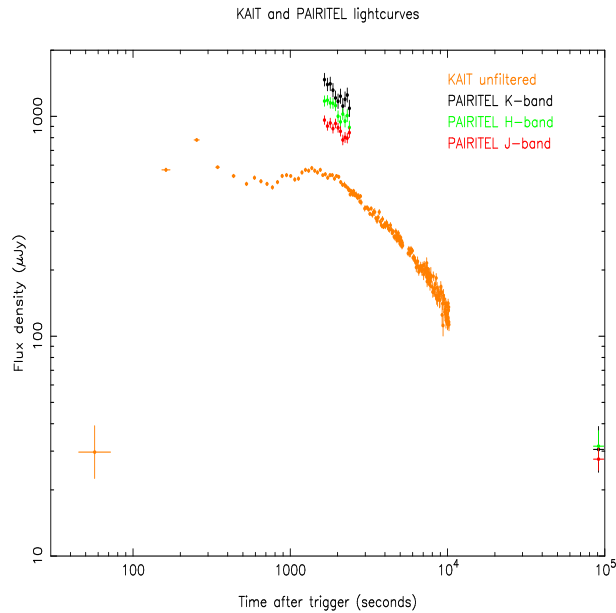


Figure 2.5: PAIRITEL and KAIT light curves for GRB 080310. The KAIT unfiltered data are calibrated to the R band. All data have been corrected for dust extinction.

et al., 2008) was well-detected in all three filters. Perley et al. (2008) also report on a spectral energy distribution (SED) constructed using data from PAIRITEL, KAIT and UVOT (Hoversten & Cummings, 2008), allowing a joint fit to be made and the estimation of a small amount ($A_V = 0.10 \pm 0.05$) of SMC-like host-galaxy extinction.

2.2.10 KAIT

KAIT, also at the Lick Observatory (Li et al., 2003), responded to the trigger and began taking unfiltered exposures starting 42 seconds after the trigger time. This work includes 206 unfiltered data points, which have been reduced in a standard way and then calibrated to the R band (Li et al., 2003). These data, once calibrated, are shown along with the PAIRITEL data in Figure 2.5.

The first KAIT data point has a central time of 57 seconds, with a total exposure time of 30 seconds. Given the highly variable nature of early-time GRB emission, the large error bars on the value, the long duration over which the magnitude was measured and (as later discussed) its outlier nature, it was felt that this magnitude did not provide a useful measure the R -band emission over this time. It was therefore excluded from later analysis.

2.2.11 Gemini

The last optical data were acquired with Gemini-North using the Gemini Multi-Object Spectrograph (GMOS; Davies et al. 1997) in imaging mode with the r band filter. The observations began at 10:22 (UT) on 19th March 2008 and consisted of 5×150 second exposures. The data were reduced using the GEMINI-GMOS routines within IRAF. No significant flux was detected at the location of the afterglow during these observations.

2.2.12 Observations from literature

Data from the Palomar 60-inch telescope (P60; Cenko et al. 2006) were obtained from the Palomar 60 inch-*Swift* Early Optical Afterglow Catalog (Cenko et al., 2009), in which the 29 GRBs between the 1st of April 2005 and the 31st of March 2008 with P60 observations beginning within the first hour after the initial *Swift*-BAT trigger are presented. Cenko et al. (2009) reduce data in the IRAF environment, using a custom pipeline detailed in Cenko et al. (2006). Magnitudes were calculated using aperture photometry and calibration performed using the USNO-B1 catalog⁷ and the data were corrected for dust extinction using the extinction maps of Schlegel et al. (1998).

Further published data for GRB 080310 were obtained from Kann et al. (2010), in which data taken by the Small and Moderate Aperture Research Telescope System (SMARTS) using A Novel Dual Imaging Camera (ANDICAM) are detailed as part of an extensive survey of optical data for GRBs in both the pre-*Swift* and *Swift* eras. Kann et al. (2010) reduce their data using standard procedures in IRAF and MIDAS. Both aperture and PSF photometry were used in the derivation of magnitudes, when comparing to standard calibrator stars.

The 0.6-m Super-Livermore Optical Transient Imaging System (LOTIS) telescope, located at the Steward Observatory (Kitt Peak, Arizona; Pérez-Ramírez et al. 2004) began R band observations of the error region of GRB 080310 at 08:38:43 UT, 44 seconds after the start of the burst (Milne & Williams, 2008). The OT detected by Chornock et al. (2008) and confirmed by Cummings et al. (2008) was not apparent in the initial images, even when stacking the first three 10 second exposures. However, the subsequent 20 second exposures do show

⁷<http://www.nofs.navy.mil/data/fchpix>

the OT without stacking, which suggests that the GRB brightened in the R band during the first two minutes after detection. A nearby USNO–B star was used to derive the R magnitude.

2.3 Modelling high–energy GRB light curves

The prompt emission of GRBs can provide clues as to the nature of the central engine it is caused by. To this end, efforts have been made to model the observed light curves taken during this period of stochastic radiation. An example of this is Kumar & McMahon (2008) in which the authors attempt to reconcile the observed prompt emission with synchrotron radiation. Synchrotron radiation occurs when a population of ultra–relativistic electrons gyrate around magnetic field lines. It is the acceleration from this circular motion which produces synchrotron emission.

To account for differences between the emission expected from this radiation mechanism the synchrotron spectrum was modified by including inverse Compton scattering. Inverse Compton scattering is a process in which photons are scattered from energetic electrons and during these scattering events remove energy from the electrons. In Kumar & McMahon (2008) the photons are scattered by the electron population directly responsible for the synchrotron emission, and so this form of inverse Compton is also known as synchrotron self Compton (SSC).

This Chapter extends the work of Willingale et al. (2010), which adopts the prompt pulse model of Genet & Granot (2009) to fit a sample of 12 GRBs. Both the modifications required to the prompt spectrum and the form of the afterglow component are discussed in detail below.

2.3.1 Initial modelling of the high–energy emission

To model the emission of GRB 080310, the BAT and XRT light curves were first fitted, before extending the model into the lower energy bands for which there were data.

The prompt emission

As discussed in the introduction, the prompt light curve for a GRB is split into a series of pulses when modelled using the Willingale et al. (2010) methodology. These pulses are also used to fit flares observed in the XRT light curve. For each pulse there are nine parameters, although several of these remained fixed, as determined by properties of the physical model.

The first two parameters of each pulse were fixed to $d = -1$ and $a = 1$, as previously discussed in the introduction. Spectrally, the form of a Band function was used, however, the difference between the two spectral indices, b_1 and b_2 , was set to be $b_1 - b_2 = 10$. This effectively produced an exponentially cut-off power-law spectrum, as the contribution above the break between the two power-laws became negligible. Often E_{pk} fell above the observed spectral range of BAT, and so in such instances was set to 200 keV at time T_{pk} . For pulses where E_{pk} could be observed, it was fitted.

To determine the remaining properties of each pulse, the light curves were analysed, and both T_{pk} and T_0 were identified by eye. This gave initial estimates for T_{pk} , T_f and T_{rise} . With these estimates in place, a fit was performed allowing the three to vary. With these more accurate values, the remaining parameters (S_{pk} , b_1 and where appropriate E_{pk}) were fitted. This was conducted using the χ^2 fit statistic.

In this fit, 16 unique pulses have been identified and can be seen to fit the BAT and XRT data accurately in Figure 2.6. In the original fit from Willingale et al. (2010) there were only 10 pulses; however, this failed to fully model some of the structure in the softest BAT band (15–25 keV) between 200 and 400 seconds. The additional pulses now provide a better fit to this time, across all the BAT and XRT bands with a reduced χ^2 statistic of 1.68 for 1,212 degrees of freedom. The quality of this fit is formally not statistically acceptable; however, the largest contribution to the χ^2 value is from small-scale intrinsic fluctuations in the data. The properties of the 16 pulses are listed in Table 2.1.

The afterglow

The prompt pulse model describes the morphology of the prompt light curve and the rapid decay phase (RDP) as observed in the high-energy bands. In addition to this, an afterglow

Table 2.1: Properties of the prompt pulses identified in the BAT and XRT light curves. These include the peak time (T_{pk}), peak energy at this time (E_{pk}), the rise time (T_{rise}) and arrival time of the last photon (T_f) for each pulse.

Pulse	T_{pk} (s)	E_{pk} (keV)	T_{rise} (s)	T_f (s)	b_1
1	-52.8	200	9.7	44.5	-1.49
2	-16.0	200	5.0	6.0	-1.20
3	-4.6	200	3.8	11.7	-0.40
4	1.8	200	2.7	17.2	-1.50
5	159.0	12.3	25.3	74.0	-0.30
6	191.6	13.4	12.4	39.8	-0.02
7	210.0	21.3	10.0	46.7	-0.16
8	235.0	58.0	8.0	24.4	-0.13
9	251.8	42.0	10.0	52.4	-0.20
10	282.0	15.8	10.0	40.0	-0.10
11	308.7	16.1	15.0	32.5	0.24
12	342.7	7.8	15.0	40.1	-0.18
13	366.0	34.3	10.0	11.5	-0.38
14	390.0	1.2	23.0	56.1	0.21
15	513.8	3.8	31.1	193.8	-1.26
16	582.1	2.4	43.9	66.5	-0.09

component was also included in the modelling as outlined in Willingale et al. (2007). The afterglow component has a functional form as outlined in Equation 2.1, which comprises an exponential phase that transitions into a power-law decay:

$$f_a(t) = \begin{cases} F_a \exp\left(\alpha_a - \frac{t\alpha_a}{T_a}\right) \exp\left(\frac{-T_r}{t}\right), & t < T_a, \\ F_a \left(\frac{t}{T_a}\right)^{-\alpha_a} \exp\left(\frac{-T_r}{t}\right), & t \geq T_a. \end{cases} \quad (2.1)$$

In Equation 2.1, $f_a(t)$ is the flux from the afterglow at time t , F_a gives the flux at the transition time between the exponential and the power-law components, T_a . T_r is the rise time and finally α_a is the index that governs the temporal decay of the power-law phase.

Combining the prompt pulses and the afterglow component the same method of fitting the data from the *Swift* BAT and XRT instruments was adopted as Willingale et al. (2010). Having first identified and fitted the individual pulses in the BAT light curve and allowing their parameters to be fitted by minimising the χ^2 fit statistic the afterglow component was then

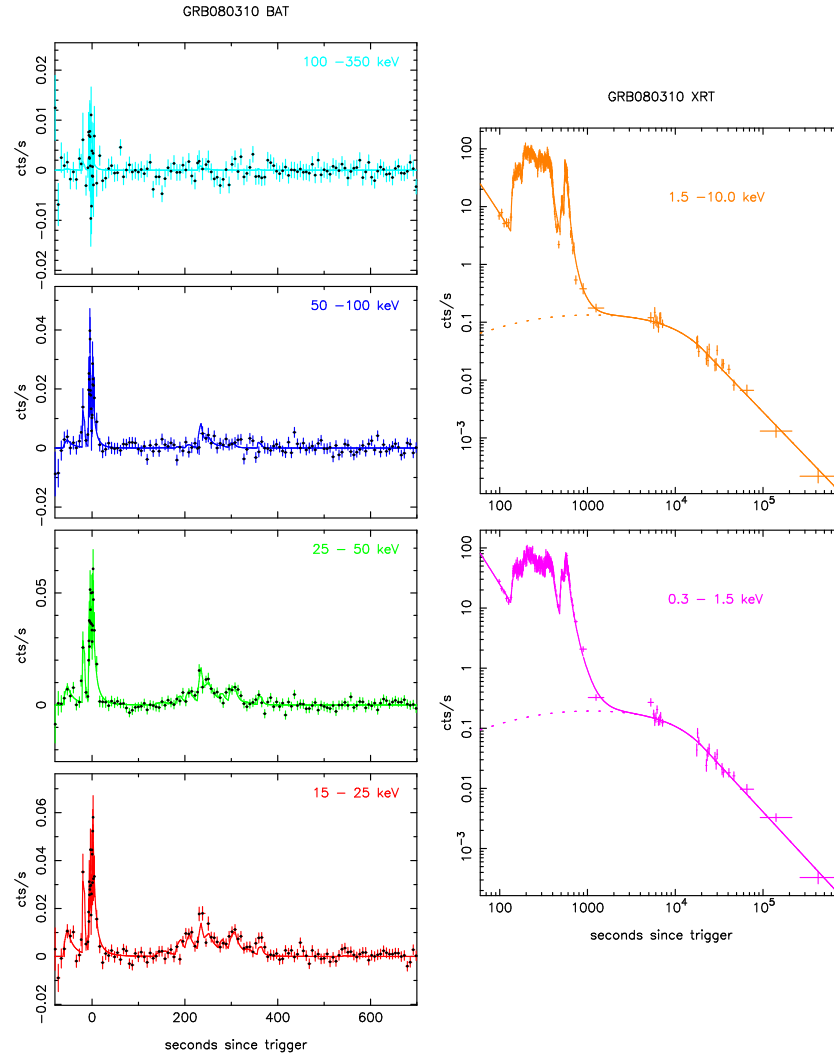


Figure 2.6: BAT and XRT data, showing the fitted Willingale et al. (2010) model. Left panels: BAT bands (Top to bottom: 100–350 keV, 50–100 keV, 25–50 keV & 15–25 keV). Right panels: XRT bands (Top: XRT hard-band, bottom: XRT soft-band). Pulse parameters have been fixed, whilst the afterglow parameters have been fitted. Solid lines show the total fit (pulses and afterglow), whilst dashed lines show only the afterglow component to the fit.

added. This was fitted by allowing the routine to find the optimum values for the characteristic times and normalising flux shown in Equation 2.1.

The simultaneous BAT and XRT fit is plotted in Figure 2.6 and shows several important characteristics of both the burst and the model. First, there is a lot of structure evident in the light curves, particularly during the first 1,000 seconds of the XRT light curves. This is described by the pulses that have been included, before the smooth decay observed is accounted for by the afterglow model.

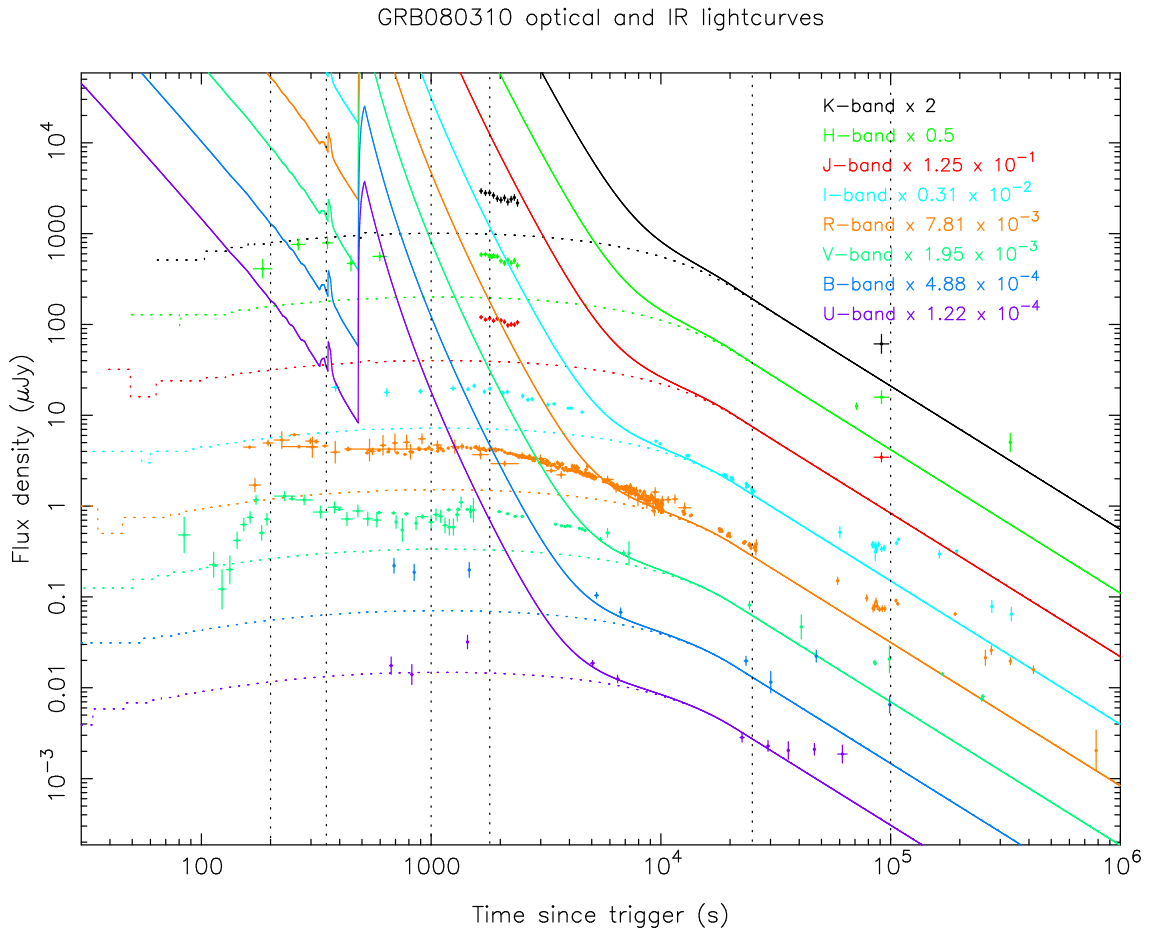


Figure 2.7: Optical and IR light curves obtained by extending the high-energy fit to the prompt pulses and afterglow component. The spectral shape of the pulses is assumed to be a Band function extrapolated back to the optical and IR data (K , H , J , I , R , V , B and U bands). The vertical dashed lines denote times of interest later discussed, at which the SED is considered in more detail. The coloured dashed lines show the afterglow component to the extrapolation for each band.

2.4 Extrapolating to the optical and NIR

Previously, no optical or IR data have been included when modelling the light curve and a fit to only the *Swift* BAT and XRT data has been produced (Figure 2.6). However, given the rapid response of optical and IR instruments to the trigger for GRB 080310 it is possible to extend the model to include these new sources of data.

The simplest approach to fitting the optical and IR light curves for GRB 080310 was to use the fitting routine from Willingale et al. (2010) and extrapolate the Band functions for both the pulses and also the afterglow to these lower energies. In this initial attempt all of the parameters previously discussed were held at the values obtained for the high-energy fit, to see what modifications might be necessary to both components.

Whilst this method provides an acceptable fit to the XRT and BAT bands, the original pulse model vastly over-predicts the optical and IR fluxes from the pulses (Figure 2.7), which implies there must be a break in the pulse spectra between the X-ray and the optical and IR energies. Such a break is expected in a synchrotron spectrum, but can also be seen in thermal spectra as the Rayleigh–Jeans tail. Additionally, the afterglow prediction from the BAT and XRT fit is not consistent with the optical data at late times where the prompt component to the light curve is negligible. Figure 2.7 also shows that the temporal decay index of the power-law phase of the afterglow gives rise to a decay which is more rapid than the optical data suggest.

An alternative method of reducing optical flux is to invoke dust absorption; however, as reported in Perley et al. (2008), extinction due to dust is low at $A_V = 0.10 \pm 0.05$ at an average time of $T_0 (+1750)$ seconds for GRB 080310. As not only the late-time emission seems unaffected by such absorption, but also by 2,000 seconds after trigger, a low energy spectral break was favoured in modelling the optical emission in preference to dust absorption. The following sections of this Chapter detail the implementation of such alterations to the Willingale et al. (2010) model.

2.5 Modifications to the model

2.5.1 An additional spectral break

To reduce the flux from each pulse in the optical and IR light curves of GRB 080310 an additional break to the spectrum for each prompt pulse was introduced. An example of such a spectrum is shown in Figure 2.8, where the regular Band function has a low-energy break below E_{pk} . To fully describe this break, three parameters are needed: a value of the break energy (E_a), the spectral index of the power-law slope in the low energy regime (p_a) and a temporal index which describes how the break energy evolves in time (d_a). The value of E_a is defined at T_{pk} , when the emission from the pulse is at a maximum. The entire pulse spectrum already evolves in time, according to the index d as shown in Equation 1.16, and so the expectation was that the time evolution of E_a would be related. Previously a value of $d = -1$ was used, which when integrating the equal arrival time surface means a pure Band

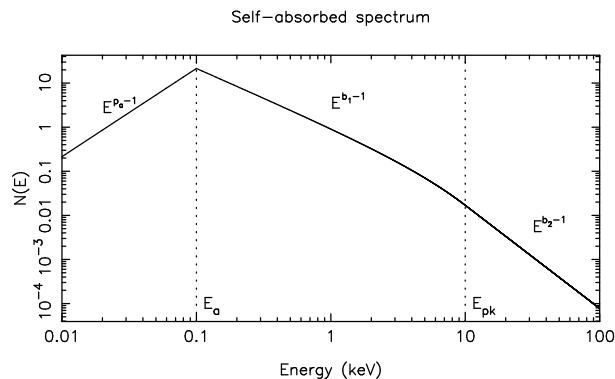


Figure 2.8: Example modified pulse spectrum including additional spectral break.

function can be recovered in the source frame given a Band function in the observed frame. Other values of d prevent assumptions to be made concerning the source spectrum. The index d_a was allowed to be fitted independently, to test whether the evolution of the break was the same as the rest of the spectrum. Again, note that only $d_a = -1$ is fully consistent with the original Genet & Granot (2009) pulse model. The functional form of the new spectral model for each pulse is shown as follows:

$$N(E) = \begin{cases} AE^{p_a-1} \exp\left(\frac{-E_a}{E_c}\right) E_a^{-\alpha}, & E \leq E_a, \\ AE^{b_1-1} \exp\left(\frac{-E}{E_c}\right), & E_a < E \leq E_{pk}, \\ AE^{b_2-1} \exp(\alpha - \beta) E_{pk}^{-(\alpha-\beta)}, & E > E_{pk}. \end{cases} \quad (2.2)$$

The model spectrum for photon emission assumes several things. First, there is a single underlying population of relativistic electrons, whose energies can be described by a broken power law such as that described in Shen & Zhang (2009). Such a spectrum of electron energies leads to a similar photon spectrum: a singly broken power-law, which corresponds to the observed Band function. However, it would be unphysical for this spectral shape to extend indefinitely to low energies, particularly as the electron energy spectrum has an associated minimum energy E_m . This minimum electron energy has a related emission energy at a frequency ν_m . With no self-absorption, the spectral index to the emission spectrum changes to $\frac{1}{3}$ at photon frequencies below ν_m , but if self-absorption is present then at low energies a steeper spectral index of 2 would be expected if the absorption frequency is less than ν_m or alternatively a spectral index of $\frac{5}{2}$ in the case of $\nu_m < \nu_a$. In the former case, if there is an

intervening spectral range between ν_a and ν_m , a spectral index of $\frac{1}{3}$ is expected between these two frequencies.

To keep the model simple, due to the limited nature of the spectral information available, only a single additional break was included in the spectrum. By allowing the resultant spectral index to be constrained by the observations, rather than assuming a value, a better understanding of the physics required to explain the spectra of prompt GRB pulses may be gained.

2.5.2 The afterglow

As seen in Figure 2.7, prompt pulses without a low-energy break significantly over-predict the observed flux in the optical and IR light curves prior to 10,000 seconds. By introducing a low-energy break to the pulse spectra, it was thought that prompt contribution could be completely removed from the total emission, and the entire light curve could be modelled with afterglow emission. One reason for considering this is the smooth nature of the optical light curves. Whilst there is some variation during the plateau seen between 200 and 3,000 seconds, this is at a low level and happens smoothly over a large period of time. If the prompt pulses observed at higher energies were also the dominant source of emission at these energies, then similar structure might be expected in the optical and IR light curves to that shown in Figure 2.6.

The first issue to address with the afterglow fit was to account for the small difference in temporal decay index (α_a) between the higher and lower energy bands. To do so, an additional parameter was included that described the difference in this index and allowed to be fitted. By including this, the slightly shallower decay of the power-law phase in the optical and IR channels could be accounted for. The change in α_a required was found to be small, at a value of approximately 0.2, but the associated errors in each instance showed it to be inconsistent with zero. This may be explained physically by a slight curvature in the spectrum of the afterglow between the optical and X-ray bands. This, however, is not a large enough difference to suggest a spectral break, such as the one introduced to the prompt pulses. The GRB afterglow flux is also thought to be synchrotron emission. However, at these late times the radiation is usually assumed to come from an optically thin plasma, and so a self-absorption break would

be expected at energies lower than the optical bands observed for GRB 080310. Contamination in the optical and IR wavebands was also ruled out as being the source of this difference as any emission from the host should be constant with time. This would add a constant offset to the data, and should the afterglow emission reach a comparable order of magnitude, a plateau at the end of the optical decay would be expected. This plateau is not observed, and the difference between the low- and high-energy temporal decay indices of the afterglow is also determined by data prior to when the host would be seen to make a significant impact on the optical and IR light curves.

After excluding the prompt components capable of rising quickly, the manner in which the afterglow rises also had to be modified, to account for the rapid increase in flux seen in the V band data at approximately 100 seconds in Figure 2.4. To do this a third part to the functional form that is shown Equation 2.1 was introduced. This extra regime is shown in the top line of Equation 2.3 and describes a power-law rise in flux, with an index of 2. The afterglow was also permitted to be launched independent of the trigger time of the GRB, by introducing a launch time (T_l), which offsets the afterglow in time to better fit the timing of the rise observed in the V -band. These modifications are shown in Equation 2.3 and are used for the afterglow-dominated modelling only. In the case of the prompt-dominated fit, the afterglow model of Willingale et al. (2007) is used once more, as explained in a later section of this Chapter.

$$f_a(t) = \begin{cases} F_a \exp\left(\alpha_a - \frac{(T_r - T_l)\alpha_a}{T_a - T_l}\right) \left(\frac{t - T_l}{T_r - T_l}\right)^2, & t \leq T_r, \\ F_a \exp\left(\alpha_a - \frac{(t - T_l)\alpha_a}{T_a - T_l}\right), & T_r < t \leq T_a, \\ F_a \left(\frac{t - T_l}{T_a - T_l}\right)^{-\alpha_a}, & t > T_a. \end{cases} \quad (2.3)$$

2.6 Afterglow dominated fit

Given the smooth nature of the optical and IR light curves, the initial use of the low-energy spectral break in the prompt pulse spectrum was to remove the prompt component to the optical light curves entirely, and explain the early-time behaviour with only afterglow emission. To do this, the prompt pulses were initially switched off from the optical and NIR fit. With these removed, the afterglow parameters T_l , T_r , T_a , F_a , α_a and the change between optical and high

energy values of α_a were fitted. Having obtained values for these parameters using the fitting routine, the prompt pulses were reintroduced, allowing p_a to be fitted, to find the minimum global break in the pulse spectra required to remove the prompt optical and IR flux. Where the fit statistic tended to unphysical values of p_a the effects of forcing p_a to take a physically motivated value were checked.

2.6.1 Light curves

Figure 2.9 shows the light curves for the best fit found using the method described above, for which a reduced χ^2 value of 2.44 with 1,642 degrees of freedom was found. The late-time XRT afterglow is not as well fitted as in the original Willingale et al. (2010) method (Figure 2.6), where only the high-energy bands were included. This is particularly the case for the last data points, and those at the transition between the prompt and the afterglow phase in the X-ray bands. This is caused by the greater number of optical points being the largest constraint on the afterglow parameters, particularly the characteristic times, T_a and T_r . Because these times have changed from the original fit, the temporal decay index in the power-law phase has reduced from $1.58_{-0.03}^{+0.04}$ to $1.30_{-0.01}^{+0.01}$. The afterglow parameters all have a reduced error in this newer fit as the optical and IR data points allow for more accurate fitting with a greater quantity of data. The characteristic times also have improved accuracy, with $T_r = 223_{-20}^{+16}$ seconds, $T_a = 6,368_{-50}^{+495}$ seconds and $T_l = 120_{-11}^{+9}$ seconds. The errors quoted in this instance were obtained when floating all of the parameters mentioned simultaneously.

Once the afterglow parameters were in place, the final bulk value of p_a was found to be 5.6, with a 1σ lower limit of 5.5 and an unconstrained upper limit. The lower limit is surprisingly tight, and likely due to the fitting routine trying to remove contributions from the brightest pulses, which therefore affects the value assigned to the weaker pulses as well. The value of 5.6 is very significantly steeper than that expected at either 2 or $\frac{5}{2}$. The suggested lower limit from the χ^2 distribution is tightly constraining, and likely due to the fitting routine trying to remove contributions from the brightest early pulses, which therefore affects the value assigned to the weaker pulses as well. The lack of an upper limit suggests that the fitting routine is attempting to remove the prompt component entirely from the optical emission, as

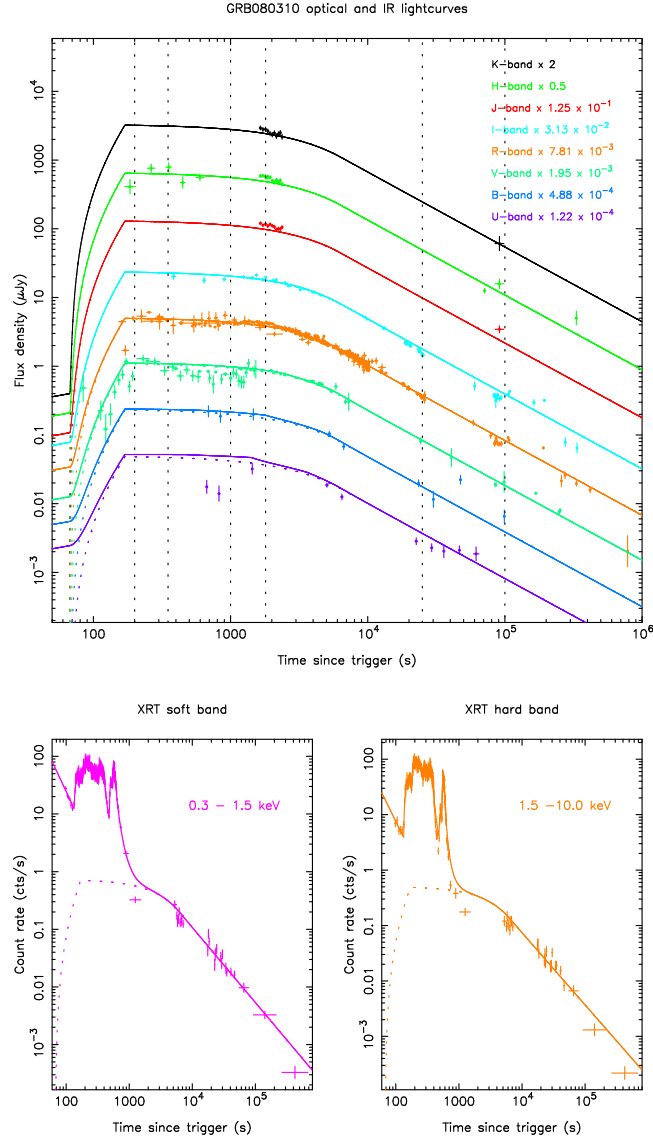


Figure 2.9: Simultaneous fit to optical, IR and XRT data, in which the early-time optical and IR are fitted by the afterglow emission. Top panel: Optical and IR bands fitted with low-energy break (K , H , J , I , R , V , B and U bands). Bottom-left: XRT soft-band fit. Bottom-right: XRT hard-band fit. The afterglow parameters are fitted, as are values for d_a , whilst $E_a = 0.3$ keV and p_a has been set to $\frac{5}{2}$. The coloured dashed lines show the afterglow component in each band. The reduced χ^2 for this fit is 2.44 with 1,642 degrees of freedom.

driven by the morphology of the light curve particularly the dense sample of KAIT data points. The shape of the curve obtained for the fit statistic when only varying p_a as the distribution is remarkably flat for a broad range of values. Looking at the fit statistic by eye, it would appear that the expected values from synchrotron or thermal spectra are not entirely ruled out, but lie within the lower limits of where the fit is a faithful representation of the data. To test this, p_a was forced to a value of $\frac{5}{2}$ for all the prompt pulses, and it was noticed that the value for the χ^2 statistic increased by a nearly negligible amount (approximately 1×10^{-3} , for 1,642 degrees of freedom). By using $p_a = \frac{5}{2}$ self-absorption becomes a viable explanation for the physical mechanism causing the observed level of optical and NIR flux. It is therefore this value that was adopted for p_a for the prompt pulses when trying to suppress them at early times in the lower energy regimes.

The broad-scale morphology of the optical and NIR light curves is described by the fast rising afterglow, with the rise observed in the V band being fitted and the level of flux of the plateau seen between 100 and 1,000 seconds being consistently modelled in five of the six bands in which it can be seen. The exception to this is that the U band model light curve morphology seems to over-predict the emission actually observed in the first 1,000 seconds, which may be a result of the correction required to removed the effects of absorption from the Lyman forest as described in the section detailing the UVOT observations. The I , R and V band data during this plateau phase do appear to have a slight dip in flux, which is not picked up by the afterglow fit. Additionally, the first V band points indicate a decline in flux prior to the launching of the afterglow. To fit this, one of the early-time pulses would have to be switched on at low energies, implying that at the earliest times the prompt component is still important in the optical and IR regimes.

The V band data between 100 and 1,000 seconds are from three sources, VLT V band, UVOT v band and the UVOT *white* filter, which is normalised to the v band. This normalisation is performed at a time when there is near simultaneous UVOT v band and *white* filter coverage. The *white* data are then adjusted at this time, to make the observed flux the same as that in the v band. The same correction factor is then applied to all the *white* filter points, which relies on an intrinsic assumption that the spectrum is not varying between the v band

and *white* filter for all observations. If the total GRB low-energy emission is primarily from the afterglow, this assumption is accurate, as the spectral break in the Band function will not migrate to the optical part of the spectrum. It was noted, upon inspection of the data, that the UVOT points between 300 and 2,000 seconds appear to not be entirely consistent with the near simultaneous VLT data. The VLT flux values have much lower associated error, which led to the reprocessing of the UVOT data, to verify the values. Doing this the same UVOT fluxes were obtained. To account for the discrepancy, a systematic error was introduced to the UVOT points at the level of 10% of the measured flux for each data point. Analysis of only the VLT data still shows the deficit of flux, which is discussed throughout this Chapter, at a level that is significant given the small errors associated with the data. As this feature is significant in instruments other than UVOT, it was believed that the discrepancy from the UVOT instrument does not impinge on the main conclusions of this work.

The temporal index d_a governing the time evolution of E_a is tightly constrained in this model, to a value of $d_a = -1.01^{+0.05}_{-0.03}$. Not only does this match the temporal evolution of the characteristic energy E_c in Genet & Granot (2009), but the 1σ errors quoted are restricting. Having analysed the one dimensional χ^2 surface, it is clear that a more rapid evolution of the temporal index allows the prompt pulses to peak at earlier times, when the normalising flux at the peak of each pulse is still significant, causing an over-prediction of early-time flux. At lower values the χ^2 distribution is fairly flat, as the prompt flux normalisation is so low that it cannot be seen to contribute to the total light curve.

Spectral Energy Distributions

Another way of comparing the model to the observed data is to consider the SED at fiducial times. The times selected are indicated in Figures 2.7, 2.9 and 2.11 as dashed vertical lines. These correspond to times of 350 seconds (where there are early-time optical data and activity in both the X-ray and γ -ray bands), 1,800 seconds (a time where the high-energy-only model shown in Figure 2.7 suggests that the afterglow is becoming significant), 2.5×10^4 and 1×10^5 seconds (both of which are later times that should be dominated by the afterglow). Figure 2.10 shows the model SED at these times and also those at both 200 and 1,000 seconds. The times

shown were chosen to both allow for comparison with the maximum number of bands (both optical and X-ray) at each time and to show times where the SED can discriminate between prompt and afterglow emission at optical and IR energies. The SEDs shown in Figure 2.10 are those for the fit where the afterglow dominates the entire low-energy emission. In each case, error bars are plotted, but in some panels are too small to be seen.

Figure 2.10 shows that by combining the prompt pulses and the afterglow component the model SEDs have complicated structure at high energies. The first panel shows the SED at 200 seconds, a time by which the first six pulses have peaked. As an example of time evolution, the spectral contribution from pulse 4 is shown with the dashed line in this and subsequent panels. The temporal evolution of pulses 4, 12 and 15 can be traced through all six panels. At 200 seconds pulse 4 is one of the three pulses causing deviation from the afterglow Band function (the others being pulses 1 and 6). Following it through all six panels of Figure 2.10 shows the general evolution of all the pulses. The peak flux reduces with time, and the energy at which this peak is seen becomes lower with increasing time also. By the late panels, the component of pulse 4 can still be seen on the axes; however, being several orders of magnitude fainter than the afterglow Band function, it does not produce an observable feature in the total SED. Because the spectral index for all the pulses is at a value of $p_a = 2.5$, before the peaks migrate to the optical regime, their contribution to the total flux at these energies is negligible. Once the peak has had time to evolve to such energies, the normalising flux has been diminished, so the pulse contributions remain negligible.

Figure 2.10 also shows that the dominant pulses in the SED of GRB 080310 do not have to be those most recently launched. Pulse 12 is emitted after pulse 4, as shown in the first two panels of the figure. Despite this, pulse 12 has disappeared entirely by 2.5×10^4 seconds, whilst the earlier pulse can still be seen on the axes, even though the modelled emission is at a level significantly below the total SED. The bottom two panels show late times in the light curve, where only the afterglow contributes flux to the total SED. Looking only at the afterglow in all six panels, it can be seen that it varies very little at early times. This is due to the combination of a quick rise time after an early launch with a late transition time between the exponential and power-law decay phase for the afterglow component. This implies that

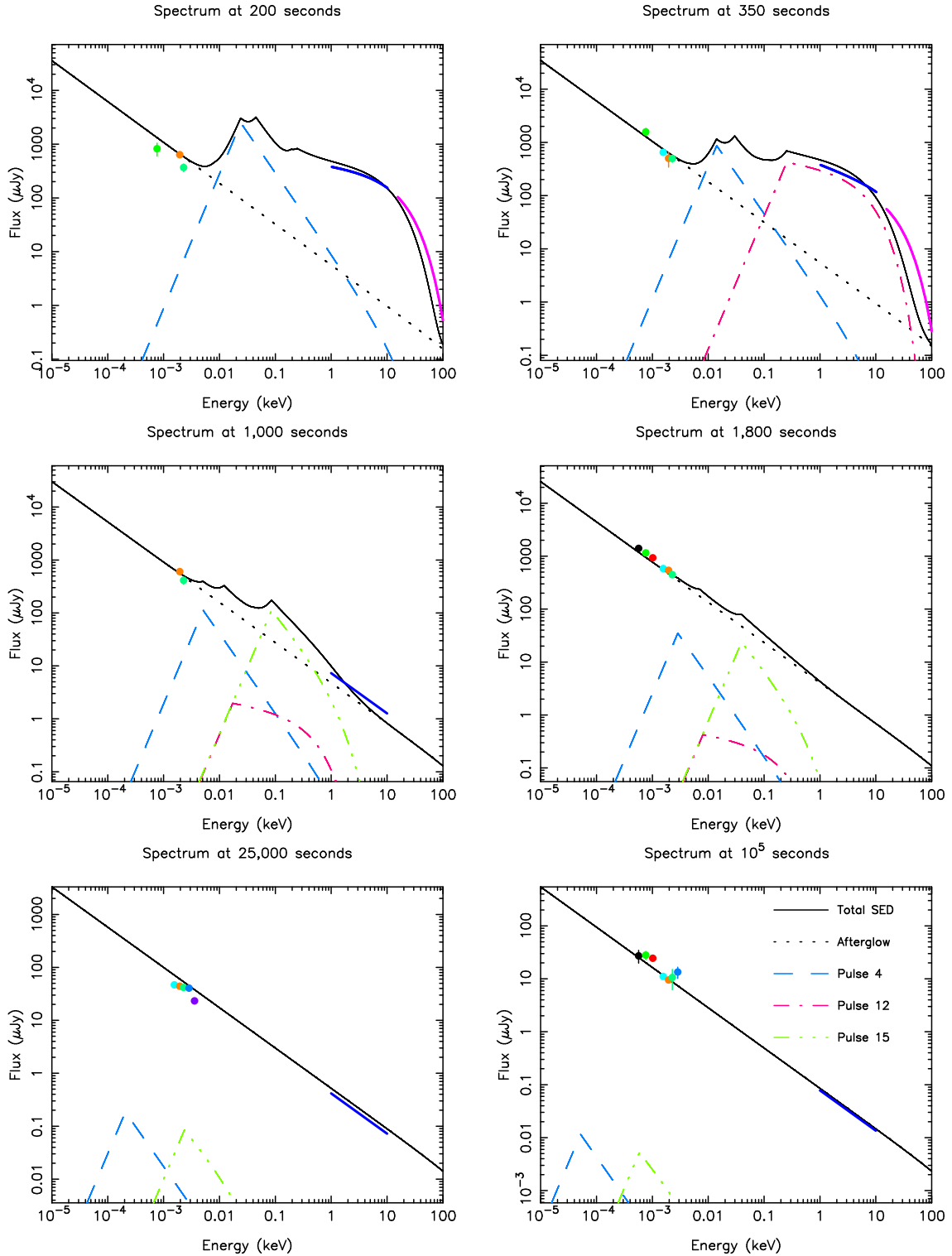


Figure 2.10: SEDs for fiducial times in the light curve of GRB 080310 using the afterglow model to fit the early-time, low-energy emission. Prompt pulses are included with a bulk value of $p_a = 2.5$. The solid line is the total SED and the dotted line is the contribution from the afterglow component. Pulses 4, 12 and 15 are also shown by the dashed and dotted lines as outlined in the key shown in the bottom-right panel. These are included as examples to show the evolution of some of the longer lasting pulses in the fit. The colours of the data points follow the same scheme as that used in the light curves, with the BAT and XRT data being represented by lines which extend along their entire coverage.

there is a period where the afterglow effectively plateaus for a few thousand seconds. This behaviour can be identified in the light curves shown in Figure 2.9.

The SEDs in Figure 2.10 suggest that the optical emission is fitted by the extrapolation of the afterglow Band function, particularly at late times. The second panel is perhaps the most puzzling as the optical and near infrared data are aligned approximately with the afterglow SED, however there is a clear dip in the light curves, which suggests that a component which simply rises then falls smoothly cannot explain the morphology that is seen. No attempt has been made to fit a low–energy break to the afterglow Band function, as discussed previously, because such a break is expected at energies well below the H band, due to the optically thin nature of the circumburst medium. Additionally, the correct level of flux has been reproduced without the introduction of a further spectral break.

2.7 Early–time prompt dominated fit

By fitting the optical and IR emission with only a significant afterglow component, there were discrepancies between the model and the data. Namely the potential decay before the sharp rise observed in the V band and the deficit in flux observed in the I , V and R bands between 300 and 2,000 seconds. Alongside this, the U band data are over predicted, which is possibly due to the absorption correction from the Lyman forest as previously discussed, or alternatively could be better described with an alternative model. In an attempt to explain these features, a model was considered where these early–times were dominated by the prompt emission in the optical and NIR regimes.

2.7.1 Light curves

First only the prompt pulses were considered, by turning off the afterglow component and fitting only prior to 2,000 seconds. Once the early–time emission was fitted, the afterglow was then included to account for the late–time emission. The potential for degeneracy between p_a and E_a was considered, as the energy difference between the X–ray data and the optical and IR bands is over two orders of magnitude, while the U and K bands are only separated by

less than a single order of magnitude. Data were not taken simultaneously in these two bands which are the most spectrally separated. It is therefore difficult to determine both E_a and p_a independently. For this reason the break energy was set to a value of 0.3 keV (at T_{pk}) which is the soft end of the XRT spectral range. This implies that the fit to the high-energy regime remains unaltered, whilst giving the maximum energy range in the SED between E_a and the optical and IR bands. Therefore the value for p_a obtained is a lower limit, as moving E_a to lower values would steepen the power-law index in the low-energy part of the spectrum.

Initial attempts to model the low-energy flux with prompt pulses held the parameters p_a , d_a and E_a to the same value for all pulses. This led to a bulk value of $p_a = 0.65^{+0.02}_{-0.02}$, which is significantly different to the spectral index of the Band function below E_{pk} , but not consistent with the expected values of p_a if self-absorption was having an effect on the emission that is observed. The 1σ limits on this value do not include $\frac{1}{3}$, which is what would be expected if there is an absence of self-absorption, and the optical and IR bands are below the emission frequency of electrons with the minimum energy in the electron population. The reduced χ^2 value is 3.61 in this instance, with 1,642 degrees of freedom. There were still some issues with this fit, such as it not describing the slight decay followed by a sharp rise in flux seen in the V band. So all pulses were allowed to have independent values of p_a , to see if this could account for the features seen in the data. The method adopted to do this remained the same as that for the bulk value of p_a , and the light curves obtained are shown in Figure 2.11.

Given the choice of two afterglow models, the original functional form of Willingale et al. (2007) and the modified version shown in Equation 2.3, it was found that in this instance the better fit was obtained with the former, as the smoother peak to the afterglow component allowed for closer fit to some of the J , H and K band data at this time. This also removed a free parameter from the fitting routine. The difference between optical and high-energy α_a was retained to describe the late-time decay. With these modifications, the early-time prompt-dominated model had a reduced χ^2 of 2.43 for 1,642 degrees of freedom. This is significantly better than the prompt model with a bulk value of p_a for all pulses, with a change in total χ^2 of over 1,850.

There are little data to constrain p_a for the first four pulses, which are predominantly

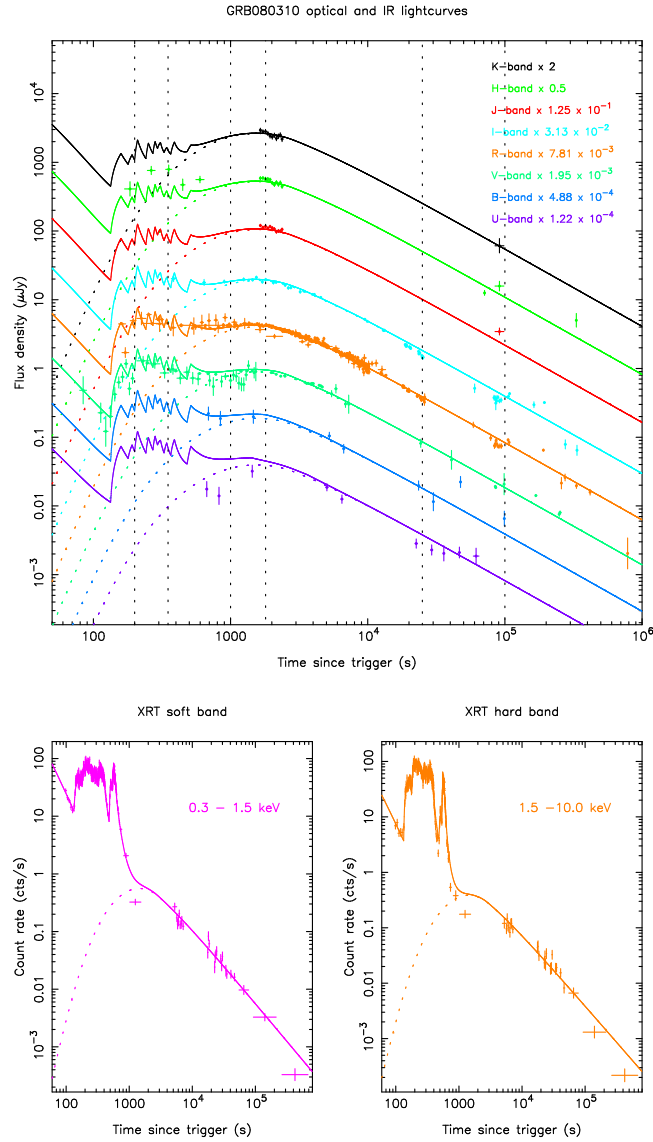


Figure 2.11: Simultaneous fit to optical, IR and XRT data, in which the early time optical and IR are fitted by the prompt emission. Top panel: Optical and IR bands fitted with low-energy break (K , H , J , I , R , V , B and U bands). Bottom-left: XRT soft-band fit. Bottom-right: XRT hard-band fit. $E_a = 0.3$ keV, p_a and d_a are allowed to float (producing a value of $d_a = -1.01$) and the afterglow parameters (T_r , T_a , α_a and F_a) are also fitted. The reduced χ^2 for this fit is 2.43 with 1,642 degrees of freedom.

observed with BAT, and so these values have large associated uncertainties. Despite this, it was clear that a large value of p_a was required for pulses 1, 2 and 4, to allow for the decay and subsequent rise seen in the V band data. The best fit to the initial decay was found by modelling it with pulse 2 and suppressing pulses 1 and 3 so that they did not contribute to the optical and IR emission observed from the beginning of the optical coverage. When actually fitted, the values of p_a for pulses 1, 2 and 4 all were larger than $\frac{5}{2}$, and so in the same manner as all the prompt pulses in the afterglow-dominated model, these were set to $p_a = \frac{5}{2}$ as Figure 2.11 shows that the sharp rise is now well fitted by the rise of pulse 4 in a similar way to the simultaneous rise seen in the XRT data. The data obtained from KAIT have an earlier point at 57 seconds, which does not show this decay; it is difficult to fit this individual point, as whilst it is at an ideal time to investigate the prompt optical behaviour of the GRB, it is a 30 second observation, and so it is an average over a time during which large variations might be expected. This is why efforts have not tried to fully explain this point with this model and it has been removed from the fitting undertaken. Indeed, non-detections from both Super-LOTIS and Rapid Telescope for Optical Response (RAPTOR; Woźniak et al. 2008) at similar times to this KAIT data point offer further evidence towards the faintness of the emission in the optical regime at this time.

Analysis of the residuals for the optical, IR, XRT and BAT data show there are three clear contributions to the total χ^2 statistic. The first contribution to the fit statistic is from the XRT afterglow component of the model. This deviates from the observed data at two times. First, the transition from the rapid decay phase to the afterglow shows an over-prediction by the model, as do the data after 10^5 seconds. The latter of the two features could be explained by a late temporal break in the X-ray afterglow. Such a break should be achromatic, and therefore also observed in the late-time optical data. The final R band observation, at approximately nine days after the trigger, is fainter than the extrapolation from the final power-law decay in the afterglow-dominated model, which would support the possibility of a jet break. With the prompt-dominated optical and IR model, there is a suggestion of either a plateau or re-brightening at approximately one day after the trigger, followed by a steeper decay. In both models, the data are too sparse to justify the inclusion of further parameters in the late-time

modelling of the optical data.

The next significant contribution to the value of χ^2 comes from the early-time REM data points between 150 and 600 seconds in the H band. These are under-predicted by the model as shown in Figure 2.11. Due to the sparse nature of the NIR data at this time, the fit is driven by the more densely sampled V and R band data. This discrepancy is better highlighted in the SEDs shown in Figure 2.12.

The other notable source of contribution to the fit statistic is the KAIT data. The data were initially reported in unfiltered magnitudes, with values ranging between 17th and 20th magnitude, and errors typically less than a tenth of a magnitude. With such small errors for over 200 data points the contribution to the total validity of the fit from the intrinsic scatter of the data set is significant, despite the fact that the data and model can be seen to agree by eye.

2.7.2 Spectral energy distributions

As can be seen in the SEDs shown in Fig. 2.12, by introducing the prompt component to the spectrum of GRB 080310, each SED has structure beyond the simple Band function of the afterglow at earlier times in the low-energy bands. For the prompt-dominated model of the early-time low-energy emission, the spectral indices typically lie in the range $-0.65 < p_a < 1$. This does not include the earliest pulses, which have a necessarily steep spectral index to prevent their emission dominating (and poorly fitting) the optical and IR light curves. These have been fixed to a value of $p_a = \frac{5}{2}$, as well as pulses 8 and 16, which also require steep indices.

Unlike in the afterglow-dominated model, the SED at 350 seconds shows the optical and IR (particularly the H band) model to disagree with the data; this is the most valuable of the SEDs in Figure 2.12, as it is one of the only two prior to the afterglow making the dominant contribution to the total low-energy emission, and of these two has the best low-energy coverage. The R , I and V band data at this time are at approximately the correct level of flux for each band, although the I band and R band deviate from the expected shape of the SED. However, the H band data (which offer the largest range of spectral information when considered with the other three bands) are notably under-predicted, as corroborated by the light curves in

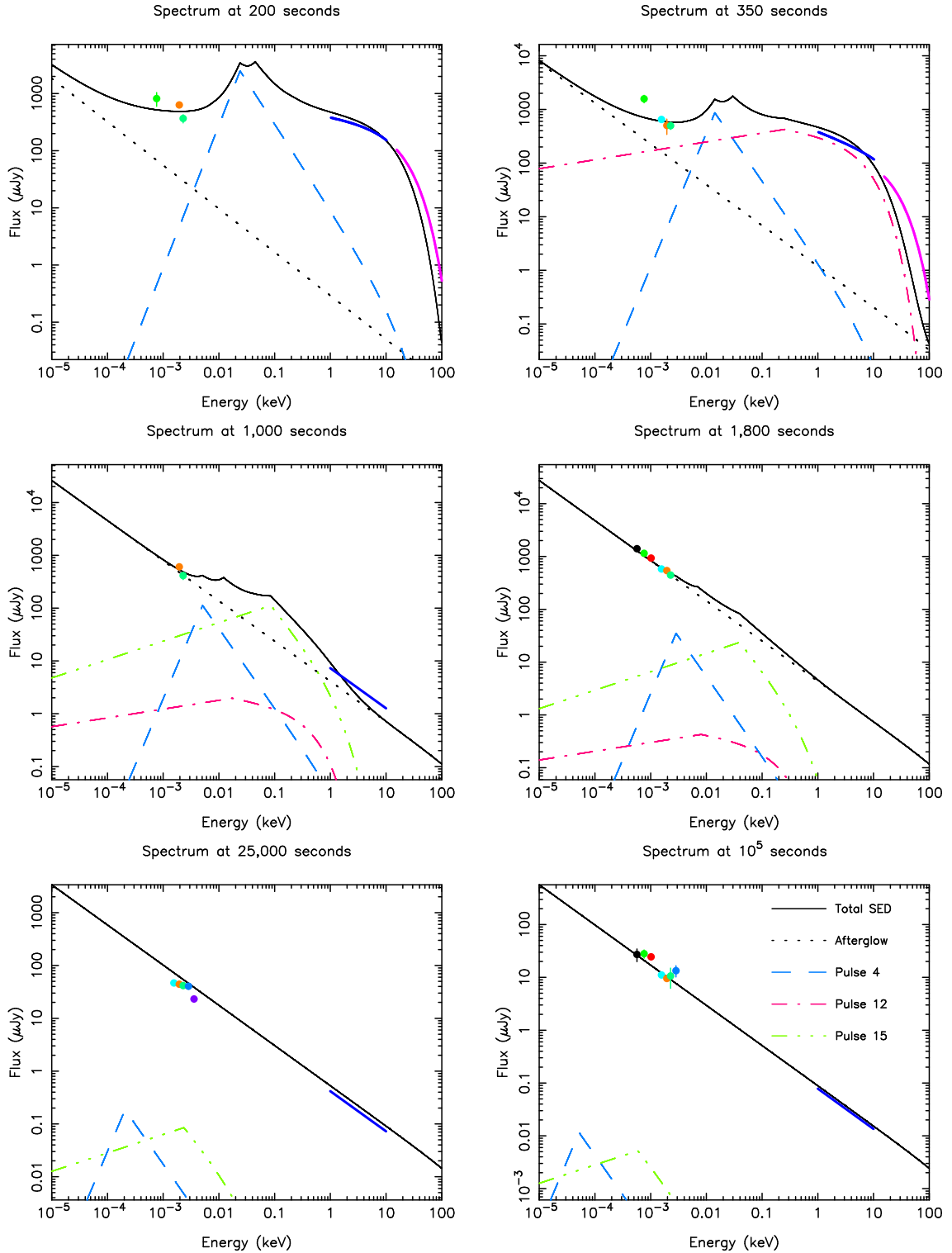


Figure 2.12: SEDs for fiducial times in the light curve of GRB 080310 using the prompt-dominated early-time model. The solid line is the total SED and the dotted line is the contribution from the afterglow component. Pulses 4, 12 and 15 are also shown by the dashed and dotted lines as outlined in the key shown in the bottom-right panel. These are included as examples to show the evolution of some of the longer lasting pulses in the fit. The colours of the data points follow the same scheme as that used in the light curves, with the BAT and XRT data being represented by lines which extend along their entire coverage.

Figure 2.11. When inspected by eye, the four bands at this time could be thought to lie on a single power-law with a spectral index similar to that of the afterglow. This would lend more credence to the afterglow-dominated early-time optical and NIR model.

The subsequent SEDs are all dominated by the Band function of the afterglow at optical and IR energies, and, despite the use of the original Willingale et al. (2007) afterglow model and changes in T_a , F_a , and T_r , the late-time fit is similar to that obtained for the afterglow-dominated fit. The optical and NIR data points are all over-predicted at 2.5×10^5 seconds, which something that can be seen by looking at the light curves, particularly in the case of the UVOT u band data. The u band data set displays some unusual characteristics, being significantly fainter than expected prior to 1,000 seconds and then appearing to plateau between 2×10^4 and 1×10^5 seconds. The removal of this data set from the analysis was considered, but as the values of parameters obtained for the best fit seem largely insensitive to the u band data they were retained. This is a result of the relatively sparse coverage in the u band, principally in comparison to that of the R band, meaning the weighting of the u band data in determining the fit statistic is small.

2.8 Discussion

For direct comparison between the two models discussed in the previous section, their parameters have been included in Table 2.2. Given the degeneracy between E_a and p_a it is not possible to simultaneously fit exact values to both without a more extensive low-energy coverage over a larger range of wavelengths. Because of this, E_a was fixed at 0.3 keV, in an attempt to find a value of p_a .

There is no clear difference in the fit statistic for either of the models presented in this work. The difference in total χ^2 is less than 30 over such a large range of degrees of freedom. Whilst numerically, this difference is in favour of the prompt-dominated early-time optical and NIR model, it was felt that the magnitude of the difference is not enough to warrant favouring one model above the other.

For the afterglow-dominated early-time model the fitted bulk low-energy spectral index

Table 2.2: Pulse p_a values and afterglow parameters for both the prompt- and afterglow-dominated early-time optical emission models. Note that the value for T_l in the prompt-dominated model is untabulated, as the Willingale et al. (2007) model was used for the afterglow in this instance. All instances where $p_a = \frac{5}{2}$ have the values fixed rather than fitted, and so no uncertainties were calculated for them.

Parameter	Parameter description	Afterglow dominated	Prompt dominated
p_a (pulse 1)	X-ray to optical spectral index	2.5	2.5
p_a (pulse 2)	X-ray to optical spectral index	2.5	2.5
p_a (pulse 3)	X-ray to optical spectral index	2.5	$-0.65^{+0.59}_{-0.59}$
p_a (pulse 4)	X-ray to optical spectral index	2.5	2.5
p_a (pulse 5)	X-ray to optical spectral index	2.5	$0.03^{+0.04}_{-0.07}$
p_a (pulse 6)	X-ray to optical spectral index	2.5	$0.11^{+0.46}_{-0.17}$
p_a (pulse 7)	X-ray to optical spectral index	2.5	$-0.11^{+0.43}_{-0.25}$
p_a (pulse 8)	X-ray to optical spectral index	2.5	2.5
p_a (pulse 9)	X-ray to optical spectral index	2.5	$-0.06^{+0.09}_{-0.01}$
p_a (pulse 10)	X-ray to optical spectral index	2.5	$-0.01^{+0.26}_{-0.26}$
p_a (pulse 11)	X-ray to optical spectral index	2.5	$-0.11^{+1.00}_{-0.30}$
p_a (pulse 12)	X-ray to optical spectral index	2.5	$0.17^{+0.19}_{-0.11}$
p_a (pulse 13)	X-ray to optical spectral index	2.5	$1.0^{+0.22}_{-0.22}$
p_a (pulse 14)	X-ray to optical spectral index	2.5	$0.04^{+0.11}_{-0.08}$
p_a (pulse 15)	X-ray to optical spectral index	2.5	$0.35^{+0.08}_{-0.09}$
p_a (pulse 16)	X-ray to optical spectral index	2.5	2.5
T_l (seconds)	Afterglow launch time	120^{+9}_{-11}	-
T_r (seconds)	Afterglow rise time	223^{+16}_{-20}	1000^{+435}_{-131}
T_a (seconds)	End time of afterglow plateau phase	6368^{+501}_{-495}	2937^{+1056}_{-1346}
α_a	Afterglow temporal decay index	$1.30^{+0.01}_{-0.01}$	$1.31^{+0.01}_{-0.01}$
$\Delta\alpha_a$	$\Delta\alpha_a$ between optical and X-ray decays	$0.21^{+0.03}_{-0.04}$	$0.18^{+0.1}_{-0.03}$
F_a ($\gamma\cdot\text{cm}^{-2}\cdot\text{s}^{-1}$)	Integrated Flux at T_a	$2.34^{+0.08}_{-0.08} \times 10^{-2}$	$2.77^{+0.23}_{-0.16} \times 10^{-2}$

for the prompt pulses is unphysically steep ($p_a = 5.6$). However, the change in fit statistic when forcing this value to one consistent with self-absorption was near negligible, which is why the less extreme value was therefore adopted. In contrast, most values of p_a are more reasonable ($-0.65 < p_a < 1$) when the early-time low-energy emission is dominated by the prompt pulses identified at higher energies. This is not, however, true for all the pulses. It was necessary to suppress pulses 1, 2, 4, 8 and 16 with positive, steep low-energy spectral indices so that the optical and IR emission was not over-predicted. To understand this behaviour the one dimensional χ^2 distribution for p_a of the earliest of these three pulses was examined. It was found that the distribution reduced asymptotically at higher values of p_a , meaning that there was no clear minimum. However, the actual reduction in the fit statistic achieved by reducing the low-energy spectral index rapidly dropped, so this decrease in χ^2 value quickly stopped making a significant difference to the quality of the total fit compared to other contributions to the χ^2 statistic. After establishing this, values of $p_a = \frac{5}{2}$ were again adopted in these instances, with a minimal increase of χ^2 being introduced as a result.

Given the variations in p_a for the prompt-dominated model, attempts were made to relate these values to other parameters of the pulses, such as pulse duration (T_{pk}) and the low energy photon index of the Band functions for each pulse (b_1). No correlations between p_a and the other pulse parameters were found.

In the afterglow-dominated fit, the prompt component is several orders of magnitude fainter than the observed emission. Additionally, with positive values of p_a , time is required for the peak of the pulse spectrum to migrate to the optical and IR bands, before which the spectrum is rising at these energies. The pulse emission is largest around E_a , the evolution of which is governed by the temporal index d_a , which has been shown to be negative. This means that the pulse energy decreases with increasing time. In addition to this, the normalisation of each pulse scales with t^{-1} , which means that when the peak of emission reaches the optical part of the spectrum the total flux is reduced. To illustrate the prompt component in this scenario, the afterglow component was subtracted from the afterglow-dominated model to produce Figure 2.13, which shows the H band prompt-only light curve that underlies the afterglow emission.

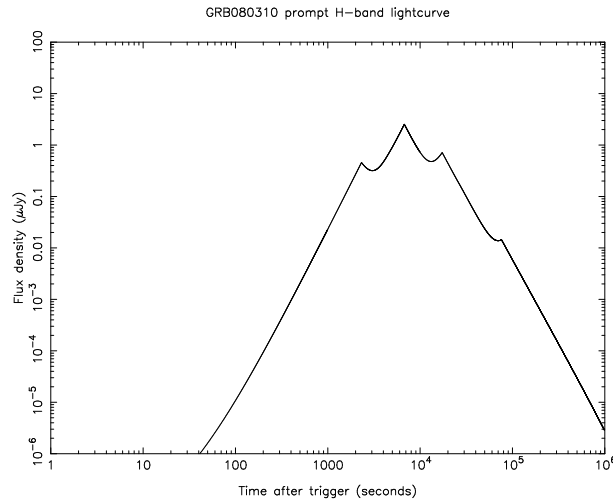


Figure 2.13: Modelled H band light curve showing the prompt component only for the afterglow-dominated fit to GRB 080310.

The afterglow-dominated, early-time optical model required three alterations to the afterglow component; a change of temporal power-law index between high and low energies, a power-law rise at early times and a variable launch time T_l . However, even with these modifications, there were several features of the data that were not entirely modelled in this scenario, including the apparent decay in the V band prior to the rapid rise and the slight deficit in flux between 300 and 2,000 seconds. The tendency towards unphysical values of p_a also suggested that fitting the early-time emission with a fast rising afterglow may not provide the best model of the observed flux. The SEDs of Figure 2.10 confirm that the afterglow-dominated fit provides a reasonable fit to the data and that at 350 seconds, which is a time where at high energies the prompt components are dominant, the afterglow Band function fits both the level and slope of the SED.

When fitting the early-time flux with the prompt pulse emission model a single value of p_a was first adopted which was held constant for all pulses. The low-energy spectral index obtained was $p_a = 0.65$; however most of the early-time emission was hidden by the tail of one of the earliest prompt pulses. Aside from a poor fit to the H band data, the fast rise seen in the V band was not well represented in this instance, so the pulses were allowed to have independent values of p_a . This produced a better fit to the data, significantly improving the χ^2 statistic. The fast rise in the V band and the small-scale variations in the light curves seem to be well represented by this model. There were, however, discrepancies with this alternative.

First, the H band data were under-predicted by the model, which can be seen in both the light curves and SEDs shown for this model. The SEDs also show that, at 350 seconds, the optical SED appears to be more accurately represented by a single power-law which agrees more with the nature of the afterglow. Three of the first four pulses (and also pulses 8 and 16) tend towards an unphysically steep spectral index when fitted. As with the afterglow-dominated model, constraining the values of p_a to $\frac{5}{2}$ in these instances does not significantly reduce the quality of the fit obtained.

The other values of p_a for the prompt-dominated fit could be consistent with the energy bands lying below the energy of emission from the least energetic electron in the relativistic population responsible for the observed photons. No relation was found between the low-energy spectral index for each pulse and any other pulse parameter, giving no insight into the cause of the variation of p_a . An interesting result is the marked difference between pulses 1, 2, 4, 8 and 16 when compared with all the other pulses. p_a for these early pulses indicates their emission is from an optically thick environment in the optical regime. Another implication is that these pulses must be launched from a different environment than the other 11 which have far shallower spectral indices at low energies.

One additional benefit to the prompt-dominated model was the ability to return to the simpler afterglow model of Willingale et al. (2007), as the rapid rise seen in the V band was attributed to the rise of pulse 4.

An alteration attempted with the prompt-dominated early-time model was to introduce an offset to the onset of the afterglow. It was hoped that by allowing the afterglow to rise earlier, the SED at 350 seconds could be reconciled with the model. This was found not to be possible, as this returned the model to something resembling the afterglow-dominated fit, and therefore it was not possible to model the small-scale variations and observed optical deficit in the plateau between 300 and 2,000 seconds.

Both of the alternative models presented in Figures 2.9 to 2.12 are poor at fitting the transition between the rapid decay phase and the afterglow plateau observed in the X-rays. Attempts were made to better model this by allowing the afterglow to rise at a later time than presented in either of the two fits highlighted in Table 2.2. By doing so, it was possible to improve the qual-

ity of the high energy afterglow fit, but to the detriment of that obtained for the optical data. With an afterglow that rises later but more quickly, the optical data between 3,000 seconds and 8,000 seconds are under-predicted by the model suggested. With a larger number of data points, and correspondingly better statistics, the optical points were those that were therefore favoured. The prompt-dominated, early-time optical and IR model described in Table 2.2 and illustrated in Figures 2.11 and 2.12 summarises this model. Unfortunately, the XRT coverage contains a gap during the afterglow plateau phase, and therefore the exact morphology of this component, which would help significantly constrain the rise of the afterglow, is unknown at these times.

An alternative suggestion, given the acceptable fit at approximately 2,000 seconds in all the available optical IR bands, to explain the factor of 2 or 3 difference between the X-ray data and model at this time would be to include a spectral break in the afterglow spectrum. Whilst this may improve the fit at these times, the later afterglow coverage between 10^4 and 10^5 seconds show both the higher and lower energy bands to be modelled at the correct level.

Additionally, a large contribution to the χ^2 distribution was from the optical and IR data, particularly the KAIT data set, with low magnitude errors. Whilst the observational errors in these data points may be as reported, each of the data sets had to be calibrated so they all were in standard bands. In doing so the systematic errors associated with these data points increased. This was considered, and a systematic error of 0.03^m was added to every optical or IR point. The quoted values for the fit statistics include this systematic source of error.

Knowing the characteristic times of the afterglow for each of the two models allows for the calculation of the initial bulk Lorentz factor in both an interstellar medium (ISM)-like or wind-dominated circumburst environment. To do so Equations 2.4 (Molinari et al., 2007) and 2.5 (Sari & Piran, 1999) were used:

$$\frac{\Gamma_{0,ISM}}{2} = \left(\frac{3E_{iso}(1+z)^3}{32\pi nm_p c^5 \eta t_{peak}^3} \right)^{\frac{1}{8}}, \quad (2.4)$$

$$\frac{\Gamma_{0,wind}}{2} = \left(\frac{E_{iso}(1+z)}{8\pi A m_p c^3 \eta t_{peak}} \right)^{\frac{1}{4}}. \quad (2.5)$$

Table 2.3: t_{peak} values and initial bulk Lorentz factors for both the prompt– and afterglow–dominated early–time optical emission models in both an ISM and wind–like environment.

Model	t_{peak} (s)	$\Gamma_{0,ISM}$	$\Gamma_{0,wind}$
Prompt	1497^{+845}_{-714}	$169.1^{+41.5}_{-21.0}$	$75.1^{+34.6}_{-11.1}$
Afterglow	1044^{+112}_{-122}	$193.6^{+43.3}_{-6.1}$	$82.2^{+36.6}_{-4.1}$

In the equations above E_{iso} is the isotropic equivalent energy of the GRB, η is the radiative efficiency of the fireball, z is the measured redshift, n is the number density of the circumburst medium and A is a normalisation for the density in the wind–like case (where $\rho \propto r^{-2}$). As with Molinari et al. (2007), it was assumed that $n = 1 \text{ cm}^{-3}$, $\eta = 0.2$ and $A = 3 \times 10^{35} \text{ cm}^{-1}$.

t_{peak} is the time at which the afterglow peaks and can be calculated using Equation 2.6, taken from Willingale et al. (2007):

$$t_{peak} = \left(\frac{T_r T_a}{\alpha_a} \right)^{\frac{1}{2}}. \quad (2.6)$$

The derived values of t_{peak} and the initial bulk Lorentz factors are shown in Table 2.3.

The calculated values show that an ISM–type circumburst medium leads to higher Lorentz factors, which is consistent with expectations, as an ISM–type environment would prove to be less dense than the remnants of the stellar wind associated with the death of a massive star. By definition the afterglow–dominated model peaks at an earlier time, which means that the initial bulk Lorentz factor is necessarily higher for this case, as demonstrated in Table 2.3. It is worth noting, however, that when considering the errors quoted, the prompt–dominated values cannot be said to be distinct from the corresponding values derived from the afterglow–dominated fit.

2.8.1 Physical implications of ν_a

Choosing $\nu_a = 0.3 \text{ keV}$ for the prompt pulses in the afterglow dominated fit was arbitrary. This can, however, be used to provide limits on physical parameters of the prompt emission. In the following section it is assumed that the pulses causing the emission are similar to those of other bursts in their microphysics, bulk Lorentz factors and locations from the centre of the explosion. By making such assumptions it is possible to calculate the magnetic field strength

of the emitting region and subsequently the number density of the electron population.

This work uses a simplified version of Equation 1.27, as it was possible to directly obtain the flux density at ν_a for each pulse, f_{ν_a} . The equivalent expression used is shown as Equation 2.7, which is rearranged so that it is possible to calculate the magnetic field strength of each pulse:

$$B = \frac{32\pi (1+z)^7 R^4 m_e^3 c \nu_a^5}{9 f_{\nu_a}^2 \Gamma^3 D_L^4 q_e}. \quad (2.7)$$

Several things are important to note about Equation 2.7. First is the strong dependence of B on key properties such as the radius from the explosion centre, R , the self-absorption frequency and the bulk Lorentz factor of the emitting material. For the Lorentz factor a value of $\Gamma = 200$ was adopted. Whilst this could be an underestimate, see for example Molinari et al. (2007), it is likely to only be so by a factor of two, leading to magnetic fields that are less than an order of magnitude lower.

More importantly, however, is the selection of R . As stated in Shen & Zhang (2009), $10^{13} < R < 10^{15}$ cm, which gives a range of two orders of magnitude. As $B \propto R^4$, the choice of R has a significant impact on the calculations. A value of $R = 10^{14}$ cm was adopted as this was in the middle of the expected range.

The flux density for each pulse was found at time T_{pk} , which is when ν_a is defined to be 0.3 keV. ν_a evolves with time, in both a wind-like and an ISM environment, meaning the values in Table 2.4 are representative of each pulse at T_{pk} .

By considering the magnetic energy density, it is also possible to find the number density of the electron distribution. In Equation 2.8, n_e is the number density of the electron distribution and ϵ_B is the fraction of the shock energy which is deposited into the magnetic field. Following the literature it was assumed that $\epsilon_B \sim 0.01$ (Sari et al., 1996).

$$B = (32\pi \epsilon_B n_e m_p)^{\frac{1}{2}} \Gamma c. \quad (2.8)$$

Also included in Table 2.4 are the isotropic energies E_{iso} for each pulse. These were obtained by integrating the light curve for the pulses individually and scaling the value by the

Table 2.4: Magnetic field strengths, number densities and isotropic energies for individual pulses.

Pulse	T_{pk} (s)	B (G)	n_e (cm $^{-3}$)	E_{iso} (ergs)
1	-52.8	5.61×10^{-3}	5.21×10^{-7}	4.15×10^{52}
2	-16.0	1.30×10^{-2}	2.77×10^{-6}	1.35×10^{52}
3	-4.6	5.65	0.53	1.85×10^{52}
4	1.8	3.34×10^{-4}	1.84×10^{-9}	5.85×10^{52}
5	159.0	142.02	333.30	3.93×10^{51}
6	191.6	203.34	683.29	4.29×10^{51}
7	210.0	159.76	421.81	4.99×10^{51}
8	235.0	298.76	1475.02	7.20×10^{51}
9	251.8	510.24	4302.39	5.29×10^{51}
10	282.0	347.88	2000.01	2.72×10^{51}
11	308.7	1974.96	6.45×10^4	4.47×10^{51}
12	342.7	143.53	340.44	1.94×10^{51}
13	366.0	255.91	1082.29	1.49×10^{51}
14	390.0	230.15	875.38	3.15×10^{50}
15	513.8	26.66	11.74	1.32×10^{51}
16	582.1	109.12	196.76	8.53×10^{50}

normalisation and the k-correction of each to find the bolometric fluence. When summed, these pulses combine to give a total prompt isotropic energy of 1.71×10^{53} ergs.

The values obtained show the some results that would be expected: that for ν_a to be at the high value assigned, the magnetic field strength, and therefore the electron population density must be high for most pulses. Using realistic values for the bulk Lorentz factor, emission radius and the microphysics plausible magnetic field strengths have been obtained. The earliest pulses appear to have weak magnetic field strengths, however, analysis of Equation 2.7 shows a strong dependence on both the bulk Lorentz factor and the radius at which collision between shells occurs. By definition the earliest pulses must be slower to allow subsequent pulses to catch them and cause a collision. As such, the Γ should be lower for these pulses, thus increasing the magnetic field strength experienced by the electron population. Additionally, if there was a lower contrast between Γ of early shells causing the first pulses, the collisions would occur at higher radii, further increasing B . Combining these two effects with the high dependences of the magnetic field strength on the two parameters would easily allow B of the first pulses to

become more in line with expectations.

The results for the middle and later pulses are consistent with those from Shen & Zhang (2009), which also shows that values of up to $B \sim 10^5$ Gauss can be reconciled with observations of the example GRBs they present. In their work a theoretically motivated value for B is used to determine R , whilst in this Chapter the methodology is reversed.

2.9 Conclusions

In this work, the pulse model of Genet & Granot (2009) has been taken and used in a similar manner to Willingale et al. (2010) to reproduce the prompt light curve of GRB 080310. Combining it with an afterglow model (Willingale et al., 2007), attempts have been made to produce a simultaneous fit to not only the data from the *Swift* XRT and BAT instruments, but also the available optical and IR data sets. The aims behind this work were to establish the origin of the observed early-time optical and IR emission, and to attribute it to either the prompt or afterglow component of the GRB.

The first conclusion of this work is that a low-energy break is required in the spectra of prompt pulses in order to fit the optical and NIR flux, regardless of its origin.

The simplest model considered for the optical and IR was to use this low-energy break to remove the prompt component entirely from the observed emission. Whilst this successfully recreated the broad-scale structure of the optical and IR light curves, and the SEDs also appear satisfactory, the value of p_a to which the fitting tended was unphysical ($p_a = 5.6$). This is inconsistent with that expected for a realistic spectrum, such as synchrotron radiation below the minimum emitted photon energy (E_m) for which p_a should be $\frac{1}{3}$ or synchrotron self-absorption, where p_a is expected to be $\frac{5}{2}$ or 2, when the self-absorption frequency is above or less than E_m respectively. However, having looked at the one-dimensional χ^2 surface for p_a , it was found that the distribution asymptotes to a better fit at large values of p_a . As a result a more realistic value of $p_a = \frac{5}{2}$ was used, which didn't significantly reduce the quality of the fit. The implications of this are that self-absorption is a necessary mechanism in order to fit the optical and NIR flux observed, when assuming the prompt pulses of the high energy light

curves do not contribute at early times in the lower energy bands.

Morphological inconsistencies in the light curves required the exploration of an alternative solution. This alternative was to allow the prompt emission to dominate the early times of the optical and IR light curves. An initial treatment of the prompt radiation, in which a single value for p_a was assigned to all pulses, proved insufficient to fit the data. Following this, by allowing the pulses to have independent values of p_a , a fit of similar statistical merit to the afterglow-dominated model was obtained (Figures 2.11 and 2.12). With this model, an additional break was still required for all the prompt pulses, but with a variety of values of p_a . For five pulses (particularly three of the earliest four) steep spectral indices were required, tending to unphysical values when fitted. As before, it was found to be possible to fix the appropriate values of p_a to $\frac{5}{2}$ without significantly altering the quality of the fit. This again suggests that self-absorption is an important mechanism by which the prompt emission is suppressed in the optical and IR regimes. For those pulses whose spectrum required a break, but not to the extent of pulses 1, 2, 4, 8 or 16, it is suggested that the break energy is at a value between the optical and X-ray bands, but given the degeneracy between p_a and E_a have not fitted it. These pulses could then also have a value of $p_a = \frac{5}{2}$, but peak at an energy nearer to that of the optical bands.

Considering pulses in the afterglow dominated model, where $\nu_a = 0.3$ keV, limits on the magnetic field, number density of the electron population and radius from the central source at which emission occurs were all considered. Using typical values for parameters such as the bulk Lorentz factor of the radiating material, a high ν_a led to high magnetic field strength in the emitting regions and thus a dense population of electrons causing the emission. This dense population is required to successfully absorb such a large portion of the expected synchrotron flux. It is also shown to be likely that shells of material emitted at earliest times have similar bulk Lorentz factors, causing collisions at higher radii and producing more realistic magnetic field strengths for these first pulses of the GRB.

From the results obtained, it is unclear whether the optical and IR emission of GRB 080310 originates from central engine or afterglow activity. Neither case accurately describes all of the data. The afterglow-dominated model is insufficient to describe all of the structure seen in the

optical light curves; however, the SEDs produced, particularly at 350 seconds suggest that the optical and NIR are more faithfully represented by afterglow emission. To help discriminate between prompt and afterglow emission as a source for early-time emission a similar analysis is required on a larger sample of GRBs. Bursts in such a sample have several important pre-requisites. First, good continuous optical data are required from very early to late times, preferably in several bands, simultaneously. Having such a data point from KAIT though, highlights that at the earliest times high temporal resolution is required too, as GRBs are highly variable during their prompt phases.

GRBs which will be the best candidates for further analysis will be those that contain pulse structure in the optical light curves. If these pulses are simultaneous with similar structure at higher energies, then it is likely they share a common origin. In contrast to this, should the pulses occur at markedly different times, then an alternative mechanism must be found to explain their behaviour. The ideal type of burst for this analysis would therefore be one which has a long duration as observed in BAT (or *Fermi*-GBM) and exhibits strong flaring behaviour after the first hundred seconds in the X-ray regime. Such times are not only feasible for ground-based follow-up, but also allow for sufficient temporal resolution to discern any features at these lower energies.

3

Broadband modelling of GRB 061121, GRB 080810 and GRB 081008

3.1 Chapter overview

In this Chapter a further three bursts, GRB 061121, GRB 080810 and GRB 081008, are analysed in a similar manner to GRB 080310. Each of these bursts have optical data beginning within the first 100 seconds after the initial BAT trigger. GRB 061121 is first considered as there is a pulse-like feature within its optical light curve. Attempts are made to reconcile this with the pulses fitted to the high-energy data from the BAT and XRT. GRB 080810 is then presented, in which a smooth optical light curve is observed. Assuming self-absorption is a suitable candidate for removing the prompt pulses from the optical data, the necessary modifications to high-energy afterglow fit are investigated. Finally, GRB 081008 is analysed with particular emphasis placed upon the simultaneous multiband observations available for the burst. Using these data attempts are made to fit a cooling break to the afterglow spectra of these bursts.

3.2 Introduction

GRB 080310, as presented in Chapter 2, was a burst for which the origin of the early-time optical emission was in question. After careful analysis the cause of this emission remains unclear, however, the use of self-absorption in the spectra of the prompt pulses was found to be necessary.

One manner by which the contribution of the prompt emission at optical wavelengths and early times can be assessed is by studying bursts containing hints of prompt features in their optical light curves. One of the most ideal candidates for this is GRB 061121 (Page et al., 2007), which is presented below. Also presented are two bursts for which optical data were available beginning prior to 100 seconds after the initial trigger. Whilst the epochs of the first optical observations are later with regards to the high-energy prompt emission, they still provide important information through their light curves at low-energies.

Another aspect of this Chapter is the comparison of the afterglow features of bursts in different spectral regimes. As discussed in §1.5 the behaviour of the observed afterglow can be markedly different when observed at separate wavelengths. This is something that can be tested even when early observations are not available. These observations are, however, preferred as they can help constrain the shape of the early afterglow prior to the plateau phase.

3.3 GRB 061121

3.3.1 Observations

GRB 061121 was observed at several different energies and was found to have a redshift of $z = 1.314$ (Bloom et al., 2006; Perley & Bloom, 2006). The following section outlines the available data.

High-energy data

GRB 061121 was detected by BAT on the 21st of November 2006. For this burst *Swift* was fortunate enough to trigger on a precursor to the main emission event (Page et al., 2006).

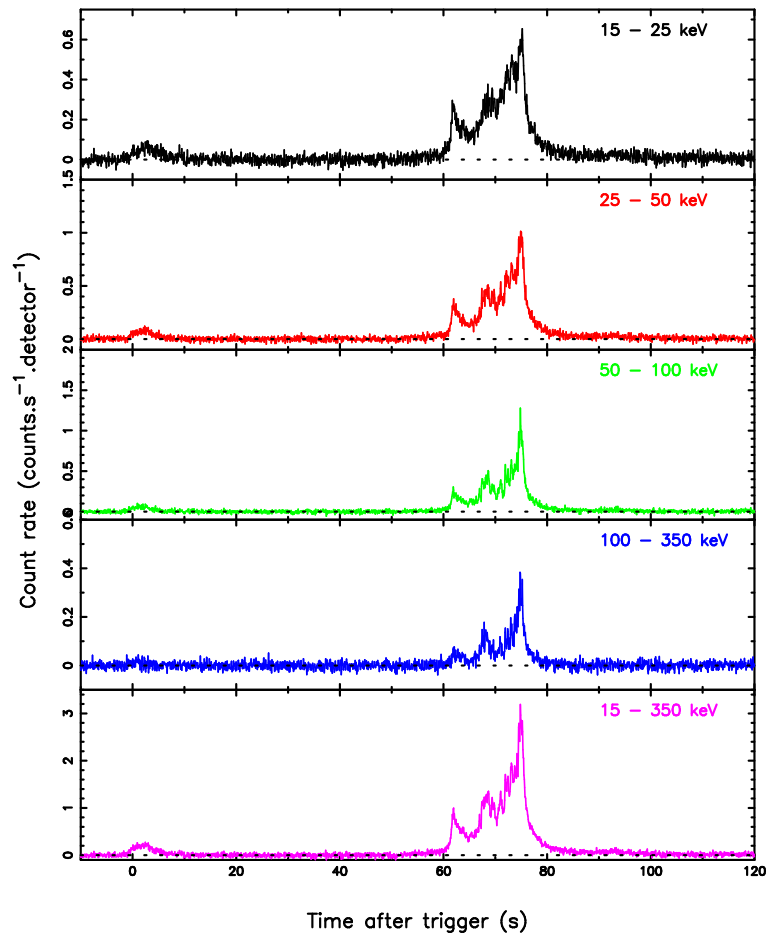


Figure 3.1: *Swift*/BAT light curve of GRB 061121. The light curve is binned with 64 ms temporal resolution, and shows the four standard BAT channels in the four top panels. The bottom panel shows the sum across all four bands.

Figure 3.1 shows the prompt light curve, which clearly illustrates the precursor event, a period of quiescence lasting approximately 50 seconds and then the main period of burst activity.

From the 15–350 keV light curve a T_{90} of 81 ± 5 seconds was determined using the standard BATTBLOCKS routine (Fenimore et al., 2006). This is dominated by the 50 seconds of quiescence following the initial precursor event. The end of the T_{90} duration contains approximately 20 seconds in which the majority of the γ -ray fluence was observed. During this time the observed prompt emission comprises of a series of overlapping peaks, the last of which is the brightest. Following the peak of this pulse, there is an exponential decay, typical of the FRED pulses seen in most GRB high-energy light curves.

In addition to BAT, both *Konus-Wind* and *Konus-A*, with spectral ranges of 20 keV–5 MeV and 10 keV–10 MeV respectively, observed the burst (Golenetskii et al., 2006). *Konus-*

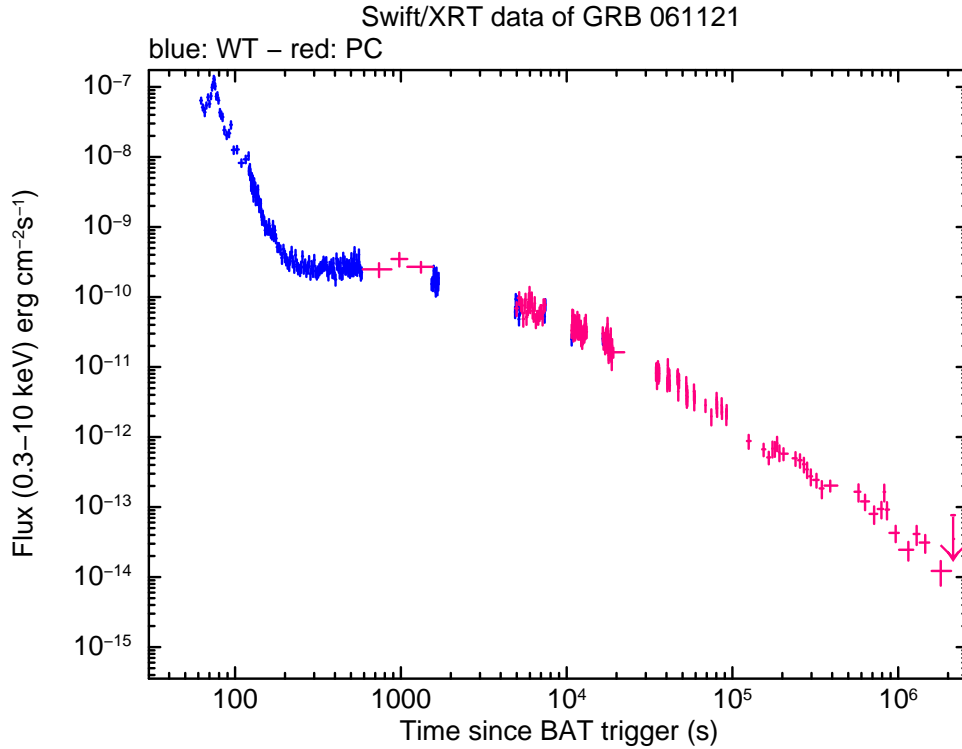


Figure 3.2: *Swift*/XRT light curve for GRB 061121. Blue points are data taken in PC mode, whilst magenta were taken using WT mode.

Wind triggered only on the main series of pulses that begin at approximately 60 seconds after the BAT trigger in Figure 3.1, whilst *Konus–A* also detected the fainter precursor event.

X–ray data

With observations starting at 62 seconds after the trigger time (Marshall et al., 2006), XRT coverage began during the time at which the GRB was active in the γ –ray regime. With a peak count rate of approximately $2,500 \text{ counts.s}^{-1}$, GRB 061121 was at that time the brightest burst detected by the XRT (Page et al., 2006).

Shown in Figure 3.2 is the XRT light curve obtained for GRB 061121. A group of peaks is first observed, which at approximately 100 seconds after the initial trigger time begins to fade as a typical RDP. Once the RDP has started, the X–ray afterglow follows the canonical model (Nousek et al., 2006) with the RDP, plateau and later decay phases all evident.

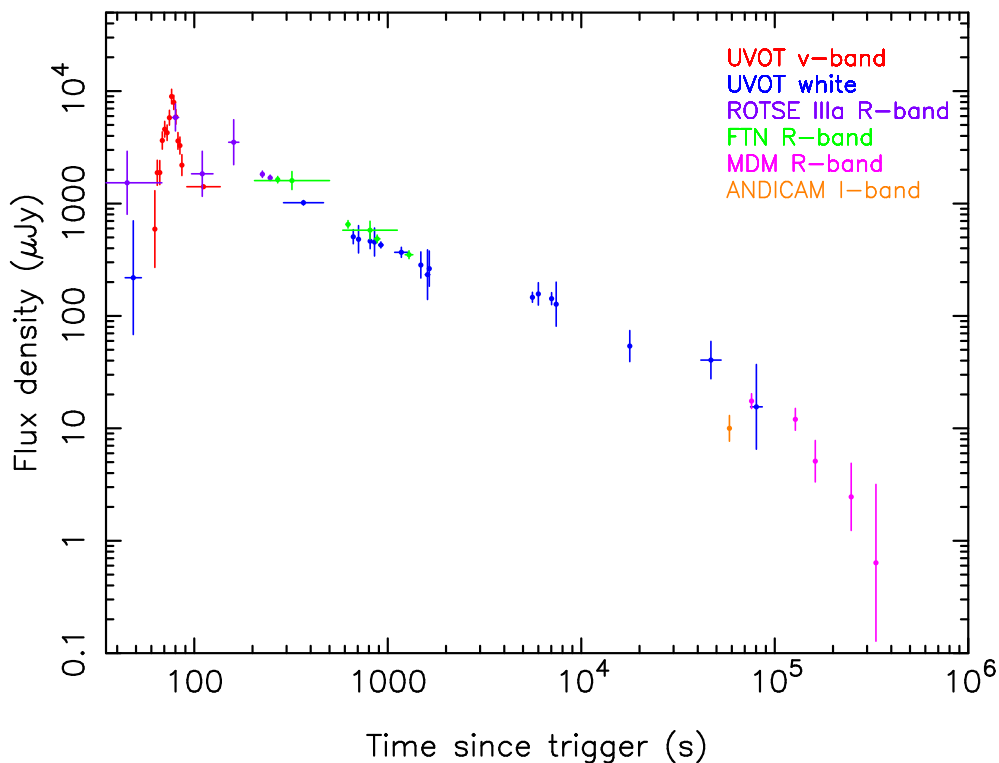


Figure 3.3: Optical data for GRB 061121. Colour coding of the points is described in the key. UVOT *white* data has been calibrated to the *v* band. The ROTSE unfiltered data has been calibrated to the *R* band.

Optical data

Thanks to the initial *Swift* trigger being caused by the precursor event shown in Figure 3.1 optical facilities were able to observe the source position whilst the main γ -ray emission was still active. A light curve containing this optical data is included in Figure 3.3.

The most accurate position derived for GRB 061121, found using UVOT, was RA(J2000) = $09^{\text{h}}48^{\text{m}}54^{\text{s}}.55$ Dec(J2000) = $-13^{\circ}11'42''.4$ (Marshall et al., 2006). Observations were taken in the *v* and *white* filters, with the latter being calibrated to the *v*-band in a similar manner to the data for GRB 080310. In Figure 3.3 the UVOT data clearly show a peak in the *v*-band observations between 60 and 100 seconds. Following this peak, the UVOT data then also decay although more slowly than the XRT light curves.

It is the peak in the optical light curve that makes GRB 061121 of such interest for the modelling outlined in this Chapter. With other GRBs, such as GRB 080310, a mechanism for reducing the observed prompt flux at optical wavelengths is required. However, GRB 061121 offers a chance to attribute a morphological feature to the prompt emission, providing more

rigorous constraints on the prompt pulse model employed.

In addition to UVOT, early-time observations were also taken using the ROTSE-IIIa telescope located in Australia. The first image was taken 20.6 seconds after the initial *Swift* trigger time, leading to the identification of a variable source at the UVOT position (Yost et al., 2006). The ROTSE data were unfiltered, however, they were calibrated to the *R* band. It was also noted that the weather conditions were windy, leading to poor seeing conditions.

Due to the sparse nature of the ROTSE data there is no definite detection of the pulse structure seen in the UVOT light curve. The sensitivity of the UVOT *white* and the ROTSE unfiltered band passes differ as a function of the wavelength within the band. the UVOT *white* filter has a higher sensitivity at $\lambda < 4500 \text{ \AA}$, whilst the ROTSE response is redder.

Later observations were also taken with several other ground-based facilities. These include FTN, the Michigan–Dartmouth–M.I.T. (MDM) 2.4 m telescope and ANDICAM. The ANDICAM observations provided a single *I* point, and upper limits in the *K* and *J* bands (Cobb, 2006). Both FTN and MDM observed the GRB after the initial pulse seen by UVOT. These two instruments observed in the *R*-band and both showed a decaying afterglow (Melandri et al., 2006; Halpern et al., 2006; Halpern & Armstrong, 2006).

As with GRB 080310, the effects of Lyman absorption were considered. This is due to intervening hydrogen along the line of sight between the source and observer. An updated version of the *GRBz* software was used that is available online¹. The absorption within the relevant optical bands was calculated based on the work of Curran et al. (2008) and Madau (1995). At $z = 1.314$ the effects within the observed low-energy bands were negligible, as at this redshift such features remain at shorter wavelengths.

Radio observations

GRB 061121 was also detected in the radio regime. The Very Large Array (VLA; Thompson et al. 1980) detected the afterglow in in the 8.46 GHz band, 18 hours after the prompt emission, with a flux of $308 \pm 48 \mu\text{Jy}$. Further radio observations were taken with the Australian Telescope Compact Array (ATCA; Frater et al. 1992) and the Westerbork Synthesis

¹<http://igmac.fmf.uni-lj.si/>

Table 3.1: Parameters of the prompt pulses identified in the BAT and XRT light curves of GRB 061121. These include the peak time (T_{pk}), peak energy at this time (E_{pk}), the rise time (T_{rise}) and arrival time of the last photon (T_f) for each pulse.

Pulse	T_{pk} (s)	E_{pk} (keV)	T_{rise} (s)	T_f (s)	b_1
1	2.9	200	3.4	4.5	-0.45
2	61.9	200	1.0	9.3	-0.27
3	68.6	200	2.2	6.7	-0.10
4	73.3	200	2.3	3.5	-0.18
5	75.0	200	1.8	2.0	0.48
6	92.9	200	3.4	8.6	-0.54
7	110.0	200	4.8	26.2	-1.97

Radio Telescope (WSRT; Hogbom & Brouw 1974) at 5.2 and 6.2 days after the trigger. These observations did not detect the afterglow from the source (van der Horst et al., 2006a,b).

The single radio flux measurement from the VLA is not included in the following analysis. Whilst it is desirable to fit the data over such a broad spectral range, the number of additional free parameters reduced the degrees of the freedom of the fit.

3.3.2 High-energy model

Using the process described in §2.3, seven prompt pulses were identified in the high-energy light curves from *Swift*, the properties of which are shown in Table 3.1. These include the precursor that triggered the BAT instrument.

In addition to the seven prompt pulses shown in Table 3.1, an afterglow was fitted to the X-ray data. The morphological model from Willingale et al. (2007) was used, the characteristics of which are shown in Table 3.2. A late temporal break was identified in the X-ray afterglow, requiring a further two parameters in the fit. These are the time at which the break occurs, T_b , and the increment by which the power-law decay steepens, α_b .

As can be seen in Figure 3.4, the combination of the prompt pulses and the morphological afterglow do well in representing the light curves seen by both the XRT and BAT instruments of *Swift*. The prompt pulses as observed in both are accurately depicted, as is the X-ray afterglow. The reduced χ^2 value for the fit is 4.49 for 606 degrees of freedom, however, which

Table 3.2: Parameters of the high-energy fitted afterglow for GRB 061121. The first column denotes the parameter and unit, whilst the second shows the value obtained. The characteristic times T_r , T_a and T_b are in units of seconds, whilst the normalisation F_m is in units of $\text{keV.cm}^{-2}.\text{s}^{-1}$.

Parameter	Value
b_a	$-0.94^{+0.08}_{-0.08}$
T_r	100.0
T_a	2886.0^{+1326}_{-745}
F_m	$0.15^{+0.01}_{-0.01}$
α_a	$0.85^{+0.19}_{-0.15}$
T_b	$1.54^{+0.41}_{-0.32} \times 10^4$
α_b	$0.66^{+0.14}_{-0.17}$

implies there are regions of the fit which are statistically unacceptable. The large fit statistic is significantly contributed to by the small scale fluctuations in the data from both the XRT and BAT. There are, however, other times when the fit is not an exact match to the data.

The first of these can be seen in the BAT light curve, during the rise of the second pulse. This is the first pulse of the main episode of emission and its initial rise is too steep in the model in the three softest BAT bands. The rapidity of this rise is necessitated by both the peak count rate of the pulse and the rise just prior to the peak. To fit both the peak and the steep rise shortly before it, a small value of T_r is required causing the poor fit at the start of the pulse.

The second region where the fit shows a discrepancy from the data is the peak of the third pulse being under-predicted in the 100–350 keV band, despite being well fitted in the other BAT bands. In a similar fashion the fifth pulse, the brightest observed in BAT, is under-predicted in only the 15–25 keV band. This pulse has a significant overlap with the preceding pulse, which peaks only 1.7 seconds earlier, making it difficult to accurately disentangle the spectral and temporal characteristics of the two.

The final noteworthy difference between the model and data detected by BAT is the decay of the fifth pulse being at a rate that is slightly too rapid in the hardest BAT band, but too shallow in the 15–25 keV band.

Turning to the XRT there are two regions where the model can be seen to differ from the data. In the hard XRT band the decay of the final pulse can be seen to over-predict the RDP, despite being a good fit in the softer 0.3–1.5 keV band. However, only being detected in the

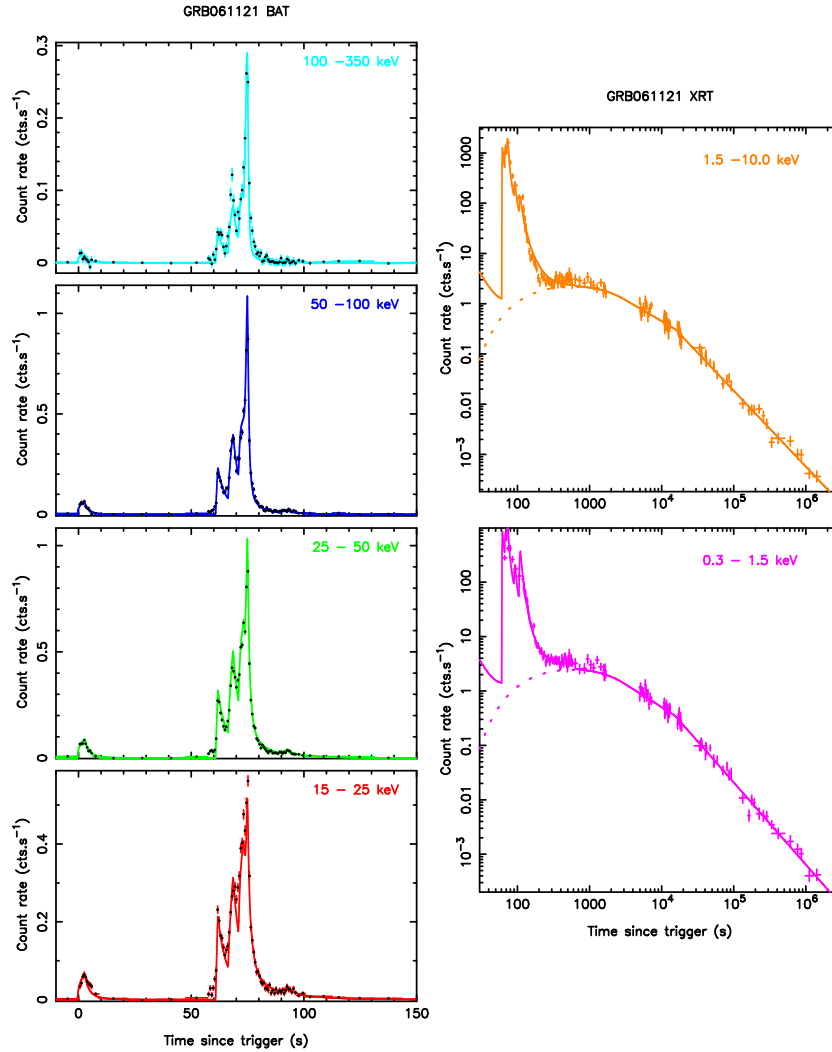


Figure 3.4: BAT and XRT data, showing the fitted BAT and XRT data for GRB 061121, showing the fitted Willingale et al. (2010) model. Left panels: BAT bands (Top to bottom: 100–350 keV, 50–100 keV, 25–50 keV & 15–25 keV). Right panels: XRT bands (Top: XRT hard-band, bottom: XRT soft-band). Solid lines show the total fit (pulses and afterglow), whilst dashed lines show only the afterglow component to the fit. This fit has a reduced $\chi^2 = 4.49$ for 606 degrees of freedom.

XRT, the spectral range over which the final two pulses are fitted is small.

Finally, the plateau region of the afterglow model under-predicts the data shortly after the transition from the RDP to the plateau phase. However, after the first orbit, the afterglow fit is a faithful representation of the data over the remaining XRT coverage.

3.3.3 Extending to low energies

As with GRB 080310 in Chapter 2, the first step in fitting the low-energy light curves was to extrapolate the high-energy fit to the bands in which further observations were taken. Initially,

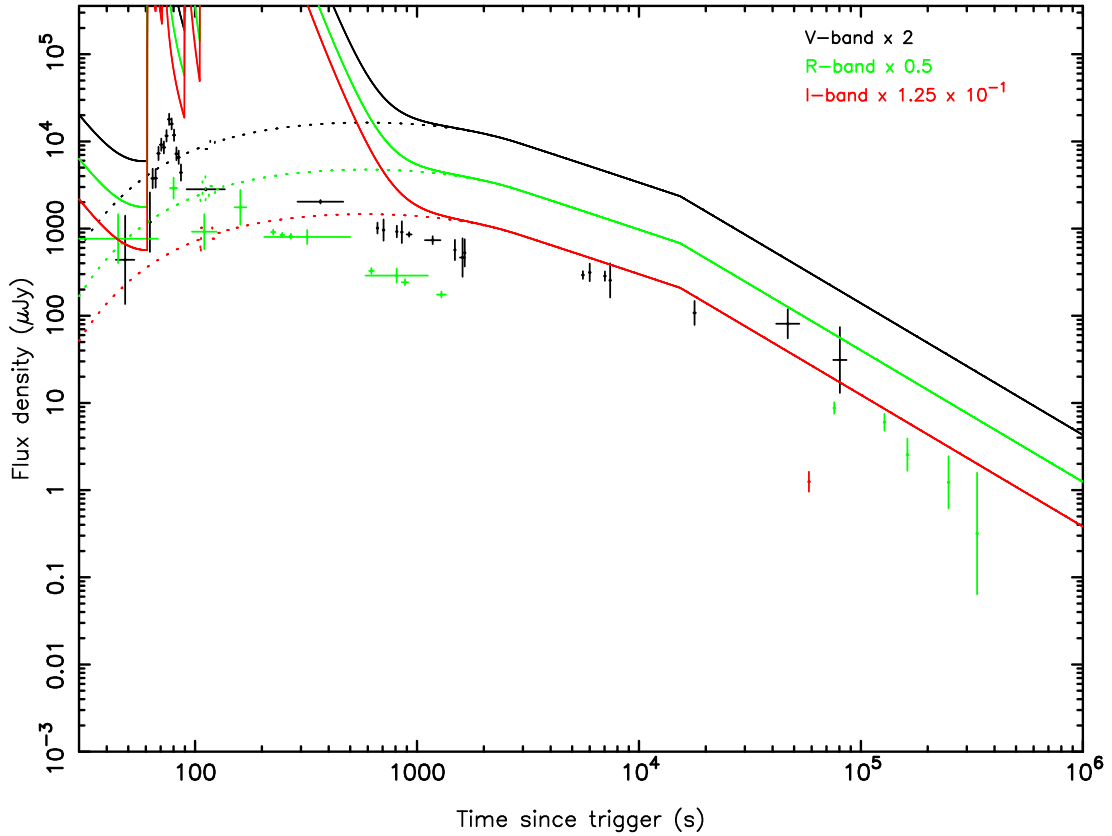


Figure 3.5: Optical light curves for GRB 061121 obtained by extending the high-energy fit of the prompt pulses and afterglow component described in §3.3.2. The dashed lines show the extrapolation of the afterglow component for each band.

the spectra for each of the pulses and the afterglow were used as presented in the high-energy fit outlined in §3.3.2. This is shown in Figure 3.5. Unlike GRB 080310, not only do the pulses over-predict the expected flux at optical wavelengths, but the model afterglow is also too bright when compared to the data. The optical data were therefore fitted independently to the X-ray data.

To initially model the afterglow, the pulses were assumed to be self-absorbed, with $p_a = 2.5$. To be sure the signal from the pulses was entirely removed from the total burst spectrum, E_a was set to be 0.3 keV once more (at T_{pk}). This proved capable of eliminating prompt contributions to the optical flux.

To reduce the optical afterglow flux, an additional spectral break was also introduced to the afterglow spectrum. In this instance it was assumed that the afterglow was slow cooling. A more thorough treatment of the afterglow would expect it to be fast cooling initially, before transitioning to the slow cooling regime, however this transition time is uncertain as it depends

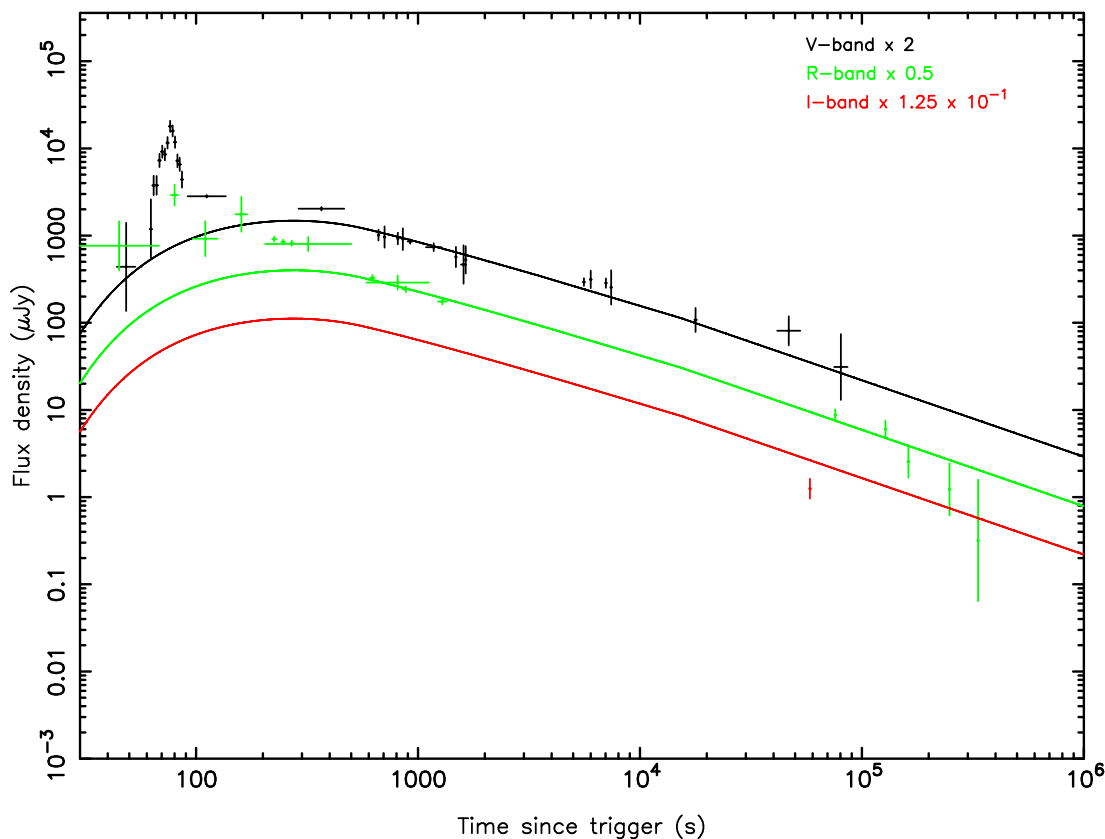


Figure 3.6: Fit achieved to optical afterglow of GRB 061121. Only optical data after 500 seconds were fitted as these were clearly due to the afterglow. This afterglow assumes a slow cooling population of electrons in an ISM type density profile.

on physical parameters of the burst such as the magnetic field strength and microphysics.

From Figure 1.14 it can be seen that the temporal evolution of the cooling break varies depending on the nature of the circumburst medium. If this medium is assumed to be similar to the ISM, and therefore have a constant density profile, $\nu_c \propto t^{-\frac{1}{2}}$. Conversely, if the environment is thought to resemble a wind-like outflow as might be expected for a massive star, $\nu_c \propto t^{\frac{1}{2}}$. Afterglow models for both types of media were produced and are discussed below.

The afterglow model shown in Figure 3.6 is that for an ISM like density profile (constant with radius). The data dominating the fit are those in the v -band prior to 1×10^4 seconds, as these are most numerous and have small errors.

The temporal break fitted to the high-energy light curves was found to be better fitted at a later time in the optical data. The value of the increment by which the power-law decay changed (α_b) was fitted but not well constrained. This is due to the data at these times having large errors and not being consistent between bands.

Table 3.3: Parameters of the optical fitted afterglow for GRB 061121. The first column denotes the parameter, whilst the second shows the value obtained for an ISM density profile and the third contains the same values for a wind-like profile. The characteristic times T_r , T_a and T_b are in units of seconds, whilst the normalisation F_m is in units of $\text{keV.cm}^{-2}.\text{s}^{-1}$. E_a is in units of keV.

Parameter	ISM value	Wind-like value
b_a	-0.94	-0.94
T_r	100.0	100.0
T_a	$129.3^{+3279.6}_{-3.9}$	$99.35^{+1.02 \times 10^4}_{-99.35}$
F_m	$0.15^{+0.31}_{-0.05}$	$0.17^{+0.29}_{-0.01}$
α_a	$1.01^{+0.14}_{-0.15}$	$0.50^{+0.15}_{-0.15}$
T_b	1.27×10^5	1.27×10^5
α_b	$2.02^{+6.14}_{-2.02}$	$2.08^{+6.05}_{-2.08}$
p_{ag}	-0.44	-0.44
E_{ag}	$0.14^{+3.07}_{-0.14}$	$0.16^{+37.80}_{-0.02}$
d_{ag}	0.5	-0.5

The afterglow parameters obtained for the fit plotted in Figure 3.6 are shown in Table 3.3. As can be seen from the errors on the fitted parameters, due to the lack of data and poor coverage, the fit is poorly constrained. Also shown are the equivalent parameters for a fit in a wind-like environment. It is important to note that $E_{ag} \propto t^{-d_{ag}}$, and so a positive value for d_{ag} in Table 3.3 corresponds to an anti-correlation between the break energy and time. E_{ag} is defined as the value of the break energy at a time T_a .

Unlike GRB 080310, a change to the temporal index of the power-law decay is not sufficient to unify the optical and X-ray afterglow data. Changes therefore had to be made to the afterglow model to account for data after 500 seconds. In the afterglow model of Willingale et al. (2007) there is no temporal evolution of spectral breaks and no energy dependence for T_a or T_r . In this model, a cooling break is added to the afterglow spectrum, with temporal evolution in accordance with theory (Granot & Sari, 2002) which, as discussed, is dependent on the nature of the circumburst medium.

The two fits for the ISM and wind-like environments are both morphologically similar. As d_{ag} is different for both, the region of the spectrum where the break occurs changes between the model. The temporal decay index α_a is notably steeper in the ISM model to compensate for this, as at late times the cooling break occurs at lower energies than the wind-like medium

model. Statistically both fits are of similar merit, with reduced χ^2 values of 1.91 and 2.14 for the ISM and wind-like models respectively. Both had 13 degrees of freedom. This a low number of degrees of freedom as it only includes optical data, and excludes the pulse like structure seen prior to 500 seconds.

With the sparse nature of the late-time data, the errors on the afterglow parameters are high. However, as can be seen be Figures 3.5 and Figure 3.6, those detailed in Table 3.3 provide a better fit to the available data after 500 seconds. The R -band data between 100 and 200 seconds look as though they could be an earlier part of the power-law decay phase of the afterglow, however it was not possible to simultaneously fit this and provide an afterglow that rose rapidly enough that it did not interfere with the optical pulse complex.

Whilst the modelling of the optical afterglow is now incompatible with the X-ray data, the ISM type afterglow detailed in Figure 3.6 and Table 3.3 is adopted in further modelling of the optical data. Similar results were also obtained using the wind-like afterglow model. The remaining aim of the study of this burst is to see whether the pulse feature in the optical data can be fitting using the same components identified in the high-energy prompt emission.

The highest peak in the optical light curve appears shortly after 70 seconds, making pulses 4 and 5 the most likely causes of the optical behaviour. Each was considered individually as the source of the optical flux. Initial attempts to use self-absorption and values of E_a that result in the correct peak flux were found to result in pulses that were too narrow. The width of each peak is determined by the high-energy fit and making them broader encroaches on the RDP phase of the X-ray light curve.

Being unable to make either of the two pulses broader, an alternative approach was adopted. Attempts to fit the correct level of flux at the peak of the optical pulse were abandoned in favour of correctly modelling the pulse tail. Simply extrapolating the high-energy fit for pulse 4 to the optical wavelengths in which there were data allowed a suitable fit to be found. This is shown in Figure 3.7, where pulse 4 over-predicts the flux at T_{pk} but correctly models the shape of the decay tail for the optical pulse complex.

That the width of the pulse in the optical regime was too narrow suggests that there may be a spectral dependence contained within T_f , which allows the width of each pulse to be higher at

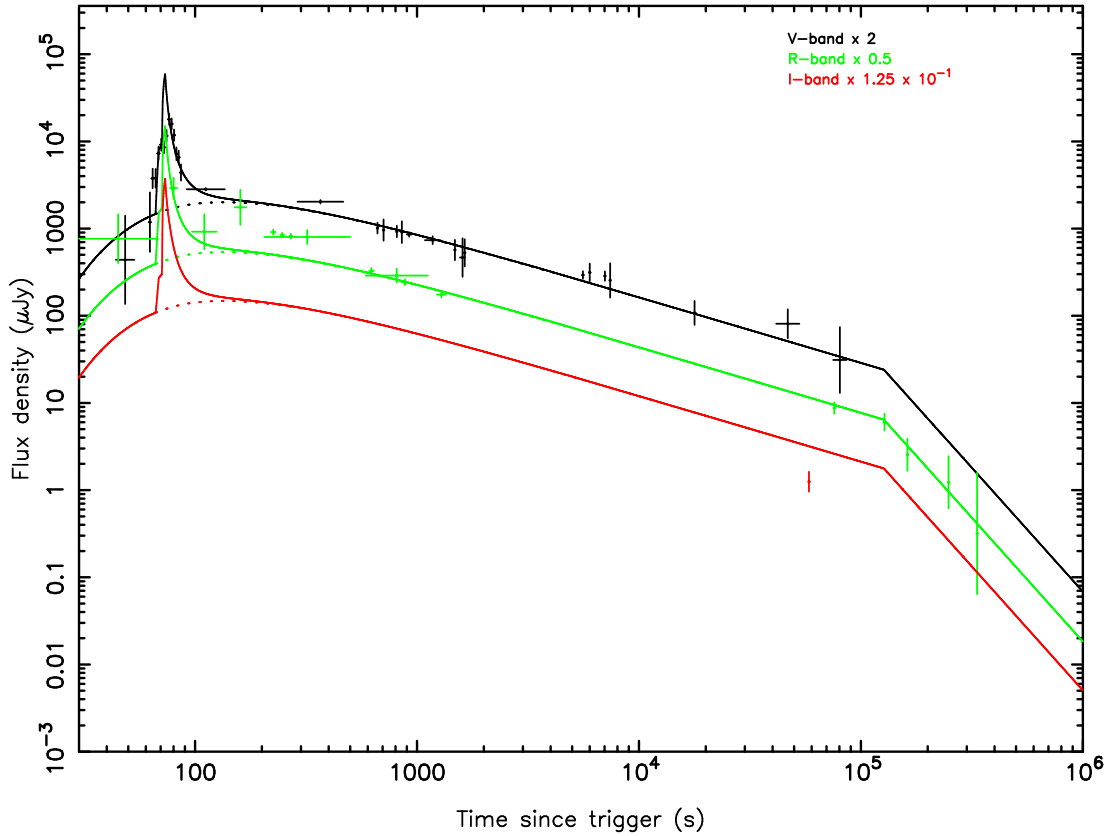


Figure 3.7: Fit achieved to optical light curves of GRB 061121 maintaining the high-energy temporal break. Pulses 1, 5 and 6 are self-absorbed, whilst the others used to fit the observed optical pulse complex. The peak flux is over-predicted as the priority of the modelling was to fit the shape of the pulse decay.

low-energies. This could have fundamental implications on the nature of the emitting regions and mechanisms responsible for the pulses.

Features within the rise of the optical pulse complex were fitted with pulse 3. To achieve this self-absorption was retained as a mechanism by which flux was reduced, but the value of E_a was fitted. By allowing this value to float, it was found that E_a for pulse 3 was 3.5 eV. This is summarised in Table 3.4. The remaining pulses were self-absorbed, with a fixed value for p_a of 2.5, and $E_a = 0.3$ keV. As with GRB 080310, the values of $\nu_{a,obs}$ were used to estimate the magnetic field strength and electron number density for each pulse. The values derived for pulse 4 assume that the self-absorption break occurs just below the optical bands at T_{pk} .

Whilst the data between 100 and 500 seconds suggest there could be a contribution from pulse 7, it was not possible to find a suitable fit to the data from the model, and so these data remain under-predicted by the total prompt and afterglow model.

Table 3.4: Physical properties of the prompt pulses for GRB 061121. The columns denotes the pulse number, observed self-absorption break energy, magnetic field strength, electron number density and pulse isotropic energy respectively.

Pulse	$\nu_{a,obs}$ (keV)	B (G)	n_e (cm ⁻³)	E_{iso} (ergs)
1	0.3	1.31	2.82×10^{-2}	6.24×10^{51}
2	0.3	0.52	4.55×10^{-3}	2.95×10^{52}
3	3.5×10^{-3}	1.48×10^{-10}	3.64×10^{-22}	4.18×10^{52}
4	1.56×10^{-3}	3.20×10^{-13}	1.69×10^{-27}	2.85×10^{52}
5	0.3	148.24	363.16	4.15×10^{52}
6	0.3	10.72	1.90	1.92×10^{51}
7	0.3	8.4×10^{-2}	1.17×10^{-4}	7.22×10^{50}

Table 3.4 suggests that the magnetic field strengths for most of the pulses are unphysically small, particularly those of pulses 3 and 4. Bošnjak et al. (2009) consider magnetic field strengths of internal shocks in the range of 10 to 1000 Gauss, meaning only two of the calculated values for GRB 061121 are consistent with expectation.

Referring back to Equation 2.7 it would appear that the estimates of either R or Γ are incorrect for these two pulses. To increase the magnetic field strength to a more physical value, either the radius from the explosion centre would have to be higher, or the bulk Lorentz factor of the material would have to be reduced. Such a change in either would reconcile pulses 1, 2, and 7 with the range from Bošnjak et al. (2009). To increase the radius of the shock, the contrast between the Lorentz factors of the colliding shells would have to be low, creating a situation where it takes longer for the second shell to catch up with the first.

Pulses 3 and 4 require more drastic alteration, as even altering both R and Γ only alters the value of B by seven orders of magnitude, which is insufficient to increase the magnetic field strength within the theoretical range expected. It is likely that whilst these shocks have a lower Γ , higher radius and lower contrast in Lorentz factors, there is still something significantly different about the physics of these shocks in comparison to the others seen in this burst. That they are atypical of other pulses is not surprising as it is rare to see pulse structure within the optical light curves of GRBs.

It is again important to note that the afterglow model employed in the fitting of the optical light curve is entirely independent of the high-energy fit and that the two are incompatible.

The Willingale et al. (2007) model is entirely phenomenological and the modelled temporal characteristics contain no dependence on the band in which observations are taken. Despite being able to correctly predict the afterglow flux using a cooling break, neither an ISM or wind-like environment is statistically favoured.

3.4 GRB 080810

GRB 080810 is another burst for which there is a broad available data set (Page et al., 2009). Detected on the 10th of August 2008 (Page et al., 2008) GRB 080810 had a measured redshift of $z = 3.355 \pm 0.005$ from the Keck High Resolution Echelle Spectrometer (HIRES; Prochaska et al. 2008), which was also confirmed by the Russian Turkish 1.5m Telescope (RTT150; Burenin et al. 2008) and the Nordic Optical Telescope (NOT; de Ugarte Postigo et al. 2008). The most accurate position obtained for this burst was from the UVOT refined analysis: RA(J2000) = 23^h47^m10^s.48 Dec(J2000) = +00°19′11″.3 (Holland & Page, 2008).

Aside from the collection of *Swift* and ground-based observations, this burst also triggered *Fermi* (Meegan et al., 2008) and *Konus-Wind* (Sakamoto et al., 2008b). The data from which are briefly discussed in §3.4.1.

3.4.1 Observations

High-energy data

The BAT detected emission from GRB 080810 in all four of the standard bands, as shown in Figure 3.8. The prompt phase is comprised of a series of pulses, several of which overlap during the first 30 seconds after the initial BAT trigger. There is then a short period of quiescence lasting approximately 10 seconds before a further two pulses which finish between and 50 and 60 seconds after the trigger time. Finally, at 100 seconds after the trigger, there is a further period of weaker emission that is most clearly detected in the softest of the BAT bands.

The measured T_{90} of GRB 080810 is 106 ± 5 seconds in the 15–350 keV range (Sakamoto et al., 2008c). This was obtained using the standard BAT analysis BATTBLOCKS routine, which was run as part of the BATGRBPRODUCTS script.

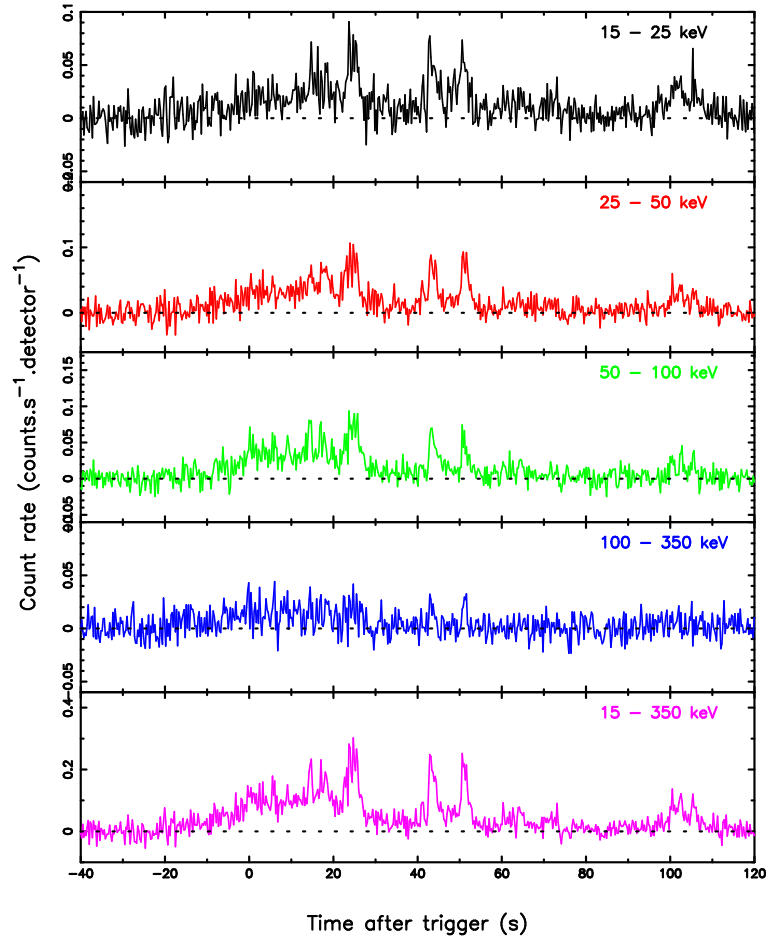


Figure 3.8: *Swift*/BAT light curve of GRB 080810. The light curve is binned with 256 ms temporal resolution, and shows the four standard BAT channels in the four top panels. The bottom panel shows the sum across all four bands.

Observations in the γ -ray regime were also conducted by the *Fermi*-GBM and *Konus-Wind*. The GBM has a higher-energy spectral coverage, particularly from the bismuth germanate scintillators (BGO). The sodium iodide detectors (NaI) which extend from 10 keV to 1 MeV provide values of T_{90} which show good correspondence with the BAT estimates of the parameter (Meegan et al., 2008). Figure 1 of Page et al. (2009) shows both the BAT and GBM light curves plotted on a common temporal axis and demonstrates that similar features are detected in both. *Konus-Wind* provided coverage in the 20 keV to 1 MeV, the results of which are reported in Sakamoto et al. (2008b).

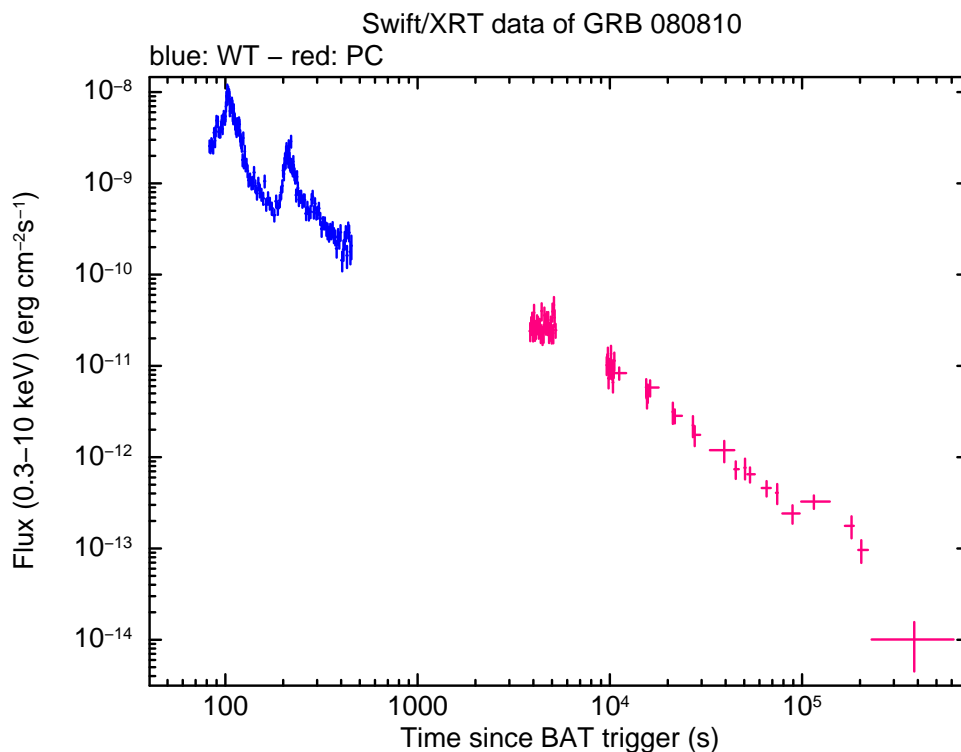


Figure 3.9: *Swift*/XRT light curve for GRB 080810. Blue points are data taken in PC mode, whilst magenta were taken using WT mode.

X-ray data

XRT coverage for GRB 080810 began at 76 seconds after the BAT trigger. As can be seen in Figure 3.9, data from the first orbit show two prominent flares, sufficiently bright to ensure the XRT took data only in WT mode throughout the orbit (Page, 2008). The first of these flares is contemporaneous with the last period of activity seen in the BAT light curves shown in Figure 3.8.

In all subsequent XRT observations of the source, the afterglow of the GRB is faint enough to allow photon counting data to be taken. The coverage of the second orbit, between 3.9 and 5.2 ks, has a near constant flux, which could be interpreted as part of the plateau phase of the proposed canonical X-ray light curve (Nousek et al., 2006). With the gap in coverage, due to the orbit of *Swift* the attribution of this data to the plateau phase retains a level of uncertainty. In the following data, from 9.6 ks onwards, there is a power-law decay. This is deviated from between 100 and 300 ks when there is a slight re-brightening before the end of the X-ray data.

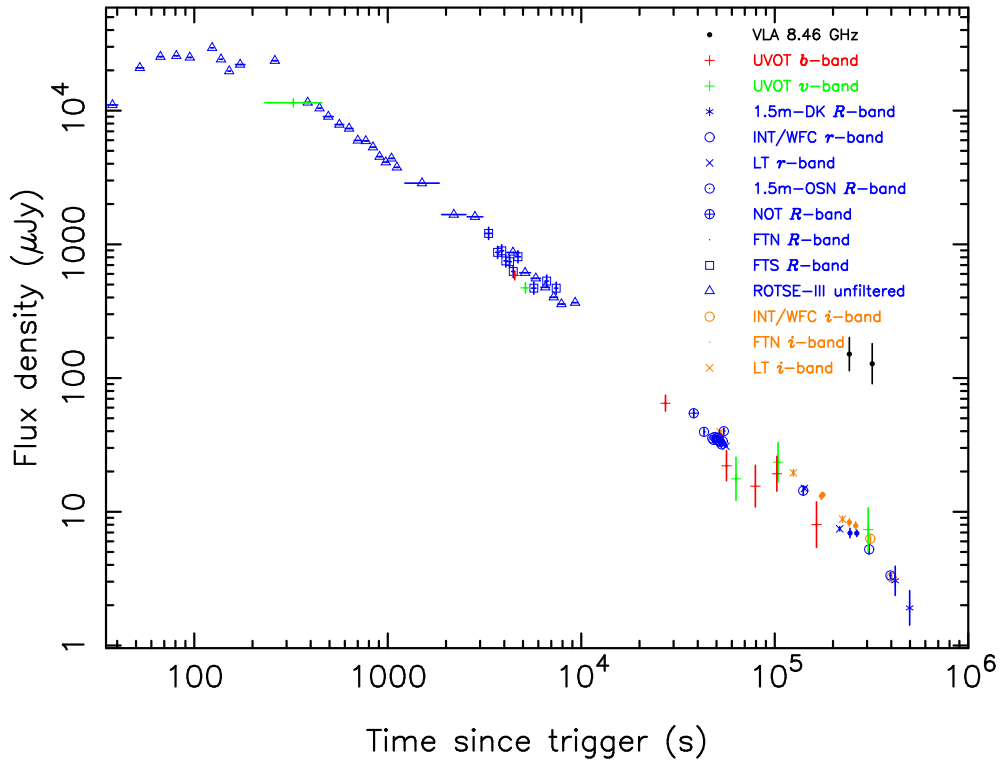


Figure 3.10: Optical data for GRB 080810. Colour coding of the points is described in the key. ROTSE-III unfiltered data has been calibrated to the R band.

Optical data

GRB 080810 had many optical observations taken from a suite of instruments. The first of these was UVOT (Holland & Page, 2008), with the afterglow being detected in the v , b and *white* filters. That only upper limits were obtained for the lower wavelength bands is unsurprising, due to attenuation from the IGM at this redshift.

Early-time data were also taken by ROTSE-IIIa, beginning at 35 seconds after the trigger (Rykoff, 2008). As shown in Figure 3.10, the ROTSE data show a brightening, followed by a plateau. At 300 seconds the data then show a smooth decay which is followed by both the ROTSE and other late-time data.

The other optical data, which follow this smooth decay are from telescopes including NOT (de Ugarte Postigo et al., 2008), 1.5m Observatorio de Sierra Nevada (OSN; de Ugarte Postigo et al. 2008), the 1.54m Danish telescope, Faulkes Telescope North and South (FTN and FTS; Guidorzi et al. 2008), the Liverpool Telescope (LT; Guidorzi et al. 2008) and the Isaac Newton Telescope Wide Field Camera (INT/WFC). Table 4 of Page et al. (2009) provides a full listing

of the available optical data for this GRB.

As with GRB 080310 and GRB 061121, the effects of absorption from the IGM along the line of sight were considered. With a redshift of $z = 3.355 \pm 0.005$, the UVOT ν - and b -band fluxes were reduced by these effects. The magnitudes by which the data were corrected were 0.2 ± 0.02 and $0.64^{+0.06}_{-0.07}$ for the ν - and b -bands respectively.

Radio data

Also shown in Figure 3.10 are the two radio detections obtained from the VLA at 8.46 GHz (Chandra & Frail, 2008). These observations were taken between three and four days after the initial detection of the burst at high energies.

3.4.2 High-energy model

Figure 3.11 shows the fit obtained to the BAT and XRT data for GRB 080810. The BAT data were difficult to fit, with particular issues arising from the first series of pulses, due to them overlapping with one another. This poses a challenge when trying to disentangle the individual contributions from each pulse.

Details of the ten pulses fitted to the XRT and BAT data are shown in Table 3.5, in which the peak times, durations and spectral parameters are shown. Each of these pulses were fitted with a Band function, but the high-energy spectral index was set to a large value, which resulted in an exponential cut-off power-law above E_{pk} .

As suggested by a reduced χ^2 value of 3.22 for 327 degrees of freedom, there are regions where this fit is unsatisfactory. The collection of the first three pulses is perhaps the largest single contribution to the value of χ^2 . Other contributions include the fourth, fifth and sixth pulse in the hardest BAT channel (and slightly the fourth in the 50–100 keV band) and the decay of the eighth pulse which peaks at 104 seconds.

The afterglow was also fitted to the late-time XRT data. Whilst the obtained models fit the observed data well, the gaps in coverage due to the orbit of *Swift* are at times which would significantly improve the constraints on the afterglow parameters. In particular the gap between the first and second orbit of XRT data appears to occur over the time in which the

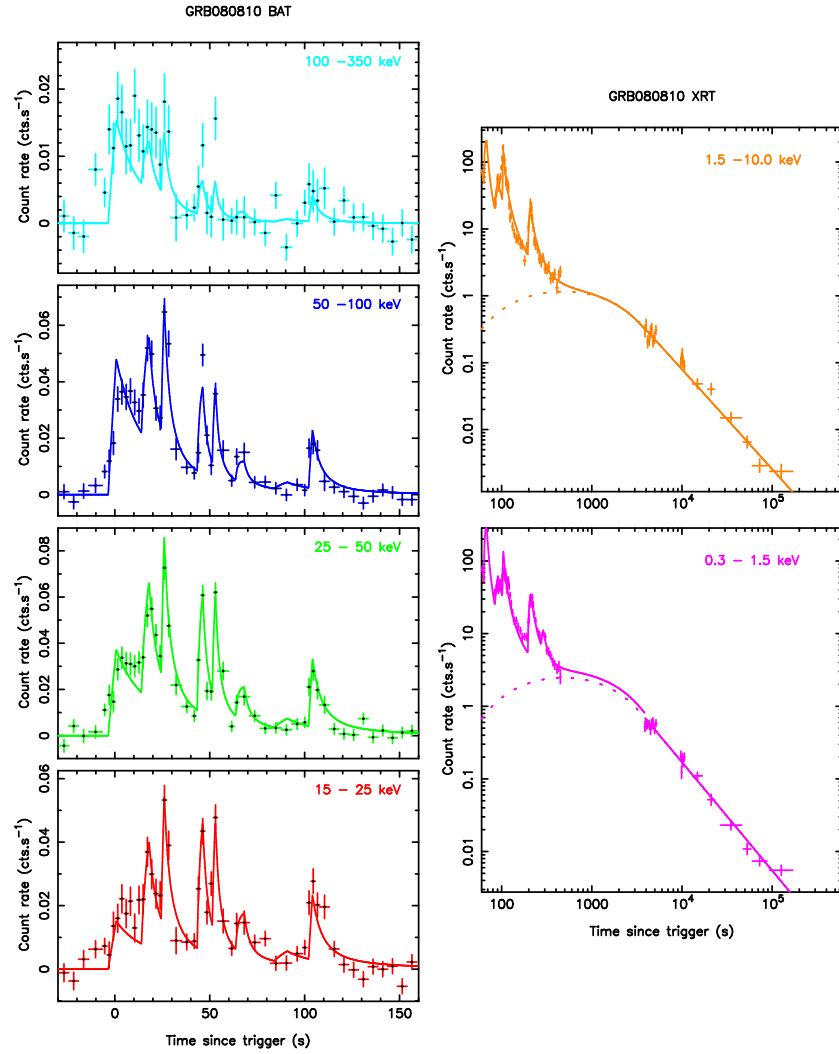


Figure 3.11: BAT and XRT data, showing the fitted BAT and XRT data for GRB 080810, showing the fitted Willingale et al. (2010) model. Left panels: BAT bands (Top to bottom: 100–350 keV, 50–100 keV, 25–50 keV & 15–25 keV). Right panels: XRT bands (Top: XRT hard-band, bottom: XRT soft-band). Solid lines show the total fit (pulses and afterglow), whilst dashed lines show only the afterglow component to the fit. This fit has a reduced $\chi^2 = 3.22$ for 327 degrees of freedom.

morphological afterglow model peaks and transitions to the power-law decay. The properties obtained for this afterglow are shown in Table 3.6, unlike in the case of GRB 061121, there was no late-time temporal break identified in this GRB.

3.4.3 Extending to low energies

Figure 3.12 shows the model obtained in the optical and radio bands when extrapolating the high-energy spectra of each pulse and the afterglow model to the optical and radio bands. As with GRB 061121, both the pulses and the afterglow are over-predicted by the model, meaning

Table 3.5: Parameters of the prompt pulses identified in the BAT and XRT light curves of GRB 080810. These include the peak time (T_{pk}), peak energy at this time (E_{pk}), the rise time (T_{rise}) and arrival time of the last photon (T_f) for each pulse.

Pulse	T_{pk} (s)	E_{pk} (keV)	T_{rise} (s)	T_f (s)	b_1
1	0.7	200	4.2	26.7	0.60
2	18.0	200	4.0	10.0	-0.23
3	26.0	200	1.6	7.0	-0.22
4	46.3	200	2.9	7.0	-0.55
5	53.0	200	1.6	5.8	-0.50
6	68.2	200	4.5	7.9	-0.75
7	90.9	200	6.8	37.9	-0.59
8	104.2	200	2.0	12.0	-0.32
9	210.0	200	15.0	58.9	-0.98
10	290.8	200	18.2	100.0	-2.63

Table 3.6: Parameters of the high-energy fitted afterglow for GRB 080810. The first column denotes the parameter, whilst the second shows the value obtained. The characteristic time T_r is in units of seconds, whilst the normalisation F_m is in units of $\text{keV.cm}^{-2}.\text{s}^{-1}$.

Parameter	Value
b_a	$-1.19^{+0.12}_{-0.26}$
T_r	100.0
T_a	3454.0^{+625}_{-533}
F_m	$8.95^{+1.26}_{-1.27} \times 10^{-2}$
α_a	$1.50^{+0.09}_{-0.07}$

that a low-energy spectral break is required in all components of the fit.

Unlike GRB 061121, there is a richer data set for the optical afterglow, and the associated errors with even the late-time data are small. As such, the data should allow for accurate values of the parameters to be determined, but also the small measurement errors of the optical magnitudes require a good fit to each to ensure a small value of fit statistic.

From the smooth shape of the optical light curve, initial attempts were made to fit the entire light curve with an afterglow. Again this was conducted independently of the high-energy fit. The removal of prompt optical contributions was achieved by invoking self-absorption for all pulses, with $\nu_a = 0.3$ keV, as defined at T_{pk} . As with GRB 061121, a cooling break was introduced to the afterglow spectrum. This provided two alternative fits, again dependent on

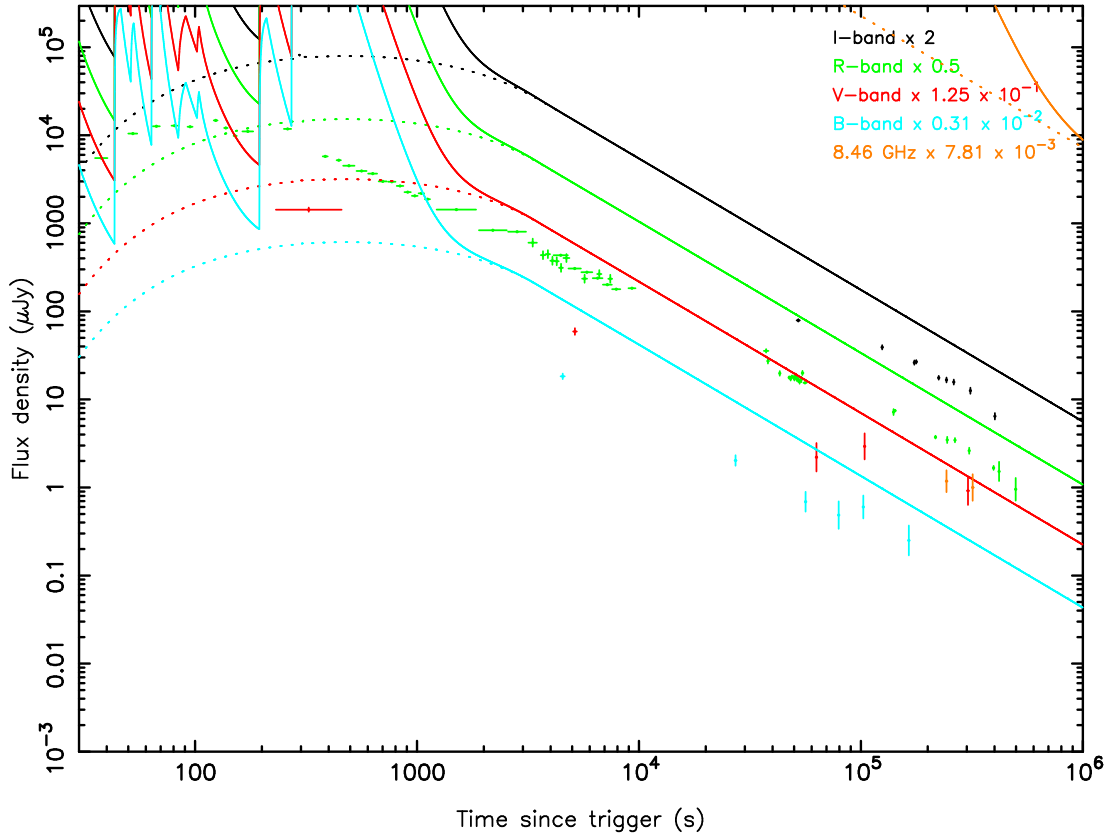


Figure 3.12: Optical light curves for GRB 080810 obtained by extending the high-energy fit to the prompt pulse and afterglow component described in §3.4.2. The dashed lines show the afterglow component to the extrapolation for each band. Note that there are two radio data points at approximately 2×10^5 seconds, appearing amongst the v -band data.

the nature of the surrounding circumburst medium. The ISM and wind-like density profile fits are shown in Figures 3.13 and 3.14 respectively, with the associated afterglow parameters and error estimates being described in Table 3.7.

The reduced χ^2 values for these fits are both reasonably high, at 18.65 and 14.21 for the ISM and wind-like fits (both with 76 degrees of freedom). These values only encompass the low-energy data and are dominated by the poor fit to the radio points. Removing the two radio points significantly improves the statistical quality of the fit, however, the optical data have small errors, and so the value remains higher than the quality of the fit might suggest by eye. The radio data could be reconciled with the model by introducing a self-absorption break to the afterglow spectrum. This has not been done due to the small number of data points which would benefit from this additional feature.

From the fit obtained, it is clear that the optical data shown for GRB 080810 can be well

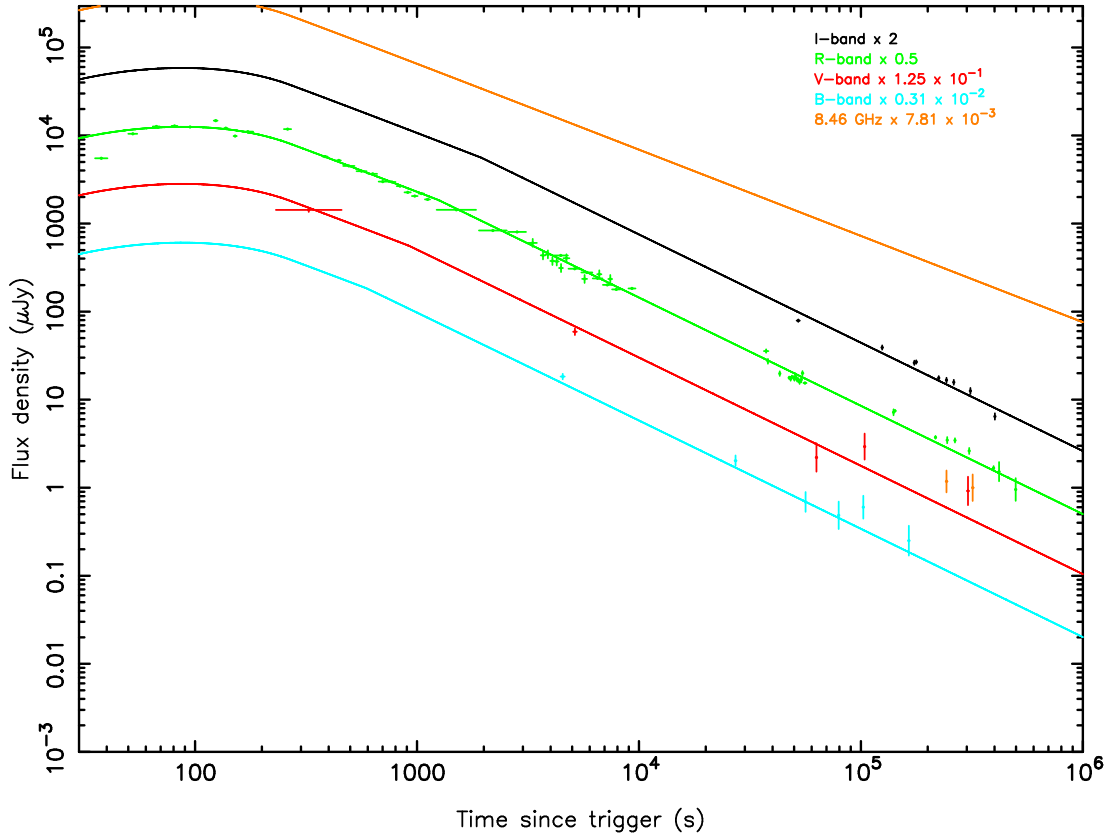


Figure 3.13: Fitted optical afterglow light curves of GRB 080810. All pulses are self-absorbed and the external medium is assumed to be constant density (ISM). Reduced $\chi^2 = 18.65$ for 76 degrees of freedom (including optical data only).

Table 3.7: Parameters of the optical fitted afterglow models for GRB 080810. The first column denotes the parameter, whilst the second and third show the value obtained in the ISM and wind-like density profile fits respectively. The characteristic times T_r and T_a are in units of seconds, whilst the normalisation F_m is in units of $\text{keV.cm}^{-2}.\text{s}^{-1}$. E_{ag} is in units of keV.

Parameter	ISM value	Wind-like value
b_a	-1.19	-1.19
T_r	$12.9^{+22.4}_{-12.9}$	$58.7^{+15.3}_{-26.5}$
T_a	$269.5^{+121.9}_{-158.6}$	$309.1^{+170.4}_{-81.9}$
F_m	$0.15^{+0.05}_{-0.07}$	$0.10^{+0.08}_{-0.10}$
α_a	$1.23^{+0.04}_{-0.05}$	$0.95^{+0.02}_{-0.02}$
p_{ag}	-0.687	-0.687
E_{ag}	$4.19^{+1.88}_{-1.78} \times 10^{-3}$	$5.46^{+19.11}_{-1.93} \times 10^{-3}$
d_{ag}	0.5	-0.5

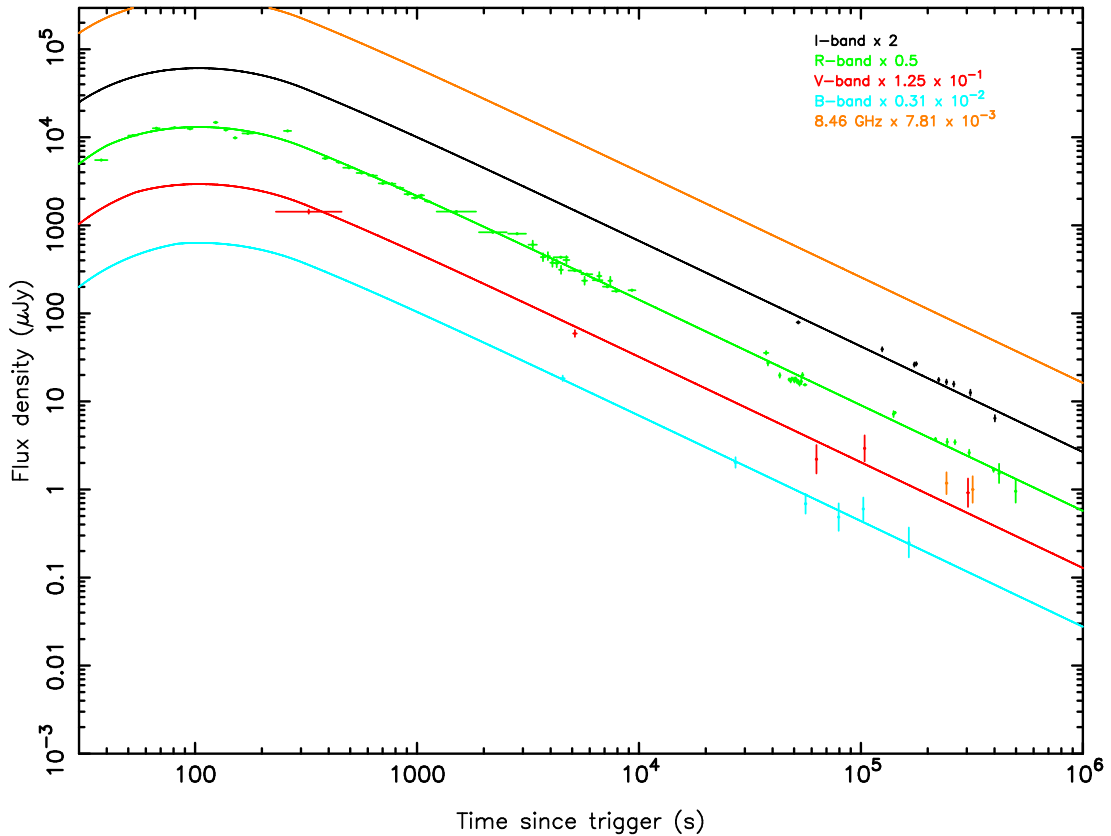


Figure 3.14: Fitted optical afterglow light curves of GRB 080810. All pulses are self-absorbed and the external medium is assumed to be wind-like. Reduced $\chi^2 = 14.21$ for 76 degrees of freedom (including optical data only).

represented by only an afterglow component. As with GRB 061121, however, this optical afterglow fit is incompatible with that used to represent the XRT data. Whilst there remains some uncertainty in the exact morphology of the X-ray light curve due to the gap in *Swift* coverage between the first two orbits, the characteristic times used to fit the optical data are unable to also fit the X-rays.

Once more, this fit offers further clarification that self-absorption is an important process in the prompt emission of GRBs, as it is used to suppress the prompt pulses at optical wavelengths. By taking the value of $\nu_{a,obs} = 0.3$ keV as an upper limit on the permissible range of self-absorption frequencies, upper limits on the magnetic field strength and electron population densities were derived for each pulse. These are shown in Table 3.8.

Unlike most of the pulses in GRB 061121, the magnetic field strengths derived for GRB 080810 are largely consistent with expectation. Again, typical values of bulk Lorentz factor and emission radius have been assumed (see §3.3.3). The values for the magnetic field strength and the

Table 3.8: Physical properties of the prompt pulses for GRB 080810. The columns denotes the pulse number, observed self-absorption break energy, magnetic field strength, electron number density and pulse isotropic energy respectively.

Pulse	$\nu_{a,obs}$ (keV)	B (G)	n_e (cm ⁻³)	E_{iso} (ergs)
1	0.3	1.96×10^5	6.38×10^8	2.19×10^{53}
2	0.3	29.81	14.69	3.47×10^{52}
3	0.3	21.80	7.86	2.60×10^{52}
4	0.3	1.38	3.16×10^{-2}	2.16×10^{52}
5	0.3	2.54	0.11	1.41×10^{52}
6	0.3	2.40	9.49×10^{-2}	8.91×10^{51}
7	0.3	116.13	222.88	8.09×10^{51}
8	0.3	38.97	25.10	1.80×10^{52}
9	0.3	127.15	267.18	2.66×10^{51}
10	0.3	248.93	1024.03	2.66×10^{50}

number density of electrons are in effect upper limits, as introducing a self-absorption break at higher frequencies would impinge upon the high-energy fit to the BAT and XRT data.

Pulse 1 of GRB 080810 is notably energetic, and appears to have a stronger magnetic field strength (and therefore electron number density). It can be seen in Table 3.5 that this pulse has a hard spectrum ($b_1 = 0.60$), which leads to both the high isotropic energy and lower flux at $\nu_{a,obs}$. It is the latter which increases the magnetic field strength, as shown in Equation 2.7. From the same Equation, it can be seen that should the radius at which shells collide to produce pulse 1 occur between a factor of two or an order of magnitude closer to the centre of the explosion, B could be brought into line with the expected range shown in Bošnjak et al. (2009).

Additional information was available for the afterglow of GRB 080810. Page et al. (2009) provide an estimate of the isotropic energy of the afterglow of 1.6×10^{52} ergs. A caveat must be noted at this point, however, that this estimate is based upon the morphology of the X-ray afterglow, rather than the optical model. From this, and Equations 2.6, 2.4 and 2.5 it was possible to estimate the initial bulk Lorentz factor of the flow at the onset of the afterglow. Using this value the minimal electron Lorentz factor was also found. These are shown in Table 3.9.

Using γ_m , Γ_{pk} and an upper limit for $\nu_{m,obs}$ as the lowest optical band observed, estimates

Table 3.9: Physical properties of the optical fitted afterglow models for GRB 080810. The first column denotes the property, whilst the second and third show the value obtained in the ISM and wind-like medium fits respectively. The time t_{peak} is expressed in units of seconds, whilst the magnetic field strength is in Gauss. The number density of the electron population is shown in cm^{-3} . p is the power-law index of the electron population distribution $N(E) \propto E^{-p}$. Note that the estimate of n_e for the wind-like environment is valid at time t_{peak} .

Property	ISM value	Wind-like value
p	$2.37^{+0.52}_{-0.24}$	$2.37^{+0.52}_{-0.24}$
t_{peak}	$53.2^{+47.6}_{-30.9}$	$138.1^{+42.1}_{-36.2}$
Γ_0	$549.2^{+213.0}_{-138.0}$	$104.4^{+15.9}_{-13.7}$
Γ_{pk}	$274.6^{+106.5}_{-69.0}$	$52.2^{+8.0}_{-6.9}$
γ_m	$13718.7^{+10626.3}_{-20065.5}$	$2606.8^{+1792.5}_{-3771.6}$
B	$5.97^{+0.17}_{-0.30} \times 10^{-2}$	$1.65^{+0.20}_{-0.42}$
n_e	$3.12^{+1.72}_{-1.13} \times 10^{-5}$	$0.66^{+0.18}_{-0.27}$

of the magnetic field strength for the afterglow at t_{peak} were derived. These were then also used to find the density of the electron population for both the ISM and wind-like circumburst medium models.

To calculate the bulk Lorentz factor for the ISM constant density profile, an estimate of n_e was required. A typical value of $n_e = 1 \text{ cm}^{-3}$ was assumed. This value is not consistent with the later derived n_e , which requires use of Γ_{pk} in its derivation. The two sources of uncertainty in this derivation are the number density and the actual value of $\nu_{m,obs}$. By holding the estimate of $\nu_{m,obs}$ constant and increasing the initial number density to 100 cm^{-3} the results remain inconsistent, with a final value of $n_e = 1.1 \times 10^{-4} \text{ cm}^{-3}$. This suggests that the ISM model isn't the best representation of the afterglow of GRB 080810.

Conversely, by using the bulk Lorentz factor for the wind-like medium, a set of results that are self consistent are obtained, with a value of $n_e = 0.66^{+0.18}_{-0.27}$ being derived. This value is valid at time t_{peak} , as the density profile evolves with radius ($n_e \propto r^{-2}$). The expected values for density are of the order 1 cm^{-3} , and so the wind-like solution appears to agree with the expected nature of the external medium.

Having also set an upper limit on $\nu_{m,obs}$ at t_{peak} it is also possible to consider whether the radio data can be explained simply by them lying below $\nu_{m,obs}$ at the time of observation. From Figure 1.14 it can be seen that the value of $\nu_{m,obs}$ evolves as $t^{-\frac{3}{2}}$, and the value for the

upper limit of $\nu_{m,obs}$ at the epoch of radio observations can be found. This was calculated to be 3.01 GHz at 2.5×10^5 seconds, and so below the radio band in which there was data. As such it is not possible to reconcile the radio data in this manner. The alternative explanation is that a self-absorption break must occur in the afterglow spectrum between the optical and radio bands.

3.5 GRB 081008

3.5.1 Observations

The final burst considered in this Chapter is GRB 081008 (Yuan et al., 2010). A redshift of $z = 1.967$ for this GRB was obtained from VLT Ultraviolet and Visual Echelle Spectrograph (UVES) and FORS2 data (D’Elia et al., 2011). This was achieved by the identification of a damped Lyman- α system and numerous metallic features. The UVOT enhanced XRT position for GRB 081008 was RA(J2000) = $18^{\text{h}}39^{\text{m}}49^{\text{s}}.86$ Dec(J2000) = $-57^{\circ}25' 54''.8$ with an 90% error radius of $1''.4$ (Evans et al., 2008).

High-energy data

BAT first triggered on GRB 081008 at 19:58:09.4 UT on the 8th of October 2008 (Racusin et al., 2008). Figure 3.15 shows the prompt light curve in each of the standard BAT channels as found by BATGRBPRODUCT. As can be seen, there are several episodes of emission detected by BAT. The first lasts for approximately 30 seconds, before a period of quiescence. A further, weaker pulse peaks at 80 seconds before another longer pulse complex. As this decays there are two additional weak pulses which extend the prompt emission duration to approximately 200 seconds. The reported BAT T_{90} for GRB 081008 is 185.5 ± 40.3 (Palmer et al., 2008).

X-ray data

Upon detecting GRB 081008 with the BAT, *Swift* slewed to allow the narrow-field instruments coverage of the source. XRT observations began 87.1 seconds after the BAT trigger time, in WT mode. The XRT refined analysis was conducted with seven orbits of data (Racusin, 2008).

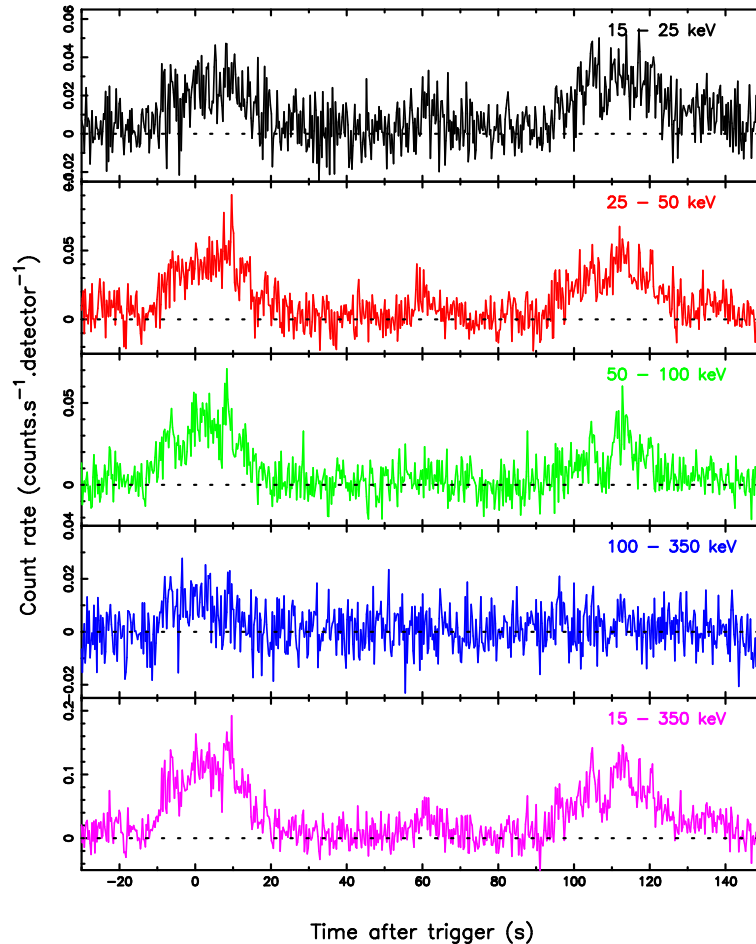


Figure 3.15: *Swift*/BAT light curve of GRB 081008. The light curve is binned with 256 ms temporal resolution, and shows the four standard BAT channels in the four top panels. The bottom panel shows the sum across all four bands.

At this point there was clear, bright structure observed up 200 seconds after the BAT trigger. This then decays, in a manner similar to the RDP, before a further X-ray flare was observed. At the end of this flare, during the transition from the RDP to the plateau phase, the XRT switched from WT mode observations to PC mode.

The X-ray light curve plateaus after the X-ray flare for the remainder of the first orbit. This flatter morphology continues for several orbits before a final, steeper power-law decay begins. These stages are all consistent with the canonical model of Nousek et al. (2006).

Optical and NIR data

Optical data were obtained from the UVOT, ROTSE-IIIc and Gamma-Ray Burst Optical/Near-infrared Detector (GROND; Greiner et al. 2008). The observations from all three of these

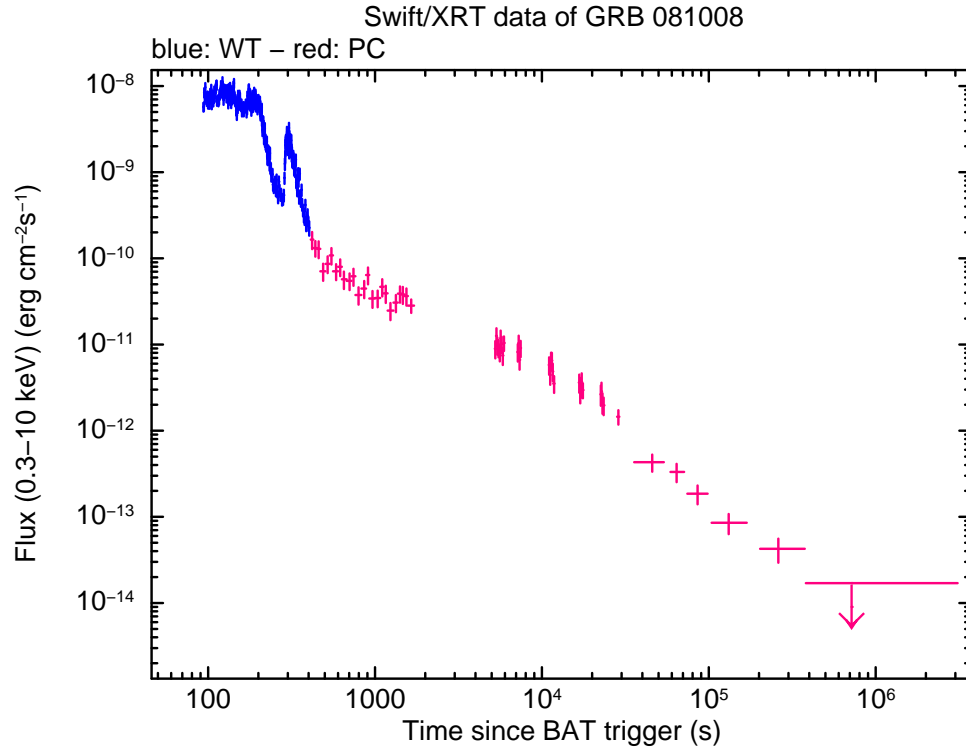


Figure 3.16: *Swift*/XRT light curve for GRB 081008. Blue points are data taken in PC mode, whilst magenta were taken using WT mode.

instruments are shown in Figure 3.10.

UVOT observations began 96 seconds after the initial BAT trigger (Racusin et al., 2008) with an optical counterpart being detected in the *white*, *v*, *b*, *u* and *uvw1* bands. After the initial 10 second *v*-band settling and 150 second *white* exposures were taken, all filters were cycled through, also producing upper limits in the *uvm2* and *uvw2* filters. These upper limits are likely due to the Lyman α break at $z = 1.967$. Further, longer duration, exposures were taken after 5 ks in all filters.

As it was not possible to correct the UVOT *white* band for host extinction, IGM absorption and Galactic extinction, the data were calibrated to the *u*-band for further analysis. Additionally, *white* data after 2×10^5 seconds were removed due to their large errors and possible host contamination. This similar to the approach adopted in Yuan et al. (2010), although the upper temporal limit used in that work was earlier at 90 ks.

ROTSE-IIIc also made observations of the optical transient associated with GRB 081008. These began 41.9 seconds after the BAT trigger time, and continued until 7.5 ks after the prompt emission. The obtained data was unfiltered, but as the ROTSE-IIIc response peaks at

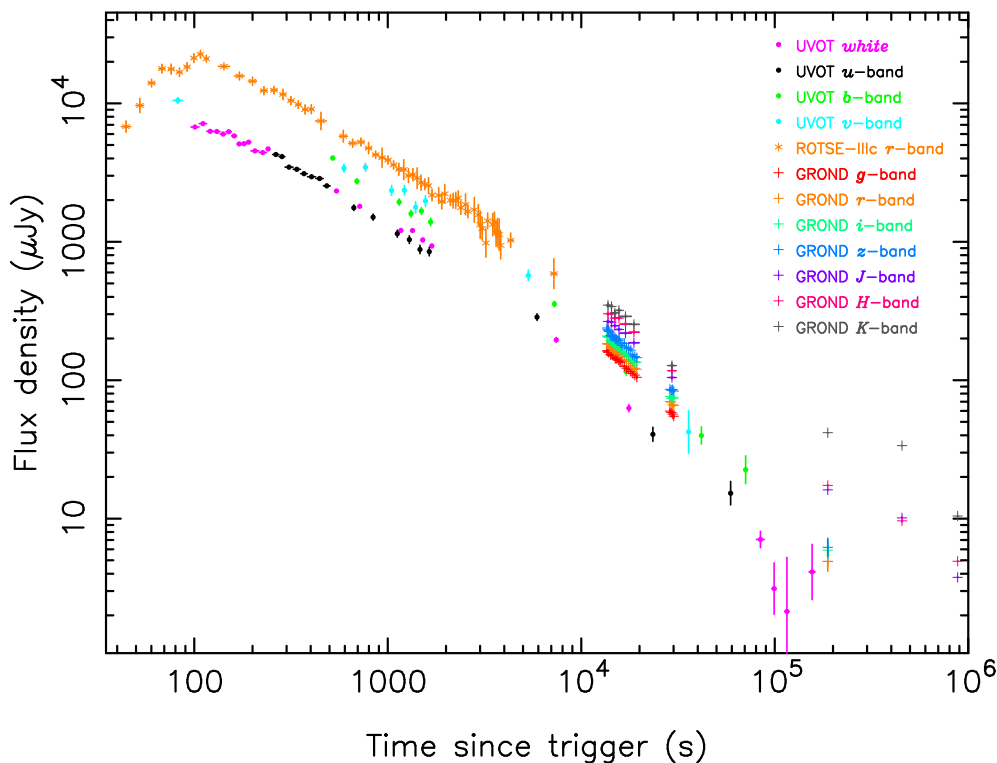


Figure 3.17: Optical data for GRB 081008. Colour coding of the points is described in the key. ROTSE–IIIc data is unfiltered but calibrated to the r -band.

r -band wavelengths, the magnitudes were calibrated to this band.

GROND also observed the source, with optical data in the g , r , i and z bands. The data from these bands were taken simultaneously, providing good coverage across a range of the GRB spectrum. GROND observations began at 13.6 ks after the trigger and continued until 30 ks. A further exposure was taken 2.2 days after the trigger, which despite the late epoch led to detections of the optical transient in all four bands.

At the same time as the optical filters, the J , H and K filters on the NIR arm also took observations each frame lasting 10 seconds. These frames were coadded to produce images of 240, 480, 1,200 and 4,800 seconds. Data reduction was performed using IRAF (Tody, 1993) in a manner like that described in Krühler et al. (2009).

The optical and NIR data were corrected for three effects: host extinction, Galactic extinction and IGM absorption. A value of $E(B - V) = 0.10$ was used for Galactic extinction from Schlegel et al. (1998). The absorption from the IGM was implemented as previously discussed. The host extinction was taken from the model included in the sample of Schady et al. (2012), in which the host is modelled using a Large Magellanic Cloud (LMC) template

where $A_v = 0.29 \pm 0.07$.

3.5.2 High-energy model

An identical methodology to GRB 080310, GRB 061121 and GRB 080810 was adopted to fit the BAT and XRT data available for this burst. First pulses were identified in the BAT and XRT light curves, with T_{pk} and T_0 being identified for each by eye. The remaining parameters not constrained by the physical model were fitted before adding in an afterglow based on the morphology of the late-time XRT afterglow. The parameters of the 12 prompt pulses used to fit both the BAT and XRT data are shown in Table 3.10, whilst the afterglow parameters are shown in Table 3.11.

In the afterglow model used for this burst a late-time temporal break was identified in the X-rays, the details of which are also included in Table 3.11. This remains consistent with the canonical model of Nousek et al. (2006), which includes a late-time break attributed to the increase of the beaming angle of the radiation within the jet. Such jet breaks are thought to be achromatic, implying if this was the source of the break seen in the X-ray light curve, a simultaneous break would be expected in the optical and NIR light curves, too.

The combination of the prompt pulses and the Willingale et al. (2007) afterglow is shown with the BAT and XRT data in Figure 3.18.

3.5.3 Extending to low energies

As with the previous bursts, the first approach adopted was to extrapolate the fitted spectra for each pulse and the afterglow model to the optical and NIR bands in which there were available data. This is illustrated in Figure 3.19. Like the other GRBs, the prompt pulses vastly over-predict the observed flux at lower energies. In this instance, similarly to GRB 061121 and GRB 080810, the afterglow also over-predicts the optical and NIR data. By eye, there is also a suggestion that the morphological shape could be improved at low-energies.

Similarly to the other two bursts in this Chapter, the pulses were first removed from the optical light curves using self-absorption. A spectral break was placed at 0.3 keV for each, when $t = T_{pk}$, with the spectral index $p_a = 2.5$. Table 3.12 shows the physical parameters

Table 3.10: Parameters of the prompt pulses identified in the BAT and XRT light curves of GRB 081008. These include the peak time (T_{pk}), peak energy at this time (E_{pk}), the rise time (T_{rise}) and arrival time of the last photon (T_f) for each pulse.

Pulse	T_{pk} (s)	E_{pk} (keV)	T_{rise} (s)	T_f (s)	b_1
1	1.3	200	10.8	18.7	0.08
2	10.0	200	3.7	12.2	-0.32
3	65.6	200	5.2	25.6	-1.07
4	98.3	200	1.9	16.3	-0.29
5	106.6	200	3.1	7.2	-0.16
6	114.6	200	3.7	8.9	-0.10
7	122.1	200	2.4	21.7	-0.50
8	142.0	200	7.2	22.0	-0.69
9	161.0	200	8.6	60.1	-1.26
10	186.6	200	4.5	6.2	-0.52
11	198.9	200	16.8	46.2	-1.37
12	298.8	200	13.6	87.6	-1.67

Table 3.11: Parameters of the high-energy fitted afterglow for GRB 081008. The first column denotes the parameter, whilst the second shows the value obtained. The characteristic times T_r , T_a and T_b are in units of seconds, whilst the normalization F_m is in units of $\text{keV.cm}^{-2}.\text{s}^{-1}$.

Parameter	Value
b_a	-1.17
T_r	100.0
T_a	2888.0
F_m	3.28×10^{-2}
α_a	1.01
T_b	1.91×10^4
α_b	1.03

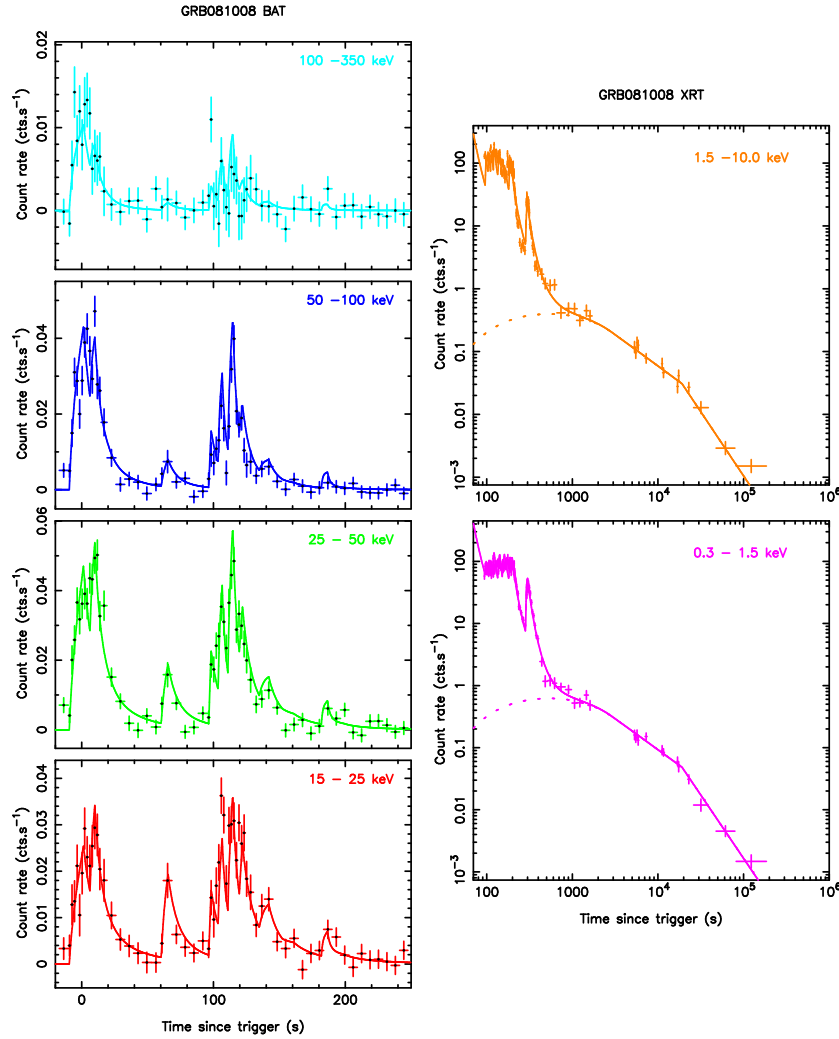


Figure 3.18: BAT and XRT data, showing the fitted BAT and XRT data for GRB 081008, showing the fitted Willingale et al. (2010) model. Left panels: BAT bands (Top to bottom: 100–350 keV, 50–100 keV, 25–50 keV & 15–25 keV). Right panels: XRT bands (Top: XRT hard-band, bottom: XRT soft-band). Solid lines show the total fit (pulses and afterglow), whilst dashed lines show only the afterglow component to the fit. This fit has a reduced $\chi^2 = 4.32$ for 441 degrees of freedom.

derived from such a spectral break for each pulse.

The majority of the pulses identified in the high-energy fit result in reasonable values for the magnetic field strength and electron number density. The main exception is pulse 3, which, as proposed for pulses of other bursts, may be accounted for by being the collision of two shells at a larger radius than that assumed. Similar arguments could also be made for pulses 9, 11 and 12, although they are less discrepant than pulse 3 and could be reconciled with expected values of B by altering the radius by only a factor of two.

The afterglow of GRB 081008 was well covered at late-times with GROND, providing

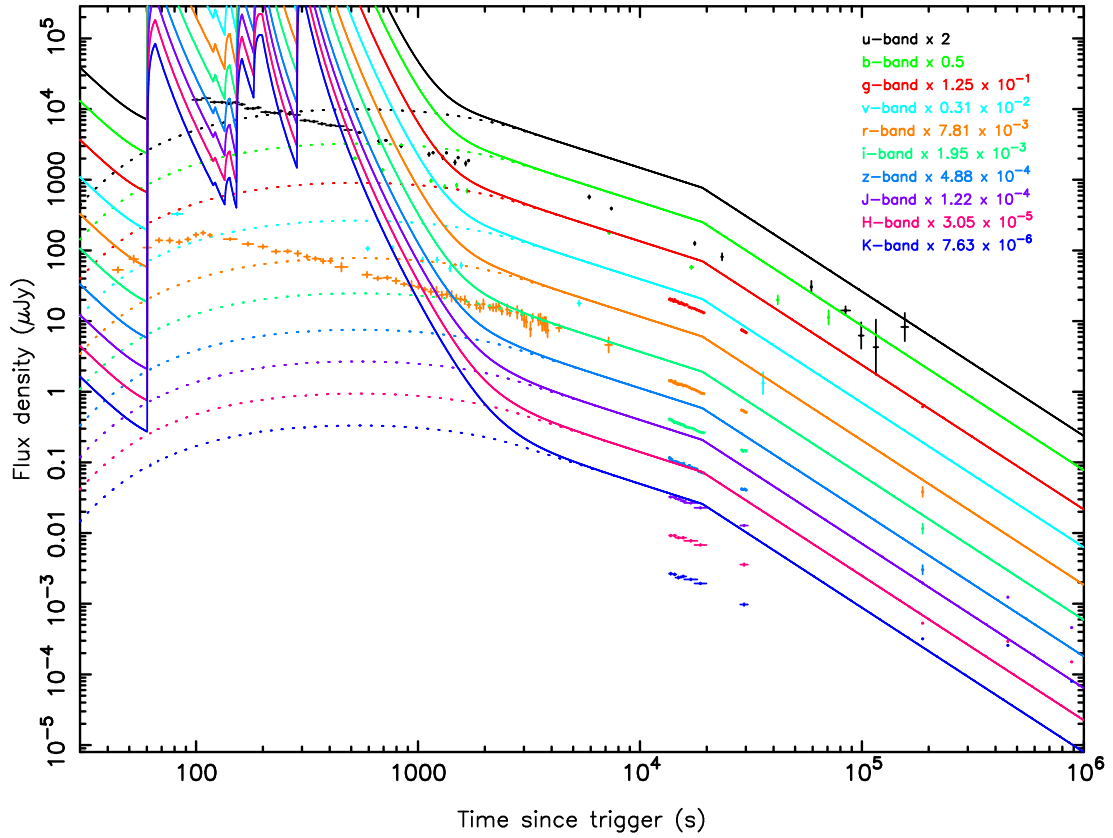


Figure 3.19: Optical light curves for GRB 081008 obtained by extending the high-energy fit to the prompt pulse and afterglow component described in §3.5.2. The dashed lines show the afterglow component to the extrapolation for each band. The UVOT *white* data have been calibrated to the UVOT *u*-band.

Table 3.12: Physical properties of the prompt pulses for GRB 081008. The columns denotes the pulse number, observed self-absorption break energy, magnetic field strength, electron number density and pulse isotropic energy respectively.

Pulse	$\nu_{a,obs}$ (keV)	B (G)	n_e (cm $^{-3}$)	E_{iso} (ergs)
1	0.3	681.75	7680.90	3.99×10^{52}
2	0.3	28.28	13.22	9.51×10^{51}
3	0.3	7.57×10^{-2}	9.47×10^{-5}	1.21×10^{52}
4	0.3	86.25	122.94	6.92×10^{51}
5	0.3	125.68	261.02	7.21×10^{51}
6	0.3	103.32	176.40	1.38×10^{52}
7	0.3	13.94	3.21	7.55×10^{51}
8	0.3	9.06	1.36	4.55×10^{51}
9	0.3	2.38	9.36×10^{-2}	2.66×10^{51}
10	0.3	98.58	106.61	1.32×10^{51}
11	0.3	2.40	9.49×10^{-2}	2.12×10^{51}
12	0.3	3.69	0.23	1.32×10^{51}

Table 3.13: Parameters of the optical fitted afterglow models for GRB 081008. The first column denotes the parameter, whilst the second and third show the value obtained in the ISM and wind-like medium fits respectively. The characteristic times T_r , T_a and T_b are in units of seconds, whilst the normalization F_m is in units of $\text{keV.cm}^{-2}.\text{s}^{-1}$. E_{ag} is in units of keV.

Parameter	ISM value	Wind-like value
b_a	-1.17	-1.17
T_r	75	$78.69^{+11.69}_{-12.47}$
T_a	$51.06^{+56.54}_{-17.08}$	$17.69^{+119.21}_{-17.69}$
F_m	$0.19^{+0.01}_{-0.01}$	$0.23^{+0.16}_{-0.04}$
α_a	$1.25^{+0.01}_{-0.01}$	$0.76^{+0.02}_{-0.02}$
T_b	1.91×10^4	1.91×10^4
α_b	$0.00^{+0.01}_{-0.00}$	$0.00^{+0.01}_{-0.00}$
p_{ag}	-0.67	-0.67
E_{ag}	$5.38^{+14.87}_{-1.67} \times 10^{-2}$	$3.13^{+19.20}_{-0.45} \times 10^{-2}$
d_{ag}	0.5	-0.5

simultaneous coverage in seven optical and NIR filters. Adhering to the same methodology as GRB 061121 and GRB 080810, a cooling break was introduced to the afterglow spectrum at E_{ag} . This led to the values shown in Table 3.13 for a cooling break that evolves according to either an ISM or wind-like external medium. The rise time was determined by eye for the ISM cooling break, and the late-time temporal break, T_b , was retained at the same time as that identified in the high-energy fit. The values of T_a , F_m , α_a , α_b and E_{ag} were then fitted. The ISM and wind-like cooling break models are also plotted in Figures 3.20 and 3.21 respectively.

The fitted models to the optical afterglow both have large values of χ^2 , even though they only include data from the optical light curves. These values result from the poor fit obtained to the ROTSE data, which are under-predicted in both cases. The ROTSE data form a large data set, however they appear discrepant in comparison to the other data. As discussed in §3.5.1, the ROTSE data were unfiltered, and then calibrated to the r band. Yuan et al. (2010) note that the large pixel size of ROTSE ($3''.4$) incurred confusion between the optical transient associated with GRB 081008 and four nearby objects. It was felt that altering the level of the ROTSE flux density to better fit the model was ad hoc, and therefore the flux was left unchanged.

Regardless of the exact level of flux density, the ROTSE data are useful as they show the rise of the optical afterglow at a time when no other observations were taken.

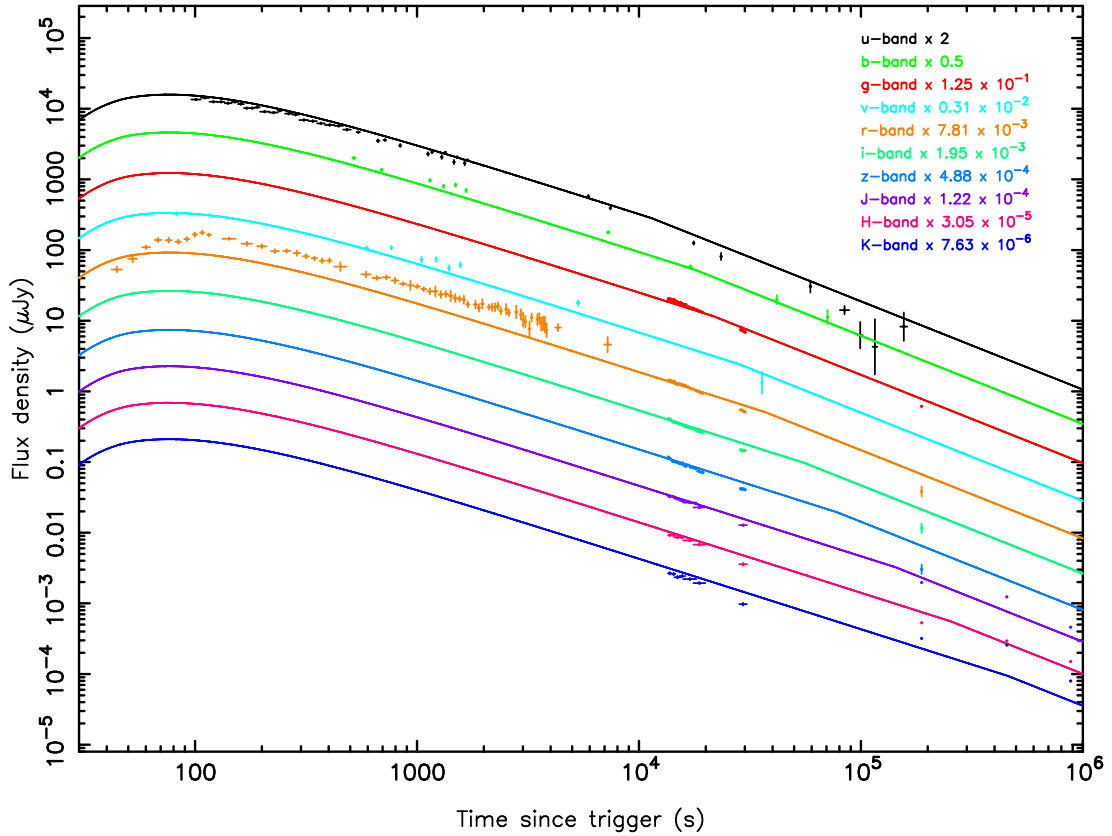


Figure 3.20: Best fit achieved to optical light curves of GRB 081008 evolving the cooling break in an ISM density profile. All pulses are self-absorbed. The value of T_b used is that obtained from the high-energy fit. The reduced $\chi^2 = 22.64$ for 253 degrees of freedom (only including optical data).

As with GRB 061121 and GRB 080810, the difference in time evolution of the afterglow cooling break does not significantly alter the early-time morphology of the light curve. Once more this is because the difference in d_{ag} is compensated for by a change in the temporal index α_a , whilst the characteristic times of the afterglow models remain similar. At later times, though, the cooling break can be seen passing through the optical bands in the ISM density profile model.

A similar fit was also conducted by Yuan et al. (2010), however no cooling break was used in the afterglow spectrum. To allow a full comparison to be made between this Chapter and Yuan et al. (2010), an afterglow was fitted using the morphology of the Yuan et al. (2010) fit, but also introducing a cooling break to the spectrum. The light curves obtained for ISM and wind-like media are shown in Figures 3.22 and 3.23.

Whilst the characteristic times of the Yuan et al. (2010) fit was retained, a slight alteration to their models was made in Figures 3.20 and 3.21. As $F(t) \propto t^{-\alpha} \nu^{-\beta}$, and the spectral

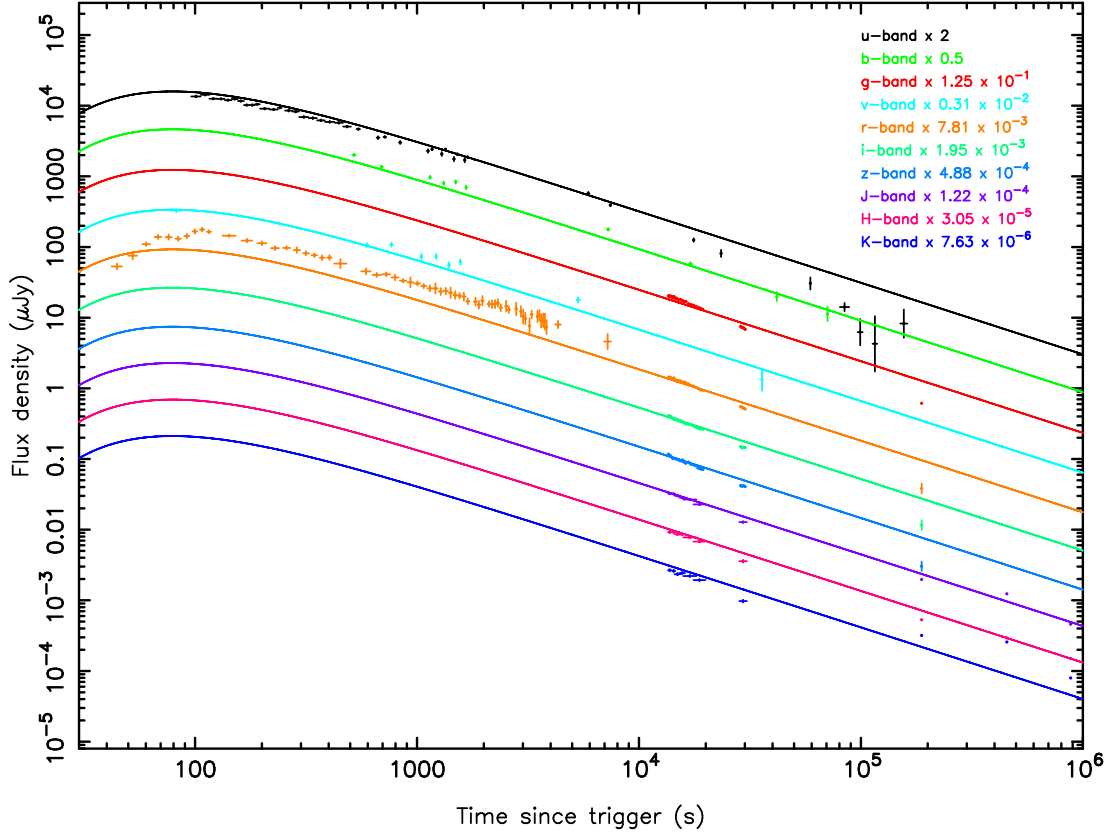


Figure 3.21: Best fit achieved to optical light curves of GRB 081008 evolving the cooling break in a wind-like environment. All pulses are self-absorbed. The value of T_b used is that obtained from the high-energy fit. The reduced $\chi^2 = 25.16$ for 253 degrees of freedom (only including optical data).

Table 3.14: Parameters of the Yuan et al. (2010) optical fitted afterglow for GRB 081008. The first column denotes the parameter and unit, whilst the second shows the value obtained using an ISM density profile. The third column shows the values using a wind-like medium. The characteristic times T_r and T_a are in units of seconds, whilst the normalization F_m is in units of $\text{keV.cm}^{-2}.\text{s}^{-1}$. The values of T_r , T_a , and T_b were fixed to the those obtained by Yuan et al. (2010). b_a was taken from the high-energy afterglow fit, p_{ag} and d_{ag} were determined by the nature of the cooling break. α_a , α_b , F_m and E_{ag} were fitted, with the latter being in units of keV.

Parameter	ISM value	Wind-like value
b_a	-1.17	-1.17
T_r	130	130
T_a	136^{+18}_{-18}	136^{+18}_{-18}
F_m	$0.042^{+0.002}_{-0.002}$	$0.053^{+0.427}_{-0.053}$
α_a	$1.15^{+0.01}_{-0.01}$	$0.81^{+0.01}_{-0.01}$
T_b	7834^{+2160}_{-2160}	7834^{+2160}_{-2160}
α_b	$0.00^{+0.01}_{-0.00}$	$0.00^{+0.01}_{-0.00}$
p_{ag}	-0.67	-0.67
E_{ag}	$1.19^{+1.57}_{-1.19} \times 10^{-3}$	$5.56^{+306.4}_{-5.56} \times 10^{-3}$
d_{ag}	0.5	-0.5

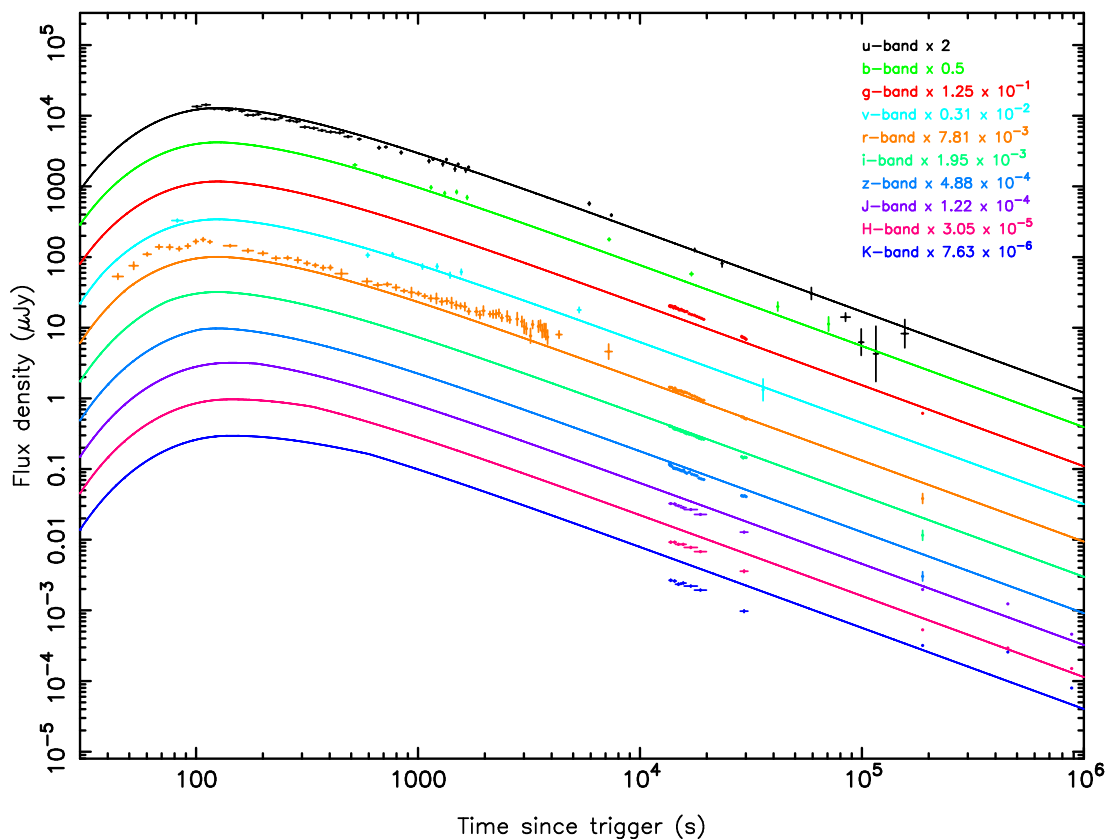


Figure 3.22: Yuan et al. (2010) fit to optical light curves of GRB 081008 assuming an ISM density profile. All pulses are self-absorbed. The reduced $\chi^2 = 38.76$ for 256 degrees of freedom (only including optical data).

index β is affected by the cooling break, the temporal indices α_a and α_b were fitted rather than constrained by the Yuan et al. (2010) values.

The models presented in Figures 3.20 and 3.21 have slightly larger χ^2 values than the corresponding fits obtained by allowing the characteristic times to also be fitted. This is because the models struggle to fit all the data simultaneously using the morphology of the Yuan et al. (2010) afterglow. Using a cooling break which evolves in a constant density profile, the shape of the Yuan et al. (2010) afterglow appears to be satisfactory, particularly when compared to the ROTSE data. However, the GROND data are poorly described at late times, indicating the resulting combination of spectral and temporal index at these times is incorrect. With a wind-like density profile, the shape of the Yuan et al. (2010) fit better describes the early time morphology of the GRB, and the GROND data is modelled approximately as well as in the fit shown in Figure 3.21. The difference in fit statistic is due to the larger average offset between the ROTSE data and the model and similarly the UVOT u -band data and model.

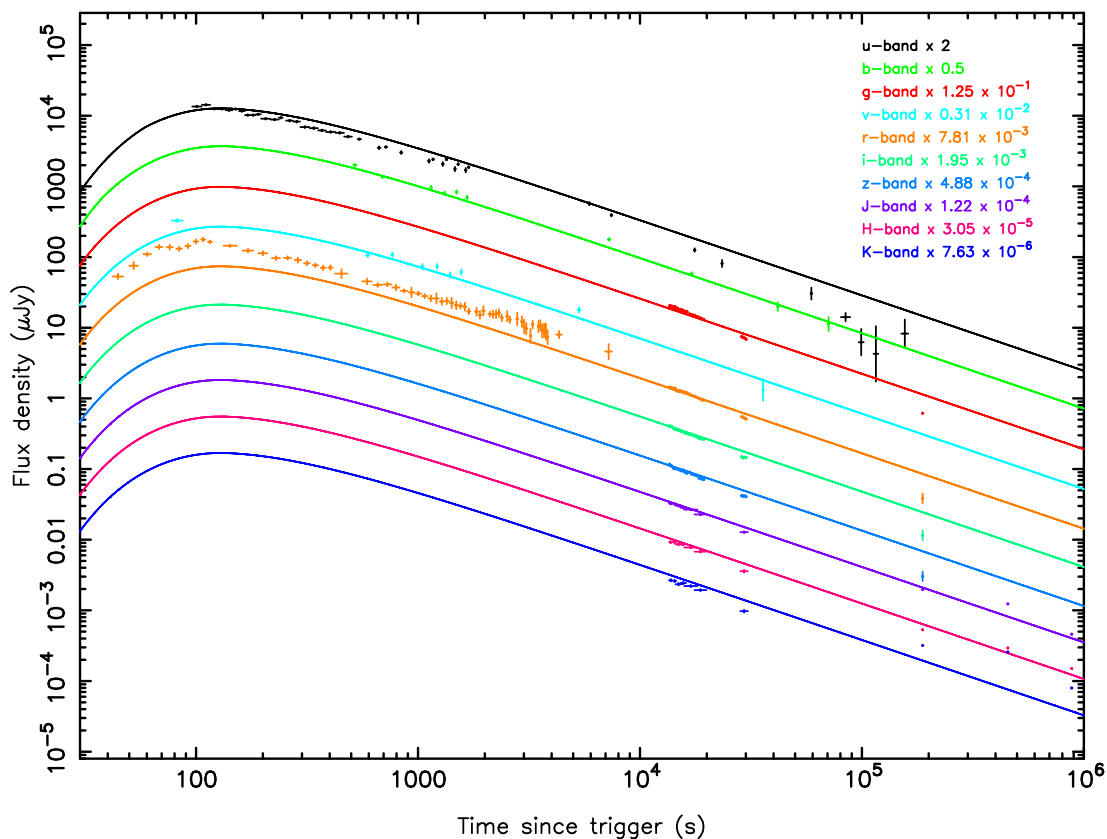


Figure 3.23: Yuan et al. (2010) fit to optical light curves of GRB 081008. All pulses are self-absorbed. The reduced $\chi^2 = 29.43$ for 256 degrees of freedom (only including optical data).

Yuan et al. (2010) fit a late break to the data but at an earlier time to that derived from the X-ray data. For the models in Figures 3.20 and 3.21 the X-ray break time was used due to its potential interpretation as a jet break, which should be achromatic. Applying the break at 7.83 ks in the Yuan et al. (2010) fits resulted in finding the light curve to be consistent with no late time temporal break.

Of the two models based on Yuan et al. (2010), the wind-like medium better represents the overall optical data set. As can be seen in Figure 3.23, the shape of the ROTSE data set is well described throughout all observations. Additionally, the local spectral index of the late-time GROND data appears correct across the seven bands using a cooling break evolving in a wind-like density profile. In the ISM density profile, the cooling break evolves in the opposite sense; $\nu_c \propto t^{-\frac{1}{2}}$ (see Figure 1.14). With this being the case, and the cooling break at T_a located at $1.19_{-1.19}^{+1.57}$ eV, by the epoch of GROND observations the additional spectral break does not affect the model at optical and NIR energies.

3.6 Conclusions

From the subset of GRBs considered in this Chapter it is clear that in every burst a low–energy spectral break must be invoked for almost all of the modelled pulses to avoid an extreme excess in flux at lower–energies. In these instances self–absorption is a suitable mechanism by which the flux can be reduced. Knowing self–absorption to be an appropriate physical model to account for the data allowed the consideration of physical parameters associated with the plasma responsible for the emission.

Whilst for GRB 061121 the exact choice of values of Γ and R may not have resulted in the best estimates of B for several pulses, given the high dependence of the magnetic field strength on these parameters, all but two of the pulses can be reconciled with expectation. The two which remain problematic are those which lead to prompt structure in the optical wavebands, indicating a fundamental difference in their nature when compared to the other modelled pulses. The pulses of GRB 080810 provided more reasonable estimates of the magnetic field strengths and electron population number density as do most modelled in GRB 081008.

With GRB 061121 there is a rare detection of what appears to be a prompt feature at optical wavelengths. Extrapolating the prompt pulses interpreted at high–energies from BAT and XRT it is possible to use the low–energy spectral break of some of the pulses to reproduce a feature at the correct peak time as the optical pulse complex. As discussed in §3.3.3, either the decay tail of the pulse or the peak flux can be fitted. Both cannot be done simultaneously, as the pulse is too narrow. The shape of this decay is due to the tip of the EATS (see Figure 1.12) passing R_f , and therefore less of the surface being within the emitting region. With the EATS being the same for all wavelengths the implications of this are potentially a difference in the emitting region between the optical and high–energy bands. For the rise and peak of the pulse to occur at the same time requires the emitting region to be the same for both energy regimes, which agrees with what should be expected from the GRB.

From calculating the upper limit of the magnetic field strength and also the number density of the electrons in the pulses, it is shown that either the pulses visible in the optical bands have weaker magnetic field strengths (and therefore lower electron densities) or they must occur at smaller radii than those which are suppressed. In reality there is likely to be a combination of

these two effects, and even with these conditions it is difficult to produce values of magnetic field strength that appear reasonable.

With all three bursts detailed in this Chapter, an afterglow of the form outlined in Willingale et al. (2007) was added to the light curve and fitted the data to a reasonable degree. To perform such a fit, several steps are necessary. Unlike in GRB 080310, the level of flux density is over-predicted in the optical bands if the Band function fit to the afterglow is extrapolated. Instead, an additional spectral break is required, and is implemented in a similar manner to the prompt pulses. This break was modelled using the expected behaviour of a cooling break as shown in Granot & Sari (2002). Knowing the change in spectral index for the cooling break allowed the energy at which it occurred to be fitted. In the cases of GRB 080810 and GRB 081008 only an afterglow component was required to fit the light curve, and a wind-like density profile appeared to provide the best fit to both afterglows.

Despite being able to implement a fit to the optical and NIR light curve the morphology in these bands is significantly different to the XRT fit. In Chapter 2, if the model presented in Willingale et al. (2007) was adhered to, the only necessary change was to the temporal index α_a governing the rate of the power-law decay. The sharp rise in this case was accounted for by the prompt pulses being present in the light curve. In this Chapter the optical light curves of GRB 080810 and GRB 081008 are such that prompt pulses cannot account for the observed morphology.

Despite the change in afterglow morphology, that the high-energy spectra can be modified with a cooling break suggests the high and low-energy emission originate from the same population of electrons. Further consideration of the physical parameters underlying the optical afterglow of GRB 080810 suggest that the favoured model has a wind-like external medium, as the obtained number density is most consistent with the initial assumptions used to derive the bulk Lorentz factor.

GRB 081008 also seems best fitted by introducing a cooling break which evolves as though through a wind-like density profile to the Yuan et al. (2010) fit for the afterglow. Unfortunately, the data reduction and subsequent calibration of the ROTSE data are both subject to confusion with nearby sources, which is suspected to be responsible for the offset between the model and

data. However, the morphology of this early-time data, and both morphology and flux density of the late-time data support such a model.

For the three bursts considered in this Chapter, the optical light curves appear to rise and peak earlier than their high-energy counterparts. Whilst the typical values of T_a occur at a couple of kiloseconds after the trigger, when determined by the optical data this value is approximately an order of magnitude smaller. These difference between optical and high-energy afterglows imply that either they are the result of two different jets, or that they are from separate parts of the same jet which are significantly different from one another.

Alongside the changes in the times T_r and T_a , and the decay index α_a , the break time as identified at high-energies is found at different times in the optical and NIR. In GRB 061121 the break is far later in the optical, although the data constraining this are poor, whilst in GRB 081008 the break occurs at only 7.8 ks. Such behaviour discourages the identification of late-time breaks in the X-ray afterglow as jet-breaks which should be achromatic.

GRB 080810 also had radio data available. Such data drastically increases the spectral range over which this afterglow model can be applied. From Figures 3.13 and 3.14 it is clear that the radio data are not well represented by the model with either form of cooling break. By calculating $\nu_{m,obs}$ at the time of these radio observations it was shown that they cannot be explained by the 8.46 GHz band lying below the emission from the minimal electron of the population. Instead self-absorption is a likely candidate once more to reduce the model flux.

To make use of any such radio observations they must be made over a broad range of time and have contemporaneous data across a similarly broad range of bands at intervening energies between the radio and X-ray bands. Unfortunately for GRB 080810 there are only 2 data points available at late times.

The sort of data required to most accurately define the afterglow spectral break is perhaps exemplified in GRB 081008. Using the GROND data available between 1×10^4 and 3×10^4 seconds, which consist of seven bands with simultaneous coverage, it has been possible to ascertain which density profile better represents the data. A single radio upper limit was obtained by ATCA, which does not allow the determination of whether the radio data are fitted by extrapolating any of the modelled spectra for GRB 081008.

One enduring result of this work is that the optical and high-energy light curves often appear independent of one another. The long term aim from this study is to modify the Willingale et al. (2007) model in a way that accounts for the difference between optical and X-ray afterglows. Such a task requires a similar treatment on a larger sample of bursts, all of which require good coverage across a broad spectral range.

Finally, the radio observations cannot be explained by the band lying below the emission from the minimal electron of the population, instead self-absorption is a likely candidate once more to reduce the model flux.

4

Simulations of bright *Swift*–BAT GRBs

4.1 Chapter overview

In this Chapter a bright subsample of GRBs observed with measured redshifts is isolated. By preserving the rest frame characteristics of each burst, the sample is simulated at a variety of redshifts to investigate the observed evolution in the characteristics of their prompt high-energy light curves.

This Chapter begins by giving some background context to the work, before describing the data used and the two methods by which it was simulated. In section §4.6 the relative merits of each simulation method are briefly discussed, before selecting one for detailed analysis. In this analysis T_{90}^* is first used to study the change in morphology of each of the bright bursts as they are simulated at progressively higher redshifts. Then some of the more notable trends in this evolution are discussed.

To produce a fuller picture of the evolution of the high-energy emission with redshift, the evolution of the hardness ratio for each burst is investigated. This is then combined with the duration of each burst to see the evolution of the bright subset in hardness–duration space.

Also considered is whether there are more suitable duration measures that can be employed to characterise the prompt emission of a burst. In §4.6.8 attempts are made to relate the maximum simulated redshift at which a GRB is detected to an intrinsic property of the brightest observed emission from that burst.

4.2 The *Swift* T_{90} distribution

Plotted in Figure 4.1 is the distribution of the 203 GRBs detected by *Swift* since launch that occurred prior to the 15th of July 2012 and have a measure of redshift (either from emission lines, absorption lines or a photometric redshift). These durations are plotted as a function of the redshift that was determined in each instance.

Figure 4.1 shows the geometric average of burst duration as a function of redshift. The geometric RMS scatter is large, and the corresponding evolution in duration has no clear trend. The values can be seen to increase slightly over almost the entire redshift range of the observed population. Whilst this could be argued to be consistent with time dilation, it could be also argued that the data is equally representative of a flat distribution. The calculated means do not include short GRBs, as short bursts tend to be observed in the more local Universe. As such they could reduce the averages of the lowest redshift bins in a manner that could be mistaken for time dilation.

The classic definition of a short GRBs is one with $T_{90} < 2$ seconds (Kouveliotou et al., 1993). However, Bromberg et al. (2012) have recently suggested that whilst this definition is valid for the BATSE, the long–short demarcation varies between instrument. Through analysis of the *Swift* population Bromberg et al. (2012) conclude that for bursts detected by BAT the division is at 0.8 seconds. It is this value that is adopted in Figure 4.1.

To place a slightly greater constraint on the data, the standard error for each bin is also shown. By taking the average duration at one of the two central bins of the averaged population, it can be seen that extrapolation both forwards and backwards in redshift suggests that the calculated values coincide with the expectations from cosmological time dilation: that the durations scale by a factor of $1 + z$. The highest redshift bursts, considered in a final bin

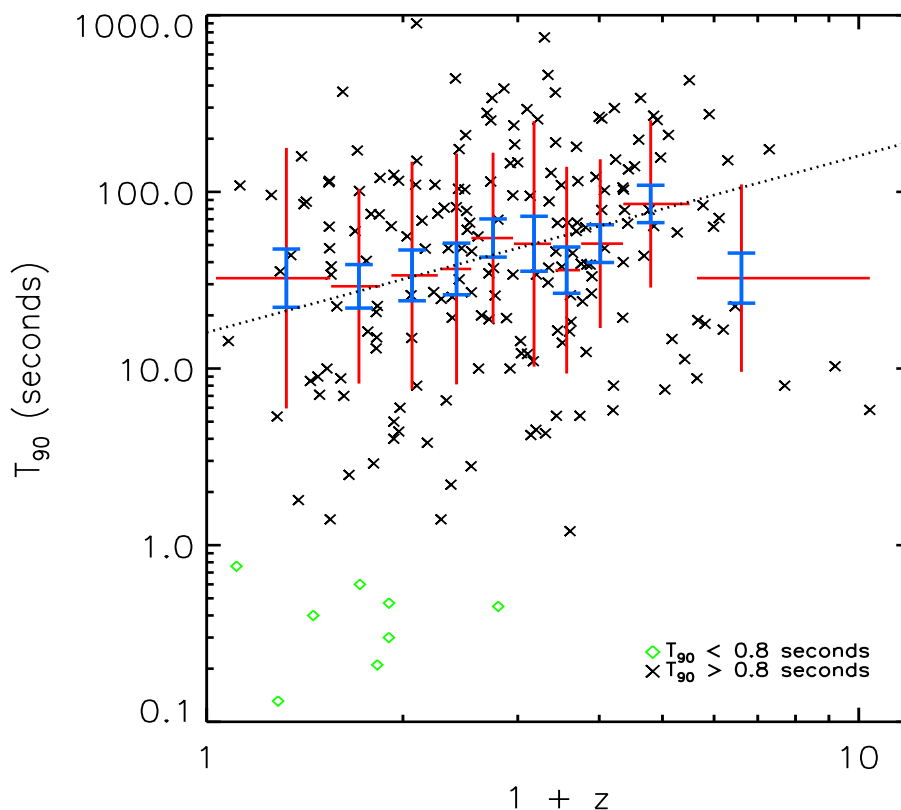


Figure 4.1: The observed distribution of T_{90} for the 203 *Swift* bursts with a redshift estimate prior to the 15th of July 2012. The red crosses show geometric averages of bursts taken with 20 bursts in each bin (except in the final bin which has 14 bursts). The red error bars shown in the vertical direction show the root mean squared (RMS) scatter calculated logarithmically. Also shown are the standard errors on each bin in blue. The dotted black line shows the expected evolution due to time dilation of the average T_{90} value at $z = 1.67$. Short GRBs are denoted by green diamonds.

where $5.65 \leq z \leq 10.4$, do not conform to this trend.

4.3 Previous work

Previous studies have simulated the high-energy prompt light curves of bursts to find whether signatures of time dilation might be detected in properties such as T_{90} (Kocevski & Petrosian, 2011). In this work the authors used prescriptions for the shape and time evolution of GRB spectra to produce light curves representative of those observed by BATSE. The conclusions drawn from these simulations showed that time dilation does not always dominate the measured duration of a burst. In some instances, the duration of a synthetic burst could be seen to

decrease as a function of the simulated redshift. This was thought to be the case particularly when the signal to noise ratio of the burst became poor. The authors also suggested that time dilation might be apparent in GRB temporal profiles that contain narrow pulses separated by periods of quiescence. In such a paradigm, it would be the average duration between peaks that would provide a signature of this time dilation. One limitation to the work presented in Kocevski & Petrosian (2011) is that the simulated light curves all contained only a single FRED pulse. This has several important implications, especially that the effects of evolving different pulses with varying temporal and spectral characteristics within a single prompt light curve could not be investigated. By simulating light curves with multiple pulses, using the two methods outlined, it is hoped this analysis can be performed.

4.4 Observations

BAT data were used in both of the methods of simulation detailed in §4.5. The data used are publicly available and were taken from the UK *Swift* Science Data Centre (UKSSDC; http://www.swift.ac.uk/swift_portal/). For the simulations that used the data directly from BAT, by correcting the measured number of counts as detailed in §4.5.1, the BAT data, auxiliary data and the Tracking and Delay Relay Satellite System (TDRSS) data were downloaded from the UKSSDC for each of the bursts in question. These raw data were processed using the standard *Swift* routine BATGRBPRODUCT.

One of the resulting outputs of BATGRBPRODUCT is a series of light curves taken at multiple temporal resolutions in either one total (15–350 keV) band or the four individual bands as used in typical BAT analysis. An example of the multiple channel light curves is shown in Figure 4.2 where the additional fifth channel is the light curve obtained when the four bands are summed. When performing simulations using the Willingale et al. (2010) pulse method these light curves were used to calculate the typical background noise on each individual channel.

XRT data have not been simulated in this work. However, as discussed below, the second method used to simulate BAT light curves uses methodology of Willingale et al. (2010). In this both the observed BAT and XRT light curves are simultaneously fitted using a combination of

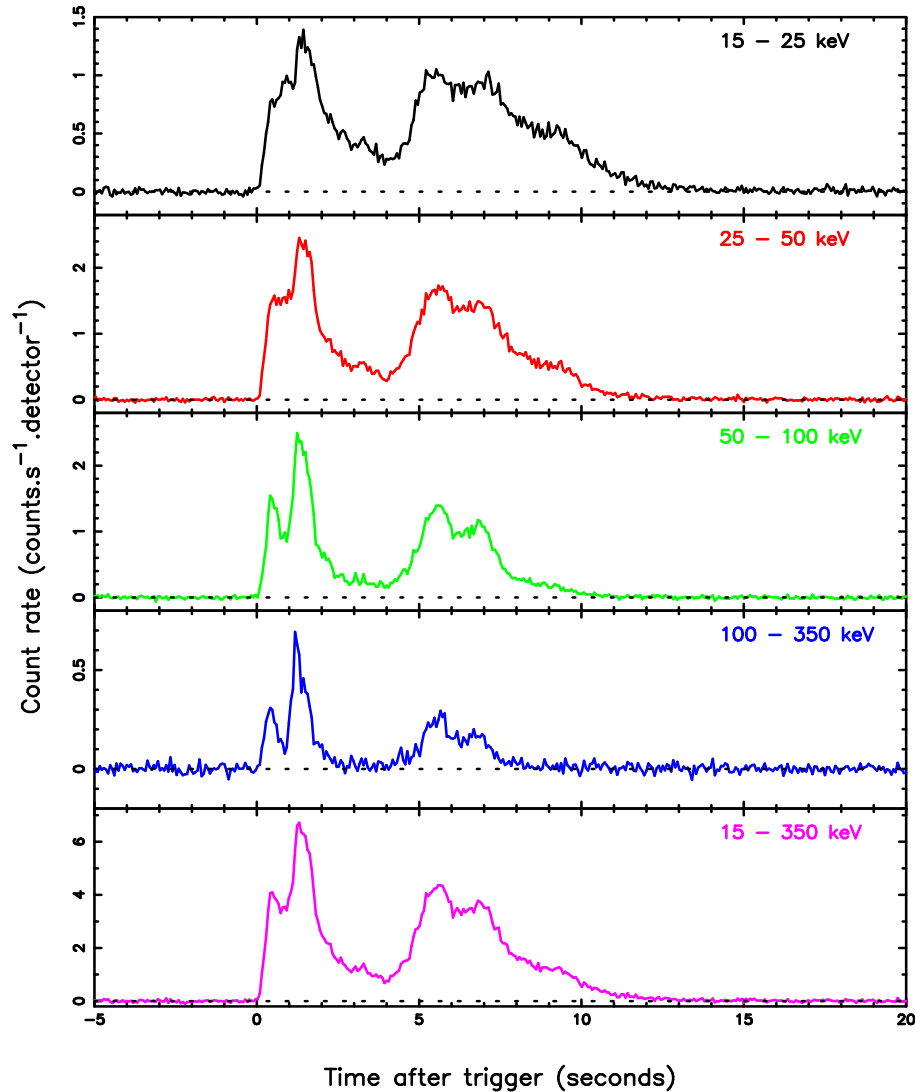


Figure 4.2: High-energy light curves of the bright burst GRB 050525A. The top four panels show the individual BAT channel light curves, in each of the four standard bands. The bottom plot shows the sum of these four across the entire BAT spectral range.

the pulse model proposed in Genet & Granot (2009) and a phenomenological afterglow model (Willingale et al., 2007). Since the work in Willingale et al. (2010) a total of 147 GRBs have been fitted using this model. 20 of these GRBs have either a tentative measurement of redshift, or none at all, and GRB 080413B was removed due to insufficient BAT data. The remaining population of 126 bursts were those from which the bright subset as detailed in §4.6.1 was chosen.

One of the criteria used to determine this sample was the availability of early-time XRT data. The Genet & Granot (2009) model includes spectral evolution, and so being able to fit the RDP, which is not seen in the BAT light curves helps constrain the duration and decay of

all pulses. In some longer duration bursts there is an overlap between the active regions of the BAT light curve and the XRT coverage. In such fortunate instances flares seen in the XRT can be matched to pulses in the γ –ray regime, providing a fuller picture of those pulses.

Because early–time XRT data are required, but an overlap with BAT activity is not, this does not bias the sample towards longer duration GRBs. The speed at which *Swift* slews to allow its narrow–field instruments access to a new GRB is determined solely by observing constraints. These include the proximity of the source to the Sun, Earth or Moon, or whether such a source is occulted by the Earth.

The final criterion used to determine the sample of bursts fitted by the pulse model was the date at which the burst occurred. Only bursts observed by *Swift* prior to the 3rd of May 2011 were included in the sample.

4.5 Modelling

The simulations used in this work were undertaken using two different methods. The first of these took data directly from the BAT instrument and, by sampling the observed spectral range that would fall within the 15–25 keV band if the burst was to occur at the simulated redshift, corrected data taken by the instrument. The second method used the prompt pulse model detailed in Willingale et al. (2010), as fitted to the observed BAT data, and evolved the characteristic times, energies and normalising fluxes that describe each pulse and the accompanying afterglow component. The former method is first described, before discussing the reasons for implementing the alternative and then detailing this in turn.

4.5.1 High redshift simulations made directly from BAT data

To simulate BAT light curves, the event lists were extracted for each burst using BATGRBPRODUCT. The additional required information included the original BAT data for each burst being considered, the BAT Ancillary Response File (ARF), the observed GRB redshift and the redshift at which the burst was to be simulated.

For each simulation there were two redshifts used; that at which the GRB was observed,

z_{obs} , and that at which it was to be simulated, z_{sim} . The final product to be produced was a simulated 15–25 keV observer frame light curve from a GRB located at z_{sim} . To do so, a light curve from the observed BAT data was extracted using the standard BATBINEVT routine. The spectral range over which this light curve was found relied on both z_{obs} and z_{sim} . Defining z_{factor} as shown in Equation 4.1, the observed light curve in the $15z_{factor}$ – $25z_{factor}$ keV range was produced. As part of the BATBINEVT algorithm the produced light curves are background subtracted. This means that, aside from the intrinsic scatter associated with fluctuations in the background, the extracted light curve is dominated by source counts only. This effectively provides the counts which, should the source be moved to z_{sim} , would fall within the observed 15–25 keV band.

$$z_{factor} = \frac{1 + z_{sim}}{1 + z_{obs}}. \quad (4.1)$$

By choosing the two bands such that the same part of the rest frame spectrum would be sampled, the luminosity within the band was considered to be held constant. Additionally, use of the k–correction was not required for the same reason.

The total flux received in the observed band can be related to the number of counts detected using Equation 4.2. This equation takes into account the total number of counts, C , the average energy for each of these counts, \bar{E} , the duration of the bin, ΔT and the effective area of the instrument at this average energy $A(\bar{E})$.

$$F = \frac{C\bar{E}}{A(\bar{E})\Delta T}. \quad (4.2)$$

As it is luminosity that is conserved, the standard relation between luminosity and flux was also used, where D_L is the luminosity distance and L is the luminosity in the rest frame band of the source (Hogg, 1999). As previously mentioned, the k–correction is not included in Equation 4.3 as the energy band at z_{obs} has been chosen to sample same rest frame spectral region as the 15–25 keV band at z_{sim} . To calculate luminosity distances a standard Λ CDM cosmology was assumed with $H_0 = 71 \text{ km.s}^{-1}.\text{Mpc}^{-1}$, $\Omega_m = 0.27$ and $\Omega_\Lambda = 0.73$.

$$L = 4\pi D_L^2 F. \quad (4.3)$$

At the observed redshift, combining Equations 4.2 and 4.3 gives a luminosity of:

$$L = 4\pi D_L (z_{obs})^2 \frac{C_{obs} \bar{E}_{obs}}{A(\bar{E}_{obs}) \Delta T_{obs}}, \quad (4.4)$$

where the quantities with the subscript ‘obs’ denote those observed at redshift z_{obs} . The same Equation can be derived for the simulated redshift, where the average bin duration and energy become $\Delta T_{sim} = \frac{1+z_{sim}}{1+z_{obs}} \Delta T_{obs}$ and $\bar{E}_{sim} = \frac{1+z_{obs}}{1+z_{sim}} \bar{E}_{obs}$, respectively.

Relating C_{sim} to C_{obs} is achieved by equating Equation 4.4 to its equivalent at z_{sim} , which becomes Equation 4.5:

$$C_{sim} = \frac{C_{obs} \bar{E}_{obs}}{A(\bar{E}_{obs}) \Delta T_{obs}} \left(\frac{D_L(z_{obs})}{D_L(z_{sim})} \right)^2 \frac{\Delta T_{sim} A(\bar{E}_{sim})}{\bar{E}_{sim}}. \quad (4.5)$$

This can be simplified to Equation 4.6:

$$C_{sim} = \left(\frac{A(\bar{E}_2)}{A(\bar{E}_1)} \right) \left(\frac{D_L(z_{obs})}{D_L(z_{sim})} \right)^2 \left(\frac{1+z_{sim}}{1+z_{obs}} \right)^2 C_{obs}, \quad (4.6)$$

$$C_{sim} = Q C_{obs}.$$

This effectively leaves a single quantity, Q , by which the observed counts in the $15z_{factor}$ – $25z_{factor}$ light curve at z_{obs} must be altered to calculate the 15–25 keV light curve at z_{sim} . This quantity, Q , now is dependent on four contributions: the change in luminosity distance, the change in BAT sensitivity, the reduction of the average energy per count and the increase in the bin size due to time dilation (the last two each contribution a factor of $\frac{1+z_{sim}}{1+z_{obs}}$ to Equation 4.6).

To illustrate the BAT sensitivity $A(E)$ is shown in Figure 4.3. As can be seen, for higher energies, which would correspond to large shifts in redshift, the integrated effective area is small as BAT becomes less sensitive to these photons.

Due to cosmological time dilation, each bin now has a duration of $64z_{factor}$ ms. As the arrival of each photon is a Poissonian process the extracted $15z_{factor}$ – $25z_{factor}$ light curve was taken and the total number of counts observed in each bin calculated (by correcting for the bin

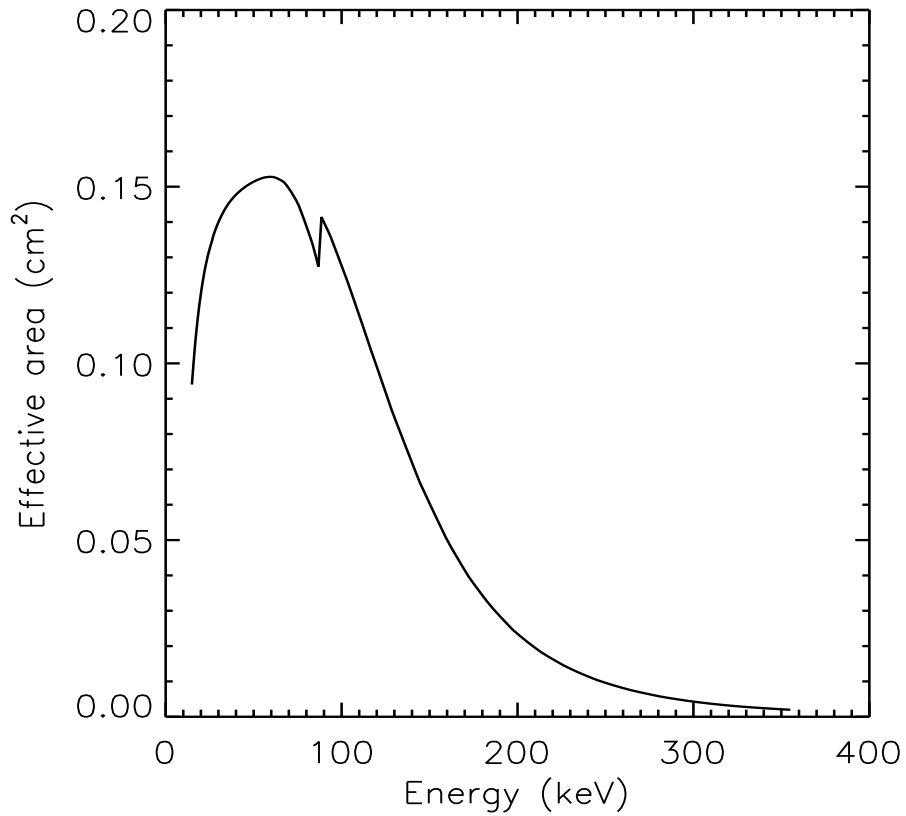


Figure 4.3: The BAT effective area per detector as a function of energy.

size and the number of fully illuminated detectors). A background was also required. To find this the RMS scatter on the light curve was found, and an offset equal to the square of this value was added.

Having the total number of counts, Q was then used to consider whether each would remain in the light curve when the source was moved to z_{sim} . To do so, a random number, R_1 , was generated from a uniform distribution ranging between 0 and 1. The value of Q also took this range, with 1 corresponding to simulating the light curve at the redshift it was observed at. Any count for which $R_1 \leq Q$ was retained in the light curve.

It was at this point the light curve was re-binned to the original 64 ms bin size. To do so, another random number was generated, R_2 . This was again drawn from a uniform distribution, ranging between 0 and 1. This number corresponded to the fraction of bin duration which had elapsed when the count arrived. The time of each event, t_{evt} , is given as expressed in Equation 4.7, where t_{st} is the time at which the bin begins.

$$t_{evt} = z_{factor} (t_{st} + 0.064R_2). \quad (4.7)$$

Knowing a time for each count, the simulated light curve was re-sampled to 64 ms temporal binning, the background offset was removed, and the light curve was returned to units of $\text{counts.s}^{-1}.\text{detector}^{-1}$. This new light curve now contained the correct number of source counts. As the total number of counts were scaled by a factor of Q , the maximum and minimum value of the background also were scaled by the same quantity. This meant the total range in the fluctuations in the new background subtracted light curve was underestimated.

To correct the background the variance on quiescent, non-slew times of both the transformed light curve and the original observed 15–25 keV light curve was calculated. The latter was also extracted from the available BAT data using the `BATBINEVT` routine. These two variances were compared, and the difference found, as shown in Equation 4.8.

$$\sigma_{diff}^2 = \sigma_{obs}^2 - \sigma_{sim}^2. \quad (4.8)$$

A further series of random numbers was then generated. These were taken from a Gaussian distribution, where $\mu = 0$ and $\sigma = \sigma_{diff}$. One random number was drawn per bin in the 64 ms simulated light curve. Each of these random numbers were added to their associated bin to increase the scatter on the simulated light curve to the level as seen in the observed 15–25 keV light curve. Once adding this additional scatter the light curve, the produced light curve contained the correct count rate from both the source and background.

4.5.2 Simulations using the prompt pulse model

The disadvantage to using the BAT data directly was the restriction imposed by the finite spectral range of the BAT. Consequently, $25z_{factor}$ had to be less than 350 keV. Aside from this, the uncertainties due to the shape of the BAT spectral response increased significantly at the upper end of this energy range reducing confidence in the simulations conducted at the highest redshifts.

To maximise the range in redshifts over which simulations could be performed using the

BAT data method, only the single 15–25 keV channel was simulated. Aside from the morphology of bursts in the higher energy BAT bands, this removed information from the simulations, such as spectral parameters including hardness ratios. Additionally, the traditional values of T_{90} considers the full BAT spectral range, as this maximises the number of photons included.

The methodology presented in Willingale et al. (2010), as summarised in Chapter 1, produces the flux light curves of all four BAT and the two XRT channels allowing a more extensive analysis of the high–energy characteristics of the prompt emission. In this Chapter, only simulated light curves in the four BAT channels have been produced. To conduct such simulations the parameters of each prompt pulse, and also the afterglow, needed to be evolved to the values that would be observed by placing the burst progenitor at a higher redshift. From Figure 1.13 of Chapter 1, which is a representation of a single pulse temporal profile, the characteristic times associated with each pulse are highlighted. These include the time over which a pulse rises (T_{rise}), the time at which the pulse peaks T_{pk} and the arrival times of the first and last photons (T_0 and T_f). The values of these at the simulated redshift were calculated using time dilation as shown in Equation 4.9, where T_{sim} and T_{obs} correspond to any of the characteristic timescales at the simulated and observed redshifts respectively.

$$T_{sim} = \left(\frac{1 + z_{sim}}{1 + z_{obs}} \right) T_{obs}. \quad (4.9)$$

In this model, the spectrum of each of the pulses is a time evolving exponentially cut–off power–law. The peak energy of the νF_ν spectrum is defined at the time when the pulse peaks in the light curve of the GRB, T_{pk} . When a pulse is moved to a different redshift, which is higher than that actually observed, time dilation causes T_{pk} to be later. As $E_{pk} \propto t^d$, where $d = -1$, $E_{pk,sim}$ is reduced as a pulse is placed at a higher luminosity distance.

$$E_{pk,sim} = \left(\frac{1 + z_{obs}}{1 + z_{sim}} \right) E_{pk,obs}. \quad (4.10)$$

Finally, each pulse has a normalising flux, which was corrected using Equation 4.11. As the normalisation corresponds to the flux across the entire BAT spectral range as observed by the instrument, the sampled part of the rest frame spectrum changes, therefore, the k–

correction, K , also was accounted for.

$$S_{pk,sim} = \left(\frac{K_{obs}}{K_{sim}} \right) \left(\frac{D_{L,obs}}{D_{L,sim}} \right)^2 S_{pk,obs}. \quad (4.11)$$

For completeness, the afterglow was also included in this model, despite BAT lacking the sensitivity to observe it. The phenomenological model described in Willingale et al. (2007) was used, evolving the temporal parameters (T_a and T_r) using Equation 4.9 and the normalisation using Equation 4.11. In some instances the afterglow contained a late temporal break, with a characteristic time, T_b , which was also dilated using Equation 4.9. The spectral model was not time evolving, so E_{pk} was set to 1000 keV for all simulations.

Once the pulse and afterglow parameters were adjusted, the parameters were processed using the same software that produced the light curves shown in Willingale et al. (2010). This provided smooth 64 ms model light curves that were background subtracted in each of the four BAT bands (light curves were also obtained in the two XRT bands, but these were not retained for later analysis).

These model light curves contained no scatter from either the source or the background, so noise was added in two stages. The first of these was to account for variations in the source photons. To do so, the count rate light curve was converted into counts, then for each bin a Poisson distribution was randomly sampled, using the modelled number of counts as the mean value of the distribution. This random number was then taken to be the new number of counts. After the source noise was added, fluctuations from the background were also required. To find these the observed light curve data from BAT was considered in each of the four bands at the time during which the GRB was defined as active. The RMS value of the errors of all points which had a rate less than 10% that of the peak flux in the light curve was then taken. Such fluxes were considered to be representative of the background only. This average noise was used as σ for a Gaussian distribution which had a mean of zero. Random numbers were drawn from this distribution and added to each bin of the four BAT channels.

4.5.3 Rate Triggering algorithm

The same triggering algorithm was implemented for both simulation methods. An average error on the data points contained within the time range shown in Equation 4.12 was calculated. $T_{start,obs}$ and $T_{stop,obs}$ are the actual start and stop times of the prompt emission, as reported by BAT.

$$\left(\frac{1+z_{sim}}{1+z_{obs}}\right)T_{start,obs} \leq t \leq \left(\frac{1+z_{sim}}{1+z_{obs}}\right)T_{stop,obs}. \quad (4.12)$$

To obtain an estimate of the noise of the prompt light curves, only those bins during the selected time period which had a flux of 10% or less of the maximum flux value in the light curve were chosen. Taking the root mean square (RMS) value of error on these bins, a representative average of the noise in the prompt light curve when dominated by background was calculated. The flux samples were then re-binned to a time scale of 1024 ms and the RMS error adjusted accordingly, which whilst reducing the temporal resolution significantly improved the signal to noise ratio of the data.

Having an estimate of error, the brightest bin in the light curve was then found and divided by the average error as previously determined. This gave a signal to noise ratio of the brightest peak, which was then compared to a threshold of 6.5σ to determine the likelihood of the simulated light curve causing a BAT trigger. This process was repeated for all four individual BAT bands, as well as the total of all four across a 15–350 keV band. Whilst it was possible to consider each energy band independently, it was the significance of the entire BAT spectral range that was used in later analysis to define whether a burst would result in a BAT trigger.

4.5.4 Measuring T_{90}

The light curves simulated directly from BAT data produced files in the standard template used by the BATTBLOCKS routine for calculating T_{90} . BATTBLOCKS uses Bayesian analysis to find robust duration measures (Scargle, 1998) including the time intervals T_{90} , T_{50} and, if required, any duration specified by the user. These correspond to the times taken to cumulate the central 90%, 50% or user defined fraction of the total fluence.

Aside from modifying the values of flux, time and error, key parameters within the data files, such as the start and stop times of the significant proportions of the light curve had to be altered. These were adjusted using the temporal factor shown in Equation 4.9.

Initially, BATTBLOCKS was implemented at a variety of temporal resolutions, starting with the 64 ms light curves that were produced by the simulations, and then binning these to coarser resolutions: 128 ms, 256 ms, 512 ms and 1024 ms. This proved useful, as when the signal became weak, the coarser temporal binning improved the signal to noise ratio, although provided poorer temporal resolution.

The pulse method of simulating bursts did not produce a standard BAT light curve file, and so the results could not be used in conjunction with the BATTBLOCKS routine. An algorithm to calculate T_{90} in a similar manner from a count rate light curve was therefore created. To distinguish between the two measures of T_{90} , this second estimate is hereafter denoted by T_{90}^* .

Using a single channel 15–350 keV light curve, the data were re–binned dynamically. The binning routine took samples and retained all bins that met a minimum signal to noise criterion (in this instance 6.5σ). Those bins which did not meet the criterion were re–sampled at a coarser resolution, and then compared to the same threshold. This process was repeated until either all bins were retained or a maximum bin size of 20 seconds was reached.

This process was used to identify the times during which each GRB was active. The counts over this time were cumulated to find the total fluence. The times at which the cumulated fluence distribution reached 5% and 95% of the total were identified. The difference between these T_5^* and T_{95}^* times was then found, producing T_{90}^* .

The choice of maximum bin size and significance threshold were initially arbitrary, at values of 20 seconds and 6σ respectively, as it was felt these were similar to the typical values that BAT uses for detection. To optimise the routine, it was used on the observed 15–350 keV light curves from BAT, to find the combination of maximum bin size and threshold that were most consistent with those reported from the original BAT observations. A maximum bin size of 20 seconds and a threshold of 6.5σ yielded the best results, which are shown in Figure 4.4. Included in the figure are all bursts that have been fitted with the prompt pulse model, and have both measures of duration across the 15–350 keV range.

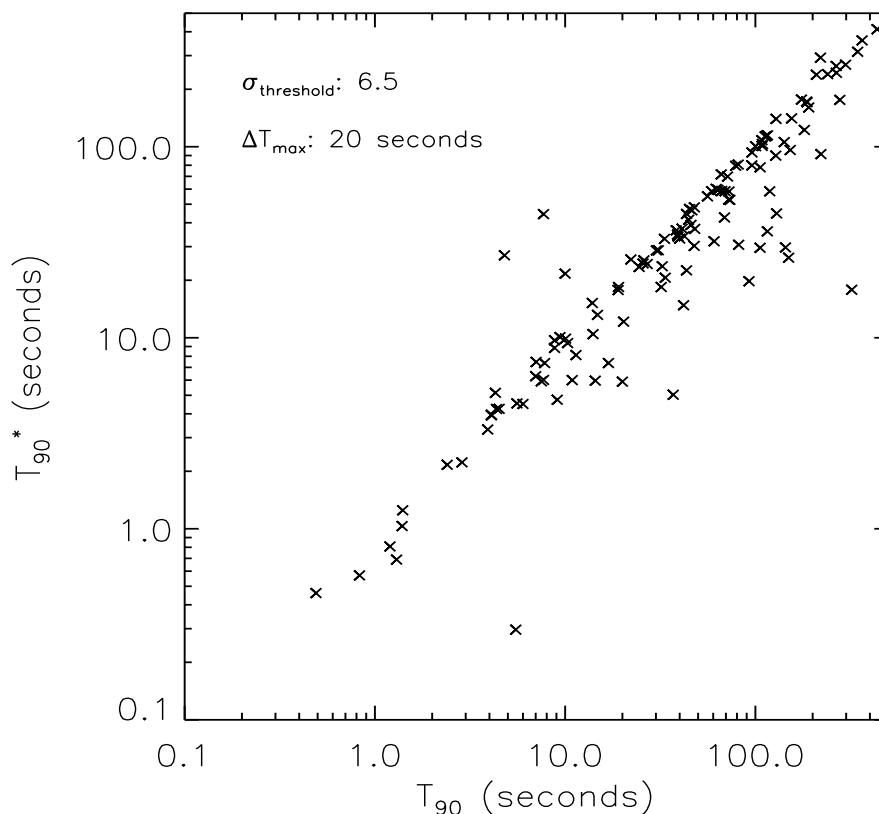


Figure 4.4: Comparison of measured T_{90} of observed BAT light curves in the 15–350 keV spectral range. In this figure the value calculated using the dynamic binning routine developed in this work (T_{90}^*) is plotted as a function of the T_{90} calculated in the standard BAT processing. $\sigma_{threshold}$ is the signal to noise ratio threshold used in the dynamic binning routine, whilst ΔT_{max} is the maximum bin size used.

To identify those burst for which T_{90} and T_{90}^* were discrepant, the ratio of the two were taken and plotted as a function of the average significance of all the bins identified in the T_{90}^* routine. Figure 4.5 shows that those bursts which are not consistent tend to be fainter and have a lower average significance of the source flux observed. Furthermore, for the majority of discrepancies T_{90}^* is smaller than T_{90} as obtained from BATTBLOCKS. It was found that these bursts differed in the identification of T_{95} , namely the end of the T_{90} period. In these instances the bursts ended with a long-lived slowly-decaying feature, such as a FRED pulse or a potential extended emission component. For these bursts, the T_{90}^* was more strict when identifying source emission. Attempts to alter this were made by changing the significance threshold for the dynamic binning, however it was found this led to more bursts for which the T_{90}^* varied notably from the BATTBLOCKS value.

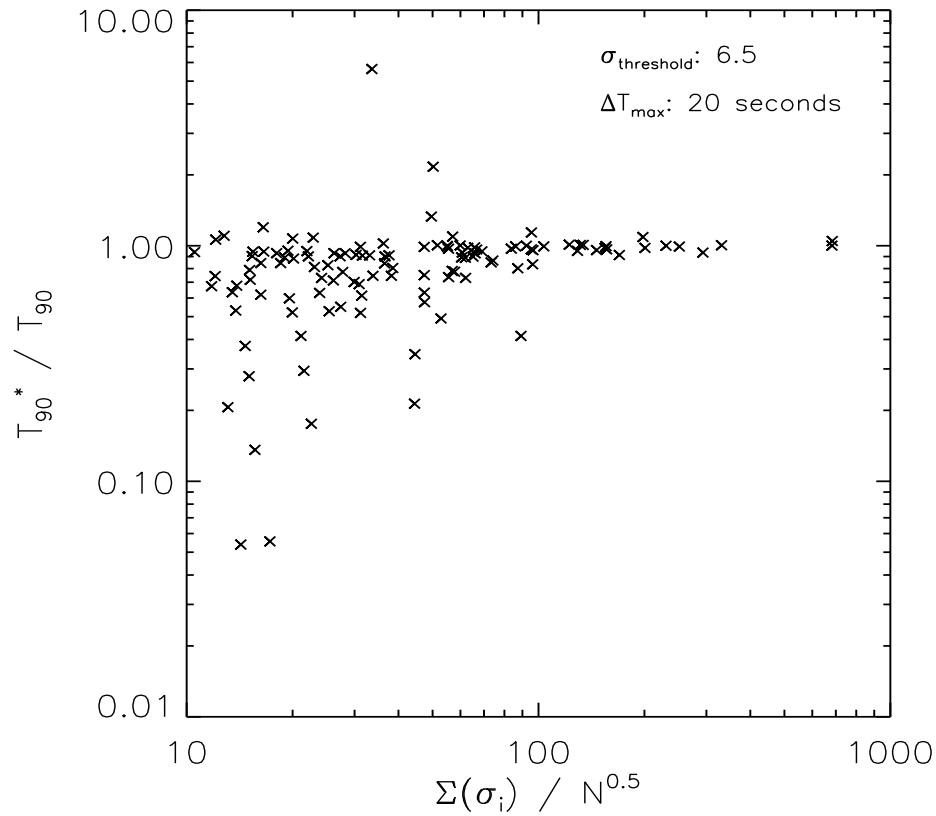


Figure 4.5: Comparison of measured T_{90} of observed BAT light curves in the 15–350 keV spectral range. In this figure the value calculated using the dynamic binning routine developed in this work (T_{90}^*) is plotted as a function of the T_{90} calculated in the standard BAT processing. $\sigma_{threshold}$ is the signal to noise ratio threshold used in the dynamic binning routine, whilst ΔT_{max} is the maximum bin size used.

Care had to be taken with faint bursts for which there was only one detected bin as the reported T_{90}^* was simply 90% of the bin duration. This was a particular problem in longer triggers, as the binning routine doubled the bin width when no significant samples were found in a single iteration. With bin sizes of 10 seconds being increased to 20 seconds, there would be many possible durations between the two widths that were overlooked by the algorithm. This became important in later analysis when the evolution of T_{90}^* was being investigated as a function of redshift, particularly at high redshifts where many of the detections were single bins at the maximum bin size.

For self-consistency the value of duration adopted in the analysis of both methods was T_{90}^* as it could be measured for the light curves of both simulation methods.

4.6 Discussion

4.6.1 Selecting a bright subsample of bursts

This work aims to specifically look at the evolution of the morphology seen in the light curves of bursts and key parameters such as T_{90}^* . With this in mind, a bright subset was selected from GRBs fitted with the Willingale et al. (2010) pulse model.

To decide which of the GRBs were to be included in the bright sample all bursts with $z_{obs} < 2$ were taken and those with at least one pulse with a peak luminosity $L_{pk} > 1.0 \times 10^{52}$ ergs.s⁻¹ were identified. This peak luminosity was calculated as shown in Equation 4.13, where A is a conversion factor between keV and ergs.

$$L_{pk} = 4\pi D_{L,obs}^2 AK_{obs} S_{pk}. \quad (4.13)$$

This process identified 16 bursts, some with multiple pulses which satisfied the luminosity threshold. These 16 GRBs and the properties of their brightest pulses are detailed in Table 4.1.

4.6.2 Choosing a simulation method

Both methods of simulation detailed in §4.5 have features that make them attractive for use in further analysis. The first method, in which BAT data is directly taken, has the advantage of being model independent and therefore makes fewer assumptions as to the nature of the prompt emission. It is, however limited in the redshift range over which it can be applied and to limit these effects only the softest BAT band was simulated. Whilst use of the pulse model assumes it to be an accurate representation of the observed data, it does provide a broader data set for later analysis. All four BAT bands are recoverable, and therefore not only can the morphology be studied in greater temporal detail, but spectral characteristics can be investigated.

Having identified the bursts which were to be simulated across a wide range of redshifts, the differences between the results of the two simulation methods were studied. The bright sample was taken and simulated using both methods. Both the evolution of T_{90}^* and detectability from each method were compared.

Table 4.1: The bright GRB subset identified for morphological study. Values of T_{90} are those obtained from the standard BAT analysis. N_p denotes the number of identified pulses used for fitting the light curves, b_1 , S_{pk} and L_{pk} all correspond to the brightest pulse in each burst. (Redshifts obtained from: 1. Foley et al. (2005), 2. Vreeswijk et al. (2007), 3. Fynbo et al. (2009), 4. Bloom et al. (2006), 5. Vreeswijk et al. (2008), 6. Wiersema et al. (2008), 7. Jakobsson et al. (2008), 8. de Ugarte Postigo et al. (2009), 9. Chornock et al. (2009), 10. McBreen et al. (2010), 11. Xu et al. (2009), 12. O’Meara et al. (2010), 13. Tanvir et al. (2010), 14. Cucchiara et al. (2011b), 15. de Ugarte Postigo et al. (2011) and 16. D’Avanzo et al. (2011)).

GRB	Redshift	$T_{90}(z_{obs})$ (seconds)	N_p	b_1	S_{pk} (keV.cm ⁻² .s ⁻¹)	L_{pk} (ergs.s ⁻¹)
GRB 050525A	0.606 ¹	8.86 ± 0.07	7	0.06	4441.78	1.08 × 10 ⁵²
GRB 060418	1.489 ²	109.17 ± 46.73	9	-0.38	576.42	1.32 × 10 ⁵²
GRB 060908	1.884 ³	18.78 ± 1.30	4	0.11	256.88	1.05 × 10 ⁵²
GRB 061121	1.314 ⁴	81.22 ± 46.40	7	0.48	2619.25	4.39 × 10 ⁵²
GRB 080319B	0.937 ⁵	124.86 ± 3.10	17	1.11	2757.78	1.98 × 10 ⁵²
GRB 080319C	1.950 ⁶	29.55 ± 9.41	3	0.01	538.89	2.40 × 10 ⁵²
GRB 080605	1.640 ⁷	29.55 ± 9.41	9	0.29	2622.20	7.63 × 10 ⁵²
GRB 090102	1.547 ⁸	29.30 ± 3.23	3	0.20	512.07	1.29 × 10 ⁵²
GRB 090424	0.544 ⁹	49.47 ± 2.27	6	0.12	5744.63	1.08 × 10 ⁵²
GRB 090510	0.903 ¹⁰	5.66 ± 1.88	1	0.52	1761.86	1.16 × 10 ⁵²
GRB 091020	1.710 ¹¹	38.92 ± 4.89	4	-0.24	354.11	1.14 × 10 ⁵²
GRB 100814A	1.440 ¹²	174.72 ± 9.47	17	0.57	482.72	1.01 × 10 ⁵²
GRB 100906A	1.727 ¹³	114.34 ± 1.59	14	0.00	636.66	2.10 × 10 ⁵²
GRB 110213A	1.460 ¹⁴	48.00 ± 16.00	6	-0.95	498.70	1.08 × 10 ⁵²
GRB 110422A	1.770 ¹⁵	25.77 ± 0.60	7	0.03	2167.60	7.60 × 10 ⁵²
GRB 110503A	1.613 ¹⁶	10.05 ± 3.41	1	-0.05	2799.08	7.81 × 10 ⁵²

Figure 4.6 shows the measured T_{90}^* of GRB 110422A for both of the simulation methods. The two lines correspond to a single set of simulations for the two methods, which showing that both produce similar values of T_{90}^* until $z \sim 4$. This suggests that whilst the burst remains bright in the 15–25 keV band the two simulation methods are consistent with each other. However, after this redshift the measured value of T_{90}^* for the BAT simulation method becomes less than that obtained for the pulse method. This is due to the observed morphology becoming weaker across all four BAT channels and requiring a fuller spectral range for detection. The pulse method, which uses a 15–350 keV spectral range, also detects the burst to a greater redshift. To verify if this was the case for all bursts, the maximum redshifts at which all 16 bursts in the sample were detected using both simulation methods were found. These are

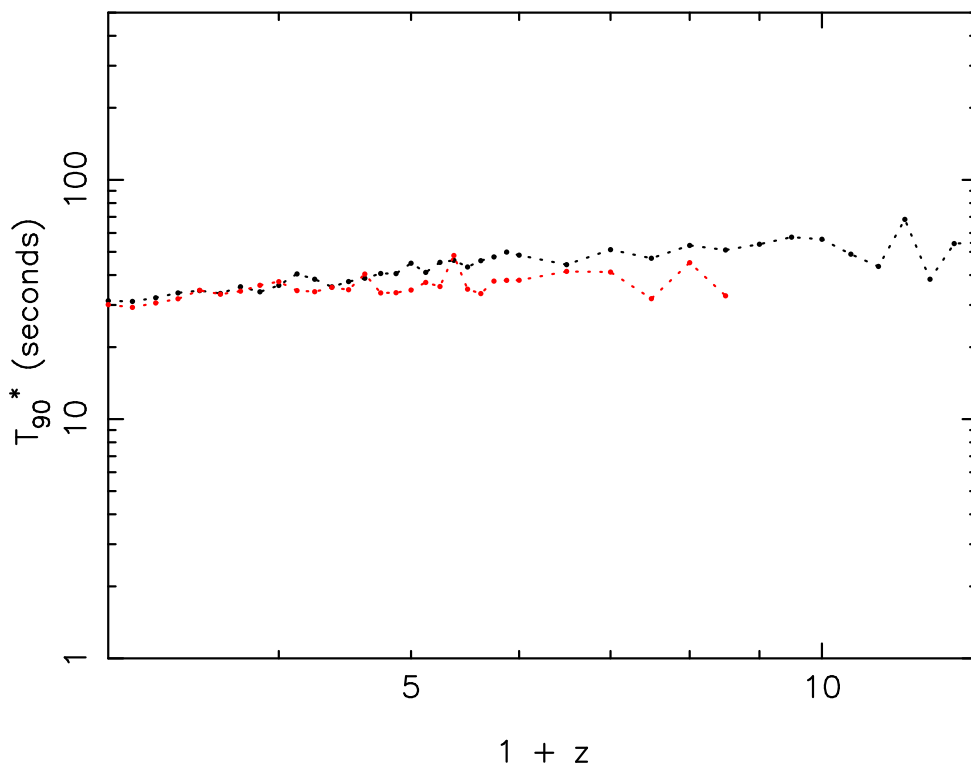


Figure 4.6: T_{90}^* measured for GRB 110422A using both simulation methods. The black line and points show the value obtained for using the 15–350 keV range and the pulse method simulations. The red line and points are for the 15–25 keV BAT data method of simulation.

illustrated in Figure 4.7.

The values for z_{max} have been calculated from a single set of simulations for each burst at each redshift, whilst to find z_{max}^* a more extensive set of pulse simulations were used. As each burst had been simulated 100 times at every value of z_{sim} using the pulse method (see §4.6.4), z_{max}^* was defined to correspond to the highest value of simulated redshift at which at least 50% of the simulations detected the specified GRB.

As expected, all the points lie above the line of equality, indicating that for each GRB $z_{max}^* > z_{max}$. There are even five instances, using the pulse method, where bursts remain visible at the maximum simulated redshift. There are only three visible upper limits on Figure 4.7 as there are two cases where the maximum redshifts coincide for separate bursts, meaning the upper limits are plotted over one another. Additionally, the short burst, GRB 090510, which is included in the bright sample is not detected for any of the simulations conducted using the BAT method.

As $z_{max} < z_{max}^*$ in all cases was attributed to the limited spectral range of the BAT method

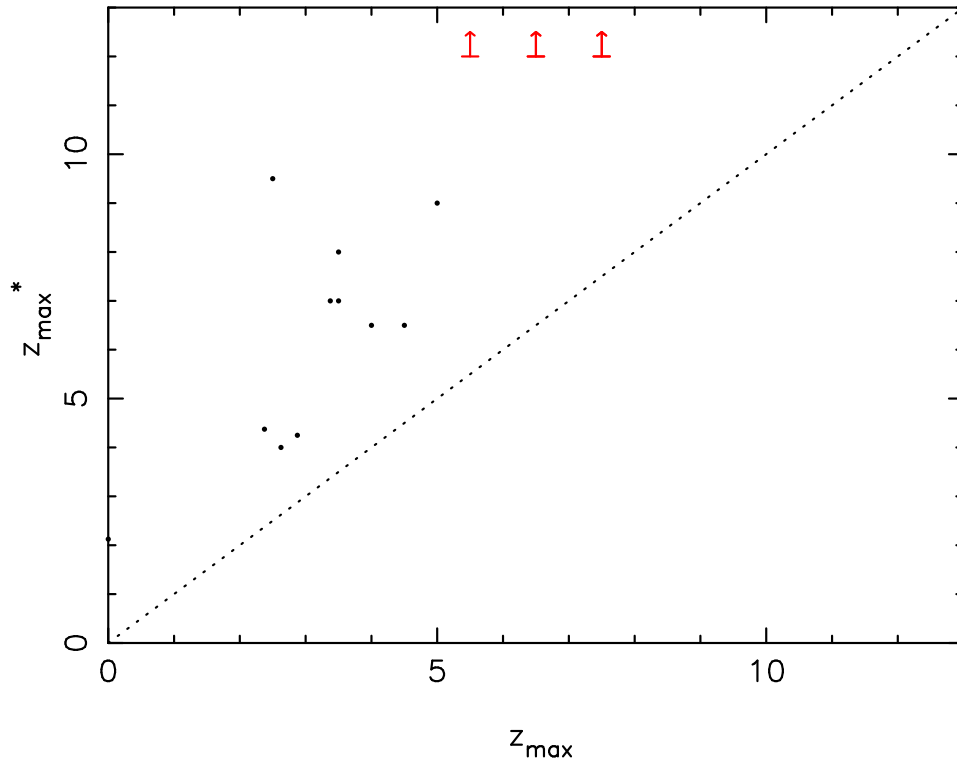


Figure 4.7: Comparison of the maximum redshift at which a burst is detected using the BAT method (z_{max}) and the pulse method (z_{max}^*). Black points denote where a maximum was found in the considered range of z_{sim} , whilst red arrows show upper limits, where using the pulse method a burst remained detectable at $z = 12$. The dotted line shows equality.

the pulse method of simulations was selected for further analysis. This allowed for a more detailed study of the evolution of the visible morphology, duration and spectral hardness over the greatest possible range of z_{sim} .

4.6.3 Evolution of morphological features

The expected evolution of the pulse model was threefold. First, the pulses become fainter, as the normalisation S_{pk} is reduced. The next effect is the time dilation of each pulse, as the temporal parameters of each are increased (T_f , T_{rise} and T_{pk}). However, as the flux received from each pulse is fainter, this may not be the dominating factor as the wings of each pulse disappears into the background noise. Finally, the time at which each pulse peaks (T_{pk}) is also dilated, meaning that the time between pulses should also increase. To illustrate some of these effects the simulated light curve of GRB 100814A is plotted at several redshifts in Figure 4.8.

Figure 4.8 shows several of the expected phenomena. The most obvious of these is that the

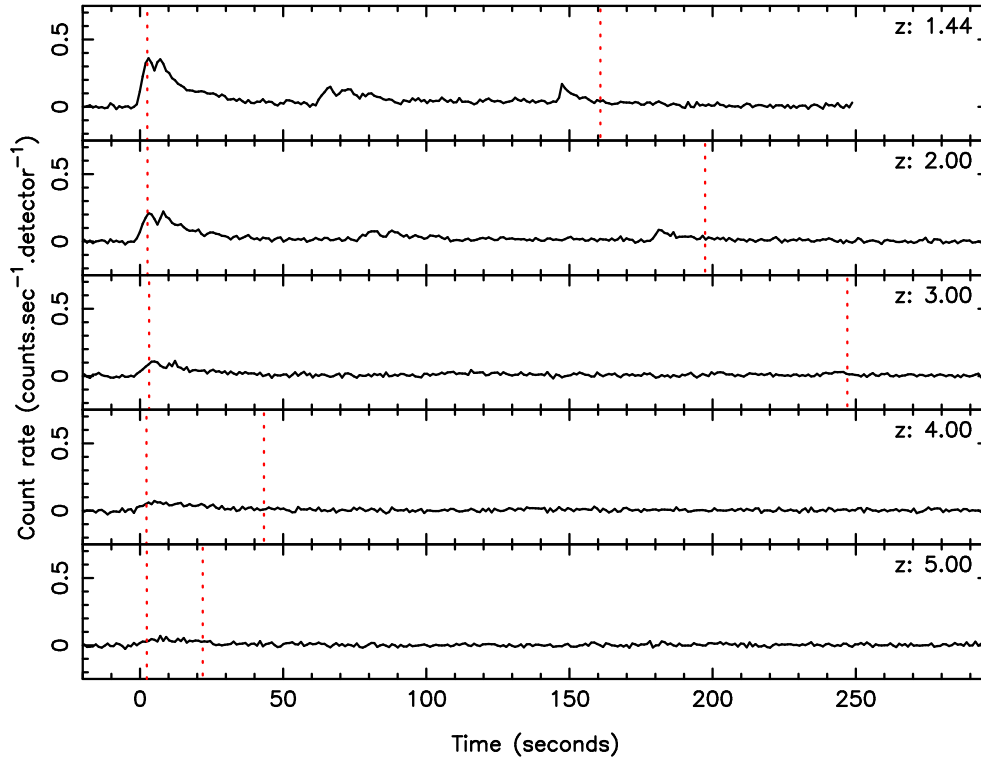


Figure 4.8: Simulations of GRB 100814A at a variety of redshifts. From top to bottom these redshifts are $z = 1.44, 2, 3, 4,$ and 5 . $z = 1.44$ is the observed redshift of the burst. The binning of this light curve is 1024 ms, and the red dotted lines show the start and end of the identified T_{90} period. To compare both the count rate and durations, both axes have been given common ranges for all five panels.

strength of the pulses is reduced as the source is moved to a higher redshift. Also, the quiescent periods between pulse activity increase as long as the pulses which border the quiescence are detected. This is well illustrated in the first three panels, and particularly the first two. After a small change in simulated redshift, the dilation of individual pulses can also be determined, although this is not a long lasting effect for most structure as the wings of each pulse are rapidly lost to the background after a moderate change in z_{sim} . It is this last effect which dominates the change in morphology between the last two panels. Between $z_{sim} = 3$ and $z_{sim} = 4$ later pulses become undetectable, dramatically reducing the measured duration.

At $z_{sim} = 4$ it is only the first features in the original light curve that can be detected, whilst by $z_{sim} = 5$ even less of these are seen due to even the brightest structure becoming comparable in flux to the intrinsic background variations.

4.6.4 Evolution of T_{90}^*

Taking the 16 bursts identified with bright pulses, each was simulated at redshifts in the range $2 \leq z_{sim} \leq 12$. This lower limit was chosen because one of the selection criteria of the bright sample was that the bursts were observed at $z_{obs} < 2$. Nearer to this lower limit, where all of the bursts were expected to remain detectable, the simulations were conducted at smaller increments in redshift ($\Delta z_{sim} = 0.125$). However, at higher redshifts there was an increased likelihood that each burst would become too faint to be detected, so after $z_{sim} = 5$ these intervals were increased to $\Delta z_{sim} = 0.5$.

To reduce the effects of the noise introduced from the background, which were particularly an issue at higher redshifts, each set of simulations were conducted 100 times per burst. The geometric average of T_{90}^* at each value of z_{sim} was taken to produce Figure 4.9.

In Figure 4.9 the bright subset has been divided to make it easier to see the evolution of each burst. The GRBs were ordered by the peak luminosities of their brightest pulses (L_{pk} , see Equation 4.13). The eight bursts with the brightest pulses are in the top panel, with the remaining eight shown in the bottom panel. The key on each shows which colour data set corresponds to each burst and is ordered by L_{pk} with the brightest burst in each panel at the top.

Figure 4.9 shows that several of the bursts in the sample behave as might be expected. There are a number of bursts which show the effects of time dilation, particularly notable amongst these is GRB 080319B (the orange data set in the top panel). Being such a bright burst, it is not surprising to see that it is detectable to incredibly high redshifts. It is also not surprising that time dilation dominates the evolution of the morphological features of the light curve. If the evolution is considered over a redshift range of $2 \leq z_{sim} \leq 7$, a power-law can be fitted to the T_{90}^* behaviour shown in Figure 4.9:

$$T_{90}^* = 24.1 (1 + z)^{0.96} . \quad (4.14)$$

When testing this line of best fit against the data, a reduced χ^2 value of 1.11 for 27 degrees of freedom was found, indicating the fit to be a close representation of the data. This index is remarkably close to a value of 1, which would suggest that during this range in redshift the

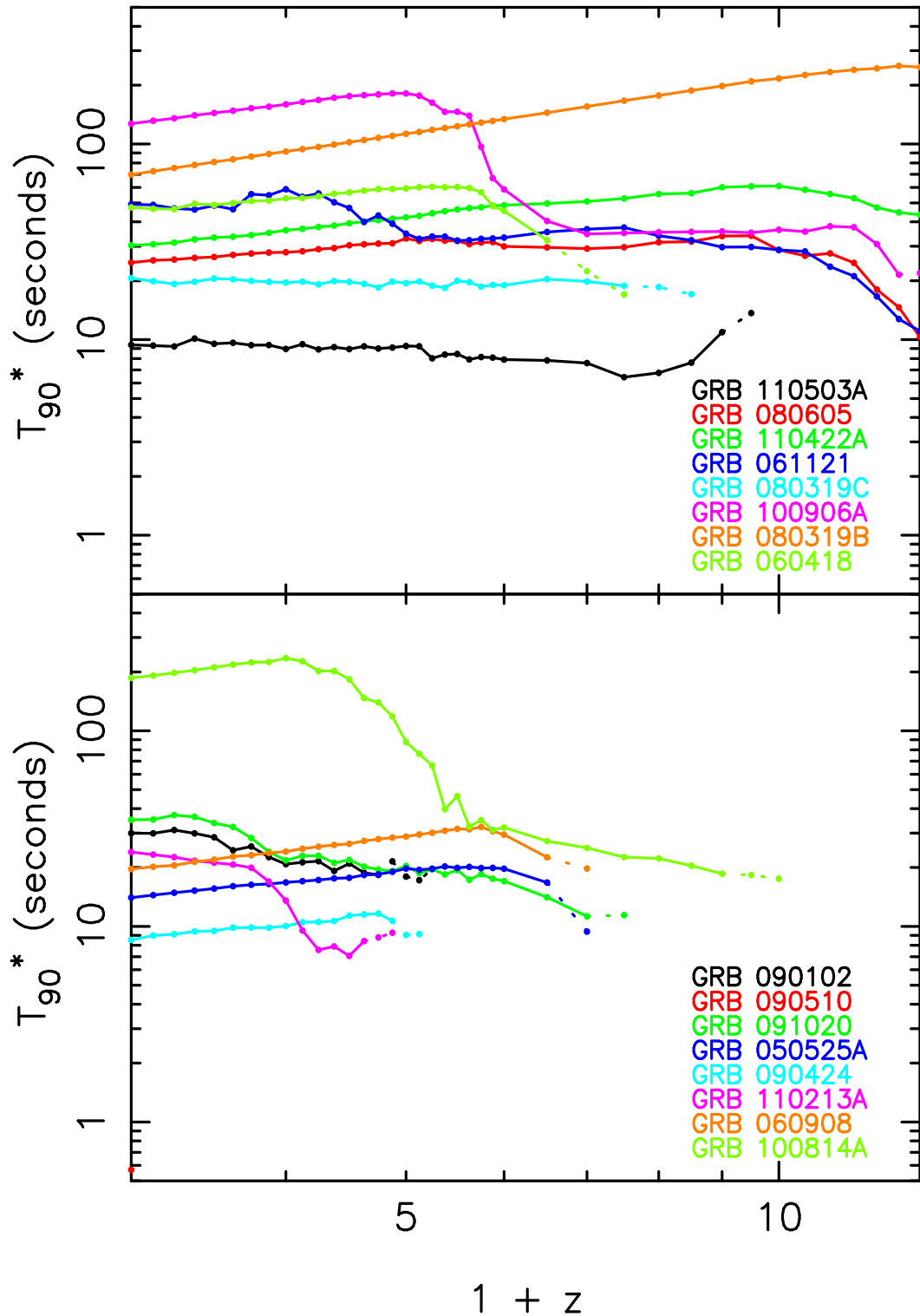


Figure 4.9: The evolution of T_{90}^* as a function of redshift for the sample of bright bursts. The sample has been split according to the luminosity of the brightest pulse in each burst (see Table 4.1), with the most luminous 8 being shown in the top panel. Solid lines show where the bursts was detected in a minimum 90% of the repeated simulations, the dotted lines show where the burst was detected in less than 90% but greater than 50% of these repeats.

evolution of T_{90}^* is dominated by cosmological time dilation. At larger redshifts the rate of increase in T_{90}^* of GRB 080319B can be seen to reduce, as the outermost features in the light curve morphology are increasingly lost into the background flux.

At low redshifts the other bright bursts for which time dilation can be seen $T_{90}^*(z_{sim})$ does not increase as rapidly. In these cases the dominant effect is still cosmological time dilation, however the lengths of the pulses at both the start and the end of the light curve are also being reduced. This loss of flux is more notable in the last detected pulse, due to the functional form of each pulse having a sharp rise and a more gradual decay.

Figure 4.9 includes an indication of the fraction of repeated simulations in which each GRB is detected has been included. Where the evolution of T_{90}^* is shown as a solid line the burst is detected in a minimum of 90% of the simulations at that specific value of z_{sim} . The dotted line shows where this fraction is between 50% and 90%. In most instances, this second regime extends for only a short period. Once the GRB is detected in less than half of the repeated simulations, the average value of T_{90}^* is not shown. At these points the average of T_{90}^* becomes erratic due to a poor peak signal to noise ratio.

For most bursts where $T_{90}^*(z_{sim})$ increases at low redshifts, the behaviour of T_{90}^* is simple: T_{90}^* increases until a particular value of z_{sim} , then reduces as the morphology in the light curve becomes too faint to detect against the background. This is the case for GRB 050525A, GRB 060418, GRB 060908 and GRB 090424. Of this sample, those bursts which simply increase in duration with increasing redshift for a small to moderate change in redshift make up one of the largest two subsets containing six of the 16 bursts in the sample. Whilst, GRB 100814A and GRB 100906A have similar behaviour at low redshifts, they differ at higher values of z_{sim} .

GRB 100906A shows a more complicated evolution in T_{90}^* . Until $z_{sim} \sim 4$ the duration can be seen to increase in a manner similar to GRB 080319B. This behaviour is therefore attributed to time dilation. In the range $4 < z_{sim} < 6$ the evolutionary track shows a reduction in T_{90}^* , after which there is a further period of less rapid time dilation before T_{90}^* begins to reduce at the upper end of the range of z_{sim} . The light curves of this burst were studied with three examples displayed in Figure 4.10. To allow weaker structure to be easily discerned from

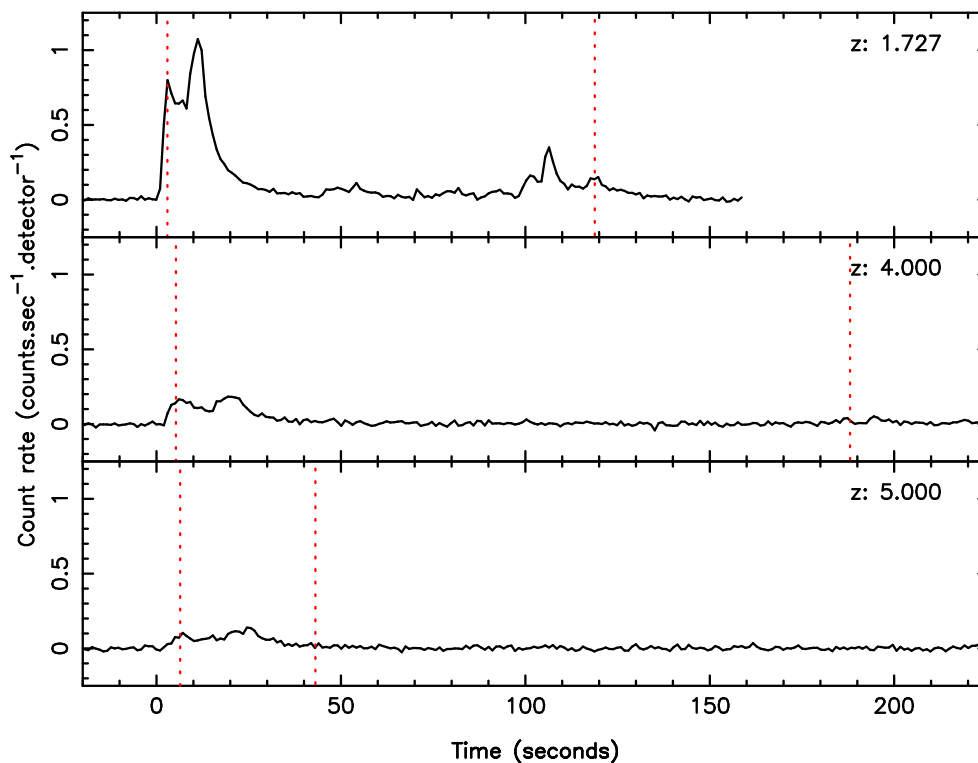


Figure 4.10: Simulations of GRB 100906A at three redshifts. From top to bottom these redshifts are $z = 1.727$, 4, and 5. $z = 1.727$ is the observed redshift of the burst. The binning of this light curve is 1024 ms, and the red dotted lines show the start and end of the identified T_{90} period. To compare both the count rate and durations, both axes have been given common ranges for all three panels.

the light curve they are displayed at 1024 ms temporal binning.

The first panel shows a simulation of the light curve at its observed redshift, containing all the morphological features modelled using the methodology of Willingale et al. (2010). Below this is a light curve simulated at $z_{sim} = 4$, shortly before the observed drop in duration. In comparison to the previous panel, the features are fainter and more spread in time. This spread is the effect of cosmological time dilation, which elongates the pulses and also the quiescent periods between them. The final panel shows a simulation at $z_{sim} = 5$, which shows the fainter structure at late times is not detected. Looking at the evolutionary track for T_{90}^* for this single set of simulations shows a single sharp drop in duration. This, however, is not reflected by the average shown in Figure 4.9, which shows a slightly more gradual change. This difference is due to the statistical fluctuations of the background noise. In some of the simulations the background is such that it allows for detection of the weaker, later pulses to greater redshifts, so increasing the average. The shape of the drop in T_{90}^* for GRB 100906A in

the redshift range $4 < z_{sim} < 6$ therefore describes change in the fraction of the simulations for which this later structure is detected.

GRB 100906A is not the only burst in the sample that shows such behaviour; another notable example is GRB 100814A. In this case the drop in duration due to the loss of a pulse take a larger range in redshift. At the end of this range of z_{sim} , the burst is only detected in a small fraction of the simulations, and so the behaviour following this cannot be described. Again, the light curves were studied directly, showing that the drop in T_{90}^* occurs over a larger range in z_{sim} because there are two pulses which are lost. This occurs at a slightly different redshift for each pulse. A similar smooth effect for both results from averaging over multiple simulations, therefore blurring the two to look like a single feature in the evolution of T_{90}^* .

From the evolution of T_{90}^* , there are two other bursts which show similar, if less pronounced, reductions in their duration: GRB 061121 and GRB 080605. For GRB 061121 it appears that loss of structure occurs in the range $3 < z_{sim} < 4$, after which there is a gentle increase in measured T_{90}^* until $z_{sim} \sim 6.5$. After this simulated redshift more structure is lost, continuing to the maximum value of z_{sim} used in this work. For GRB 080605 the change is a more gradual transition in the range $4 < z_{sim} < 5$. This behaviour shows the loss of the first pulse in the light curve, which peaks approximately 5 seconds before the next one. As the second pulse has a rise time of over 2 seconds, the actual time between visible emission from both pulses is short. Even when accounting for the increased redshift from $z_{obs} = 1.640$ to $z_{sim} \sim 4$, this difference between T_{pk} values remains less than 11 seconds. After the first pulse, which unusually is weaker than later features, is lost, there is a slight increase in duration until $z_{sim} \sim 8$, after which further structure is lost.

Of the remaining bursts, most show a simple decrease in duration as a function of redshift. In the cases where there are few modelled pulses in the light curve, this is due to the loss of flux from the first and last pulses being more rapid than the effects of time dilation, indicating steep pulse spectra. For the GRBs in which many (up to 10) pulses have been identified, it is the complete loss of weaker pulses at late times that causes the reduction in measured T_{90}^* . Once this process has finished, the remaining (previously bright) structure is now faint enough that the loss of flux from them again dominates over the effects of time dilation.

There are two final bursts in the sample which behave unexpectedly. GRB 090510 was included in the sample based on the brightness of its morphological features, however, unlike the other GRBs in the sample it is a short burst. Detected at $z = 0.903$, it is already significantly evolved by $z_{sim} = 2$. Being a short burst it also has a hard spectrum, with E_{pk} well outside in the original observed BAT data. This means that the single modelled pulse becomes faint at a rapid rate. Figure 4.9 shows that at no point in the range of considered z_{sim} values is GRB 090510 detected in 90% of the simulations. It is however detected in over 50% of the simulations for the first simulated redshift, at $z_{sim} = 2$.

Finally, GRB 110503A appears to have an approximately constant duration for a moderate range of redshifts, in which it is likely that the effects of time dilation and the loss of fainter flux balance out. However, at $z_{sim} \sim 6$ there is an increase in the duration. The scatter in the values of T_{90}^* at these high redshifts for GRB 110503A is large, indicating high uncertainties in the displayed values due to a poor signal to noise ratio.

By ranking the bright subset of GRBs by the luminosity of the brightest pulse, it is not surprising to see that those bursts which contain the brightest features are, on average, detected to higher redshifts. The one exception to this statement is GRB 100814A, which has the faintest pulse meeting the sample criterion. Whilst the luminosities of the brightest pulses in the other bursts are all greater, the brightest pulse in GRB 100814A has spectral index $b_1 = 0.57$, this corresponds to a photon index of $\alpha = -0.43$, which is one of the shallowest in the sample. This more gradually changing spectrum is also seen in the brightest pulses of those bursts which are detected out to $z_{sim} = 12$.

4.6.5 Evolution of hardness ratio

To calculate the hardness ratio, each of the four standard BAT bands were considered and individually binned by significance. The channels were binned individually to account for an effect known as spectral lag that is observed predominantly in long GRBs (for example, see Norris et al. 2000). In such bursts it is common to observe a delay between the emission associated from a single pulse in differing energy bands. By using the cross–correlation function between two high–energy bands it can be shown that the prompt emission of a long burst rises

earlier in the harder of the two bands. Additionally, it is also notable that the softer flux from features in the light curve tend to be longer lived than at higher energies.

After binning the BAT light curves dynamically, the significant fluence was then summed by determining all bins with a flux above the threshold previously determined (6.5σ). The ratio of this total fluence in two separate bands was then taken (dividing the harder band by the softer band), giving a simple measure of the spectral characteristics of each GRB. For greater consistency with other reported hardness ratios, the bands used were the 25–50 keV and 50–100 keV channels of BAT.

There are three types of value this hardness ratio can take: being greater than 1 denotes that there is more fluence in the harder channel, a value less than 1 occurs when there is more low energy fluence and when the hardness ratio is precisely 1 the same total fluence is detected in both bands. Figure 4.11 shows the evolution of the hardness ratio for each of the sixteen bursts in the bright sample.

For those bursts with the brightest features, such as GRB 080319B, the evolution of the hardness ratio as a function of redshift behaves as might be expected: the value is less than 1, and decreases with increasing redshift. This indicates that at higher redshifts more of the observed fluence is detected in the softer BAT bands. This corresponds to the evolution of the observed spectrum that occurs for each pulse as a burst moved to greater luminosity distance. As such, the peak in the νF_ν spectrum migrates to lower energies and the spectrum softens, directly resulting in a reduction in hardness ratio.

Such simple behaviour is not seen in all instances, however. In those bursts for which some pulses become undetected, resulting in a reduction in measured duration, there is often an associated increase in hardness ratio (for example GRB 100814A and GRB 100906A). This is due to the pulses that are lost often being later, fainter pulses, and so are softer to begin with. When they become undetected they remove a contribution of softer emission from the light curve and an increase in average hardness ratio.

This spectral hardening is also seen in some of the bright bursts that remain detected over a broad range of redshifts. GRB 110503A, GRB 080605 and GRB 100906A have bright features with some of the highest values of α in the sample, meaning the spectrum takes longer to

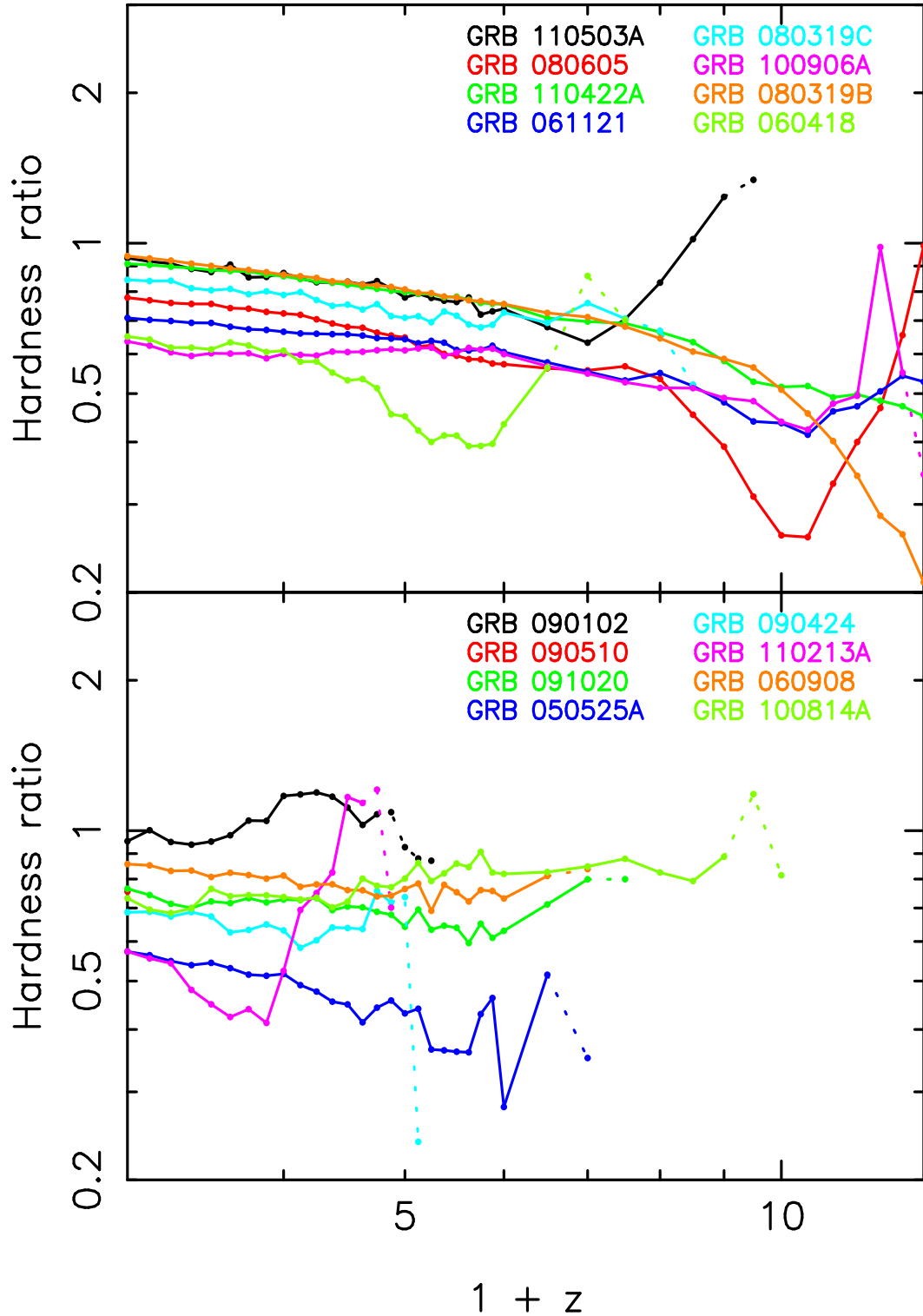


Figure 4.11: The evolution of the $S(50 - 100 \text{ keV})/S(25 - 50 \text{ keV})$ hardness ratio as a function of redshift in a sample of bright bursts. The sample has been split according to the luminosity of the brightest pulse in each burst (see Table 4.1), with the most luminous 8 being shown in the top panel. Solid lines show where the bursts was detected in a minimum 90% of the repeated simulations, the dotted lines show where the burst was detected in less than 90% but greater than 50% of these repeats. Each burst is represented by a different colour data set, with an identical colour scheme to Figure 4.9.

become softer. As these are the morphological features which remain at high redshifts, when the weaker, softer structure becomes too faint detect, the hardness ratio of the burst sharply increases. In some instances, this hardening is sufficient to make the hardness ratio greater than 1 (indicating more flux is detected in the harder band).

The evolution in hardness ratio for some of the bursts can be seen to be erratic. These tend to be GRBs whose T_{90}^* decreases across the entire range of z_{sim} and are amongst the weaker bursts in the bright subset. This evolution is potentially due to there not being a single dominant pulse in the light curve. Instead there are several pulses of similar strength but differing spectral indices. As such, the rates at which they become undetectable vary, and so the behaviour observed in the hardness ratio is complicated. However, complimentary behaviour is not necessary in the evolution of T_{90}^* if the two pulses defining the beginning and the end of this duration remain detected throughout the relevant redshift range. Instead structure can be lost in the intervening period causing a longer extent of quiescence.

4.6.6 Evolution in the hardness–duration plane

Combining Figures 4.9 and 4.11, resulted in a hardness–duration plot, similar to those first published in Kouveliotou et al. (1993), from which the long–soft and short–hard burst paradigm was first proposed. This is shown in Figure 4.12.

For those bursts in which time dilation is the dominant effect over a particular range in redshift, the hardness ratio tends to become softer over the same range. This evolution of a burst towards a longer, softer state is what is expected for those GRBs which are bright enough to not lose structure. Time dilation ensures that structure becomes both longer in duration and separated by longer quiescent periods, whilst spectral evolution ensures the spectrum peaks at softer energies. The best example of this behaviour is in the brightest burst in the sample, GRB 080319B, for which this is the only type of evolution seen in the hardness–duration plane. Six other bursts (GRB 050525A, GRB 060418, GRB 060908, GRB 080605, GRB 090424 and GRB 110422A) show similar behaviour, but over a more restricted range in redshift. Commonly, after this period of time dilation, the remaining structure is faint, and so the burst becomes shorter as less of the morphology is detected. The features that are no longer de-

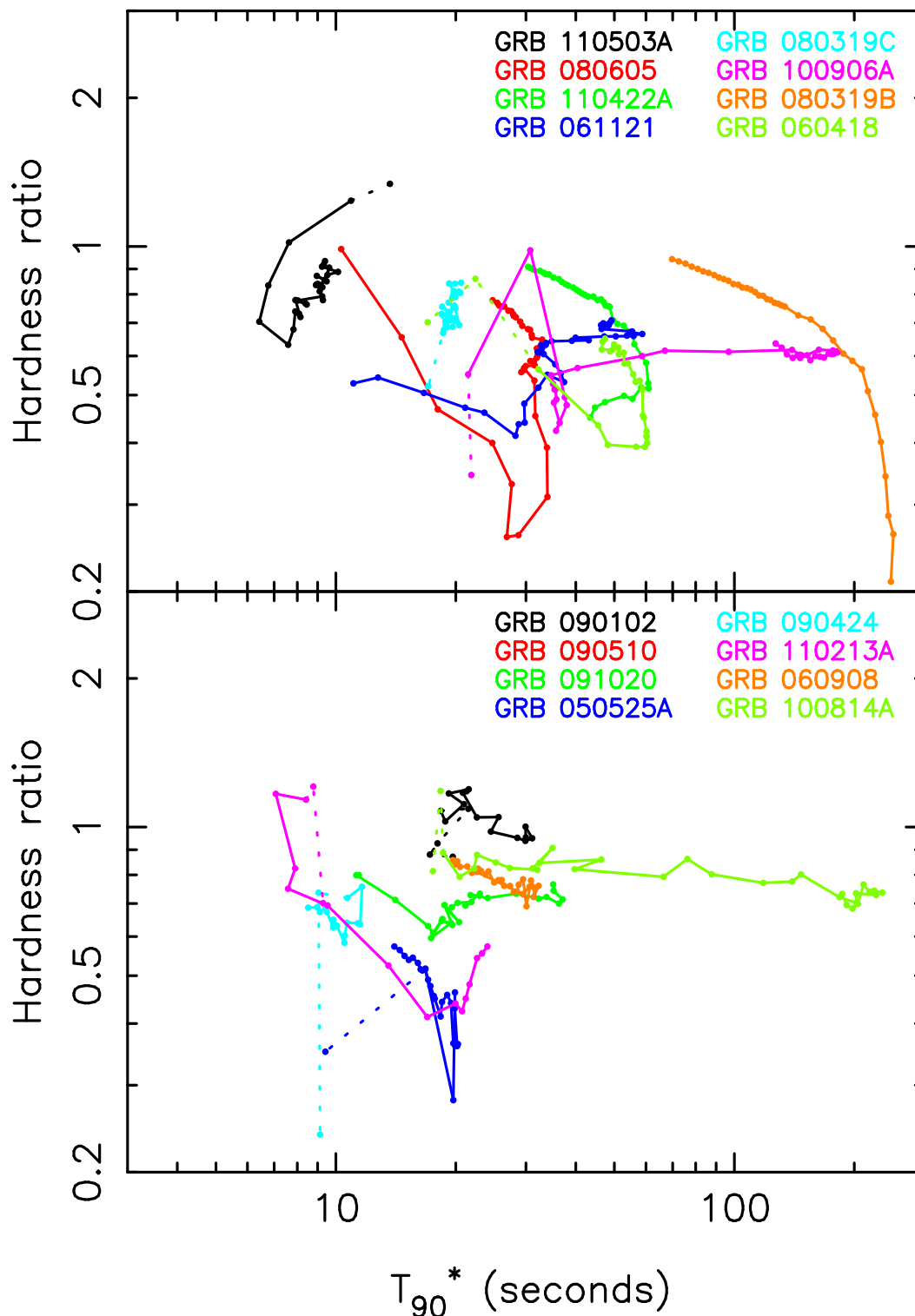


Figure 4.12: The evolution of the positions in the hardness–duration plane for the sample of bright bursts. The sample has been split according to the luminosity of the brightest pulse in each burst (see Table 4.1), with the most luminous 8 being shown in the top panel. Solid lines show where the bursts was detected in a minimum 90% of the repeated simulations, the dotted lines show where the burst was detected in less than 90% but greater than 50% of these repeats. Each burst is represented by a different colour data set, with an identical colour scheme to Figure 4.9.

tected tend to be the later structure, which is spectrally softer than the earlier emission, and so this reduction in duration is often accompanied by an increase in the corresponding hardness ratio.

Another large subset of the bright sample show evolution from longer, harder light curves to shorter, softer structure. This occurs whilst the change in duration is gradual for each. In these cases it is believed that the gradual reduction in duration is due to the loss of fainter parts of pulses. This continues until the later pulse is entirely lost, but as this happens gradually, the spectra of the remaining pulses have softened sufficiently to prevent the increased hardness ratio seen when a pulse suddenly stops being detected.

GRB 090510 is only detected at one redshift and so its evolution cannot be studied, however there are other bursts which exhibit strange behaviour over a sufficient range in redshift to be discussed.

GRB 090102 is a burst which shows a continual decrease in measured T_{90}^* , but also becomes spectrally harder as it does so. This burst only contains three pulses, of which only one is detected by $z_{sim} = 2$. The behaviour in the hardness–duration plane is due to the broadening of this one remaining pulse, which has a value of $b_1 = 0.2$. As such, whilst fainter structure from the wings of the pulse are lost, only the harder core remains.

Figure 4.12 also highlights another interesting feature seen predominantly in the brightest bursts of the sample. After a period of time dilation there is, in four cases (GRB 060418, GRB 080605, GRB 110213A and GRB 110503A) a period where the detected prompt emission becomes harder. Whilst this has been discussed briefly in §4.6.5, by showing the same feature in Figure 4.12 the corresponding evolution in time can be simultaneously studied. The apparent trend, for all four, is that after a period of spectral softening, the duration begins to reduce, before the hardness ratio increases. Whilst this increase in hardness ratio occurs, the duration can either increase or decrease, which is believed to be due a combination of the brightness and spectrum of the remaining bright pulse. If the remaining detected pulses are either spectrally soft or faint then the dominant effect will be a reduction in duration due to the loss of fainter flux in the wings of the pulse. However, if the pulse is still bright and has a high value of b_1 then such a pulse will remain visible, and could perhaps exhibit the characteristic

evolution of time dilation.

The final two bursts that show unusual behaviour are GRB 100814A and GRB 100906A. This can be attributed to the fact that these two bursts are those which show the most pronounced and sudden loss of late time pulses. Both GRBs have a rapid loss in duration, which was expected to be accompanied to by a similarly discernible increase in hardness ratio. In the case of GRB 100814A there is a gradual upwards drift in hardness ratio, before the values become erratic due to the remaining pulse structure becoming faint. GRB 100906A shows the same sudden reduction in duration, however there is a simultaneous, if slight, reduction in the hardness ratio. In this instance it is concluded that the contribution to the total hardness ratio from the final structure is small with respect to the fraction from the earlier, brighter structure. As a result of which, the dominant spectral evolution seen is from the softening of the earlier pulse structure. This effect is somewhat mitigated by the loss of the later pulse responsible for the drop in T_{90}^* , however the softening of the earlier structure remains the dominant effect, and so the total hardness ratio reduces.

4.6.7 An alternative measure of duration

In an attempt to further remove the effects of background noise when quantifying a duration associated with each prompt light curve, an alternative measure of duration was also taken. From the dynamic binning routine, it was possible to define a bright core of the prompt emission. The brightest bin in the re-binned light curve was found (with flux F_{max}) and used to define a brightness threshold ($F_{thresh} = 0.5F_{max}$). The durations of all bins which were above this threshold were summed to give a measure of the bright core of emission. This was termed the core time T_c , and measures the period of time over which the source can be considered to be ‘on’. Measures such as T_{90}^* and T_{90} have the potential to include quiescent periods between regions of activity, whereas T_c is insensitive to such times of inactivity. A similar measure, T_{45} , has previously been considered in works such as Reichart et al. (2001). The evolution of T_c is shown in Figure 4.13.

The behaviour of T_c can be seen to be simpler than that of T_{90}^* . In most instances it can be seen to increase, even in bursts where T_{90}^* is seen to reduce with increasing redshift. The rate of

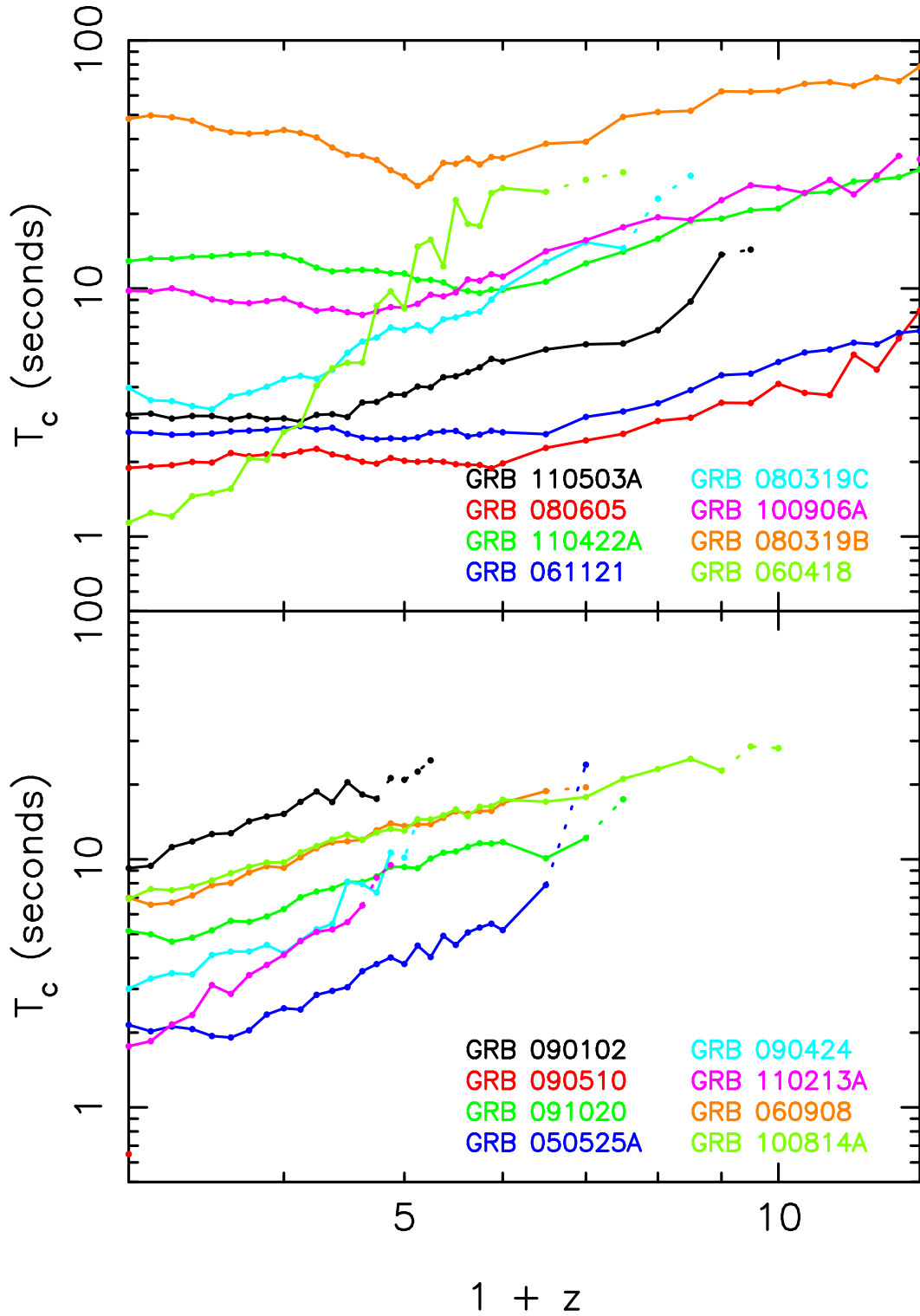


Figure 4.13: Evolution of core time, T_c , for the bright sample of bursts. The sample has been split according to the luminosity of the brightest pulse in each burst (see Table 4.1), with the most luminous 8 being shown in the top panel. Solid lines show where the bursts was detected in a minimum 90% of the repeated simulations, the dotted lines show where the burst was detected in less than 90% but greater than 50% of these repeats. Each burst is represented by a different colour data set, with an identical colour scheme to Figure 4.9.

this increase, however, is often greater than any seen for T_{90}^* , indicating that time dilation alone is not responsible for the evolution. This is caused by the reduction of F_{max} alongside time dilation. Those bursts with the largest normalisations (S_{pk}) also tend to have steeper spectra, implying that as the spectra soften, the flux from these pulses reduces more quickly than their fainter counterparts. This allows weaker structure that isn't included in the bright core at low redshifts to become part of the core at higher values of z .

Interestingly, those bursts which exhibit the effects of cosmological time dilation in their T_{90}^* evolution show a different trend in T_c . For some GRBs (such as GRB 061121 and GRB 080605) the measured value of T_c remains constant over a broad range of redshifts, before increasing like the rest. It was believed that in these instances the time dilation of the bright core is balanced by the loss of structure in pulses. Also, their observed light curves contain more than one very bright pulse, which have similar spectral indices. This means that they reduce in flux at a comparable rate allowing T_c to remain approximately constant. After a moderate change in redshift, however, time dilation becomes the dominating factor, as with the other bursts in the bright sample.

Having organised the bursts shown in Figure 4.13 the luminosity of the brightest pulses in each GRB, it is those burst with both a high luminosity and high b_1 that exhibit such a reduction or plateau in T_c . In the case of GRB 080319B the most luminous pulse identified in the light curve has the highest value of b_1 of the identified bright pulses ($b_1 = 1.11$), indicating that it should be expected to be long lived, particularly in comparison with the other pulses in the light curve. Other structure may initially contribute to the core time at low values of z_{sim} , however it will decay at a faster rate due to the relative values of b_1 , and therefore no longer be sufficiently bright to contribute to the duration of the bright core. Eventually, it is only brightest, hard pulses which contributes to the light curve, and therefore the time dilation of these pulse becomes the dominant effect, which is demonstrated in the higher redshift behaviour in Figure 4.13.

GRB 060814 shows a marked rise in T_c as a function of z_{sim} . Such a rise is highly incompatible with cosmological time dilation, and so the light curves of the burst were analysed. This burst contains two strong morphological features in its prompt emission: a weak series

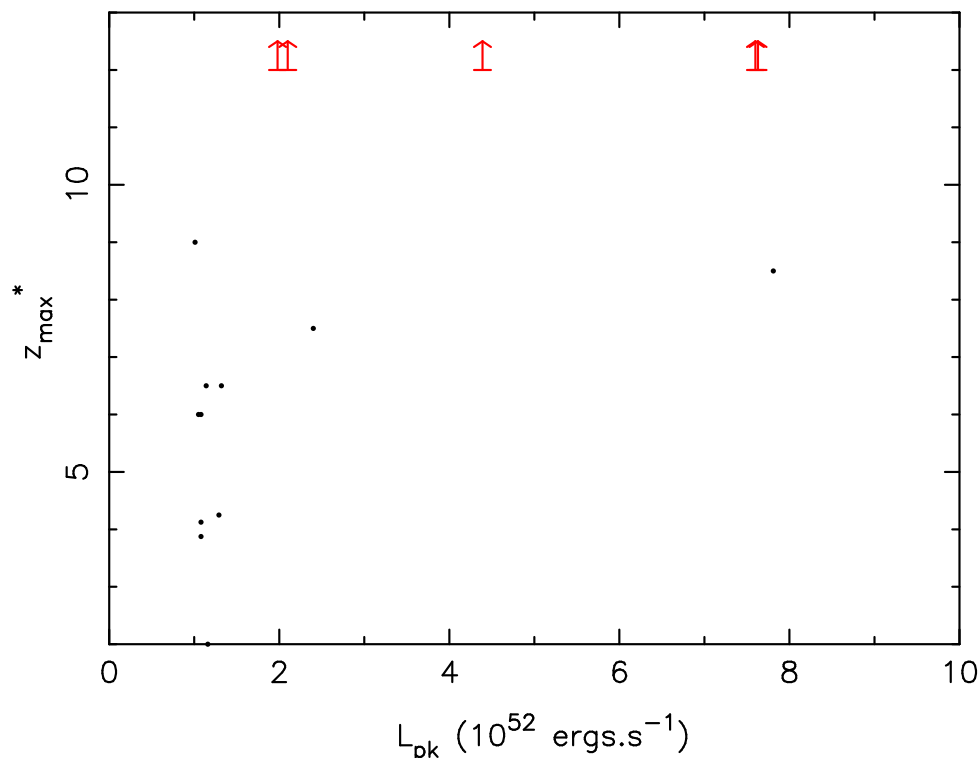


Figure 4.14: z_{max}^* shown as a function of L_{pk} for the most luminous pulse in each burst. Where a burst was detected at the maximum value of z_{sim} used ($z_{sim} = 12$) a lower limit is plotted.

of overlapping pulses followed by a single bright pulse. Initially, it is the last bright pulse that is only included in T_c , however due to its spectral index the pulse becomes faint at a more rapid rate than the early features in the light curve. As this happens, these features are able to be included in T_c at higher values of z_{sim} causing the rapid increase in T_c .

4.6.8 Dependences of z_{max}^* on pulse characteristics

Having established the values of z_{max}^* for each burst, as shown in Figure 4.7, a relation between this value and a characteristic of each burst was desired. At values of z_{sim} shortly prior to a burst becoming too faint to be detected, the structure which remains detected is the brightest pulse. Initial attempts were therefore made to relate z_{max}^* to the intrinsic luminosity of the brightest pulse as detailed in Table 4.1.

Whilst Figure 4.14 shows that all GRBs with pulses where $L_{pk} > 3 \times 10^{52}$ ergs.s $^{-1}$ are detected to at least $z_{max}^* = 8.5$, there is no clear dependence on luminosity amongst the fainter pulses. Below $L_{pk} = 3 \times 10^{52}$ ergs.s $^{-1}$ there is a collection of z_{max}^* values spanning the entire

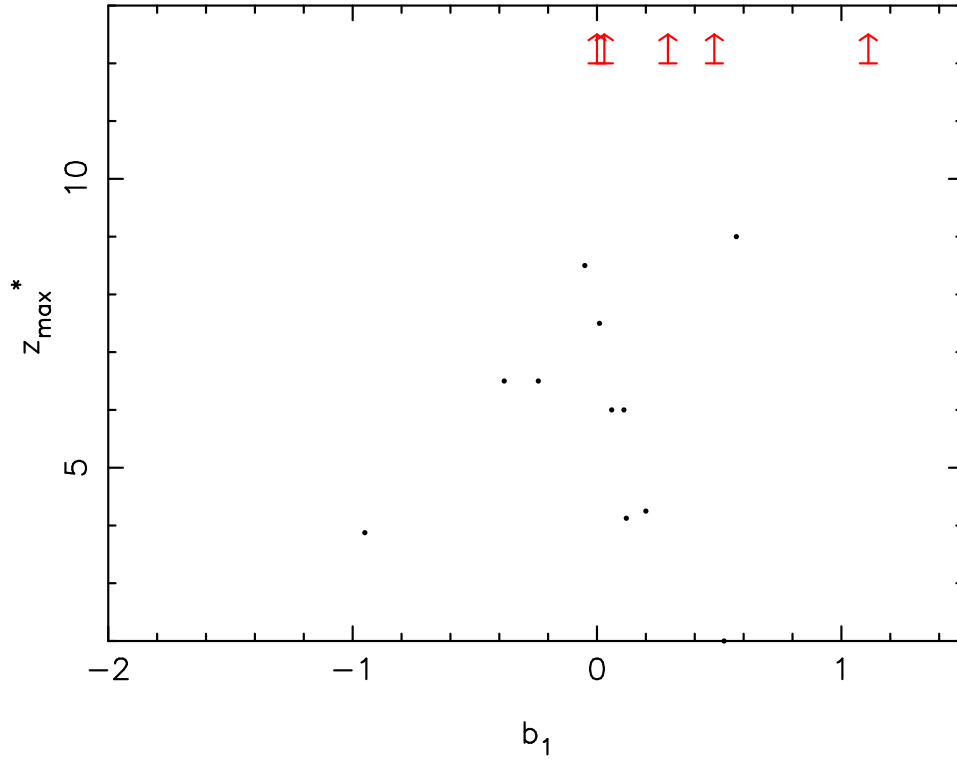


Figure 4.15: z_{max}^* shown as a function of b_1 for the most luminous pulse in each burst. Where a burst was detected at the maximum value of z_{sim} used ($z_{sim} = 12$) a lower limit is plotted.

range of z_{sim} . The steepness of the spectrum below E_{pk} was therefore considered, to see if it also had an effect, which is shown in Figure 4.15.

It is difficult to conclude from Figure 4.15 whether there is a loose trend. This is due jointly to a low sample size and the fact that for five bursts only lower limits are found. The single data point with $z_{max}^* = 2$ is GRB 090510, which is the short burst previously discussed. With the exception of GRB 090510, it could be claimed that there is the tendency for bursts whose brightest pulses have higher values of b_1 to be, on average, detected to higher redshifts. This would agree with expectation, as a higher value of b_1 indicates that the spectrum is less dominated by emission at lower energies.

The final factor that could be considered to have an effect is the redshift at which the burst was actually observed (z_{obs}). Those GRBs with a lower value of z_{obs} will have undergone a greater change in spectrum, as the energy at which the $\nu F\nu$ spectrum peaks is determined by Equation 4.10. When z_{obs} is lower, for any given value of z_{sim} , T_{factor} is greater, and therefore $E_{pk,sim}$ shifts to lower energies by a greater amount. This is shown in Figure 4.16, in which there appears to be no solid correlation between the z_{obs} and z_{max}^* .

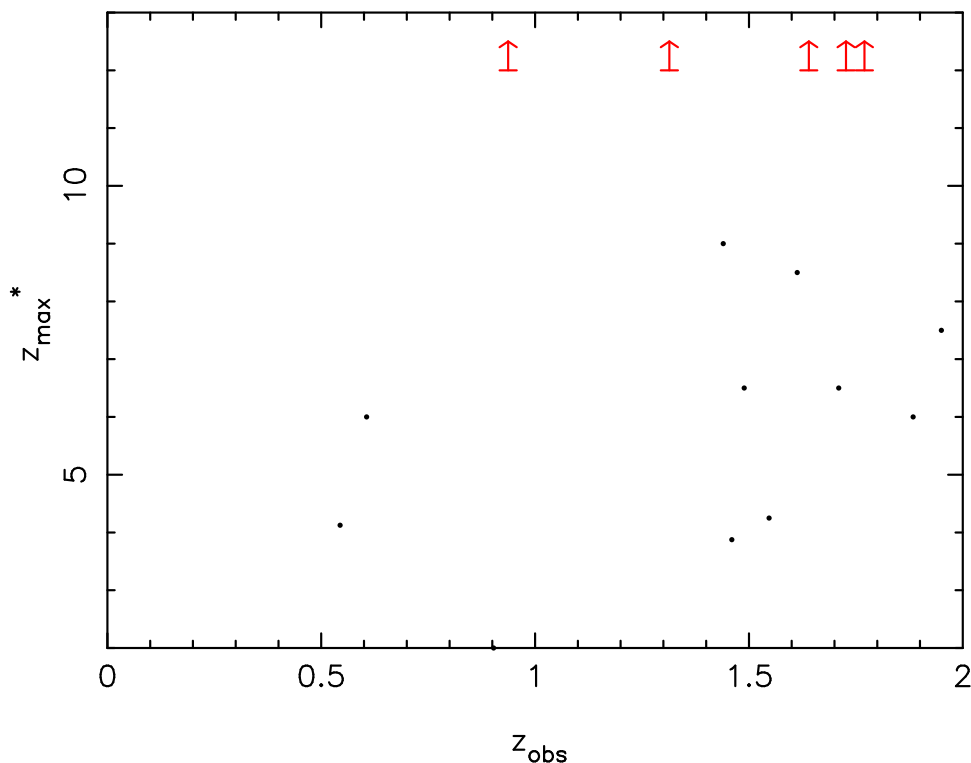


Figure 4.16: z_{max}^* shown as a function of z_{obs} for each burst. Where a burst was detected at the maximum value of z_{sim} used ($z_{sim} = 12$) a lower limit is plotted.

Having identified three potential characteristics upon which z_{max}^* may depend, it was concluded that it is likely a combination of the first two that are most important. Bursts with intrinsically luminous pulses whose spectra are shallower (and therefore have a higher relative contribution from higher energies) will be detected to high simulated redshifts.

4.7 Conclusions

By isolating *Swift* GRBs with bright morphological features in their high–energy prompt light curves, the evolution of structure as each burst is moved to a higher simulated redshift has been studied.

Two methods of simulation were considered, both of which are detailed in §4.5. The first method takes photons received by BAT, and considers those that would fall in the 15–25 keV band, should the source frame properties of the burst be conserved when the GRB progenitor is moved to higher redshifts. This number of photons is then corrected for cosmological and instrumental effects. This method of simulation is initially attractive as it is entirely model

independent, thereby resulting in fewer assumptions being made about the observed emission.

Due to the large correction factors associated with the change in effective area at high values of z_{sim} and the ability to only simulate the 15–25 keV band the alternative method was more extensively used. This second method took the prompt pulse model discussed in Chapter 1 and applied it to a sample of 147 bursts. Of these 147, only 16 fulfilled all the selection criteria required for detailed study. By altering the properties of the modelled pulses (both their spectral and temporal parameters), it was possible to infer the BAT prompt light curve.

Part of the T_{90}^* algorithm determined whether a simulated GRB would have caused a rate trigger. This has led to a conservative estimate of the detected fraction of the sample at each redshift, due to the triggering criteria of BAT. Whilst it is possible for a rate trigger to also satisfy the image trigger criteria, an image trigger may not cause a rate trigger. Therefore there are some instances where the simulated light curves may have been sufficient to cause an image trigger but were deemed undetected.

Useful information was extracted from the simulated prompt light curves by measuring durations and hardness ratios in a homogeneous manner. Due to the format of the light curves produced by the simulation software, it was not possible to use the standard *Swift* routine BATTBLOCKS to estimate T_{90} . Instead an equivalent quantity, T_{90}^* , was designed to emulate the mechanism by which T_{90} is traditionally calculated. This met with success when tested on real light curves observed bursts with a good signal to noise ratio, as shown in Figures 4.4 and 4.5. In the case of fainter bursts, or those with a slow final decay, this estimate of duration was found to be more conservative than the value obtained from BATTBLOCKS.

Studying the evolution of T_{90}^* as a function of redshift revealed a complicated interplay between several competing factors. Figure 4.9 illustrates these effects clearly, with three important situations arising. Time dilation is clearly seen for some bursts (most notably GRB 080319B), during z_{sim} ranges when there is no complete loss of structure. GRB 080319B is the single burst in the sample whose rate of increase in T_{90}^* is most consistent with a factor of $(1 + z)$. For other bursts in which there is a similar power-law increase in T_{90}^* with respect to redshift the rate of dilation is slightly reduced. This is most likely due to the simultaneous loss of fainter parts of the pulses which are included at the extremes of the T_{90}^* interval.

This second effect can be seen in the evolution of other bursts, for which T_{90}^* gradually reduces as fainter morphology is lost. There is, however, another method by which T_{90}^* is reduced that is best demonstrated by GRB 100814A and GRB100906A. In such instances, late time structure becomes too faint to detect, and so only earlier structure is included in the T_{90}^* interval. When this occurs there is a large drop in measured duration, before either time dilation, or a more gradual loss of structure becomes the dominant behaviour once more.

When considering these three effects in the evolution of T_{90}^* it is not surprising that the observed population shows a broad diversity in measured duration. Another factor, which is not considered in this work, is that the number of pulses contained within a single burst appears to be random. When all of these factors are combined, it can be seen that there is no single dominant behaviour in the evolution of all bursts. Therefore, it is unlikely that a signature from time dilation should be seen when the observed population of bursts are examined as a whole.

The hardness ratios of the bright sample of bursts were also studied. The prevalent behaviour, particularly during redshift ranges in which time dilation is observed in T_{90}^* , is for bursts to become softer. This coincides with E_{pk} being reduced due to an increased simulated redshift. Some bursts are also seen to become harder (particularly at higher redshifts, when structure is at its faintest). In one instance, GRB 100814A, this increase in spectral hardness is accompanied by the loss of later, spectrally softer pulses.

The information from Figures 4.9 and 4.11 were coupled by producing a hardness–duration plot. Figure 4.12 illustrates this, showing how the evolution of both the spectral and temporal characteristics are related. This highlights the tendency for some bursts to be governed by cosmological time dilation and evolve to a prompt light curve containing longer, softer structure. It also shows bursts which are dominated by the gradual loss of fainter structure, most of which also become spectrally softer due to spectral evolution. Also shown are those bursts which have one or more of their later pulses fade below the level of detectability, causing a large drop in duration and in at least one case an associated hardening of the average prompt emission.

Finally, an alternative measure of duration has been introduced, T_c . This core time demonstrates more simple evolution with respect to redshift than T_{90}^* , as it only measures the brightest

parts of the prompt light curve morphology. This simple behaviour still contains a degree of scatter due to the number, duration and spectral indices of the pulses in any single light curve. As with other measures of GRB emission, it is the intrinsic variations between sources that mask any potential redshift indicator. As identified in Figure 4.1 there are variations within the population spanning at least two orders of magnitude. When the range in redshifts over which GRBs are routinely observed is only a single order of magnitude, any signature of cosmological time dilation is hidden by this scatter in the population.

One of the initial aims of this study was to investigate whether the effects of cosmological time dilation could be observed when evolving observed GRB prompt light curves. Figure 4.1 tentatively suggests that such evolution can be observed when averaging the entire population. By identifying 16 bright bursts, and simulating them each 100 times at each value of z_{sim} a large population of 1,600 light curves has been created that can be averaged in order to provide a better statistical study of time dilation. This is a significantly larger sample than the available population of bursts with measured redshifts (now approximately numbering 200). Whilst the total simulations provide a large sample size, the templates corresponding to these light curves still remain few. This has produced, therefore, a study which whilst instructive requires further work.

5

Simulations of GRBs at high redshifts

5.1 Chapter overview

In this Chapter, the work of Chapter 4 is extended. Both the entire fitted GRB population with redshifts and also a synthetic sample of bursts are used to do so. The evolutionary behaviour of the total observed population is studied and compared to observations of four high redshift bursts.

Finding that few GRBs remain detectable once simulated at the required redshifts, a synthetic population is created. This synthetic population is modelled on the observed distribution of bursts by using the distributions of pulse parameters actually fitted to BAT light curves. With a synthetic sample of 1,000 GRBs the statistics at high redshifts are improved, and more reliable results from the simulations are obtained.

In this Chapter comparisons are also made to previous work conducted by Kocevski (2012), to ensure the obtained results are consistent with previous studies.

In a final piece of analysis, the effects on measured burst properties using an improved instrument are considered. To make a direct comparison with previous samples, the same

synthetic sample is used in this analysis as previously discussed.

5.2 Introduction

Gamma-ray bursts (GRBs) have become a useful tool in directing the attentions of astronomers to galaxies that might otherwise require large and deep surveys to locate. Due to their unprecedented luminosities ($\sim 10^{51}$ ergs.s $^{-1}$) GRBs have been detected at redshifts as high as $z = 9.4$ (Cucchiara et al., 2011a), dating back to only 524 million years after the Big Bang. This means that such events can be used as diagnostic tools of the early Universe at a mass range that is otherwise inaccessible.

Through continuing efforts to obtain the data necessary to determine redshifts of bursts or their host galaxies, the population of GRBs with a measured redshift now numbers in excess of 200 (see, for example, Xiao & Schaefer 2011), with several found at $z > 6$. Whilst such events are rare their counterparts at more moderate redshifts are more frequent and, thanks largely to *Swift*, are numerous enough to make both quantitative and qualitative statements regarding the environments of their progenitors. Given that the Universe evolved significantly over the range of ages sampled, it is unclear whether the insight gleaned from nearer events is applicable to these rarer high redshift bursts. This is one of questions addressed in this work.

Simulations of the prompt emission of GRBs have been performed before, most recently including Kocevski (2012) as shown in Figure 5.1. To identify potential signatures of time dilation, Kocevski (2012) defined the shape and time evolution of GRB spectra to produce light curves similar to those observed by the BATSE. The simplest expectations for such simulations would be that time dilation should dominate the evolution of any measured duration. Instead, Kocevski (2012) showed that even for an ideal instrument with no detector noise, T_{100} (their temporal diagnostic of the prompt emission) did not increase at as fast a rate as cosmology would predict. When detector noise is included, this discrepancy is increased, with the evolutionary track also taking a different shape. T_{100} is seen to rise initially, again at a slower rate than cosmological time dilation alone would dictate. Eventually a point is reached where the duration stops increasing and begins to fall. This is due to the detector noise obscuring weaker

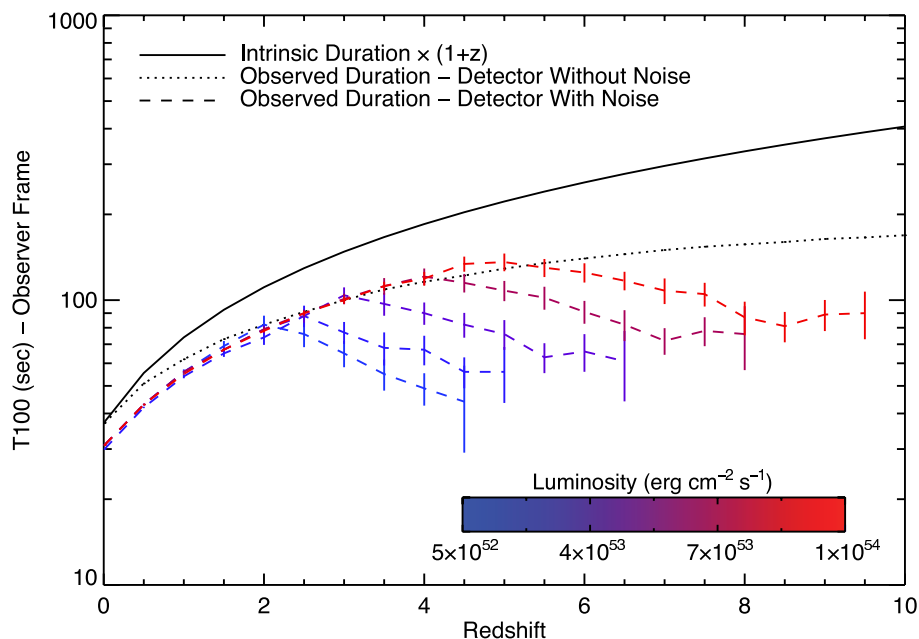


Figure 5.1: Figure taken from Kocevski (2012) showing the recovered T_{100} durations for simulations of bursts with a single pulse. The duration is measured in the observer frame.

parts of the light curve. The redshift at which this occurs is strongly related to the intrinsic luminosity of the pulse being modelled (each light curve consisting of a single pulse), with weaker pulses experiencing this turnover in the measured duration at smaller redshifts.

The work of this Chapter builds on both the work of Chapter 4 and Kocevski (2012) by simulating prompt light curves constructed using the prompt pulse model of Genet & Granot (2009) which is fitted following the methodology of Willingale et al. (2010). In §5.3 the available observational data are discussed, including a detailed description of four high redshift GRBs. Following this in §5.4 the details and creation of the synthetic sample are described.

5.3 Observations

As with Chapter 4 extensive use is made of the BAT on-board *Swift*. As previously discussed in §4.4, the four channel light curves are taken and, in conjunction with the 0.3–1.5 keV and 1.5–10.0 keV bands of the XRT are fitted with the prompt pulse model described in §1.6.

In the next section BAT and XRT observations of the four high redshift GRBs are presented in detail.

5.3.1 High redshift GRBs

The first GRB considered in detail in this Chapter is GRB 080913 (Greiner et al., 2009), a burst for which no flux was observed in the range $7,500 \text{ \AA} < \lambda < 9,400 \text{ \AA}$, leading to the interpretation of the onset of a Gunn–Peterson trough at a redshift of $z = 6.695 \pm 0.025$. Analysis of the high–energy emission as seen by the BAT on board *Swift* showed that the burst had a $T_{90} = 8 \pm 1$ seconds (Stamatikos et al., 2008).

More recent bursts have been observed at even greater redshifts than GRB 080913. These include GRB 090423 (Tanvir et al., 2009), which has the highest spectroscopically confirmed redshift of any burst to date at $z = 8.23^{+0.06}_{-0.07}$. GRB 090423 had a BAT $T_{90} = 10.3 \pm 1.1$ seconds (Palmer et al., 2009).

Within a week of this object being observed, GRB 090429B was detected. Initially observed with *Swift* (Ukwatta et al., 2009) the high–energy morphology as seen by BAT is dominated by a single period of activity at the trigger time leading to a $T_{90} = 5.5 \pm 1.0$ (Stamatikos et al., 2009). GRB 090429B has a photometric redshift of $z = 9.4^{+0.12}_{-0.34}$ (Cucchiara et al., 2011a).

The final burst included in the high redshift sample is GRB 100905A. This was another GRB detected by *Swift* (Marshall et al., 2010), with $T_{90} = 3.4 \pm 0.5$ seconds (Barthelmy et al., 2010). From the initial analysis of the ground–based observations taken by the GROND and the United Kingdom Infrared Telescope (UKIRT; Casali et al. 2007) it appears GRB 100905A occurred in range $7 < z < 7.5$. The total 15 – 350 keV light curves for all four of the high redshift bursts are included in Figures 5.2 to 5.5.

When considering the four bursts as a joint sample it is interesting to note that these durations all lie within a range $0.4 < \frac{T_{90}}{(1+z)} < 1.26$ seconds. This is a very restricted part of the total distribution and suggests that there are intrinsic similarities between the emission being observed in the four cases. The hardness ratios for the four are also similar, further suggesting that the four GRBs might share common properties in their source frame.

That all four bursts have durations which, when corrected into the source frame, are shorter than 2 seconds is of interest as this time marks the classic boundary between long and short bursts. It is important to remember, however, that the demarcation in duration between long

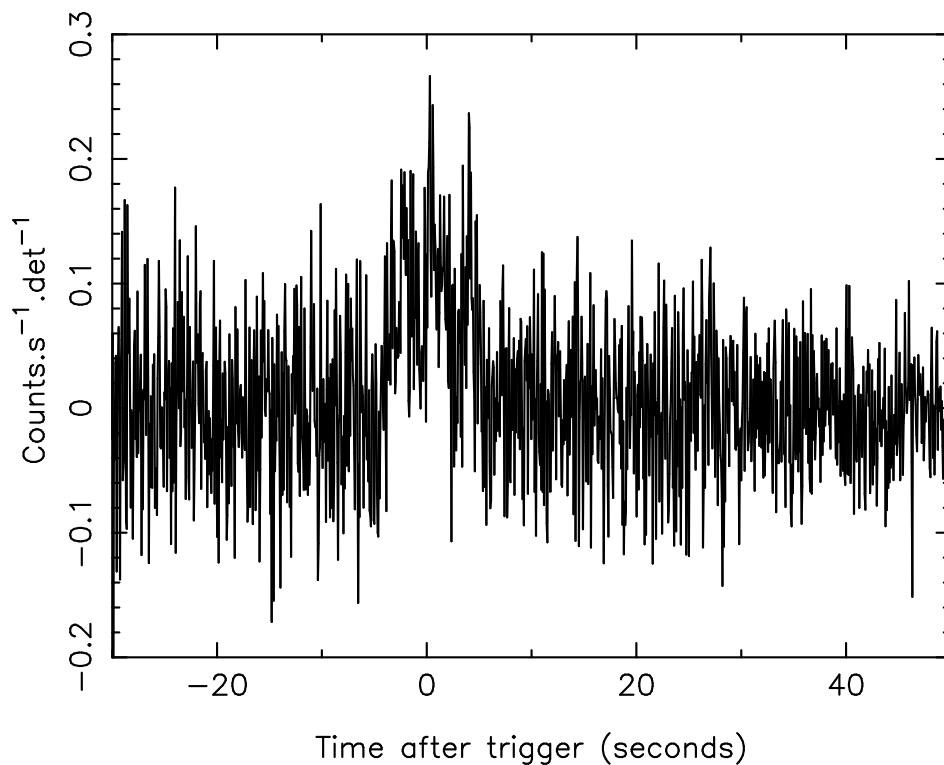


Figure 5.2: 15 – 350 keV BAT light curve of GRB 080913

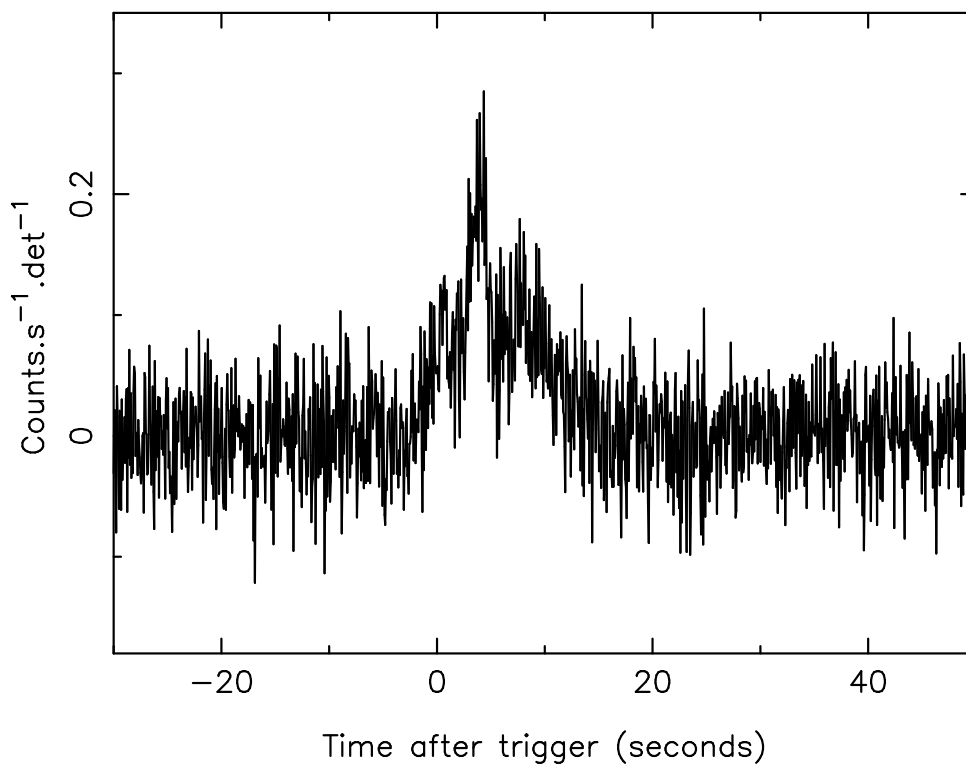


Figure 5.3: 15 – 350 keV BAT light curve of GRB 090423

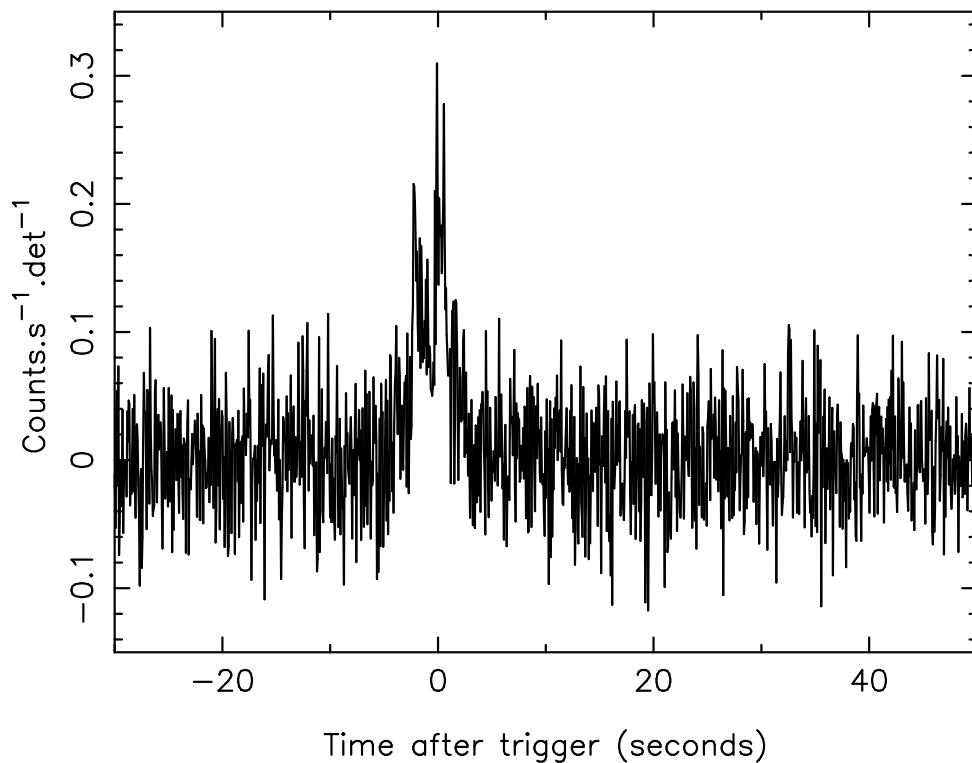


Figure 5.4: 15 – 350 keV BAT light curve of GRB 090429B

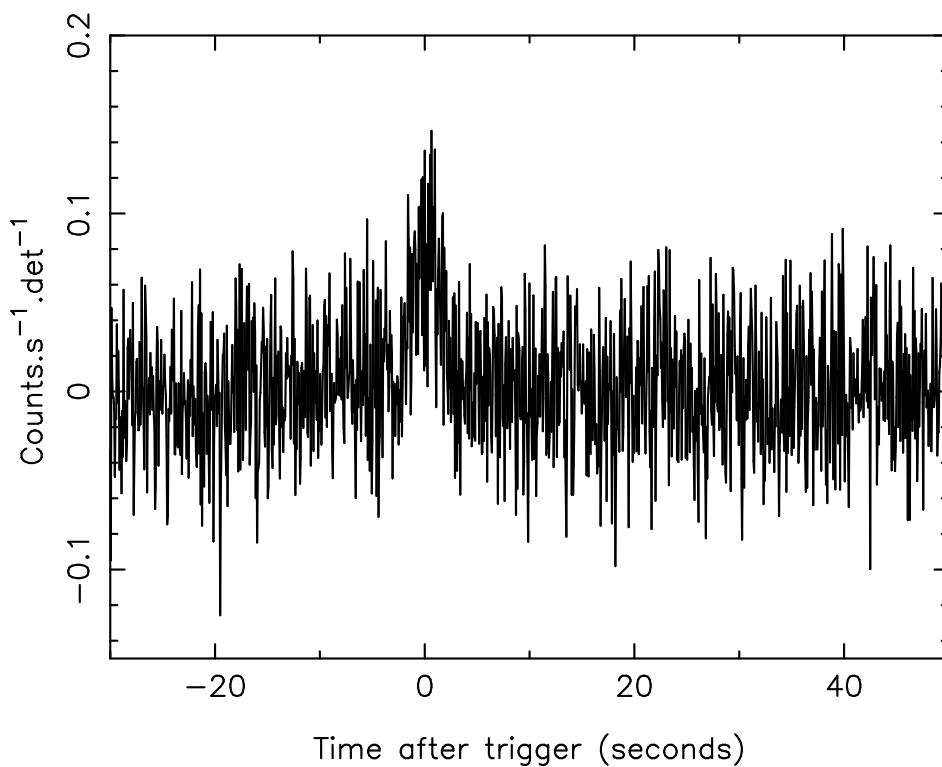


Figure 5.5: 15 – 350 keV BAT light curve of GRB 100905A

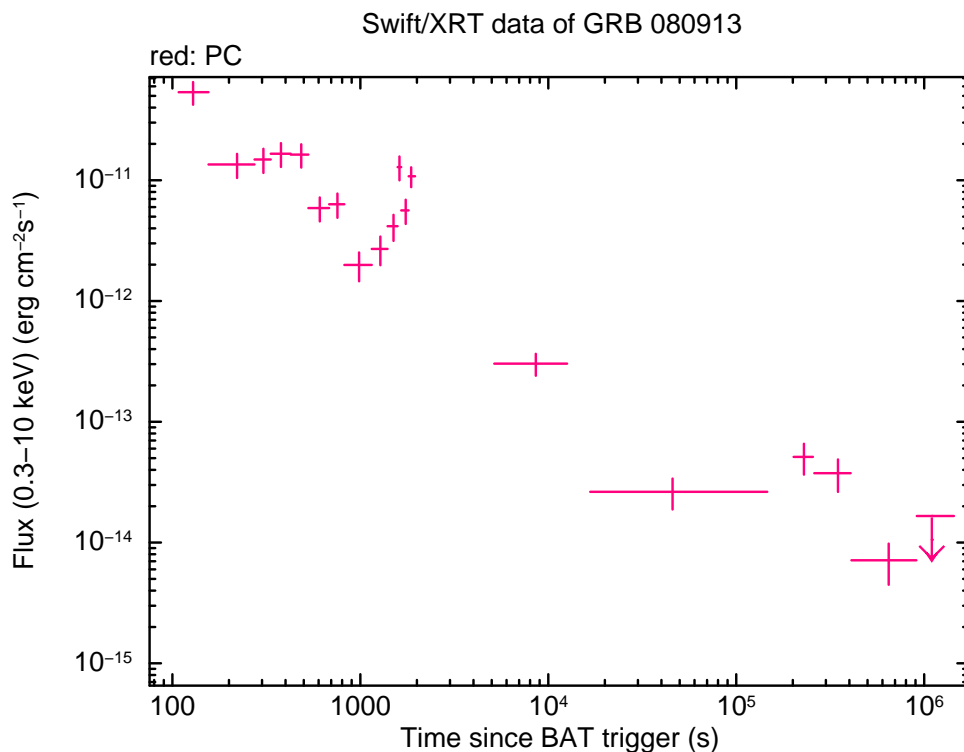


Figure 5.6: 0.3 – 10 keV XRT light curve of GRB 080913

and short GRBs is a distinction made entirely based on the observed frame values of T_{90} , which for these bursts are typically 10 seconds. Additionally, analysis from Bromberg et al. (2012) suggests this division to be at a lower value in the *Swift* population. In this Chapter, real and simulated BAT data have been used to ascertain whether these low T_{90} high redshift bursts are atypical or simply representative of the complete long GRB population.

For further insight into the nature of these bursts, the XRT light curves obtained for each are shown in Figures 5.6 – 5.9. It is difficult to identify some of the canonical behaviour expected in X-ray GRB light curves (Evans et al., 2009; Nousek et al., 2006). The onset to features such as the rapid decay phase (RDP) should be expected to occur later after the trigger due to cosmological time dilation. With the exception of GRB 090429B flares are seen in the XRT light curves of the bursts shown. Such features would correspond to pulses too weak to be detected by BAT due to its smaller dynamic range and higher energy spectral coverage. As the detected flux in the XRT is faint in comparison to other bursts, the quality of the light curves is poorer, resulting in greater difficulty in determining the exact X-ray morphology.

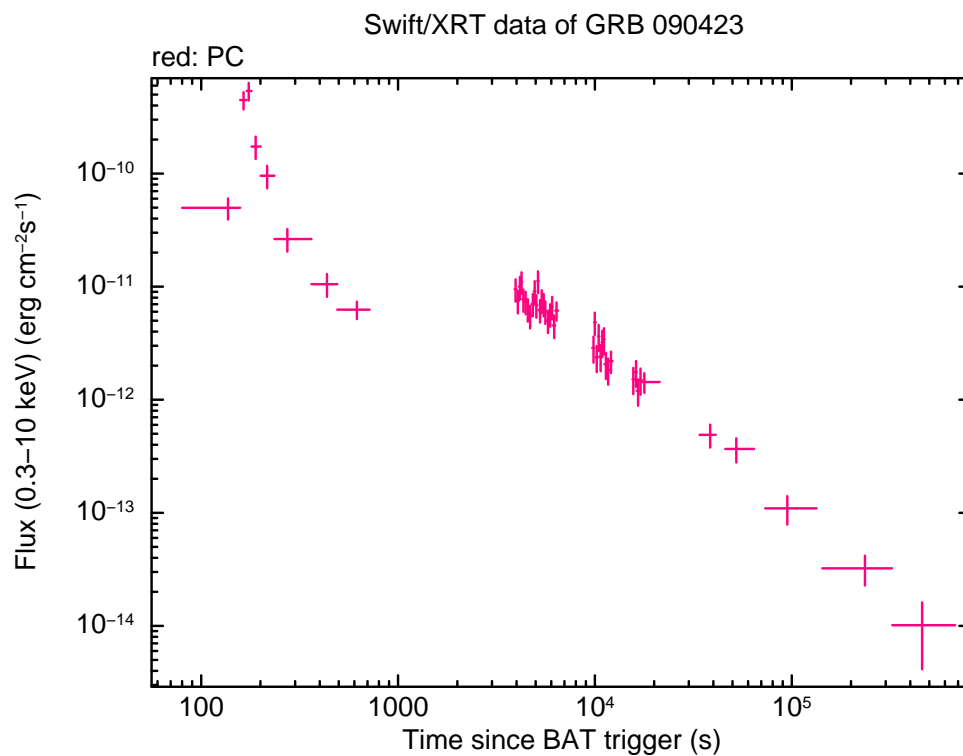


Figure 5.7: 0.3 – 10 keV XRT light curve of GRB 090423

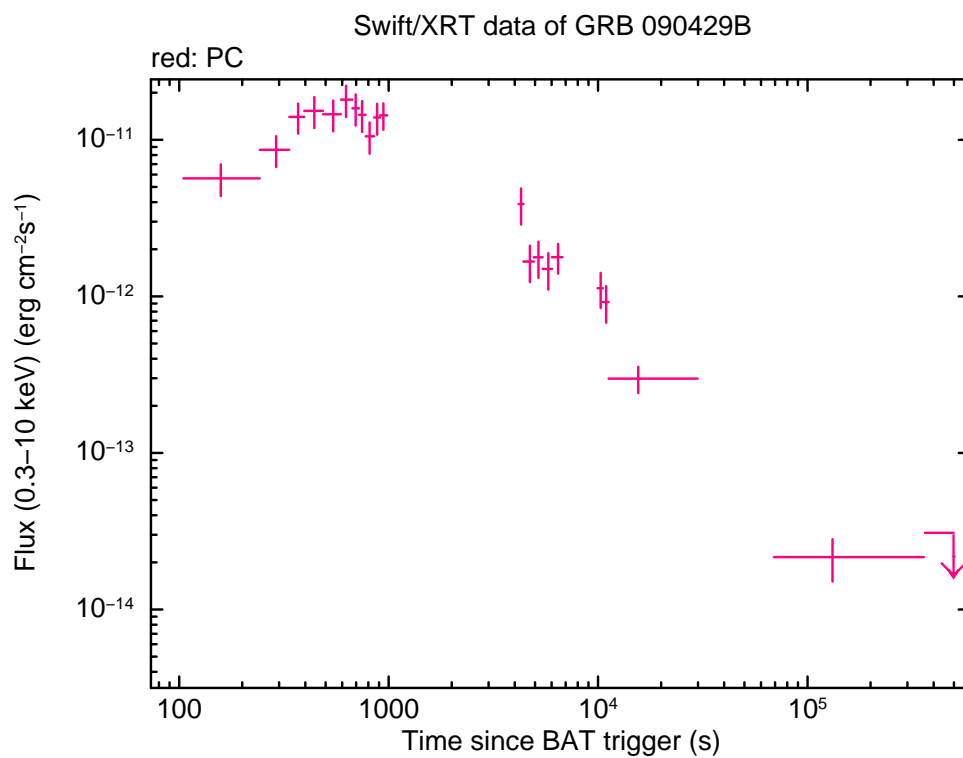


Figure 5.8: 0.3 – 10 keV XRT light curve of GRB 090429B

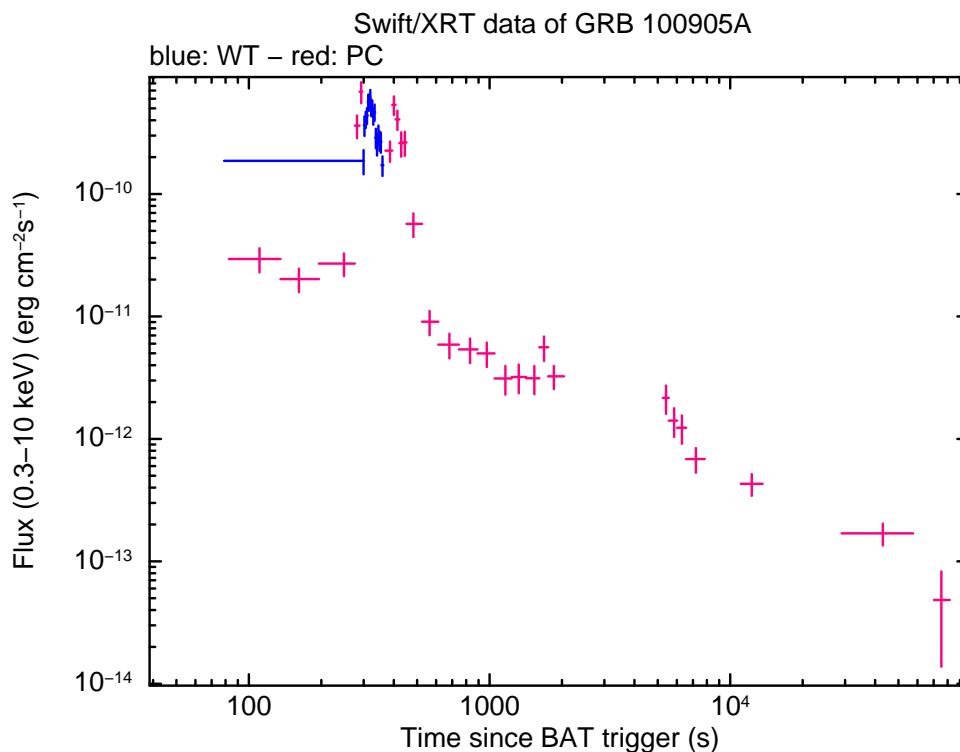


Figure 5.9: 0.3 – 10 keV XRT light curve of GRB 100905A

5.4 Modelling

The prompt pulse model as detailed in §1.6 was used. Pulses have been fitted to the observed BAT and XRT data for 147 bursts. Of these, 126 have been considered in this Chapter due to early XRT coverage and available redshift measurements. By evolving the characteristic times, energies and normalising fluxes that describe each pulse and the accompanying afterglow component as detailed in §4.5.2, each burst was simulated at a variety of redshifts. The results of this are discussed in §5.5.1.

5.4.1 Creating a sample of synthetic bursts

With a high attrition rate in the detected population (see §5.5.1) there are too few actual bursts detected at high simulated redshifts to compare the observed high redshift GRBs to their low redshift analogues. A fully synthetic population of 1,000 GRBs was therefore also produced. With a population of such size, the number of bursts detected at such redshifts should significantly increase. Detailed below is how this sample of synthetic bursts was produced, and how

it has been made to reflect the actual observed GRB population.

Three key variables were identified upon which the duration of a burst relied. These were the number of pulses in the light curve, N_p , the average duration of each of these pulses, \bar{T}_f , and finally the average delay between subsequent pulses \bar{T}_g (where for pulse N , $T_g = T_{pk,N} - T_{pk,N-1}$). The quantity \bar{T}_g is analogous to the average pulse delay as suggested by Kocevski (2012). These parameters were combined to create a proxy that could be used to estimate the T_{90} of each of the bursts already observed and fitted. All three durations, T_{90} , \bar{T}_f and \bar{T}_g , were evaluated at a common redshift of $z = 2$, as the synthetic population was initially generated at this redshift, before evolving it to higher luminosity distances.

The best statistical fit found is shown in Equation 5.1, where A and B are constants that were fitted. It is interesting to note that \bar{T}_g does not appear in this expression. A model with a similar value of χ^2 was found including the average delay between pulses, but this reduced the number of degrees of freedom, so the model with the fewest free parameters was chosen.

$$T_{90} = A\bar{T}_f N_p^B. \quad (5.1)$$

Values for A and B were found using a χ^2 fitting routine, the results of which are demonstrated in Figure 5.10.

To begin simulating each synthetic burst, a random value was then chosen from the cumulated normalised distribution of measured T_{90} values once placed at $z = 2$. To estimate N_p a random value was similarly drawn from its observed cumulated distribution. To ensure that self-consistency, the N_p distribution was split into three bins based on the value of T_{90} for the burst in the $z = 2$ frame. This meant the distribution of N_p as a function of T_{90} remained realistic, without producing large number of bursts with either short durations and many pulses, or conversely a very long duration burst with a single pulse. The real and synthetic populations of N_p are shown in Figure 5.11.

Once values of T_{90} and N_p were established, corresponding values of \bar{T}_f were calculated using Equation 5.1 and the fitted values for A and B . For each of the pulses in the sample the fraction of the average duration was calculated.

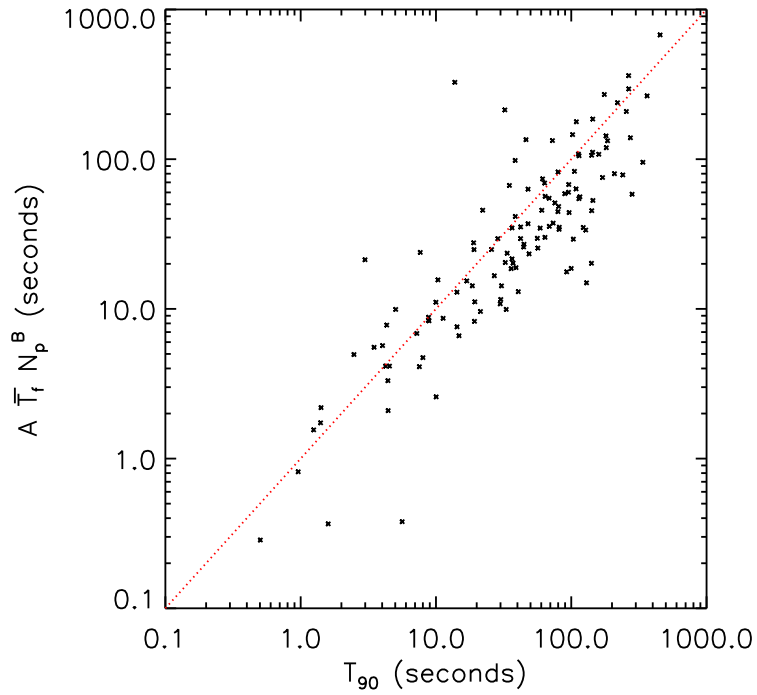


Figure 5.10: The fitted model of duration, as described in Equation 5.1, as a function of the T_{90} value as measured by BAT. In this fit $A = 0.64^{+0.09}_{-0.09}$ and $B = 0.93^{+0.07}_{-0.06}$. Equality is shown by the red dotted line.

$$f(\bar{T}_f) = \frac{T_f}{\bar{T}_f}. \quad (5.2)$$

Having a mean value of pulse duration for every burst, this had to be converted to an actual duration for each individual pulse. To do so, the distribution of $\frac{T_f}{\bar{T}_f}$ for real bursts was used, once shifted to $z = 2$ (as shown in Figure 5.12). By drawing numbers from this, the individual pulse durations were calculated by multiplying the random fractions by the average pulse duration for that burst.

To find the time each pulse peaked, random numbers from a uniform distribution were used once more. The first pulse was set to peak at $T_{pk} = 0$ seconds. For subsequent pulses, the uniform random number drawn was used to determine the fraction of T_{90} which had elapsed by the time the pulse peaked.

Some of the remaining parameters, such as the normalisation, rise time of each pulse and the corresponding spectral index were found to be related to T_f . For the pulse normalisation,

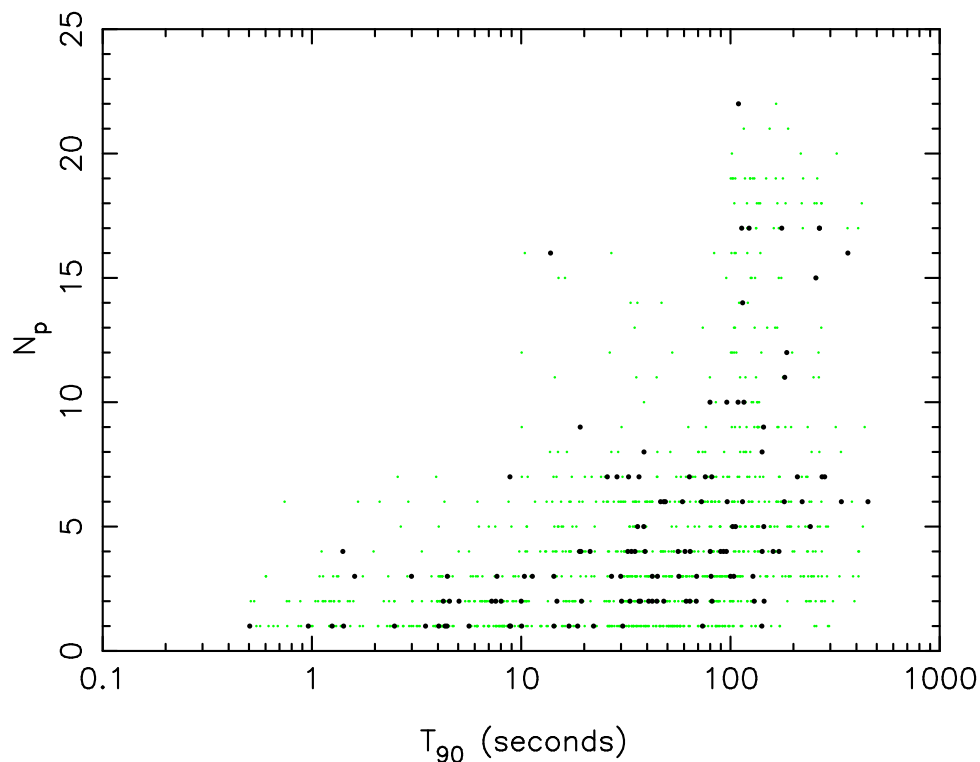


Figure 5.11: A graph comparing the distribution of the synthetic values of N_p as a function of measured T_{90} to the fitted observed bursts. The synthetic GRBs are denoted by green points, whilst the black points correspond to real bursts.

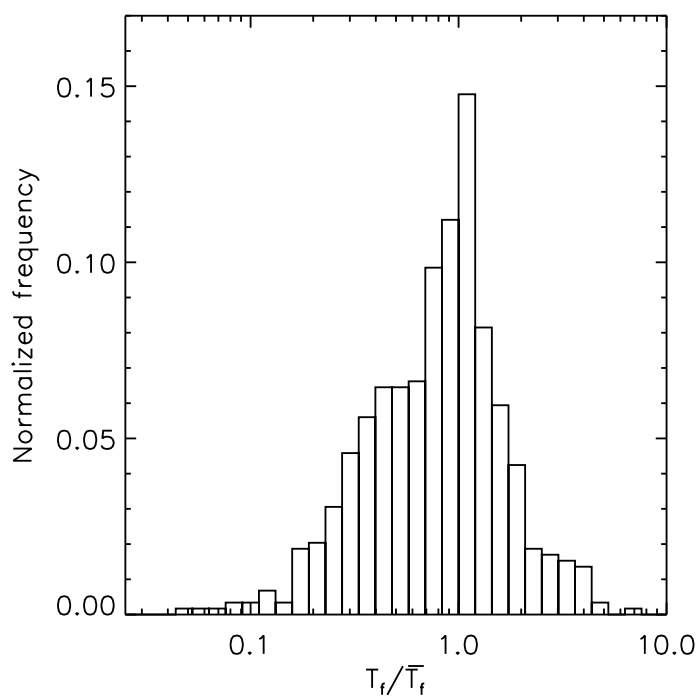


Figure 5.12: Distribution of $\frac{T_f}{\bar{T}_f}$ for all bursts corrected to a common redshift of $z = 2$. The frequencies in each bin of the histogram have been normalised using the total number of bursts in the sample.

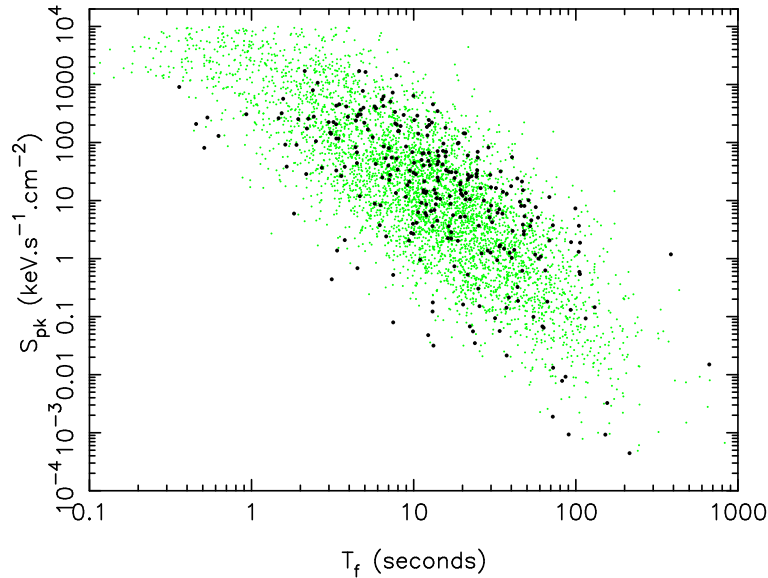


Figure 5.13: Observed and synthetic values of S_{pk} as a function of T_f . Black points show the observed values (once shifted to $z = 2$) and green points show the resulting synthetic population at the same redshift.

S_{pk} , and the rise time, T_r , a power-law dependence on T_f was fitted. For the spectral index of the pulse, b_1 , a log-linear relation was used. Scatter in the relations was also accounted for in the form of a Gaussian distribution. As with T_f , all pulse parameters were first altered so they were at a common redshift. For the durations, this was a simple matter of using Equation 4.9, where $z_{sim} = 2$. For the normalisation, the k-correction also had to be considered, and so Equation 4.11 was used. Care was taken to only include pulses observed by BAT, as the pulse fitting routine also identified X-ray flares as seen by the XRT. The synthetic and observed distributions of b_1 , S_{pk} and T_r as functions of T_f are shown in Figures 5.13 – 5.15.

Adhering to the methodology of Willingale et al. (2010) and the manner in which subsequent light curves of observed bursts were fitted, the values of the remaining parameters were fixed. The index governing the temporal evolution of E_{pk} was set to $d = -1$, which is consistent with synchrotron radiation. For the majority of the observed GRBs the value of E_{pk} was not within either the BAT or XRT spectral range, and so was fixed to be 200 keV. This corresponds to the peak of the νF_ν spectrum at the time T_{pk} when the pulse peaks temporally.

To ensure that the synthetic population of bursts were as faithful representations of the observed counterparts on which they were based synthetic afterglows were also included. The afterglow parameters that were required were the spectral index, b_a , the temporal index of

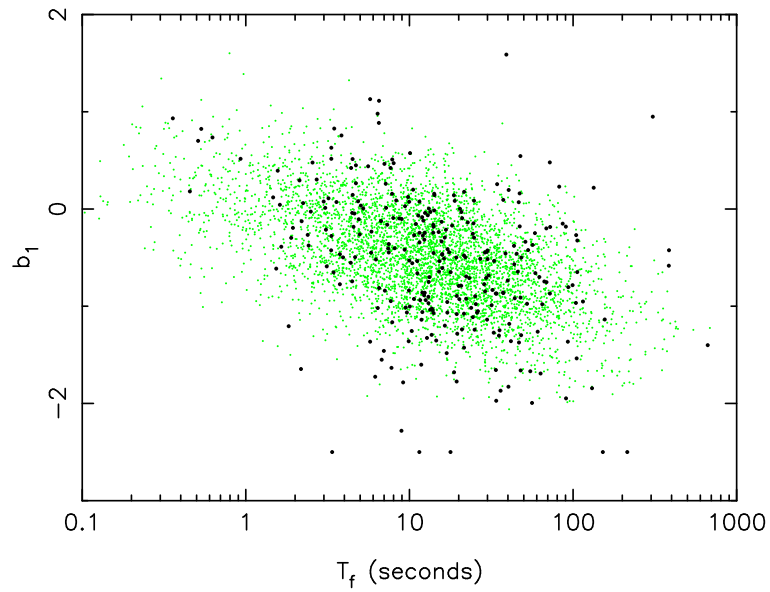


Figure 5.14: Observed and synthetic values of spectral index, b_1 , as a function of T_f . Black points show the observed values (once shifted to $z = 2$) and green points show the resulting synthetic population at the same redshift.

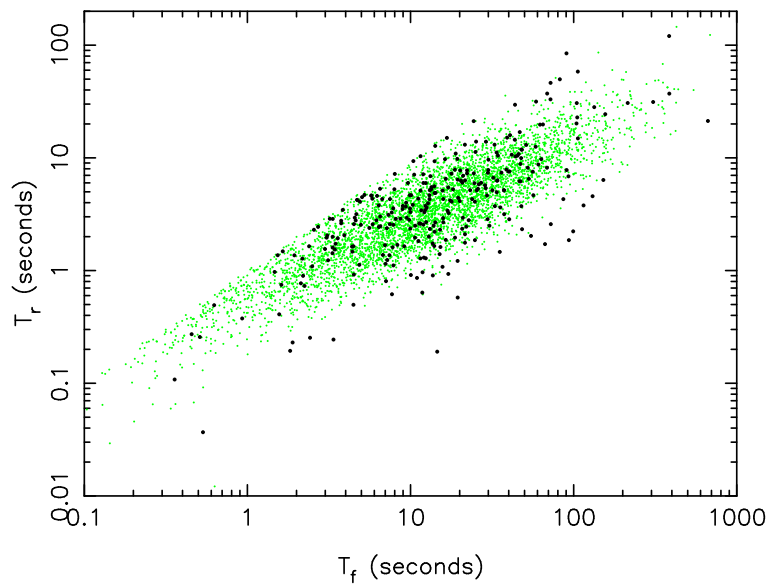


Figure 5.15: Observed and synthetic values of T_r as a function of T_f . Black points show the observed values (once shifted to $z = 2$) and green points show the resulting synthetic population at the same redshift.

b_a , g_a , the afterglow rise time, T_r , the transition time between the exponential and power-law regimes in the morphology, T_a , the normalising flux across the XRT band, S_a , and finally the temporal index describing the power-law decay phase, α_a . Additionally, if a late temporal break was identified in the observed BAT and XRT light curves, a further two parameters were required to fully describe it. These were the time at which the power-law broke T_b and increment by which α_a changed, α_b . For a fuller description of the morphological afterglow see Willingale et al. (2007). As with the prompt pulse parameters, all times were dilated so that they corresponded to what would be expected at a common redshift and the normalisation was altered to reflect the change in luminosity distance.

As with the prompt pulses, several of the afterglow parameters were fixed to predetermined values. These were the rise time, $T_r = 100$ seconds and $g_a = 0$, the latter implying that the spectrum of the afterglow does not evolve with time. T_a for each of the 1,000 synthetic afterglows was simulated in a similar manner to T_f for the synthetic pulses; the observed values were cumulated and uniform random numbers used to interpolate values from the cumulative distribution. b_a , S_a and α_a were determined using their relations to T_a in the method described for the secondary prompt pulse parameters.

To determine whether a late temporal break was present in the synthetic afterglows, the fraction of observed afterglows containing one was calculated. A uniform random number was drawn for each of the synthetic afterglows, if it was less than or equal to this fraction, a late break was included. T_b and α_b were calculated using the same methodology as the other afterglow parameters.

As with the observed population of bursts, the pulse and afterglow characteristics were evolved with redshift to see how the total light curve and measurable parameters such as T_{90} evolved as a function of redshift.

The processes used in these simulations are the same as those employed for the bright bursts subset of Chapter 4. The durations measured were therefore T_{90}^* , as described in §4.5.4. The determination of whether a light curve had sufficient signal to cause a rate trigger is also detailed in §4.5.3.

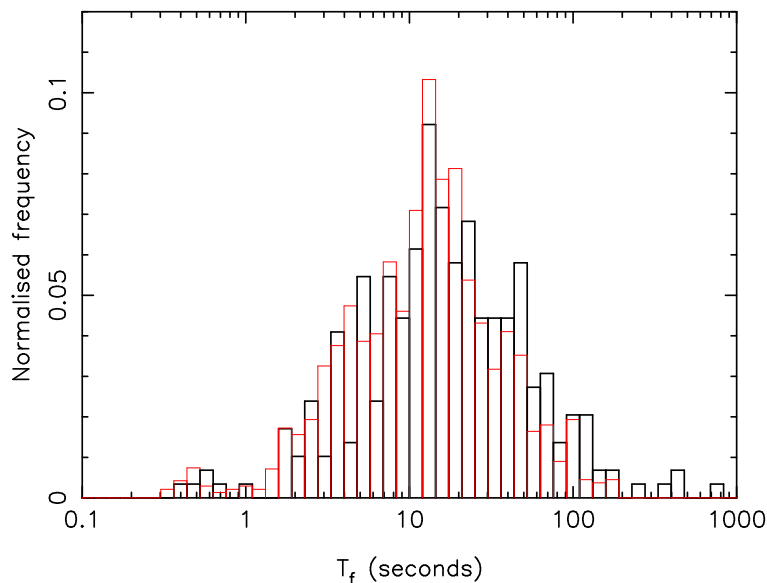


Figure 5.16: Comparison between observed and synthetic T_f distributions. The black population is the observed distribution and the red population contains the synthetic pulses. To allow a direct comparison both populations have been normalised to a total sample size of 1.

5.4.2 A critical evaluation of synthetic pulse parameters

The synthetic distributions of S_{pk} , b_1 and T_r as shown in Figures 5.13, 5.14 and 5.15 follow the trends of their observed counterparts. However, more careful analysis of them shows that the distributions appear to be narrower than the observed populations of pulses. To investigate the causes of this first the observed and synthetic distributions of T_f were compared, as shown in Figure 5.16.

Figure 5.16 shows via direct comparison that the distribution of synthetic pulse T_f values is a good representation of the broad morphology of those T_f values observed in real bursts once redshifted to $z = 2$. The two differ slightly at higher values of T_f , with there being more observed pulses with $T_f > 40$ seconds. Whilst this leads to a slight discrepancy between the two populations, most of these long duration pulses are likely to be X-ray flares fitted to the XRT data, which are not seen in the BAT light curves.

A simpler method of generating T_f for each synthetic pulse would have been to use the observed distribution, corrected to $z = 2$, as a probability distribution. However, by considering $\frac{T_f}{T_f}$ the pulses produced more accurately reflect the total duration of the GRB. In this way more realistic light curves with self-consistent sets of pulses are produced.

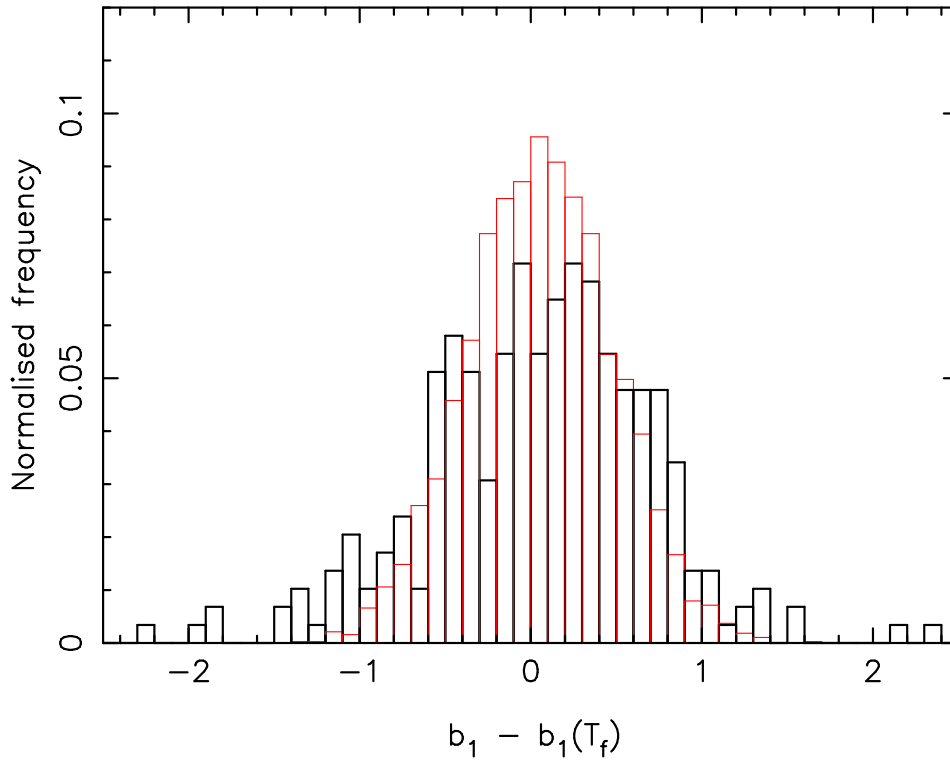


Figure 5.17: Scatter in b_1 real and synthetic distributions. The black distribution corresponds to the observed GRB pulse population shifted to $z = 2$, whilst the red distribution is the synthetic pulse population.

To produce the full set of pulse parameters, S_{pk} , b_1 and T_r were obtained using the observed dependencies on T_f . It is at this point that the discrepancy was thought to arise. To investigate this the scatter of both the observed and synthetic populations of S_{pk} , b_1 and T_r was found.

To calculate the spread of the data, the model value of the parameter (S_{pk} , b_1 and T_r) was calculated using T_f . The difference between this and the actual value was taken. Histograms of these values are shown for b_1 and T_r in Figures 5.17 and 5.18, respectively.

Figure 5.17 clearly illustrates that the synthetic population is more centrally condensed about the log–linear model of $b_1(T_f)$ than the observed population to which $b_1(T_f)$ was fitted. The result of this is that the hardest and softest pulses of any given duration are removed from the synthetic population. These are not numerous, though.

As the population is averaged, at low simulated redshift the effects of altering these pulses should not be pronounced, as at these redshifts there are a large number of other pulses detected within the synthetic burst population. However, having steep spectra, in both a positive and

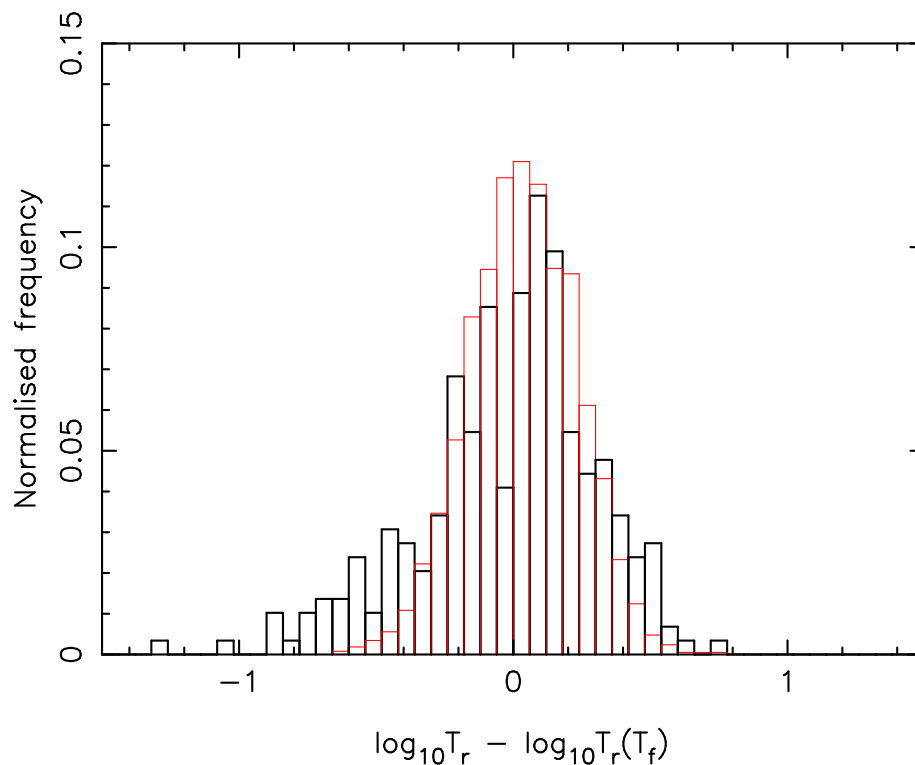


Figure 5.18: Scatter in T_r real and synthetic distributions. The black distribution corresponds to the observed GRB pulse population shifted to $z = 2$, whilst the red distribution is the synthetic pulse population

negative sense, makes a significant impact on the received flux from a pulse at high redshifts. The spectral break E_{pk} evolves as shown in Equation 4.10. As such, it migrates to lower energies at higher redshifts. If b_1 is both steep and negative, as E_{pk} shifts to lower energies the received flux from such a pulse would fall rapidly as a function of redshift. As such it would be expected that these pulses would not be detected at high redshifts.

Conversely, with harder spectra, where b_1 is steep and positive, it would be expected that the pulse would remain detected up to high redshifts providing the normalisation S_{pk} is not small. As a result, even when other structure in the synthetic burst is no longer detectable, such a pulse should remain visible in the high-energy light curve. With a dearth of such pulses, the number of bursts detected at the highest redshift may be under-estimated.

The fit to the observed T_r distribution at $z = 2$ was performed using a power-law. As such, when calculating the difference between the ideal synthetic value of $T_r (T_f)$ and that used once scatter had been included the difference was actually take between $\log_{10} T_r$ and $\log_{10} T_r (T_f)$. As with b_1 the synthetic population is narrower than the observed population on which it is

modelled.

Unlike the synthetic b_1 population, the difference in the T_r distributions is asymmetric, with a larger number of bursts missing when $\log_{10} T_r - \log_{10} T_r(T_f) < 0$. The asymmetry is due to the population having a hard upper limit of $T_r < T_f$, that is that the pulse must rise within its total duration.

That there are pulses missing in the synthetic population with $\log_{10} T_r - \log_{10} T_r(T_f) < 0$ implies that the population is missing some of the fastest rising pulses. This does not affect the likelihood of a pulse being detectable, as S_{pk} and T_{pk} are independent of the rise time. The important effect that these longer rise times has is to lengthen the observed duration of the pulse. Should these pulses be the first or only detected pulse in a GRB light curve, then the measured duration of that burst will be accordingly longer. The amount by which the T_{90}^* estimate would be expected would be small, however, as each pulse has a FRED format, with the exponential decay dominating the pulse duration. Additionally, if there are quiescent regions of the GRB light curve between detected pulses, then the slight increase in T_r will become negligible in comparison to the duration of these regions.

5.5 Discussion

5.5.1 Pulse simulations of real bursts

The 126 bursts which had both been modelled using the Willingale et al. (2010) methodology and had a measured redshift were simulated. To allow the calculation of properties such as the average T_{90}^* within the population the values of z_{sim} that were used were held constant for all bursts. The simulations began at $z_{sim} = 2$ and, in increments of $\Delta z_{sim} = 0.5$, were conducted up to $z_{sim} = 12$.

Approximately half of the total sample had $z_{obs} > 2$, and so these bursts had instances where they were simulated at redshifts lower than those at which they were observed. Whilst those pulses which were observed were successfully transformed to z_{sim} it is important to note that it was not possible to infer any structure that may also have been visible should the burst have occurred at a lower redshift. As such the durations for any burst when $z_{sim} < z_{obs}$ may be

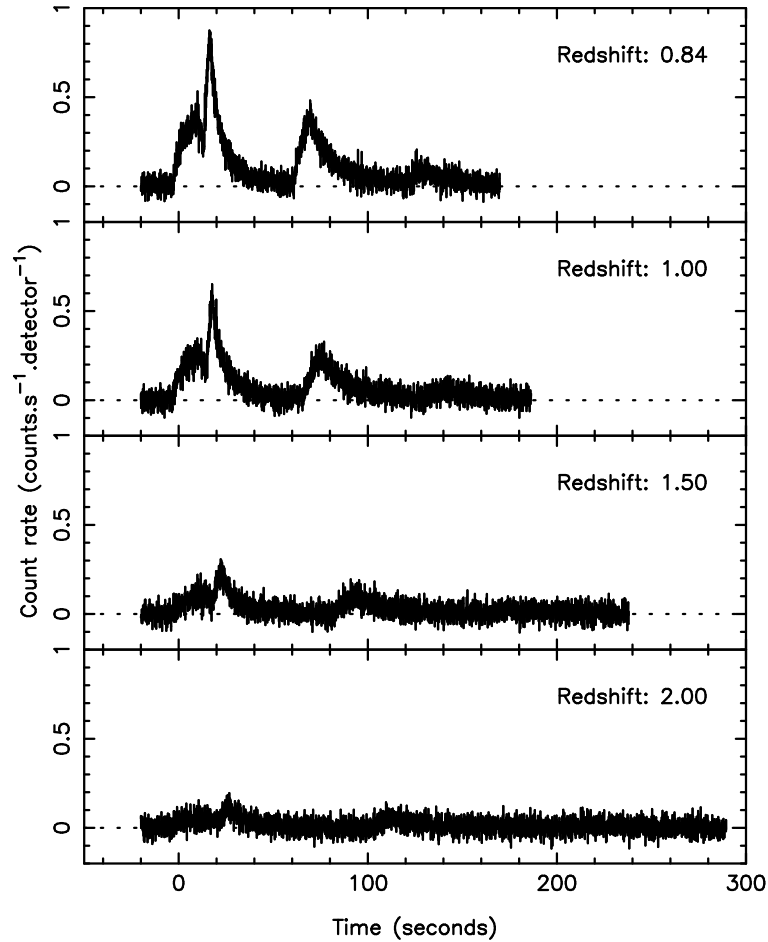


Figure 5.19: Simulations of the 15 – 350 keV band for GRB 060814. The values of z_{sim} used for each light curve are displayed on each panel.

underestimated due to the lack of this weaker structure. These pulses could be undetected at high redshifts due to either lower values of S_{pk} , steep pulse spectra or a combination of both.

As an example of the evolution observed, Figure 5.19 shows the 15 – 350 keV light curve for GRB 060814 at a variety of simulated redshifts. This is a good example of the loss of structure previously discussed. Had GRB 060814 been observed at $z = 2$, then several of the pulses seen at z_{obs} would not be identified in the light curve. Additionally, the signal to noise ratio of those features which could have been modelled would have been lower, thereby reducing the accuracy of the fitted parameters.

The number of pulses identified in each GRB was studied as a function of the observed redshift, as shown in Figure 5.20. With the exception of the highest redshifts the $N_p(z_{obs})$ distribution has a large amount of scatter that appears to be constant in redshift. For the highest redshift GRBs, this is not the case, with a tendency for these bursts to have two or three

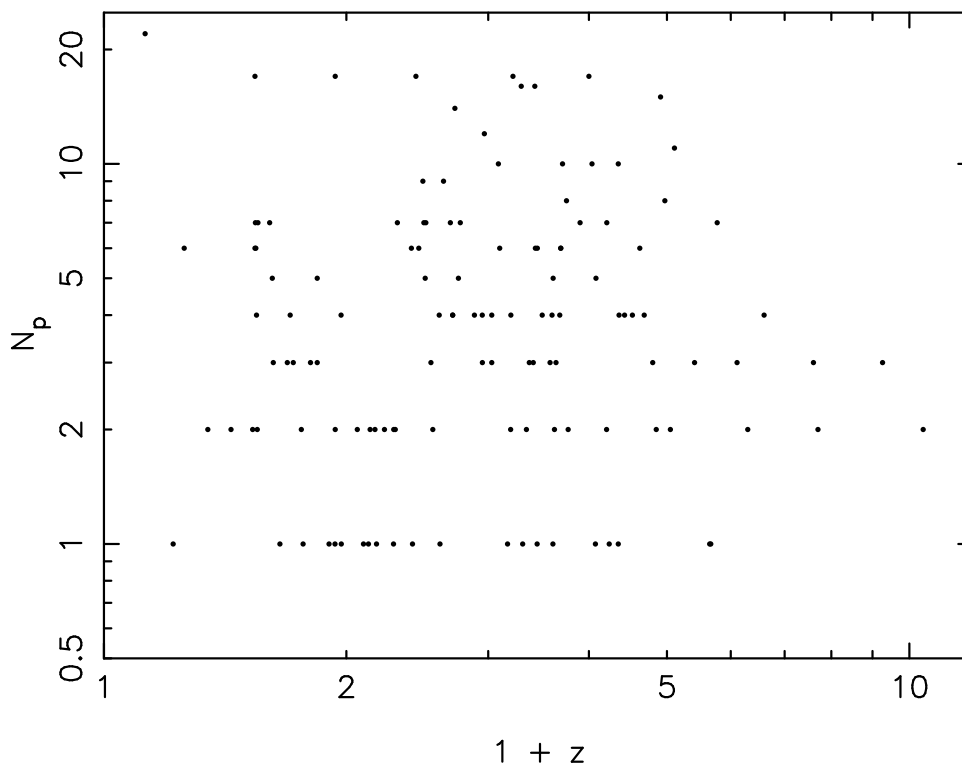


Figure 5.20: Number of pulses, N_p , modelled within each prompt light curve as a function of z_{obs} .

identified pulses.

Having used the T_{90}^* algorithm on each of the simulated light curves, it was possible to determine to which values of z_{sim} each GRB was detected. The fraction of the burst population that was detected at each value of z_{sim} was compared to the fraction detected at $z_{sim} = 2$. Figure 5.21 shows that of the 107 bursts that are detected at $z_{sim} = 2$, 21 would be observed at $z_{sim} = 12$. Whilst this appears to be a high fraction, it is important to remember that $z_{sim} - z_{obs}$ in some cases is quite low as there are 13 bursts where $z_{obs} > 4$. In these cases the corresponding value of z_{factor} is limited to 2.6, creating only a small change in the modelled pulse parameters.

One of the most notable characteristics of the highest redshift bursts observed is their duration. The four examples considered explicitly in §5.3.1 all have measured T_{90} values of approximately 10 seconds. Whilst the sample size remains small, it might be expected that a burst containing several bright pulses could remain detected with a quiescent period lengthened by increased time dilation. Such a burst would result in a longer measured duration. In Chapter 4 the evolution of T_{90}^* for a bright subset of bursts was investigated. For these GRBs, it was

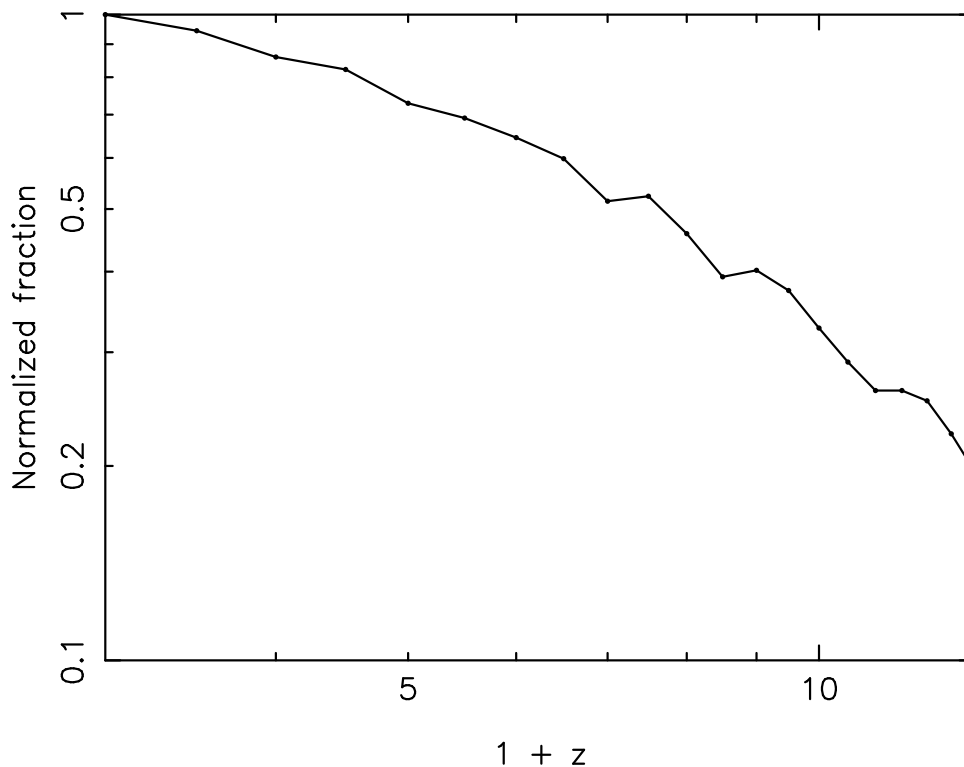


Figure 5.21: Detected fraction of real burst population as a function of simulated redshift. The values have been normalised using the total number of bursts detected at $z_{sim} = 2$.

noted that those examples where time dilation dominated the behaviour of the light curve to redshift comparable with bursts such as GRB 090423 or GRB 090429B were few. Instead, two other effects were also important: the gradual loss of the edges of pulse structure which could lead to the sudden loss of a pulse entirely. Those bursts which were bright enough to be detected at $z_{sim} = 8$ were few, with the typical measured T_{90}^* being in excess of 20 seconds. Such measurements prove to be inconsistent with those taken for the four high redshift bursts that have been discussed in detail.

Unlike in Chapter 4 the entire sample of bursts has been considered rather than a bright subset. In Chapter 4 each burst was simulated 100 times to improve the signal to noise properties of $T_{90}^*(z_{sim})$. Whilst the statistics of this study are poorer per burst, there is a significant gain from each set of simulations having a unique combination of pulses. Additionally, the non-detection of some of the bursts is also instructive, as it allows the fraction of bursts not powerful enough to be detected from their light curves at each value of z_{sim} to be considered.

Figure 5.22 shows the evolution of this average T_{90}^* . Due to the large amount of scatter in the observed T_{90} distribution (see Figure 1 of Chapter 4) and the power-law behaviour of

cosmological time dilation, the geometric average was used. The error bars on each of the blue bins containing observed GRBs denote the standard error in each case. The extent in the redshift axis shows where the minimum and maximum redshifts of the bursts within each bin lie. These bins were selected to contain equal numbers of bursts, with all but the final bin containing 20 GRBs. The final bin lacked sufficient bursts to retain the same bin size, and so it is the average of only 14 bursts.

Figure 5.22 shows several important features. The first of these is that the evolution of the average T_{90}^* of the total population does not follow time dilation. The average of the entire sample is denoted by the solid black line, and it shows little evolution with z_{sim} . This is despite some bursts becoming too faint to be detected. Initially, there is an offset between the average simulated T_{90}^* and the first bin containing the average of the observed population. This is because the evolutionary track of T_{90}^* is the average across the entire population, whilst the bin at $z_{sim} \sim 2$ contains an average of only 20 bursts. With bursts at lower redshifts containing a slightly lower duration (see Figure 1 in Chapter 4), the total average is reduced in comparison. The T_{90}^* track shows good agreement with the final average point, however this average has large associated errors. To further highlight the diversity within the bin, we have shown the four highest redshift GRBs separately with the red points. As can be seen, these lie significantly below the average values shown for both the 14 highest redshift bursts and the T_{90}^* track.

To further understand the sample in detail, it was split according to a luminosity threshold. The prompt parameters of each pulse within a light curve were analysed with three subsamples being selected based on the value of L_{pk} of each pulse. A threshold of $L_{pk} = 1 \times 10^{51}$ ergs.s⁻¹ was set to which each pulse was compared. This threshold was defined as a luminosity to group together bursts of similar intrinsic properties. This also takes account of the spectral index b_1 alongside the peak flux S_{pk} , allowing any splitting of the population to be based on a fuller description of each pulse.

The three categories chosen were: bursts with no pulses exceeding the L_{pk} threshold, bursts with a single pulse exceeding the threshold and finally bursts with more than one pulse exceeding the threshold. It was thought bursts with fainter pulses would become undetectable

at lower values of z_{sim} and exhibit rapid loss of structure, therefore having a similarly rapid fall in T_{90}^* . Bursts with a single bright pulse might be expected to become longer in duration, however this effect would be mitigated to some extent by the loss of flux from the wings of the pulse. This effect may not dominate initially, whilst weaker structure which did not meet the L_{pk} criterion is lost. Bursts containing multiple bright pulses may show similar initial losses of weaker structure, however, after this it is the time dilation of the quiescent periods between bright pulses that would be expected to dominate the T_{90}^* evolution.

The results shown in Figure 5.22 are not what was expected. None of the bursts which were identified as being faint, were detected at $z_{sim} = 2$, which is why the track for this subset is absent from the plot. The subset of GRBs containing multiple bright pulses remain close to the total average. This is particularly the case at higher values of z_{sim} as this subset begins to further dominate the total population. After $z_{sim} = 8$, only bursts with multiple bright peaks are detected.

The subset with only one pulse which exceeds the L_{pk} threshold mimics the average population, as the average T_{90}^* remains approximately constant with z_{sim} . Interestingly, the final few points on the evolutionary track for the single bright pulse subset enter the region of the panel where the observed highest redshift bursts are found. This is encouraging for further analysis, however the population of detected bursts in this subset is limited. Beyond $z_{sim} = 6$ only one GRB is consistently detected until $z_{sim} = 8$. This does not provide a firm basis from which to link the observed high redshift bursts to a subset of the lower redshift population. Instead, it encourages use of the same analysis on the larger sample of synthetic GRBs to improve the statistics of the population.

In Figure 5.23 the evolution of the hardness ratio taken between two of the BAT bands is shown. To calculate this hardness ratio, the 25–50 keV and 50–100 keV bands were binned by significance, as described in §4.5.4. The total significant fluence was found in each band, by summing the fluence in each bin which met the signal to noise ratio criterion. The hardness ratio was then calculated by taking the ratio between the two fluences.

As with Figure 5.22 values from observed GRBs have also been included. The number of observed bursts for which the hardness ratio could be calculated was fewer than those with

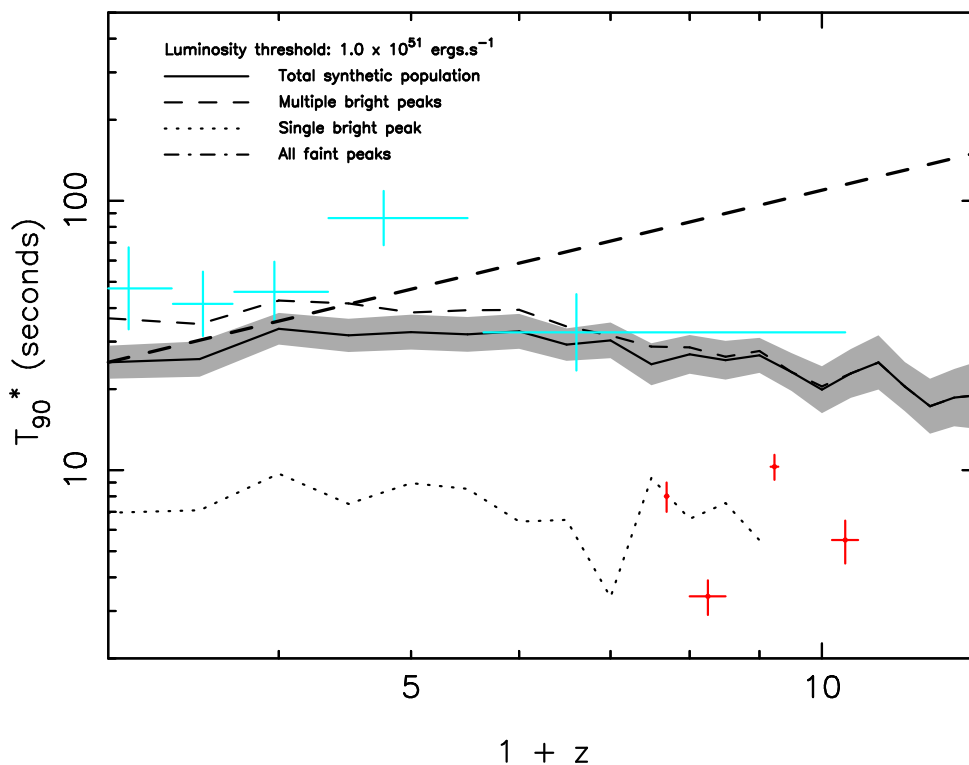


Figure 5.22: The evolution of geometric mean T_{90}^* as a function of z_{sim} for real bursts. Red points are the four example high redshift bursts and blue points are the geometric mean of all bursts within particular redshift bins. Each of the lines shows a track for a different subset of bursts. The solid black line is the average of all detected observed GRBs at each value of z_{sim} . The grey region surrounding this track shows the standard error. The other tracks correspond to whether bright pulses were present in the burst. The dashed line denotes the average track of burst with a minimum of two bright pulses, the dotted line shows the track for bursts with only one bright pulse and the dot-dashed line is for bursts with only faint pulses. An additional heavy dashed line shows the expected effects on the average T_{90}^* of the BAT sample should the population evolve due to cosmological time dilation alone.

T_{90}^* estimates. This was due to the requirement of significant fluence in both the 25–50 keV and 50–100 keV bands whilst in calculating T_{90}^* significant fluence was only necessary in a channel spanning total BAT spectral range. Each of the blue data points represents an average of 15 GRBs, with the remaining four high redshift bursts displayed separately.

The observed bursts show a tendency for those at higher redshifts to be spectrally softer than their low redshift counterparts. Simulations of the observed population show that the broad evolution of hardness ratio as a function of z_{sim} is for bursts to become softer. These effects are discussed in Chapter 4 for the sample of bright bursts presented in that work. From Figure 5.23 the evolution of hardness ratio does not appear to coincide with that of observed bursts. It is clear, however, in Figure 5.23 that the small number statistics of the sample again limit the accuracy of determining the average behaviour of the population, was the case for

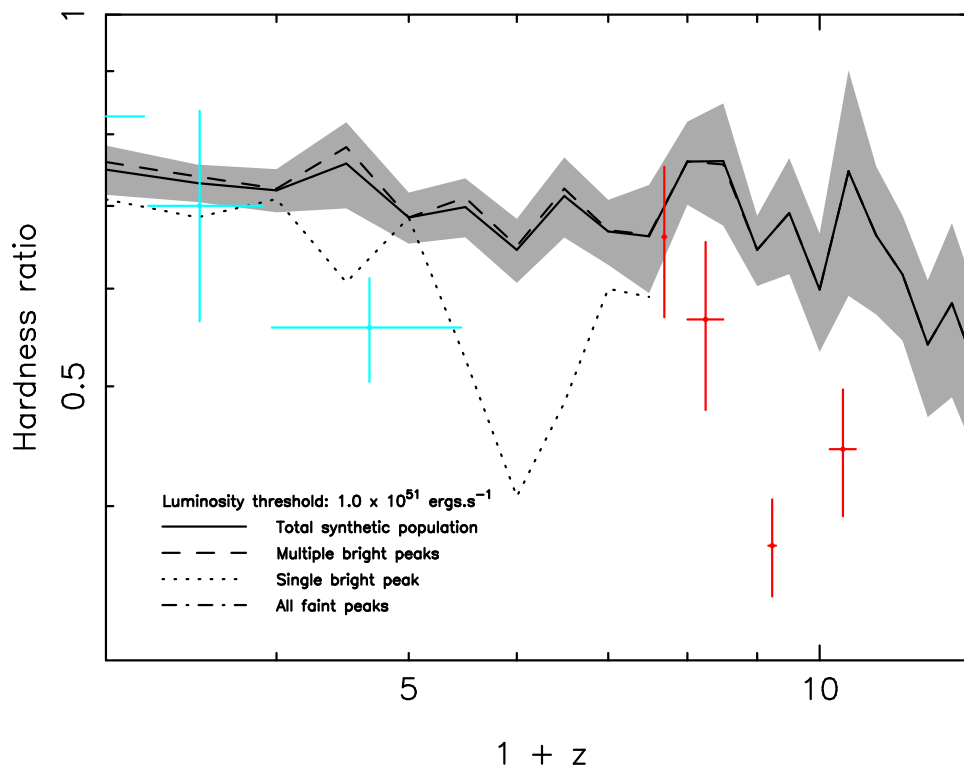


Figure 5.23: The evolution of the average hardness ratio $S(50 - 100\text{keV})/S(25 - 50\text{keV})$ as a function of z_{sim} for real bursts. Red points are the four example high redshift bursts and blue points are the geometric mean of all bursts within particular redshift bins. Each of the lines shows a track for a different subset of bursts. The solid black line is the average of all detected observed GRBs at each value of z_{sim} . The grey region surrounding this track shows the standard error. The other tracks correspond to whether bright pulses were present in the burst. The dashed line denotes the average track of burst with a minimum of two bright pulses, the dotted line shows the track for bursts with only one bright pulse and the dot-dashed line is for bursts with only faint pulses.

T_{90}^* .

5.5.2 The synthetic population of bursts

To judge whether the population of GRBs synthesised was appropriate to evolve in redshift, the measured T_{90}^* distribution was compared to that of the real burst sample fitted with prompt pulses. This is shown in Figure 5.24, where the red distribution is the synthetic population and the black distribution is for the observed bursts. To allow an accurate comparison between the two, values of T_{90}^* have been calculated with the GRBs all corrected to a common redshift of $z_{sim} = 2$ and normalised. As can be seen, the two distributions are similar, implying that the synthetic bursts faithfully model the real population of bursts. To verify this a Kolmogorov-Smirnov (K-S) test was used on the two populations. This statistical test finds the probability

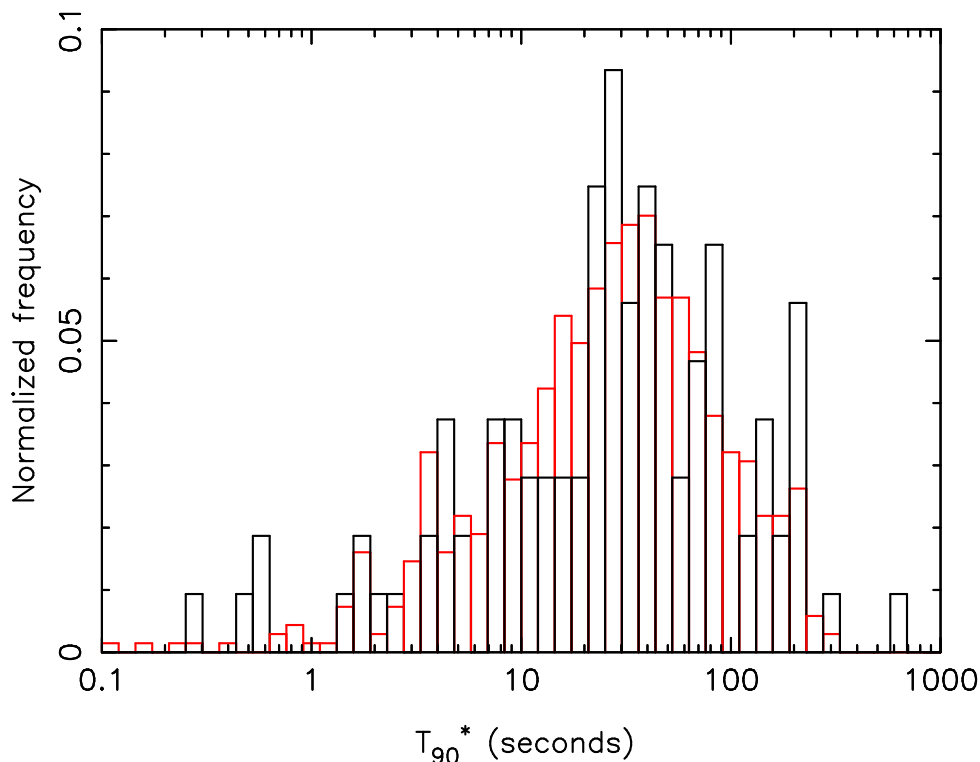


Figure 5.24: Distributions of T_{90}^* corrected to $z_{sim} = 2$. The red distribution is the synthetic population, whilst the black distribution is the observed distribution of bursts. Both populations have been normalised by the total number of detected bursts (126 real bursts, and 659 synthetic bursts).

that the data from two samples are drawn from the same distribution. This produced a K-S statistic of 0.06 with a probability of 0.89. With probabilities nearer 1 indicating that the two data sets are likely to be derived from the same parent population, this indicates that the distribution of T_{90}^* for the synthetic bursts is an acceptable representation of the real distribution. These synthetic bursts were then simulated at the same values of z_{sim} as those used for the observed bursts.

Having a fully synthetic population of bursts simulated at a succession of common redshifts, the number detected at each of these redshifts were evaluated to consider the evolution in detectability. This is shown in 5.25. It is important to note, however, that whilst this provides information about the fraction of bursts observed when viewed within the jet, it does not account for GRBs that occur but are not beamed towards the observer. This is therefore not a fraction of the total population of GRBs occurring, but instead of the observable population. At a redshift of $z_{sim} = 2$, where the sample is first generated, 659 bursts are detected at a threshold of 6.5σ . This reduces to 207 bursts at $z_{sim} = 12$, still providing significant numbers

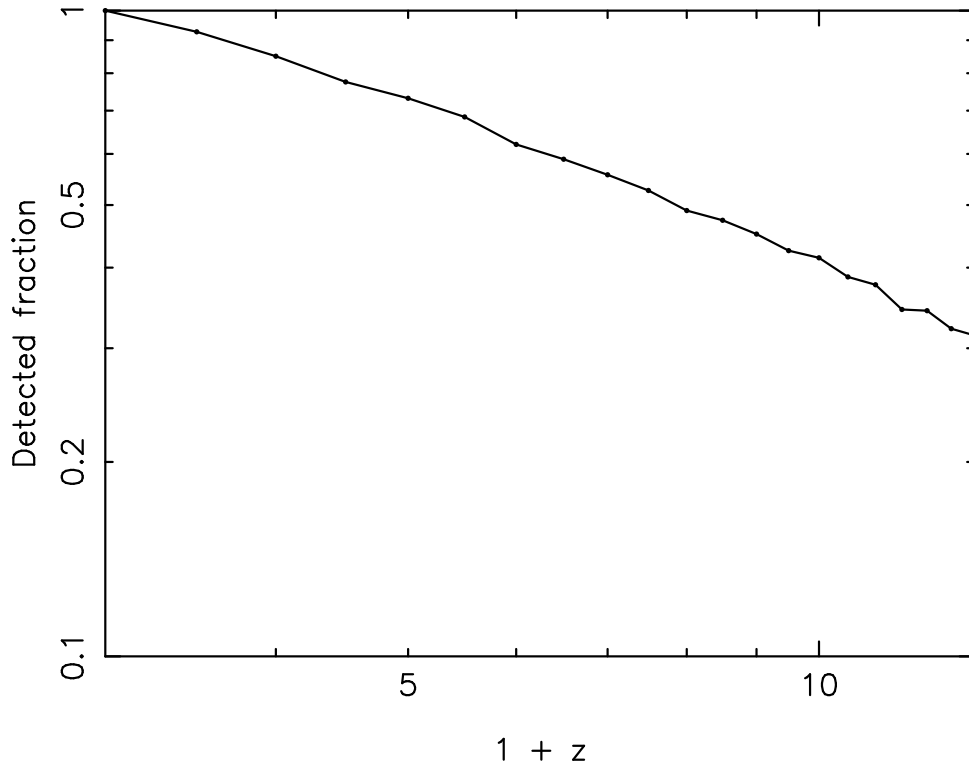


Figure 5.25: Detection frequency of synthetic burst population as a function of simulated redshift. The values have been normalised using the total number of bursts detected at $z_{sim} = 2$.

for statistical analysis of the population at high redshift.

Figure 5.26, in a similar way to Figure 5.22, shows the average T_{90}^* both across the entire population and the previously defined subsets of GRBs. Figure 5.26 shows this geometric average remains approximately flat over the entire range of z_{sim} as do the real bursts shown in Figure 5.22.

There are 225 bursts which contain no pulses satisfying the L_{pk} criterion, of which 2 are detected at $z_{sim} = 2$, and none thereafter, which is why Figure 5.26 does not show the evolutionary T_{90}^* track for this burst subset.

In Figure 5.26 the single bright pulse subset remains approximately constant in average T_{90}^* with respect to z_{sim} . There is a slight drift, suggesting an increase in T_{90}^* until $z_{sim} \sim 8$, however this change is minimal. Unlike the observed population when evolved as shown in Figure 5.22, this subset does not correspond well with the observed high redshift burst T_{90}^* values. This is most likely due to the improved statistics of the synthetic population. There are a few bursts which individually mimic these high redshift GRBs. Such bursts form a small fraction of the subset, implying it is unlikely that if the high redshift GRBs belonged to this

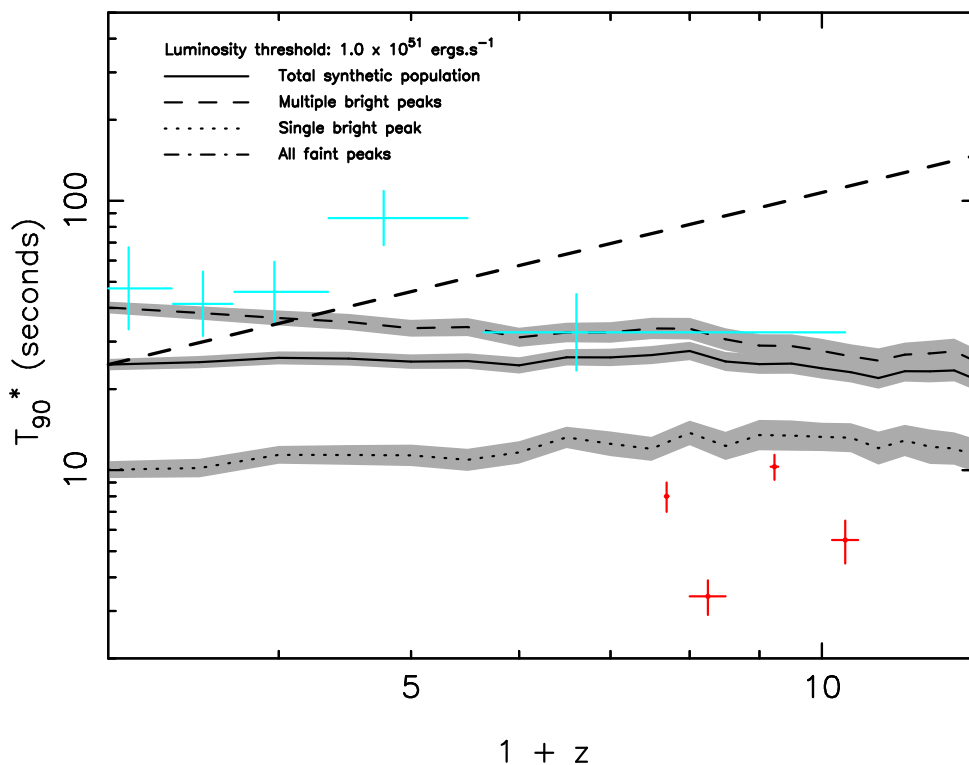


Figure 5.26: The evolution of synthetic geometric mean T_{90} with redshift for the synthetic sample of GRBs. Red points are the four example high redshift bursts and blue points are the geometric mean of all bursts within particular redshift bins. Each of the lines shows a track for a different subset of bursts. The solid black line is the average of all detected synthetic GRBs at each redshift. The grey region surrounding this track is the 90% confidence interval. The other tracks correspond to whether bright pulses were present in the burst. The dashed line denotes the average track of burst with a minimum of two bright pulses, the dotted line shows the track for bursts with only one bright pulse and the dot-dashed line is for bursts with only faint pulses. An additional dotted line shows the expected effects on the average T_{90} of the BAT sample should the population only evolve due to cosmological time dilation.

subset of bursts, they would all have such durations.

The T_{90}^* behaviour of the multiply bright pulse subset is interesting when considered with respect to GRBs observed in the range $2 < z_{sim} < 6$. The evolutionary track of T_{90}^* can be seen to agree, within the standard error with four of the five points showing averages of observed durations within those redshift ranges.

Additionally, T_{90}^* reduces across the entire of z_{sim} for this subset. It is believed this is due to those bursts with more than one pulse satisfying the L_{pk} criterion being likely to contain additional weak pulses. It is the evolution, and resulting loss, of this weaker structure that causes a reduction in duration. As the value of z_{sim} at which each pulse is first completely lost is different, the reduction in duration is more smooth than the sharp decreases observed in individual bursts as shown in Chapter 4. In the range of $5 < z_{sim} < 7$ this reduction in

T_{90}^* is halted temporarily. This is due to the weaker structure already being lost prior to these redshifts, and the time dilation of the remaining bright structure. Above these values of z_{sim} even some of the brighter structure becomes difficult to detect, once more leading to a decrease in the average measured T_{90}^* for this subset of the synthetic GRBs.

The probability of all four high redshift bursts discussed in §5.3.1 being observed with $T_{90}^* < 10$ seconds was also considered. The average redshift of the four was first calculated and found to be $\bar{z} = 7.89_{-0.11}^{+0.07}$. The nearest value of z_{sim} used in the systematic simulations was $z_{sim} = 8$, and so the synthetic population was considered at this value of redshift. First looking at the total population, it was found that of the 319 synthetic bursts detected at $z_{sim} = 8$, 79 had $T_{90}^* < 10$ seconds. If the distribution of T_{90}^* is considered to correspond to the probability distribution of a burst having a specific T_{90}^* , this fraction translates to a probability of 0.248 that $T_{90}^* < 10$ seconds. This will be the case for each of the four bursts, which means that the probability of all four having such a low duration would be 3.76×10^{-3} . Repeating the same analysis, with just the subset of bursts containing a single bright pulse yields a probability of 0.27 (18 out of 66 detected GRBs) that an individual burst has $T_{90}^* < 10$ seconds. If it is assumed that all four belong to the single bright pulse category, the probability of them all being as short in duration as observed is 5.53×10^{-3} , and therefore highly unlikely.

Another obvious division to make in the GRB population is between long and short bursts. As simulations of the synthetic population all begin at $z_{sim} = 2$, the average redshift of all real bursts for which a $T_{90} < 2$ seconds was reported was found. From this sample an average redshift of $\bar{z}_{short} = 0.85$ was calculated. The threshold of $T_{90} < 2$ seconds was therefore relaxed to reflect the discrepancy between \bar{z}_{short} and the minimum value of z_{sim} . Assuming cosmological time dilation to provide an upper limit on the expected duration of a burst, the T_{90} threshold was modified using Equation 5.3, giving a new upper limit of $T_{90,max} = 3.23$ seconds, where $z_{sim} = 2$ and $T_{90,obs} = 2$ seconds.

$$T_{90,max} = \frac{1 + z_{sim}}{1 + \bar{z}_{short}} T_{90,obs}. \quad (5.3)$$

From Figure 5.24 it is clear that this upper limit only probes the short tail of the total T_{90} distribution, which reduces the number of bursts available for such analysis to 43. With short

duration bursts the duration of the few pulses present are short. As can be seen from Figures 5.13 and 5.14 such pulses tend to be brighter and spectrally harder. As a result of this, only 2 of the 43 bursts identified as short in the synthetic sample are detected at $z_{sim} \geq 6$. The durations for these two bursts are $T_{90}^* \sim 1.9$ seconds, which are considerably shorter than the real high redshift GRBs observed at these redshifts. This is due to the loss of flux from the pulse wings being a stronger effect than that of time dilation.

Importantly, though, this analysis indicates that the observed high redshift GRB sample is not due to short GRBs. Considering the fraction of detected short bursts in the synthetic sample, only 0.41 short GRBs would be expected to be detected at $z = 8$ in the observed sample of 203 GRBs. Aside from seeing more bursts than expected from the short population, the measured duration is far too short to explain the observed high redshift sample. Finally, the hardness ratio of the synthetic short bursts detected at high redshifts is too high to be compatible with the observed high redshift sample.

As with the real population of bursts, the evolution of hardness ratio with z_{sim} was also investigated to produce a fuller picture of the prompt emission. By using the synthetic sample a clearer evolution of hardness ratio as a function of z_{sim} can be seen in Figure 5.27. There is a more statistically significant evolution from harder average prompt emission to softer radiation.

There are other features of Figure 5.27 that are of interest. The total average track passes directly through where the observed high redshift bursts can be seen to lie. Additionally, there is a marked difference between those bursts with single or multiple bright pulses. On average, those with a single bright pulse tend to be spectrally harder, although fewer are detected. This is most likely due to only the bright core of the bright pulse being detected. The spectrum of the bright pulse then shifts to lower energies at T_{pk} as z_{sim} increases, making the total hardness ratio lower.

From Figures 5.26 and 5.27 it is interesting to note that the temporal characteristics of the high redshift bursts are not well represented by the synthetic population, however the spectral characteristics are better described by the same simulations.

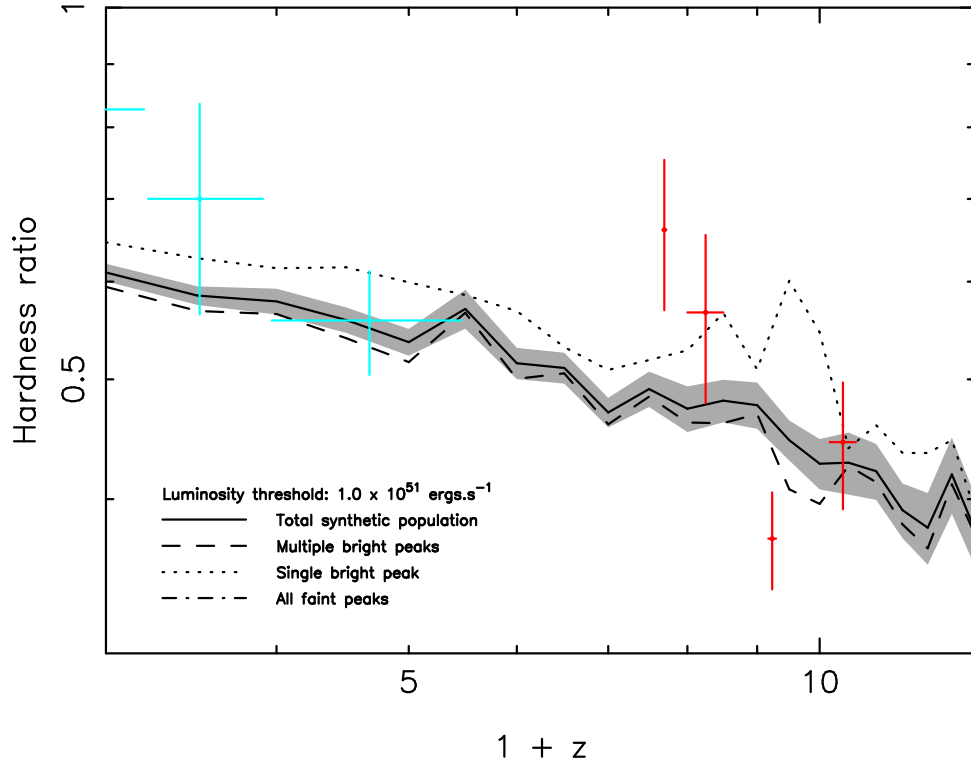


Figure 5.27: The evolution of the average hardness ratio $S(50 - 100\text{keV})/S(25 - 50\text{keV})$ as a function of z_{sim} for synthetic bursts. Red points are the four example high redshift bursts and blue points are the geometric mean of all bursts within particular redshift bins. Each of the lines shows a track for a different subset of bursts. The solid black line is the average of all detected synthetic GRBs at each value of z_{sim} . The grey region surrounding this track shows the standard error. The other tracks correspond to whether bright pulses were present in the burst. The dashed line denotes the average track of burst with a minimum of two bright pulses, the dotted line shows the track for bursts with only one bright pulse and the dot-dashed line is for bursts with only faint pulses.

5.5.3 Comparisons to previous work

This work was also compared to that conducted by Kocevski (2012) (see Figure 5.1). To do so, a GRB light curve containing a single pulse was created. To define the characteristics of this pulse the distributions of b_1 , T_r and T_f were considered and took the mean average values. d , E_{pk} and T_{pk} were fixed at values previously discussed for the synthetic sample. Equation 5.4 was used to calculate S_{pk} ,

$$S_{pk} = \frac{L_{pk}}{AK4\pi D_L^2}, \quad (5.4)$$

where A is a correction factor between keV and ergs, K is the k-correction and D_L is the luminosity distance. For this analysis, S_{pk} was defined at $z_{sim} = 2$ and the mean values of b_1 ,

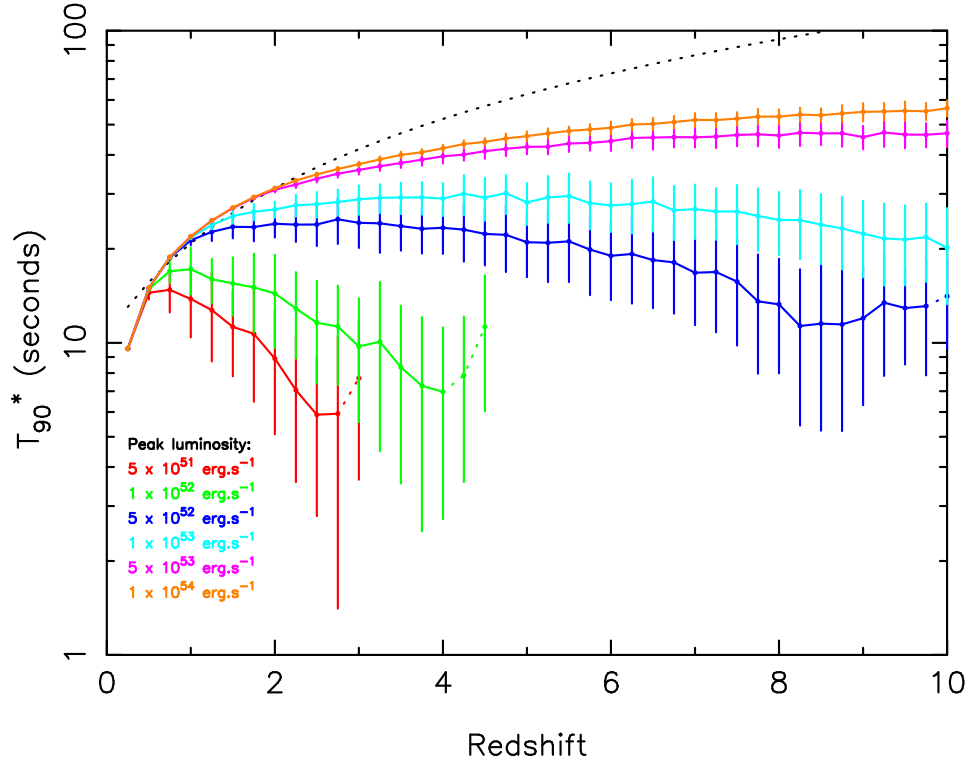


Figure 5.28: Measured duration of light curves containing a single pulse as a function of simulated redshift. Each data set corresponds to a different luminosity pulse, as indicated by the key. The dotted black line corresponds to the expected evolution due to time dilation. The error bars on each point are the RMS error. Solid lines correspond to where the repeated simulations detected the burst in at least 90% of all simulations. Dotted lines correspond to where bursts were recovered in at least 50% of all simulations.

T_r and T_f were also obtained once all pulses from GRBs were shifted to this common redshift. Kocevski (2012) considered values of luminosity between $5 \times 10^{52} \text{ erg.s}^{-1}$ and $1 \times 10^{54} \text{ erg.s}^{-1}$. The luminosity in this work was defined as the peak brightness of each pulse, L_{pk} , which was measured at T_{pk} . As the range in Kocevski (2012) is towards the bright end of the pulse distribution, this range was extended to $5 \times 10^{51} \text{ erg.s}^{-1}$. The value of S_{pk} for a pulse is not, however, independent of its other characteristics. This is illustrated in Figure 5.13, which shows the anti-correlation between S_{pk} and T_f . As T_f is also related to T_r and b_1 for each pulse, changing S_{pk} should also result in an associated change in these parameters. However, to illustrate the effects of only changing the luminosity (not the duration) of a pulse, T_f , T_r and b_1 were held constant whilst varying S_{pk} .

The results from Figure 5.28 agree qualitatively with those obtained by Kocevski (2012). After $z_{sim} \sim 2$, the evolution of duration increases at a slower rate than that expected by

cosmological time dilation. The two brightest data sets show an increase in T_{90}^* across the entire range of z_{sim} , with the brightest of the two recovering a longer duration after $z_{sim} \sim 2$. The light curves of with fainter pulses than this show a more complicated evolution. After a point in redshift, which appears to be related to the luminosity of the pulse the duration begins to reduce. As L_{pk} decreases the redshift at which this occurs can be seen to also reduce, and the subsequent rate at which T_{90}^* reduces becomes larger. This is perhaps what is expected, as the fainter pulses become of comparable signal to the background level at a relatively lower value of z_{sim} . Therefore the effects of losing the wings of the pulse into the noise are more pronounced earlier in its evolution with redshift.

Also seen is a rise in the uncertainty in the measured value of T_{90}^* , as illustrated by the increase in the RMS values in Figure 5.28. This is due to the observed flux from each pulse becoming fainter with redshift. As such, it is harder to isolate the end of the observed emission from the background noise, introducing a larger associated error with the measured time.

Having discussed the parameters of a pulse which can affect the measured duration in Chapter 4, the spectral index associated with a pulse was also considered important. With spectra that are steep, the observed flux can be expected to reduce more rapidly. To investigate this a bright pulse was modelled with $L_{pk} = 1 \times 10^{53}$ ergs.s⁻¹ and varying values of b_1 . The chosen value of L_{pk} was high to allow the effects of the change in spectral index to be visible over a broad range of redshifts. The spectral index was set to values within the observed distribution of fitted prompt pulses, as shown in the key of Figure 5.29.

As b_1 increases, the total recovered duration is longer. This is because the shape of the spectrum causes more flux to be received at relatively higher energies, contributing to the total pulse emission.

The rise in T_{90}^* prior to $z_{sim} \sim 1$ in both Figures 5.28 and 5.29 is steeper than that predicted by time dilation alone. The amount by which the increase due to time dilation is exceeded depends on the shape of the spectrum. At each value of z_{sim} a different part of the rest frame spectrum is seen in the BAT band. In some instances, the value of b_1 prior to E_{pk} leads to a rising spectrum, which allows the burst to remain bright for longer. Coupling this effect with the dilation of all the characteristic times of the pulses leads to a larger rate of increase in T_{90}^* .

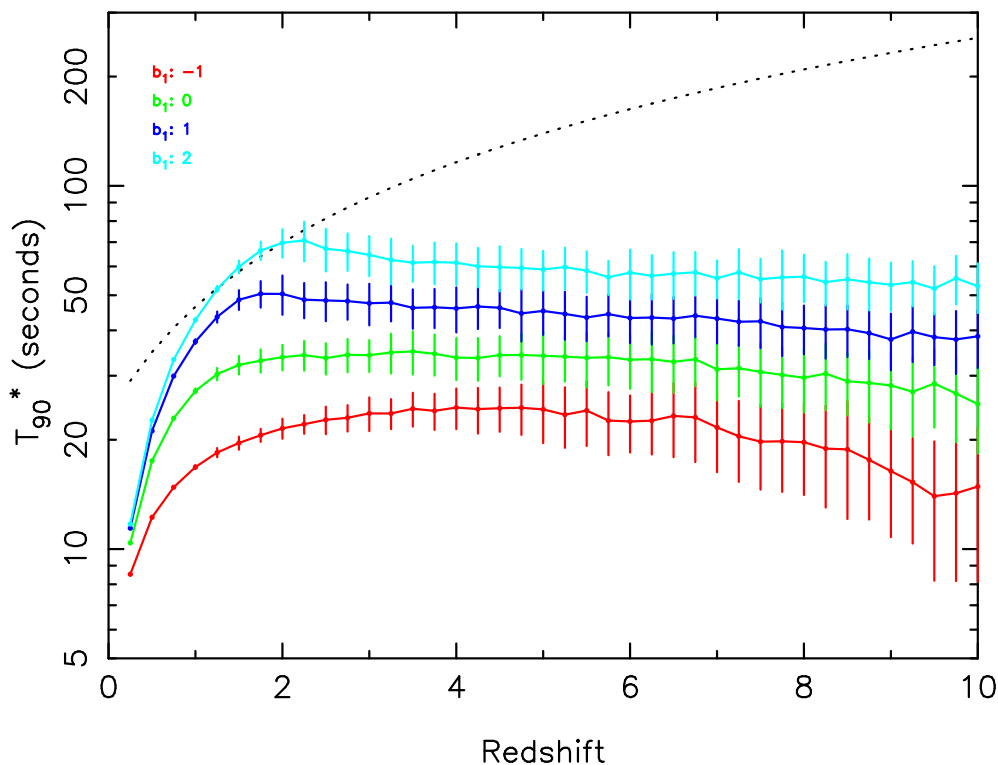


Figure 5.29: Measured duration of light curves containing a single pulse as a function of simulated redshift. Each data set corresponds to a pulse with a different value of b_1 , as indicated by the key. The dotted black line corresponds to the expected evolution due to time dilation. The error bars on each point are the RMS error. In all instances the bursts were recovered in at least 90% of all simulations.

The effect is short lived, however, as eventually E_{pk} (which is defined to be 200 keV at T_{pk} at $z_{sim} = 2$) enters the BAT band. After this redshift, the high-energy spectral cut-off encroaches further into the band, mitigating the increase from the low-energy spectral shape. As b_1 was held constant when varying L_{pk} , the low redshift morphology of the brightest simulations in Figure 5.28 agree with Figure 5.29.

5.5.4 An improved instrument

A common conclusion from studies such as this is that to fully answer the questions posed by the observed high redshift GRBs a larger sample is required. There are only a handful of ways in which this can be achieved: by increasing the time over which observations are taken with current instrumentation or by creating and implementing a new generation of instruments. Such new instruments can be improved by either increasing the sky coverage or the sensitivity of the detector. There are instruments such as the *Fermi* GBM that offer high sky coverage,

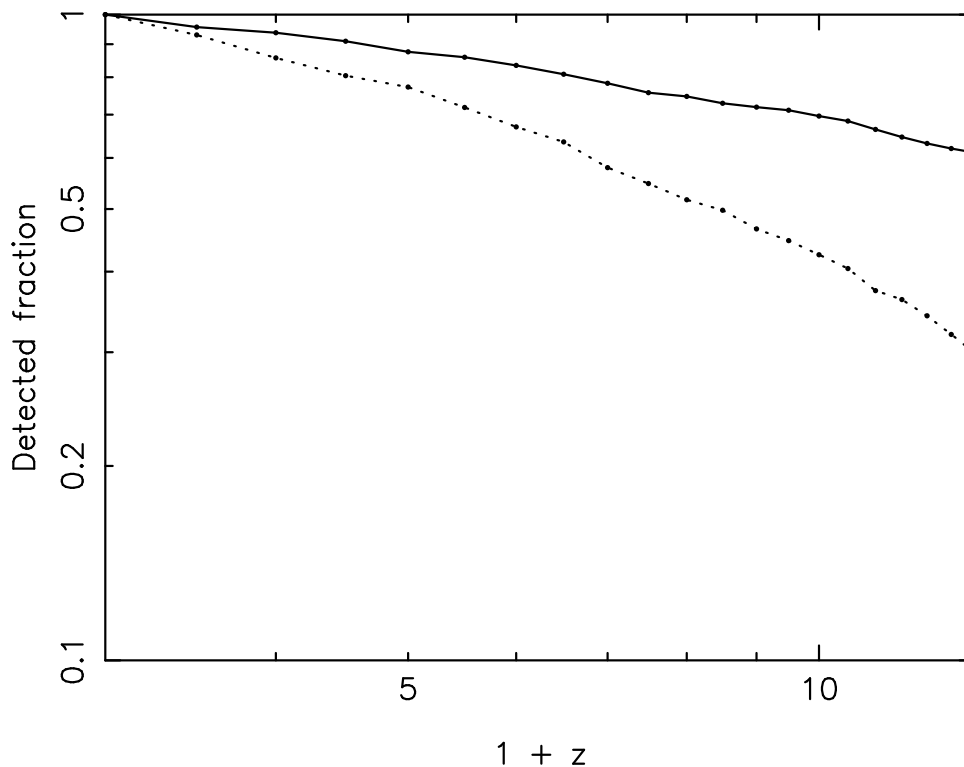


Figure 5.30: Detected fraction of the synthetic sample of GRBs. The solid line shows the detected fraction of the synthetic sample for an instrument with ten times the sensitivity of the current BAT instrument. The dotted line shows the detected fraction detected with BAT. This is the same as the curve shown in Figure 5.25, but is included to show the improved performance. The fraction detected is normalised using the total detected at $z_{sim} = 2$.

however the localisation of the detected bursts is poor, reducing the capability of ground-based follow-up.

Instead, this analysis considers the results of making the BAT instrument an order of magnitude more sensitive. To mimic this, the normalisation of each pulse was increased by a factor of 10. The synthetic population was then simulated in an identical fashion to that outlined in §5.5.2.

The first notable feature of the synthetic simulations, when observed using the improved instrument, is that a larger fraction of the population is detected at any given value of z_{sim} , as shown in Figure 5.30. Of these bursts, more belong to either of the bright categories defined by the L_{pk} criterion.

The blue and red points shown on Figures 5.22 and 5.26 are not included in Figure 5.31. The average values were obtained by using the T_{90}^* algorithm on the observed BAT light curves for all bursts with a redshift measurement. These have not all been fitted with the prompt pulse

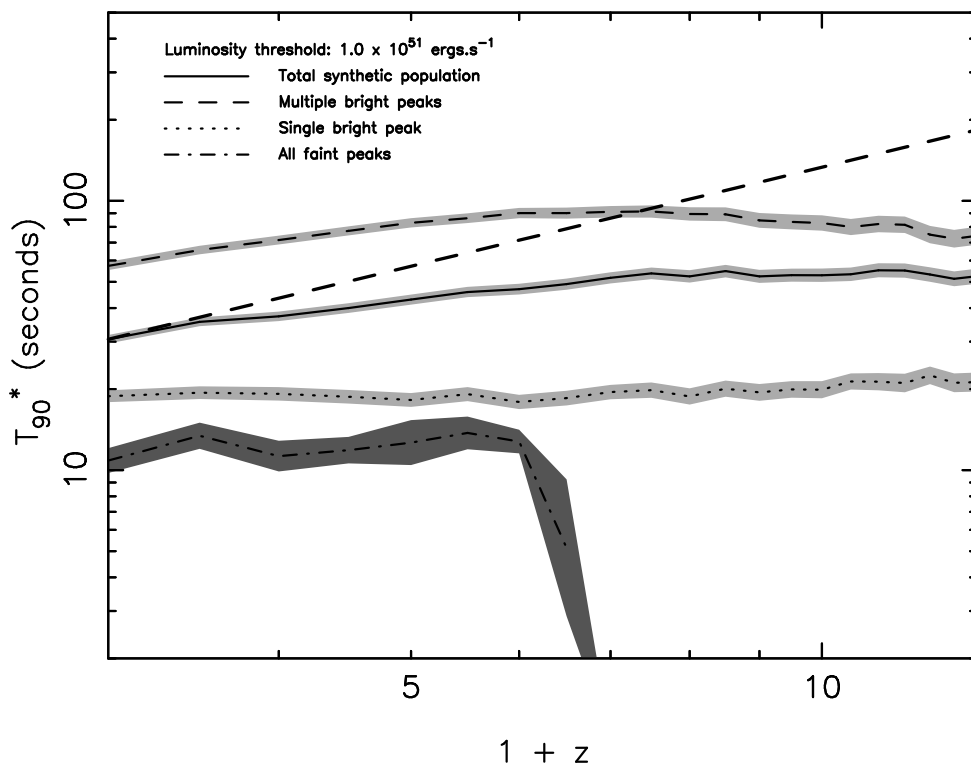


Figure 5.31: The evolution of synthetic geometric mean T_{90} with redshift for the synthetic sample of GRBs as detected by an instrument modelled to be an order of magnitude more sensitive than BAT. Each of the lines shows a track for a different subset of bursts. The solid black line is the average of all detected synthetic GRBs at each redshift. The grey region surrounding this track is the 90% confidence interval. The other tracks correspond to whether bright pulses were present in the burst. The dashed line denotes the average track of burst with a minimum of two bright pulses, the dotted line shows the track for bursts with only one bright pulse and the dot–dashed line is for bursts with only faint pulses. An additional dotted line shows the expected effects on the average T_{90} of the BAT sample should the population only evolve due to cosmological time dilation.

model, and therefore it is not possible to increase the expected source frame properties of all the bursts.

Figure 5.31 shows that with an increased sensitivity the recovered T_{90}^* averages are slightly higher than those obtained for the corresponding simulations of the synthetic sample shown in Figure 5.26. This is due to the improved signal to noise ratio allowing all pulses to be discerned for longer periods in their prompt light curves.

The evolution of the average across the entire synthetic population shows an increase by a factor of two across the entire range of z_{sim} . This increase occurs primarily in the range $2 < z_{sim} < 6$, and when $z_{sim} > 2.5$ is at a rate that is significantly less than that prescribed by cosmological time dilation. This evolution is largely due to the change in relative contributions from the multiple and single bright burst categories.

The subset of bursts containing a single pulse which exceeds the luminosity criterion remain similar to the results obtained using the same population and standard BAT sensitivity. The measured duration is approximately constant across the entire range of simulations. As with the average across the total population, the GRBs do not follow the track expected from time dilation due to the loss of both the wings of pulses and entire pulses at late times.

The subset of GRBs with multiple bright pulses shows a smooth increase in measured T_{90}^* as a function of z_{sim} . After $z_{sim} \sim 5$ this increase is halted, and a slight reduction of duration is seen. This is due to the loss of weaker structure. These effects occur at a much higher simulated redshift than the simulations conducted using the standard BAT sensitivity, which is indicative of the increased sensitivity improving the signal to noise ratios for this structure.

As those bursts belonging to the faint subset now have an improved signal to noise ratio, there is a range of z_{sim} over which some are detected. The behaviour of T_{90}^* during this time is erratic due to a low number of GRBs detected within the subset.

For this set of simulations, the evolution of hardness ratio with respect to z_{sim} has also been investigated, as shown in Figure 5.32. The behaviour of the total average, and the averages of the single and multiple bright pulse GRBs are similar to that shown in Figure 5.27. The evolution of hardness ratio appears to be slightly smoother in these subsets, and by $z_{sim} = 12$, the average hardness ratio attained is slightly softer than that shown in Figure 5.27.

With an improved sensitivity a small number of bursts in the faint category have also been detected. The evolutionary track for this subset shows a marked increase in hardness ratio. Initially, at $z_{sim} = 2$, there are 86 bursts identified in this category with sufficient flux to measure a hardness ratio. This number quickly dwindles, and consequently is unreliable when $z_{sim} \geq 4$, as there are only 4 bursts detected at $z_{sim} = 4$, and only a single GRB is detected beyond this point in simulated redshift. Prior to $z_{sim} = 4$, the behaviour of the hardness ratio remains interesting, however. With a significant number of GRBs detected at these simulated redshifts, the observed radiation is seen to increase in hardness. It is believed this is due to the loss of weak soft emission at late times, leaving only the brightest cores within the light curves. As previously discussed, these cores are harder than the tails of each pulse.

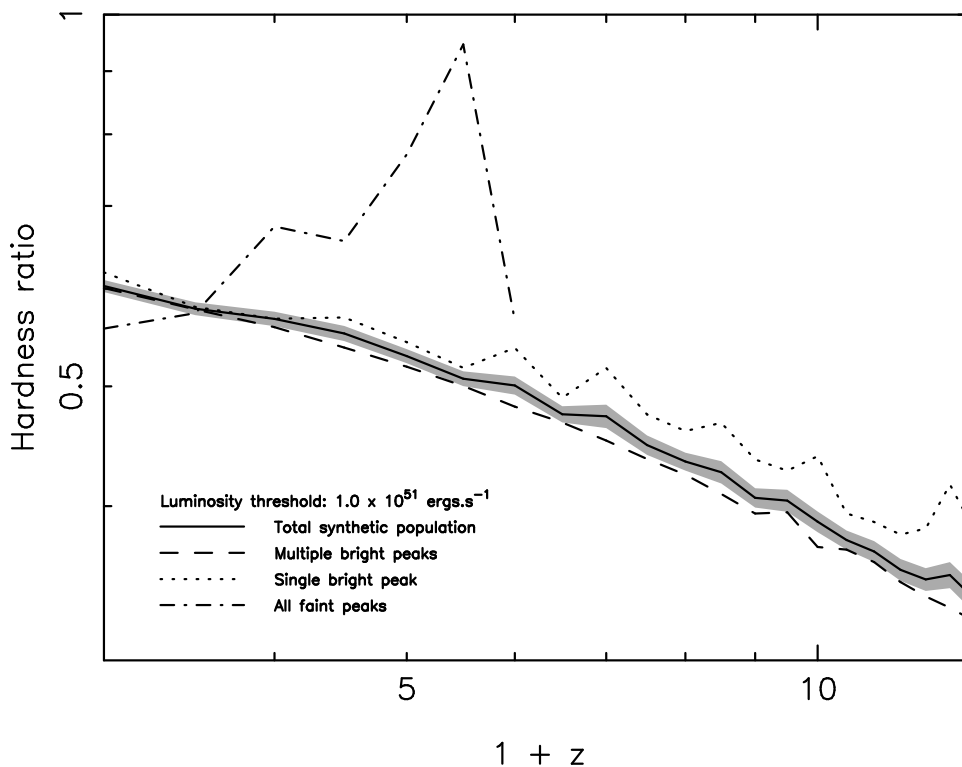


Figure 5.32: The evolution of the average hardness ratio $S(50 - 100\text{keV})/S(25 - 50\text{keV})$ as a function of z_{sim} for synthetic bursts using an instrument an order of magnitude more sensitive than BAT. Each of the lines shows a track for a different subset of bursts. The solid black line is the average of all detected synthetic GRBs at each value of z_{sim} . The grey region surrounding this track shows the standard error. The other tracks correspond to whether bright pulses were present in the burst. The dashed line denotes the average track of burst with a minimum of two bright pulses, the dotted line shows the track for bursts with only one bright pulse and the dot-dashed line is for bursts with only faint pulses.

5.6 Conclusions

This work was conducted with the aim of determining whether high redshift bursts are atypical of the rest of the BAT GRB population. By accounting for the effects of a changed luminosity distance in the parameters that determine the strength and duration of each pulse, the effects of observing bursts which remain invariant in their rest frames were investigated at a variety simulated redshifts. This showed how T_{90}^* and hardness ratio would evolve for the average of the entire population.

Simulations were conducted of bursts fitted with the Genet & Granot (2009) model in the redshift range of $2 < z_{sim} < 12$. To determine whether the high redshift GRBs, such as GRB 090423, belong to a particular subset of bursts, the observed population was split based on the rest frame luminosity (L_{pk}) of each peak at T_{pk} . Doing so suggested that the high

redshift burst durations might be consistent with bursts containing a single pulse with $L_{pk} > 1 \times 10^{51}$ ergs.s⁻¹. That being said, there is only one burst detected at $z_{sim} = 8$, giving poor statistics to make this comparison.

The average hardness ratio of each population was found to not coincide with the high redshift sample. Again, the low number of detected bursts at these values of z_{sim} reduced the strength of any conclusions drawn from such analysis.

To counter the effects of a small population detected at high redshifts, a synthetic sample of 1,000 bursts was created. This sample size is approximately an order of magnitude larger than the number of observed GRBs on which the analysis has been conducted. Indeed, at $z_{sim} = 8$, in the category of bursts containing a single bright pulse there are 66 detected synthetic bursts using the T_{90}^* algorithm. From these simulations, however, it appears that such GRBs have an average T_{90}^* too long to explain the observed high redshift GRBs. Whilst there are a handful of bursts that have comparable durations, they are in the minority. Even when considering the single bright pulse subset of the population, approximately three bursts with $T_{90}^* > 10$ seconds would be expected for each GRB that is shorter than this threshold. Indeed, the probability of all four bursts having such low durations, by chance, is 5.53×10^{-3} , which clearly indicates a discrepancy between the higher and lower redshift populations.

Conversely, the behaviour of the average hardness ratio of the synthetic population agrees with the observed values at high redshift. This suggests that the typical high redshift GRB, as derived from properties of the entire sample would be expected to be long and spectrally soft. What is instead observed are a handful of shorter duration ($T_{90} \sim 10$ seconds) spectrally soft GRBs. It is impossible to perform the reverse simulations, as the structure that is not luminous to be detected at such high redshifts cannot be inferred at lower redshifts. Due to this, it cannot simply be said that should such a burst be observed at lower redshift the observed duration would be shorter and the hardness ratio would be harder.

Producing the population of synthetic GRBs relied heavily on the prescription created for T_{90} . It began by assuming that T_{90} would be comprised of contributions from three sources. These were the average duration of the pulses, the average delay pulses and finally the number of pulses present. Whilst each of these could be combined to produce a model of T_{90} , a simpler

proxy was found. It is surprising that the average delay between pulses can be omitted from this prescription, however, this suggests that the average pulse duration and average delay are intrinsically linked.

Given that different pulses within the same prompt light curve can have very different spectral properties, any observed duration, such as T_{90} from any given burst largely depends on the redshift at which it occurs. It is therefore important to note that T_{90} definitely does not reflect any source frame characteristics of a GRB.

Comparisons between this work and similar studies were also made to establish whether this study was consistent with previous results. Figure 5.28 is designed to be analogous, using the simulation method employed in this work, to the results from Kocevski (2012) as shown in Figure 5.1. It was found that similar results could be created from a single pulse GRB of varying luminosity. To extend this the importance of the low energy spectral index in determining the measured duration of a pulse is also demonstrated.

One final aspect to this work was to consider what might be possible given a higher instrumental sensitivity. In Figure 5.30 it is demonstrated that by increasing the BAT sensitivity by an order of magnitude the number of detected synthetic bursts at $z_{sim} = 8$ is also doubled, from 319 to 642 out of 1,000. At redshifts higher than this, the gain in detected burst fraction becomes higher, which would lead to an invaluable increase in the total number of detected high redshift bursts. Such improvements to a BAT-like instrument are unpractical, given the necessary increase in size of the optics.

Aside from a higher detected fraction of bursts, the results from the synthetic sample also show that more of the signal from the burst is recovered, as the emission within the tail of each pulse is more significant. As such the duration T_{90}^* is longer for each individual burst. The hardness ratio evolves in a similar manner to that seen when simulations are conducted using the standard BAT response. The slight difference is that more soft flux is recovered in relation to harder flux at high values of z_{sim} , reducing the measured hardness ratio at these simulated redshifts.

The simulations presented in this work suggest that, with improved statistics of a synthetic sample, the observed high redshift sample of GRBs are somewhat unusual. Whilst the

spectral characteristics of the average simulated burst appear to coincide with bursts such as GRB 090423, the measured average duration T_{90}^* does not. It is indeed possible to produce synthetic bursts that would produce T_{90}^* and a hardness ratio compatible with the observed high redshift sample, and these are included within the average values of both. The fraction of the total sample which comprises of such bursts is low, however, which implies that a far more longer duration high redshift GRBs would be expected. This discrepancy between the observed high redshift GRBs and simulation of their low redshift counterparts suggests a fundamental difference between the two populations.

As the rest frame durations of the observed high redshift sample become smaller than the division between short and long bursts, also considered was whether the high redshift population could be a result of high redshift short bursts. As a consequence of the expected number of such bursts at high redshift, the simulated durations and also hardness ratios, however, the sample of short bursts within the synthetic sample are also insufficient to reflect the observed high redshift sample.

To fully answer whether the high redshift population is unusual, a higher sample size is still required. Without a more statistically significant population of observed GRBs it remains impossible to determine whether the current sample is truly representative of the high redshift population, or whether small number statistics have biased observations to date.

6

Conclusions and future work

6.1 Conclusions

6.1.1 GRB 080310

As discussed in §1.5, the available data for GRBs at lower-energies do not consistently agree or disagree with the corresponding γ -ray and X-ray light curves. In an attempt to identify the origin of the early-time emission of GRB 080310 in the optical bands, Chapter 2 extends the high-energy Willingale et al. (2010) fit to include the full broadband data set.

Regardless of this origin, it is shown that a low-energy spectral break is necessary between the optical and X-ray bands to avoid vast over-prediction of prompt flux at optical and NIR wavelengths. In many cases self-absorption was the mechanism imposed to reduce this prompt flux.

The afterglow model required slight alteration in its late time power-law decay, however the spectral shape appears consistent. By either introducing a sharper rise to the afterglow model, or by using the rapid rise of contemporaneous prompt pulses, a fit can be obtained

to the optical light curves. Their morphology appears better fitted by the pulses, whilst the SED at 350 seconds is best represented by the afterglow. With such conflicting evidence, it is difficult to decide which of the alternatives provides a more faithful representation of the data. It is important to note that even when the early-time data is fitted with prompt pulses, some of the pulses identified in the BAT light curve must be self-absorbed.

6.1.2 GRB 061121, GRB 080810 and GRB 081008

Furthering the work of Chapter 2, another three bursts were analysed in a similar manner. All three required self-absorption in the spectra of at least some of their pulses in order to not over-predict the optical flux.

Further to this, when assuming physically motivated values for the bulk Lorentz factor and radius of emission from the explosion centre, most pulses can be shown to have magnetic field strengths which agree with the expected ranges. These can also be used to derive the number densities of the electron populations responsible for the self absorption, showing them to be higher than the typical circumburst medium values.

Unlike GRB 080310, the afterglow in each of the three bursts also required a low-energy spectral break. Following the theoretical expectations from the literature, the characteristics of this break were set to follow a those of a cooling break. In this way it was possible to reconcile the spectrum of the high-energy fit with the level of flux observed in the optical and NIR bands. As the temporal evolution of the cooling break frequency depends on the nature of the circumburst medium, both an ISM and wind-like density profile were modelled. Whilst both environments can model the low-energy data to a reasonable degree, it is the wind-like environment that appears to better satisfy the constraints of the data. Additionally using a wind-like environment to calculate the peak Lorentz factor of the afterglow results in a self-consistent solution for the expected number density of the electron population of GRB 080810.

Accounting for this spectral break in the afterglow SEDs did not fully reconcile the extended high-energy model with the optical data. The characteristic times that define the shape of the afterglow were not compatible with the optical and NIR light curves. Instead, the optical data was fitted independently and it was found in each case that the optical afterglow peaked

earlier than its high-energy counterpart. This suggests either the two arise from different jets or significant spectral evolution between two separate emitting regions within the same jet. When present, late-time breaks in the afterglow were found to not be achromatic, occurring at different times in the optical and X-ray regimes. Understanding the nature of the differences between the two afterglow morphologies can lead to a better understanding of the nature and propagation of the external shock which causes the afterglow.

GRB 061121 was discovered due to BAT triggering on a precursor event. Consequently, there were UVOT observations during the main emission episode. During this time an optical pulse complex was identified, to which prompt pulses were fitted. Using extrapolations from pulses observed with the BAT and XRT the time at which the pulses occurred could be matched. It was not possible to simultaneously fit the decay and peak flux of the pulse complex. This implies that there may be a fundamental difference between the emission of optical and high-energy radiation during the prompt phase of GRBs.

6.1.3 Simulations of bright GRBs

To understand the observed population of GRBs at high redshift a sample of bright bursts was isolated in Chapter 4. These GRBs were chosen to allow evolution of simulated light curves to be analysed over a broad range in redshifts.

Two simulations methods were considered, the first being model independent but ultimately limited by the BAT response and in the information that could be extracted from it. Only a single band was simulated, to maximise the range of redshifts over which the simulations were performed. This redshift range was limited by two factors: first that the upper limit of the sampled band had to remain within the BAT spectral range and, second, the shape of the effective area curve of BAT. Whilst in theory, the BAT response covers a maximum energy of 350 keV, the effective area at these high energies is greatly reduced. With a correspondingly large correction from the effective area term in Equation 4.6, a greater uncertainty in the obtained values was found. For this reason the upper limit in energy to which the analysis was performed was further restricted.

The second method, which employed the Genet & Granot (2009) model has several clear

advantages. The simulations produced provide full four-band coverage of each burst at every redshift. Also, having a fitted model means that there is no restriction based upon the spectral coverage of the original burst observations. Unlike the previous method, this analysis is now model dependant, and therefore relies on the validity of the Genet & Granot (2009) model.

After demonstrating a consistency between the two methods, the latter was adopted for a fuller analysis of the evolution of each burst. The durations recovered were found to depend on three factors: time dilation, gradual loss of pulse tails and the sudden complete loss of pulses as the flux falls below the sensitivity of the instrumentation.

The evolution of hardness ratios for the sample agreed with expectations: bursts become softer at higher redshifts. This behaviour is not ubiquitous, however, with some instances of spectral hardening being seen. These episodes coincide with the loss of later, softer emission from the light curve.

An alternative measure of duration is also considered in Chapter 4 in which the brightest regions of the light curve are isolated. By considering only a core of bright emission, quiescent period in the light curve that would remain included by T_{90} are removed. This gives a quantity more indicative of central engine activity, which is referred to as the core time, T_c . The behaviour of T_c with respect to redshift appears simpler, in most cases, than that of T_{90} , however the scatter between bursts remains high.

Briefly discussed is the maximum redshift to which each burst could be detected. It is found that five GRBs are visible when simulated at $z = 12$. Detecting bursts to such high redshifts furthers the use of GRBs as objects which could probe the early Universe.

6.1.4 Simulations at high redshifts

To improve the statistics of simulations at high redshifts, a larger realistic sample was created of synthetic GRBs. The morphology of these synthetic bursts was designed to replicate the observed population of GRBs.

In producing this synthetic sample a proxy for T_{90} was used, which depended on both the number of pulses within a burst and the average duration of these pulses. Interestingly it was found that adding the average delay between pulses to the formulation of this proxy did not

improve it sufficiently to overcome the reduction in free parameters. Such a parameterisation of burst duration is interesting as it provides insight into what defines the length of the emission episode. A further conclusion is that there is a potential relation between the average delay between each pulse in a bursts and the corresponding average pulse duration.

Once propagated to high redshift the resulting simulations suggest that the probability of the four observed high redshift bursts having such a duration is negligible. This strongly implies that there is a distinct evolution in the characteristics of bursts between the local Universe and high redshifts that cannot be accounted for simply by the cosmological effects associated with an increased luminosity distance.

6.2 Future work

The work contained in Chapters 2 and 3 can be furthered in the first instance be fitting more bursts with broadband multi-wavelength data sets. A candidate for this is GRB 110205A (Zheng et al., 2012; Cucchiara et al., 2011b), which has extensive observations from both *Swift* and numerous ground-based facilities. Of particular interest is the optical data which, in a similar manner to GRB 061121, contains prompt optical activity and additionally the rise of the optical afterglow. The size of this sample is only strictly limited by the availability of comprehensive optical and NIR data.

Having invoked self-absorption to explain the observed low-energy emission in the fitted bursts, further work could determine the physical parameters of the plasma associated with the GRB. This would require coverage of a high quality so the location of the spectral break could be determined in a manner similar to that achieved for the afterglow of GRB 081008. Work such as Shen & Zhang (2009) relate such this spectral break to several key physical parameters of the of the prompt emission site, allowing more information to be determined from such bursts.

In a similar manner, investigating the link between the optical and high-energy afterglows can be used to gain a better insight into the nature of the discrepancy between the two. Differences between these morphologies could arise from several scenarios, including different

jets or the emission in each band arising from different parts of the same jet. In the latter case there would have to be significant spectral evolution between the two regions, which could be a direct consequence of the physics of the external shock model. In short, further broadband modelling would help garner the required information to understand the occurring phenomena within both the prompt and afterglow emission of GRBs.

References

- Ackermann M., et al., 2010, *ApJ* , 716, 1178
- Adelman-McCarthy J. K., et al., 2007, *ApJS* , 172, 634
- Appenzeller I., et al., 1998, *The Messenger*, 94, 1
- Band D., et al., 1993, *ApJ* , 413, 281
- Barthelmy S. D., et al., 2005, *Space Sci. Rev.*, 120, 143
- Barthelmy S. D., et al., 2010, *GRB Coordinates Network*, 11218, 1
- Beardmore A. P., Osborne J. P., Starling R. L. C., Page K. L., Evans P. A., Cummings J. R., 2008, *GRB Coordinates Network*, 7399, 1
- Berger E., 2009, *ApJ* , 690, 231
- Berger E., 2011, *New A Rev.*, 55, 1
- Berger E., et al., 2005, *ApJ* , 634, 501
- Bertin E., Arnouts S., 1996, *A&AS* , 117, 393
- Bissaldi E., et al., 2011, *ApJ* , 733, 97
- Blandford R. D., McKee C. F., 1976, *Physics of Fluids*, 19, 1130
- Bloom J. S., Kulkarni S. R., Djorgovski S. G., 2002, *AJ* , 123, 1111
- Bloom J. S., Perley D. A., Chen H. W., 2006, *GRB Coordinates Network*, 5826, 1
- Bloom J. S., Sigurdsson S., Pols O. R., 1999, *MNRAS* , 305, 763
- Bloom J. S., Starr D. L., Blake C. H., Skrutskie M. F., Falco E. E., 2006, in C. Gabriel, C. Arviset, D. Ponz, & S. Enrique ed., *Astronomical Data Analysis Software and Systems XV* Vol. 351 of *Astronomical Society of the Pacific Conference Series*, *Autonomous Observing and Control Systems for PAIRITEL, a 1.3m Infrared Imaging Telescope*. p. 751
- Boella G., Butler R. C., Perola G. C., Piro L., Scarsi L., Bleeker J. A. M., 1997, *A&AS* , 122, 299
- Bošnjak Ž., Daigne F., Dubus G., 2009, *A&A* , 498, 677
- Bromberg O., Nakar E., Piran T., Sari R., 2012, *ArXiv e-prints*
- Burenin R., Khamitov I., Galeev A., Bikmaev I., Sakhbullin N., Pavlinsky M., Sunyaev R., Eker Z., Kiziloglu U., Gogus E., 2008, *GRB Coordinates Network*, 8088, 1
- Burrows D. N., et al., 2005, *Space Sci. Rev.*, 120, 165

-
- Campana S., et al., 2006, *Nature*, 442, 1008
- Casali M., et al., 2007, *A&A* , 467, 777
- Castro Cerón J. M., Michałowski M. J., Hjorth J., Malesani D., Gorosabel J., Watson D., Fynbo J. P. U., Morales Calderón M., 2010, *ApJ* , 721, 1919
- Castro Cerón J. M., Michałowski M. J., Hjorth J., Watson D., Fynbo J. P. U., Gorosabel J., 2006, *ApJL* , 653, L85
- Cenko S. B., et al., 2006, *PASP*, 118, 1396
- Cenko S. B., et al., 2009, *ApJ* , 693, 1484
- Chandra P., Frail D. A., 2008, GRB Coordinates Network, 8103, 1
- Chornock R., Foley R. J., Li W., Filippenko A. V., 2008, GRB Coordinates Network, 7381
- Chornock R., Perley D. A., Cenko S. B., Bloom J. S., 2009, GRB Coordinates Network, 9243, 1
- Christensen L., Hjorth J., Gorosabel J., 2004, *A&A* , 425, 913
- Cobb B. E., 2006, GRB Coordinates Network, 5878, 1
- Colgate S. A., 1968, *Canadian Journal of Physics*, 46, 476
- Conconi P., et al., 2004, in A. F. M. Moorwood & M. Iye ed., *Society of Photo-Optical Instrumentation Engineers (SPIE) Conference Series Vol. 5492 of Presented at the Society of Photo-Optical Instrumentation Engineers (SPIE) Conference, The commissioning of the REM-IR camera at La Silla.* pp 1602–1612
- Cool R. J., Eisenstein D. J., Hogg D. W., Blanton M. R., Schlegel D. J., Brinkmann J., Lamb D. Q., Schneider D. P., vanden Berk D. E., 2008, GRB Coordinates Network, 7396, 1
- Covino S., et al., 1999, *A&A* , 348, L1
- Covino S., et al., 2002, *A&A* , 392, 865
- Covino S., et al., 2003, *A&A* , 400, L9
- Covino S., et al., 2004, in A. F. M. Moorwood & M. Iye ed., *Society of Photo-Optical Instrumentation Engineers (SPIE) Conference Series Vol. 5492 of Presented at the Society of Photo-Optical Instrumentation Engineers (SPIE) Conference, REM: a fully robotic telescope for GRB observations.* pp 1613–1622
- Covino S., et al., 2008, GRB Coordinates Network, 7385, 1
- Covino S., Tagliaferri G., Fugazza D., Chincarini G., 2008, GRB Coordinates Network, 7393, 1
- Cucchiara A., et al., 2011a, *ApJ* , 736, 7
- Cucchiara A., et al., 2011b, *ApJ* , 743, 154

-
- Cummings J. R., et al., 2008, GRB Coordinates Network, 7382, 1
- Curran P. A., Wijers R. A. M. J., Heemskerk M. H. M., Starling R. L. C., Wiersema K., van der Horst A. J., 2008, *A&A* , 490, 1047
- D'Avanzo P., D'Elia V., di Fabrizio L., Gurtu A., 2011, GRB Coordinates Network, 11997, 1
- Davies R. L., et al., 1997, in Ardeberg A. L., ed., Society of Photo-Optical Instrumentation Engineers (SPIE) Conference Series Vol. 2871 of Society of Photo-Optical Instrumentation Engineers (SPIE) Conference Series, GMOS: the GEMINI Multiple Object Spectrographs. pp 1099–1106
- de Ugarte Postigo A., Aceituno F., Castro-Tirado A. J., 2008, GRB Coordinates Network, 8090, 1
- de Ugarte Postigo A., Castro-Tirado A. J., Gorosabel J., 2011, GRB Coordinates Network, 11978, 1
- de Ugarte Postigo A., Jakobsson P., Malesani D., Fynbo J. P. U., Simpson E., Barros S., 2009, GRB Coordinates Network, 8766, 1
- de Ugarte Postigo A., Thoene C. C., Fynbo J. P. U., Hjorth J., Jakobsson P., Bahhidi Z., Grundahl F., Arentoft T., 2008, GRB Coordinates Network, 8089, 1
- D'Elia V., Campana S., Covino S., D'Avanzo P., Piranomonte S., Tagliaferri G., 2011, *MNRAS* , 418, 680
- Devillard N., 1997, *The Messenger*, 87, 19
- Eichler D., Livio M., Piran T., Schramm D. N., 1989, *Nature*, 340, 126
- Evans P. A., et al., 2009, *MNRAS* , 397, 1177
- Evans P. A., Goad M. R., Osborne J. P., Beardmore A. P., 2008, GRB Coordinates Network, 8347, 1
- Fenimore E., et al., 2006, GRB Coordinates Network, 5831, 1
- Fermi E., 1949, *Physical Review*, 75, 1169
- Fishman G. J., Meegan C. A., 1995, *ARA&A* , 33, 415
- Fishman G. J., Meegan C. A., Parnell T. A., Wilson R. B., Paciesas W., Mateson J. L., Cline T. L., Teegarden B. J., 1985, in F. C. Jones ed., International Cosmic Ray Conference Vol. 3 of International Cosmic Ray Conference, Burst and Transient Source Experiment (BATSE) for the Gamma Ray Observatory (GRO). pp 343–346
- Fishman G. J., Meegan C. A., Watts Jr. J. W., Derrickson J. H., 1978, *ApJL* , 223, L13
- Foley R. J., Chen H.-W., Bloom J., Prochaska J. X., 2005, GRB Coordinates Network, 3483, 1
- Fong W., Berger E., Fox D. B., 2010, *ApJ* , 708, 9
- Fox D. B., et al., 2005, *Nature*, 437, 845

-
- Frail D. A., Kulkarni S. R., Berger E., Wieringa M. H., 2003, *AJ* , 125, 2299
- Frater R. H., Brooks J. W., Whiteoak J. B., 1992, *Journal of Electrical and Electronics Engineering Australia*, 12, 103
- Fruchter A. S., et al., 1999, *ApJL* , 519, L13
- Fruchter A. S., et al., 2006, *Nature*, 441, 463
- Fukugita M., Shimasaku K., Ichikawa T., 1995, *PASP*, 107, 945
- Fynbo J. P. U., et al., 2009, *ApJS* , 185, 526
- Galama T. J., et al., 1998, *Nature*, 395, 670
- Gehrels N., et al., 2004, *ApJ* , 611, 1005
- Genet F., Granot J., 2009, *MNRAS* , 399, 1328
- Goad M. R., et al., 2007, *A&A* , 476, 1401
- Golenetskii S., Aptekar R., Mazets E., Pal'Shin V., Frederiks D., Cline T., 2006, *GRB Coordinates Network*, 5837, 1
- Granot J., Piran T., Sari R., 1999a, *ApJ* , 513, 679
- Granot J., Piran T., Sari R., 1999b, *ApJ* , 527, 236
- Granot J., Piran T., Sari R., 2000, *ApJL* , 534, L163
- Granot J., Sari R., 2002, *ApJ* , 568, 820
- Greiner J., et al., 2008, *PASP*, 120, 405
- Greiner J., et al., 2009, *ApJ* , 693, 1610
- Guidorzi C., Bersier D., Tanvir N., 2008, *GRB Coordinates Network*, 8099, 1
- Halpern J., Armstrong E., 2006, *GRB Coordinates Network*, 5851, 1
- Halpern J. P., Mirabal N., Armstrong E., 2006, *GRB Coordinates Network*, 5840, 1
- Hartmann D., Woosley S. E., Epstein R. I., 1990, *ApJ* , 348, 625
- Henden A., 2008, *GRB Coordinates Network*, 7631
- Hogbom J. A., Brouw W. N., 1974, *A&A* , 33, 289
- Hogg D. W., 1999, *ArXiv Astrophysics e-prints*
- Holland S. T., Page K. L., 2008, *GRB Coordinates Network*, 8095, 1
- Hoversten E. A., Cummings J. R., 2008, *GRB Coordinates Network*, 7398, 1
- Jakobsson P., Vreeswijk P. M., Xu D., Thoene C. C., 2008, *GRB Coordinates Network*, 7832, 1

-
- Kann D. A., et al., 2010, *ApJ* , 720, 1513
- Klebesadel R. W., 2010, in Chincarini G., D’Avanzo P., Margutti R., Salvaterra R., eds, The Shocking Universe - Gamma Ray Bursts and High Energy Shock Phenomena Vol. 102, The discovery of gamma-ray bursts. pp 111–120
- Klebesadel R. W., Strong I. B., Olson R. A., 1973, *ApJL* , 182, L85+
- Kocevski D., 2012, in Proceedings of the Gamma-Ray Bursts 2012 Conference (GRB 2012). May 7-11, 2012. Munich, Germany. Published online at <http://pos.sissa.it/cgi-bin/reader/conf.cgi?confid=152>; <http://pos.sissa.it/cgi-bin/reader/conf.cgi?confid=152>; id.17 On The Lack of Time Dilation Signatures in Gamma-ray Burst Light Curves
- Kocevski D., Petrosian V., 2011, ArXiv e-prints
- Kouveliotou C., Meegan C. A., Fishman G. J., Bhat N. P., Briggs M. S., Koshut T. M., Paciesas W. S., Pendleton G. N., 1993, *ApJL* , 413, L101
- Krühler T., et al., 2009, *ApJ* , 697, 758
- Kumar P., McMahon E., 2008, *MNRAS* , 384, 33
- Le Floch E., et al., 2003, *A&A* , 400, 499
- Leibler C. N., Berger E., 2010, *ApJ* , 725, 1202
- Levan A. J., et al., 2007, *MNRAS* , 378, 1439
- Li W., Filippenko A. V., Chornock R., Jha S., 2003, *PASP*, 115, 844
- Madau P., 1995, *ApJ* , 441, 18
- Malesani D., et al., 2004, *ApJL* , 609, L5
- Margutti R., Guidorzi C., Chincarini G., Bernardini M. G., Genet F., Mao J., Pasotti F., 2010, *MNRAS* , 406, 2149
- Marshall F. E., et al., 2010, GRB Coordinates Network, 11214, 1
- Marshall F. E., Holland S. T., Page K. L., 2006, GRB Coordinates Network, 5833, 1
- McBreen S., et al., 2010, *A&A* , 516, A71
- Meegan C., et al., 2009, *ApJ* , 702, 791
- Meegan C. A., et al., 2008, GRB Coordinates Network, 8100, 1
- Meegan C. A., Fishman G. J., Wilson R. B., Horack J. M., Brock M. N., Paciesas W. S., Pendleton G. N., Kouveliotou C., 1992, *Nature*, 355, 143
- Melandri A., et al., 2006, GRB Coordinates Network, 5827, 1
- Melandri A., et al., 2012, ArXiv e-prints
- Mészáros P., 2006, Reports on Progress in Physics, 69, 2259

-
- Metzger M. R., Djorgovski S. G., Kulkarni S. R., Steidel C. C., Adelberger K. L., Frail D. A., Costa E., Frontera F., 1997, *Nature*, 387, 878
- Milne P. A., Williams G. G., 2008, GRB Coordinates Network, 7387
- Molinari E., et al., 2007, *A&A* , 469, L13
- Monet D. G., et al., 2003, *AJ* , 125, 984
- Nakar E., 2007, *Phys. Rep.*, 442, 166
- Norris J. P., Marani G. F., Bonnell J. T., 2000, *ApJ* , 534, 248
- Nousek J. A., et al., 2006, *ApJ* , 642, 389
- Nysewander M., Reichart D. E., Crain J. A., Foster A., Haislip J., Ivarsen K., Lacluyze A., Trotter A., 2009, *ApJ* , 693, 1417
- O'Brien P. T., et al., 2006, *ApJ* , 647, 1213
- Oke J. B., Gunn J. E., 1983, *ApJ* , 266, 713
- O'Meara J., Chen H. W., Prochaska J. X., 2010, GRB Coordinates Network, 11089, 1
- Paciesas W. S., et al., 1999, *ApJS* , 122, 465
- Paczynski B., 1986, *ApJL* , 308, L43
- Paczynski B., 1990, *ApJ* , 363, 218
- Page K. L., 2008, GRB Coordinates Network, 8087, 1
- Page K. L., et al., 2006, GRB Coordinates Network, 5823, 1
- Page K. L., et al., 2007, *ApJ* , 663, 1125
- Page K. L., et al., 2008, GRB Coordinates Network, 8080, 1
- Page K. L., et al., 2009, *MNRAS* , 400, 134
- Page K. L., Starling R. L. C., Osborne J. P., Troja E., Morris D., 2006, GRB Coordinates Network, 5832, 1
- Palmer D. M., et al., 2008, GRB Coordinates Network, 8351, 1
- Palmer D. M., et al., 2009, GRB Coordinates Network, 9204, 1
- Panaitescu A., Mészáros P., Gehrels N., Burrows D., Nousek J., 2006, *MNRAS* , 366, 1357
- Pérez-Ramírez D., Park H. S., Williams G. G., the Superlotis Team 2004, *Astronomische Nachrichten*, 325, 667
- Perley D. A., Bloom J. S., 2006, GRB Coordinates Network, 5825, 1
- Perley D. A., Bloom J. S., Li W., 2008, GRB Coordinates Network, 7406, 1
- Piran T., 1999, *Phys. Rep.*, 314, 575

-
- Piran T., 2004, *Reviews of Modern Physics*, 76, 1143
- Poole T. S., et al., 2008, *MNRAS* , 383, 627
- Popham R., Woosley S. E., Fryer C., 1999, *ApJ* , 518, 356
- Prochaska J. X., Murphy M., Malec A. L., Miller K., 2008, GRB Coordinates Network, 7388, 1
- Prochaska J. X., Perley D., Howard A., Chen H.-W., Marcy G., Fischer D., Wilburn C., 2008, GRB Coordinates Network, 8083, 1
- Quimby R. M., et al., 2006, *ApJ* , 640, 402
- Racusin J. L., 2008, GRB Coordinates Network, 8349, 1
- Racusin J. L., et al., 2008, GRB Coordinates Network, 8344, 1
- Rees M. J., 1966, *Nature*, 211, 468
- Rees M. J., Meszaros P., 1994, *ApJL* , 430, L93
- Reichart D., et al., 2005, *Nuovo Cimento C Geophysics Space Physics C*, 28, 767
- Reichart D. E., Lamb D. Q., Fenimore E. E., Ramirez-Ruiz E., Cline T. L., Hurley K., 2001, *ApJ* , 552, 57
- Roming P. W. A., et al., 2005, *Space Sci. Rev.*, 120, 95
- Ruderman M., 1975, in Bergman P. G., Fenyves E. J., Motz L., eds, *Seventh Texas Symposium on Relativistic Astrophysics Vol. 262 of Annals of the New York Academy of Sciences, Theories of gamma-ray bursts.* pp 164–180
- Ruderman M. A., Tao L., Kluźniak W., 2000, *ApJ* , 542, 243
- Rybicki G. B., Lightman A. P., 1979, *Radiative processes in astrophysics*
- Rykoff E. S., 2008, GRB Coordinates Network, 8084, 1
- Sakamoto T., et al., 2008a, *ApJ* , 679, 570
- Sakamoto T., et al., 2008b, GRB Coordinates Network, 8101, 1
- Sakamoto T., et al., 2008c, GRB Coordinates Network, 8082, 1
- Sakamoto T., et al., 2008d, *ApJS* , 175, 179
- Sari R., 1998, *ApJL* , 494, L49
- Sari R., Narayan R., Piran T., 1996, *ApJ* , 473, 204
- Sari R., Piran T., 1999, *ApJ* , 520, 641
- Sari R., Piran T., Narayan R., 1998, *ApJL* , 497, L17+
- Savaglio S., Glazebrook K., Le Borgne D., 2009, *ApJ* , 691, 182

-
- Scargle J. D., 1998, *ApJ* , 504, 405
- Schady P., et al., 2007, *MNRAS* , 380, 1041
- Schady P., et al., 2012, *A&A* , 537, A15
- Schlegel D. J., Finkbeiner D. P., Davis M., 1998, *ApJ* , 500, 525
- Schmidt W. K. H., 1978, *Nature*, 271, 525
- Shen R., Zhang B., 2009, *MNRAS* , 398, 1936
- Skrutskie M. F., et al., 2006, *AJ* , 131, 1163
- Spruit H. C., 1999, *A&A* , 341, L1
- Stamatikos M., et al., 2008, GRB Coordinates Network, 8222, 1
- Stamatikos M., et al., 2009, GRB Coordinates Network, 9290, 1
- Stanek K. Z., et al., 2003, *ApJL* , 591, L17
- Starling R. L. C., et al., 2011, *MNRAS* , 411, 2792
- Stetson P. B., 1987, *PASP*, 99, 191
- Svensson K. M., Levan A. J., Tanvir N. R., Fruchter A. S., Strolger L.-G., 2010, *MNRAS* , 405, 57
- Tanvir N. R., et al., 2009, *Nature*, 461, 1254
- Tanvir N. R., Wiersema K., Levan A. J., 2010, GRB Coordinates Network, 11230, 1
- Testa V., et al., 2004, in H. Lewis & G. Raffi ed., Society of Photo-Optical Instrumentation Engineers (SPIE) Conference Series Vol. 5496 of Presented at the Society of Photo-Optical Instrumentation Engineers (SPIE) Conference, AQuA: an automatic pipeline for fast transients detection. pp 729–737
- Thompson A. R., Clark B. G., Wade C. M., Napier P. J., 1980, *ApJS* , 44, 151
- Thompson C., 1994, *MNRAS* , 270, 480
- Tody D., 1986, in D. L. Crawford ed., Society of Photo-Optical Instrumentation Engineers (SPIE) Conference Series Vol. 627 of Society of Photo-Optical Instrumentation Engineers (SPIE) Conference Series, The IRAF Data Reduction and Analysis System. pp 733–+
- Tody D., 1993, in Hanisch R. J., Brissenden R. J. V., Barnes J., eds, Astronomical Data Analysis Software and Systems II Vol. 52 of Astronomical Society of the Pacific Conference Series, IRAF in the Nineties. p. 173
- Tokunaga A. T., Vacca W. D., 2005, *PASP*, 117, 421
- Tosti G., et al., 2004, in A. F. M. Moorwood & M. Iye ed., Society of Photo-Optical Instrumentation Engineers (SPIE) Conference Series Vol. 5492 of Presented at the Society of Photo-Optical Instrumentation Engineers (SPIE) Conference, The REM optical slitless spectrograph (ROSS). pp 689–700

-
- Tueller J., et al., 2008, GRB Coordinates Network, 7402, 1
- Ukwatta T. N., Barthelmy S. D., Evans P. A., Gehrels N., Markwardt C. B., Page K. L., Palmer D. M., Rowlinson B. A., Siegel M. H., Stamatikos M., Vetere L., 2009, GRB Coordinates Network, 9281, 1
- van der Horst A. J., Wijers R. A. M. J., Rol E., 2006a, GRB Coordinates Network, 5871, 1
- van der Horst A. J., Wijers R. A. M. J., Rol E., 2006b, GRB Coordinates Network, 5874, 1
- Vestrand W. T., et al., 2005, *Nature*, 435, 178
- Vreeswijk P. M., et al., 2007, *A&A* , 468, 83
- Vreeswijk P. M., Jakobsson P., Jaunsen A. O., Oslo U., Ledoux C., 2008, GRB Coordinates Network, 7391, 1
- Vreeswijk P. M., Smette A., Malesani D., Fynbo J. P. U., Milvang-Jensen B., Jakobsson P., Jaunsen A. O., Oslo U., Ledoux C., 2008, GRB Coordinates Network, 7444, 1
- Wainwright C., Berger E., Penprase B. E., 2007, *ApJ* , 657, 367
- Wiersema K., Cucchiara A., Levan A. J., Rapoport S., Schmidt B. P., Bersier D., Perley D., Cenko S. B., Tanvir N. R., 2012, GRB Coordinates Network, 13276, 1
- Wiersema K., Tanvir N., Vreeswijk P., Fynbo J., Starling R., Rol E., Jakobsson P., 2008, GRB Coordinates Network, 7517, 1
- Willingale R., Genet F., Granot J., O'Brien P. T., 2010, *MNRAS* , 403, 1296
- Willingale R., O'Brien P. T., Osborne J. P., Godet O., Page K. L., Goad M. R., Burrows D. N., Zhang B., Rol E., Gehrels N., Chincarini G., 2007, *ApJ* , 662, 1093
- Woosley S., Janka T., 2005, *Nature Physics*, 1, 147
- Wozniak P., Vestrand W. T., Wren J., Davis H., 2008, GRB Coordinates Network, 7403, 1
- Wu X. F., Dai Z. G., Liang E. W., 2004, *ApJ* , 615, 359
- Wynne C. G., 1968, *ApJ* , 152, 675
- Xiao L., Schaefer B. E., 2011, *ApJ* , 731, 103
- Xu D., Fynbo J. P. U., Tanvir N. R., Hjorth J., Leloudas G., Malesani D., Jakobsson P., Wilson P. A., Andersen J., 2009, GRB Coordinates Network, 10053, 1
- Yost S. A., Schaefer B. E., Yuan F., 2006, GRB Coordinates Network, 5824, 1
- Yuan F., et al., 2010, *ApJ* , 711, 870
- Yuan F., Quimby R., Swan H., Akerlof C., 2008, GRB Coordinates Network, 7411, 1
- Zerbi R. M., et al., 2001, *AN*, 322, 275
- Zhang B., Fan Y. Z., Dyks J., Kobayashi S., Mészáros P., Burrows D. N., Nousek J. A., Gehrels N., 2006, *ApJ* , 642, 354
- Zheng W., et al., 2012, *ApJ* , 751, 90